Correlation of Near-infrared Chemical Imaging of Pharmaceutical Dosage Forms with their Dissolution Performance.

Lisa Jane Makein

A thesis submitted in partial fulfilment of the requirements of the University of London for the degree of Doctor of Philosophy in the Faculty of Medicine

The School of Pharmacy
University of London
29/39 Brunswick Square
WC1N 1AX, UK

2007

This thesis describes the research conducted at Pfizer Ltd. in Sandwich between September 2003 and August 2006 under the supervision of Prof. A. C. Moffat, Dr. R. D. Jee and Dr. F. C. Clarke.

I certify that the research described is original and that any parts of the work that have been conducted by collaboration are clearly indicated. I also certify that I have written all the text herein and have clearly indicated by suitable citation any part of this dissertation that has already appeared in publication.

Signature

08/09/07
Date

Abstract

Dissolution testing within the pharmaceutical industry provides valuable information regarding the drug release. Near-infrared microscopy (NIRM) imaging falls under the process analytical technology (PAT) heading promoting process and product understanding and can provide information related to problems, including dissolution. The aim of this research is to extend these findings with respect to NIRM imaging and dissolution with the emphasis on understanding the possible sources of variations observed.

A number of studies are presented retrospectively to gain an understanding of factors that influence both the images and dissolution. Changing blending time, compression force, particle size and sample ages were shown to affect both the images and dissolution profiles for a number of products. A comparison of the findings from investigative studies on one Pfizer product to a real dissolution example showed similar changes.

Correlation of the imaging and dissolution gave product specific results. No general statements could be made about NIRM and dissolution that would apply to any pharmaceutical product.

This work shows that it should be possible to use NIRM imaging as a method to control processes at an intermediate stage to provide information about the dissolution of a specific product and potentially allow remedial action to be taken.

Acknowledgements

Firstly I would like to thank Steve Hammond and Fiona Clarke, my industrial supervisor at Pfizer P.A.S.G for providing this opportunity for me and for all the subsequent help that was provided along the way, in both a work and personal context, I really appreciated it, thank you.

Thanks also go to my university supervisors Prof. Tony Moffat and Dr Roger Jee for the provision of academic guidance and regular challenges to my work in order to try and obtain the best results. I would also like to thank Mark Smith from P.A.S.G for all the times he helped with my questions on statistics and Excel as well as being kind enough to let me borrow a copy of his thesis.

As dissolution was not my forte when starting this work and as such I was in regular contact with a number of people regarding the apparatus, profiling and samples without whom I would have been totally stuck, so thanks go to Gary Bulgin from Caleva GB, Greg Dowds from CSP, Steve Griffiths from Light Pharma, Colin Dye from Zeiss and Phil Rogers from Pfizer for all their suggestions and help with my issues. This is also extended to Spectral Dimensions as they provided valuable training and problem solving from an imaging aspect.

I would like to acknowledge my colleagues in the former Root Cause Analysis group, Jordan, Christina and Linda as well as Jenny and the industrial trainees present over my three years, Linsey, Laura, Gillian, Joanne and Eilidh as they all made it a very enjoyable place to work as well as providing heads to bounce ideas off and help when required. I was very sad to leave them.

Finally I'd like to express my gratitude to my family as without their support over this time in my life, be it emotional, financial or just a well timed cup of tea, I wouldn't have managed quite so well. Especially I need to thank Joe for being so understanding, believing in me and trying so hard to help. It may not have seemed like it at the time, but I am very grateful for all you have done (and put up with!). Reaching this point had seemed so far away for so long, but I am glad to finally make it here.

Table of Contents

Abbreviations

AAPS	American Association of Pharmaceutical Scientists
AC	accelerated conditions
ALS	alternating least squares
AOTF	acoustic optical tunable filter
API	active pharmaceutical ingredient
ATR	attenuated total reflection
AUC	area under the curve
BCS	Biopharmaceutics Classification System
CCD	charge-coupled device
CDER	Centre for Drug Evaluation and Research
CGMP	Current good manufacturing practice
DCP	dibasic calcium phosphate
DE	dissolution equivalence
DPA	Division of Pharmaceutical Analysis
DPI	dissolution performance issue
EP	European Pharmacopoeia
FDA	Food and Drug Administration
fMRI	functional magnetic resonance imaging
FPA	focal plane array
GC	gas chromatography
Ge	Germanium
HCl	hydrochloric acid
HPLC	high performance liquid chromatography
HPMC	hydroxypropyl methylcellulose
ICH	International Conference on Harmonisation
InGaAs	indium gallium arsenide
InSb	indium antimonide
IR	infrared
I-R	immediate-release
JP	Japanese Pharmacopoeia
LCTF	liquid crystal tuneable filter
LM	lactose monohydrate
magst	magnesium stearate
MCC	microcrystalline cellulose
MCR	multivariate curve resolution
MCT	mercury cadmium telluride
MED	mean equivalent diameter
MIR	mid-infrared
MIRM	mid-infrared microscopy
MSV	mean score value
NCDA	National Centre for Drug Analysis
NIR	near-infrared
NIRM	near-infrared microscopy
NIRS	near-infrared spectroscopy
NMR	nuclear magnetic resonance

NDA	new drug application	SIMS	secondary ion mass spectroscopy
NN	nearest neighbour	SNR	signal-to-noise ratio
OOS	out of specification	SNV	standard normal variate
PAT	process analytical technology	SPD	sample preparation device
PC	principal component	SLS	sodium lauryl sulphate
PCA	principal component analysis	%STD	percentage standard deviation or normalised standard deviation
PEG	polyethylene glycol	SVD	single value decomposition
PLS	partial least squares	UMAB	University of Maryland at Baltimore
PRESS	predicted residual error sum of squares	USP	United States Pharmacopoeia
PVS	PharmaVision system	UV	ultraviolet
QC	quality control	ZnSe	zinc selenide
RM	Raman microscopy	2D	two-dimensional
%RSD	% relative standard deviation	3D	three-dimensional
RSS	Residual sum of squares	XPS	x-ray photoelectron spectroscopy

1 Introduction

1.1 Understanding Pharmaceutical Product Performance

The pharmaceutical industry is under increasing pressure to boost its production efficiency, but without losing final product consistency. Within manufacturing, the production of pharmaceutical dosage forms is a multi-stage process which can involve any number of unit processes such as milling, granulation or drying. A recent Process Analytical Technologies (PAT) initiative by the Food and Drug Administration (FDA) placed a major emphasis on the use of more reproducible, rapid and commercially viable techniques for process control (Department of Health and Human Services, FDA, 2004). This initiative can only lead to an increase in the monitoring of the unit processes via technologies such as near-infrared spectroscopy (NIRS), which is now well established within the pharmaceutical industry with applications ranging from identification of input materials to testing of the final dosage forms. However, the release of a product from production to market is still typically based on measurements of the physical and chemical properties of a sub-sample of the final dosage forms from a batch. The physical characteristics measured can include hardness, friability and weight. The chemical aspect of testing is centred on the active pharmaceutical ingredient (API) present. The amount of API in each dosage form (potency) is measured, then this is compared across the samples from the batch to give the content uniformity if the API is <25% m/m.

The manner and the duration of the API release are monitored through dissolution testing, but there is no insight into what may cause any problems arising. The majority of the quality tests require the sample to be destroyed, which makes it difficult to investigate any anomalies which may occur.

It is understandable for the quality control (QC) to be focused on the API as this is the most important component with respect to efficacy of the product for its intended use. However, there will be a number of other components present in the formulation. These “inert” ingredients, which are often overlooked by traditional testing, form a complex matrix, and they can exert a large influence on the properties of the final dosage form as well as factors that can affect the processing of the blend. As previously mentioned, NIRS is already in use for pharmaceutical testing and operating at a macro-scale it provides average chemical information for the whole sample analysed. Wavelength shifts and peak shape can give an indication of chemical interaction, but this does not provide any information about the properties of the sample matrix, such as the component distribution (Lewis *et al.*, 2005). Near-infrared microscopy (NIRM) is a technique where NIRS is combined with a microscope (Section 1.6.3). NIRM can enable the composition of the matrix at a micro-scale to be evaluated but, in addition, a spatial aspect of the components' distribution within the sample is gained. Chemical images can be produced by combining the chemical and physical/spatial information of each blend component revealing the physical interactions taking place. These micro-scale properties and excipient interactions can have an impact on stability, bio-availability, dissolution, blend uniformity, hardness and tablet sticking during compression (Clarke and Hammond, 2003; Clarke, 2003). From findings where NIRM has been used in a problem solving capacity, it was recognised that it would be beneficial to be able to predict physical properties or certain behavioural aspects of the final dosage forms at the macro-scale level from the chemical images. Inconsistencies with the dissolution performance of a product are a common complaint within the pharmaceutical industry. As a result of this, dissolution has been selected as the macro-scale property that will be investigated to predict a product's behaviour using NIRM imaging in this thesis.

1.2 Pharmaceutical Applications of Near-infrared Spectroscopy

In pharmaceutics, the determination of certain physical parameters associated with dosage forms are of great importance with regards to checking product consistency as well as fulfilling the regulatory release specifications. NIRS has been employed as an analytical tool in various different situations for the determination of these physical parameters. For example, it can be used on powdered excipients, APIs and blends for identification (Kramer and Ebel, 2000; Wargo and Drennan 1996; Grummisch, 1998), determination of crystallinity (Seyer *et al.*, 2000), particle size (O'Neil *et al*, 1998; O'Neil *et al.*, 1999; Plugge and van der Vlies, 1996; González and Pous, 1995), granulation monitoring (Day, 2001) and on-line blending homogeneity purposes (El-Hargrasy *et al.*, 2001; Aldridge *et al.*, 1996; Hailey *et al.*, 1996; Blanco *et al.*, 1998). In a study by Blanco (Blanco *et al.*, 1999) a system combining reflectance NIRS with a fibre-optic module allowed the measurement of the API in a blend in varying physical forms, including powder, tablet cores and coated tablets, without the need for any sample manipulation.

This can be used to promote process understanding, control and robustness. However, it is beneficial to analyse samples in the form in which they would be present when they reach the consumer i.e. in their final dosage form, as physical changes can occur upon compression or encapsulation of the blend.

As NIR radiation can penetrate compacted material, it can be used on samples such as tablets to provide an enormous amount of spectral information. A study of sample depth by Clarke *et al* (2002) found the information depth, DP_{50}, (where the substrate signal had half the initial intensity) had an exponential relationship with wavelength. The values ranged from ~27 μm at 2380 nm to ~180 μm at 1100 nm, therefore the tablet thickness must be taken into consideration at the shorter wavelengths. However the exponential relationship with depth was assumed but not proven and the wavelength differences observed would be sample dependant.

NIRS has been applied to the discrimination of polymorphic forms of APIs as they exhibit different IR spectra and hence different NIR spectra (Blanco and Villar, 2000, Lyon *et al.*, 2003, Gimet and Luong, 1987). Different polymorphs of the same substance can vary in their physical and chemical properties such as solubility, dissolution rate, melting point, resistance to degradation and these will therefore determine their therapeutic efficacy (Aaltonen *et al.*, 2003).

Tablet hardness is also a standard measurement made during the production and process monitoring of solid dosage forms. The tablet hardness is actually the compressive strength of the tablet. It is measured because if a tablet is too 'soft' it can disintegrate in transport, but also if it is too 'hard' then it may not dissolve adequately (www.engsys.co.uk, Nov 2003). The current methods of testing are destructive to the tablet and NIRS was shown to be successful in the prediction of tablet hardness to the precision of the conventional testing (Morisseau and Rhodes, 1997, Donoso *et al.*, 2003).

NIRS can also be used to determine degradation products (Drennan and Lodder 1990), film coatings (Kirsch and Drennan, 1995, Andersson *et al.*, 1999) moisture content (González and Pous, 1995, Webster *et al.*, 2003, Derksen *et al.*, 1998, Han and Falkner, 1996) and potency (Drennan and Lodder, 1993, Laasonen *et al.*, 2003, Trafford *et al.*, 1999; Eustaquio *et al.*, 1998, Merkle and Kovar, 1998, Gottfries *et al.*, 1996, Habib and

Kamel, 2003, Corti *et al.*, 1999, Broad *et al.*, 2001, Webster *et al.*, 2003) in intact tablets, including tablets containing the same API, but at two different dose strengths (Blanco *et al.*, 2000). In all cases the conventional requirement for sample preparation is bypassed reducing the opportunity for contamination or operator error.

Out with the pharmaceutical industry there are many other applications for NIRS. These range from determination of moisture in grains and seeds (Norris and Hart, 1996, Wesley *et al.*, 2005), fat content in meat, starch and lipids in flour in food and agriculture (Drennan *et al.*, 1991), moisture content in powdered milk (Nagarajan *et al.*, 2006) to the identification of woods for restoration work in historical buildings where there are legal requirements to be met (Nair and Lodder, 1993). NIRS has been used to predict the decline of hemlock trees in the USA (Pontius *et al.*, 2005), for the screening of food to ensure there has been no adulteration (Downey *et al.*, 2006) and raw material identification for paints and inks (Trenka and Oelichmann, 2002). From a biological angle, NIRS has been used to measure the blood content and flow in tissue (Rendell *et al.*, 1998), the examination of other samples from humans such as hair, skin and urine (McClure and Stanfield, 2002), obesity studies in rats (Buice *et al.*, 1998) and has applications in stroke research (Dempsey *et al.* 1997)

There are some more forensic approaches that have been employed whereby NIRS has been used to distinguish between genuine and counterfeit drug samples (Scafi and Pasquini, 2001). It has also been shown that NIR can be used in the detection of capsule tampering (Lodder *et al.*, 1987). Both natural and synthetic fibres can be evaluated by NIRS including wool, cotton and nylon as well as having some polymer applications for plastic laminates for example (Davies, 1987).

The use of NIRS extends into the semi-conductor industry, where it has been used to monitor the concentration of the solution used to clean the wafers produced through a Teflon tube (Lee *et al.*, 2005).

Dissolution and Disintegration

Of the various types of quality testing performed on solid dosage forms, dissolution is one of the most important. The drug availability can be controlled fundamentally by various pharmaceutical factors. Methods of predicting the dissolution rate of solid dosage forms have been investigated using NIRS (Gray, 2004). A correlation has been found between NIRS in transmission and the dissolution results for immediate release benzodiazepine tablets (Schatz *et al.*, 2003) and again for diffuse reflectance applied to clonazepam tablets (Freitas *et al.*, 2005). Another study was carried out on carbamazepine, a drug used to control epileptic seizures, as variations in effectiveness have been reported resulting in a fatality and a fifty million tablet recall (Zannikos *et al.,* 1991; Drennan, 1991). It was suggested that the presence of moisture was detrimental to the dissolution of the tablets e.g. if they were stored in a high humidity area by the patient such as a bathroom the effectiveness of the tablets would decrease. The results of the study showed that after exposure to water vapour, the branded tablets analysed gave a significant decrease in their dissolution rate, which was predictable over a four day period using NIRS.

Tablet disintegration, which is closely related to dissolution, has been investigated using theophylline tablet blends of the same formulation, but with varying disintegration times induced by changing the compression at which the tablets were manufactured. It was found that as the disintegration time increased, there was an increase in the NIR absorbance measured and using a calibration model, the disintegration time could be predicted from the NIRS results (Donoso and Ghaly, 2004, Donoso and Ghaly, 2005).

1.3 Dissolution

As previously mentioned, dissolution is one of the most important physical tests performed on a product. “The rate of solution of solid substances in their own solutions” was the title of the first paper on dissolution in 1897 (Noyes and Whitney, 1897). Subsequently, dissolution testing has become a well established, standardised method that has been made a regulatory requirement for the approval of all new drugs by the FDA. It is used to measure the performance of drug products and is an important method for assessing dosage form consistency and reproducibility between different batches of the same product, batches before and after certain changes (e.g. formulation), batches from different suppliers and results from different laboratories. In this context it has proven a useful tool for formulation development as well as quality control, which has lead to the mandatory status of the test within the international pharmacopoeias for solid dosage forms.

After a product has been orally administered by a patient, the rate of release and absorption of the API from that product will be governed by a number of factors. These include the solubilisation of the API under *in vivo* conditions i.e. the dissolution and the permeability across the gastrointestinal tract (Centre for Drug Evaluation and Research (CDER), FDA, 1997). Dissolution provides information on the *in vitro* availability of an API under simulated *in vivo* conditions. As this dissolution step is critical to the release of the API, the *in vitro* results might be applicable to the prediction of the *in vivo* behaviour. Prior to performing *in vitro* dissolution testing on a new drug application (NDA), dissolution specifications must be established to try and guarantee batch-to-batch consistency and to highlight when potential issues with *in vivo* bioavailability may occur. The Biopharmaceutics Classification System (BCS) can be used for this purpose.

1.3.1 Biopharmaceutics Classification System

The Biopharmaceutics Classification System was developed by Amidon *et al.* in the 1990's. The general guidance and regulatory standards on dissolution introduced by the FDA were too generalised to be of use when it came to product regulation and this type of examination tended to be on a product-by-product basis. This lead to the rationalisation that these regulatory standards may be simplified if drugs and drug products could be compartmentalised and defined under different, more general headings. This lead to the creation of the BCS to classify drugs based on their aqueous solubility and intestinal permeability (Amidon *et al.*, 1995).

It has been found that problems with immediate-release (I-R) formulations can arise where there have been dissolution differences observed *in vitro* for two products, but the drug concentration time profiles in blood were similar. This implies that the *in vivo* dissolution is not the rate-limiting step and any differences seen in the blood concentration profiles would be due to a differing rate of a physiological process occurring. The situation can also arise where two products have met the relevant dissolution specification, but differences are observed in the blood concentration profiles. These inconsistencies in highlighting situations of bio-in-equivalence have proved an obstacle in the assessment of bioequivalence by dissolution testing. The BCS however, offers a framework for developing more consistent dissolution specifications for the evaluation of bioequivalence (Hussain *et al.*, 1999). The BCS has subsequently been used as a benchmark in the regulation of bioequivalence of oral drug products (Gohel and Mehta, 2005). A guidance document from the FDA describes when requests to waiver the *in vivo* bioavailability and/or bioequivalence of IR products can be made by the use of the BCS (CDER, FDA, 1997).

The classification arose from consideration of drug dissolution and absorption models, which indicated that the there are three dimensionless parameters that are crucial in controlling drug absorption. These parameters are an Absorption Number (*An*), a Dissolution Number (*Dn*) and a Dose Number (*Do*) signifying the fundamental processes of membrane permeation, drug dissolution and dose occurring respectively. A theoretical basis, with significant implications for drug bioavailability and bioequivalence standards, was conceived to provide a means for determining when and under what conditions a correlation between *in vitro* and *in vivo* data would be anticipated.

Class	Solubility	Permeability	In vitro-in vivo (IVIV) Correlation Expectation
I	High	High	IVIV correlation of dissolution rate is slower than rate of gastric emptying, otherwise there is limited* or no correlation.
II	Low	High	IVIV correlation expected if *in vitro* dissolution rate is similar to *in vivo* dissolution rate, unless dose is very high.
III	High	Low	Absorption (permeability) is rate determining and limited or no IVIV correlation with dissolution rate.
IV	Low	Low	Limited or no IVIV correlation expected.

* Limited correlation means that the dissolution rate, although not rate determining may be similar to the absorption rate and the extent of correlation will depend on the relative rates.

Table 1-1: Biopharmaceutical Classification System (Amidon *et al.*, 1995)

The basis of the BCS is summarised in Table 1-1. For class I drugs with high solubility and permeability, the rate limiting step to drug absorption will be drug dissolution. The recommendation here is to measure the profile in several different media and at multiple time points. However, the rate limiting step in absorption can be gastric emptying when the dissolution rate is very fast and in this case no correlation to dissolution rate will be expected. From observations of gastric emptying times, it has been suggested that a dissolution specification of 85% dissolved in less than 15 minutes may ensure bioequivalence in I-R dosage forms. For class II drugs, with low solubility and high permeability, the dissolution profile must be very clearly defined and reproducible. Drug dissolution is the rate determining step in drug absorption and the absorption is usually slower than for class I drugs. For good correlations to be made, the dissolution method and media used must reflect the *in vivo* controlling process and it is recommended to measure the profile using multiple media. For class III drugs with high solubility and low permeability, the permeability is the rate determining step in the drug absorption. The dissolution profile has to be well characterised, but the rate and extent of drug absorption can be extremely variable in this class. If the dissolution is fast, as in class I when 85% is dissolved in less than 15 minutes, then any changes seen in the absorption will be the result of variations in the gastrointestinal transit and related processes rather than aspects of the dosage form. For class IV drugs with low solubility and low permeability there can be significant problems associated with providing effective oral delivery (Amidon *et al.*, 1995; CDER, FDA, 1997). The overall aim is to be able to develop specifications for a product that will ensure bioequivalence in future batches that are manufactured to fall within the dissolution specifications deemed acceptable. The method needs to be discriminatory and sensitive to variables that affect the dissolution rate (Brown *et al.*, 2005).

1.3.2 Dissolution Testing

The procedure for testing is defined in the Dissolution <711> and <724> Drug release United States Pharmacopoeia (USP) General Chapters. A variety of test conditions and apparatuses are described depending on the nature of the dosage form requiring the test. Typical testing would utilise 900 ml of a buffer solution or a hydrochloric acid (HCl) solution for the dissolution medium, which has been de-aerated prior to use. This would be used with apparatus 1 (baskets) or apparatus 2 (paddles) in a glass dissolution vessel at a constant temperature of 37 ± 0.5 ^{0}C, Figure 1-1. Apparatus 1 would typically use a rotational speed of 100 rotations per minute (rpm) while apparatus 2 would use 50 rpm. In the majority of dissolution testing performed, whether it is baskets or paddles, sampling is required at specific time-points. For I-R products these can be in the region of 15, 30, 45 and 60 minutes and for single point measurements this could be at 30 or 45 minutes. The apparatus required for a particular product is specified in the monograph for that product, along with the rpm, height of the basket/paddle, medium, measurement wavelength for the API, acceptance criteria and sampling time points to use.

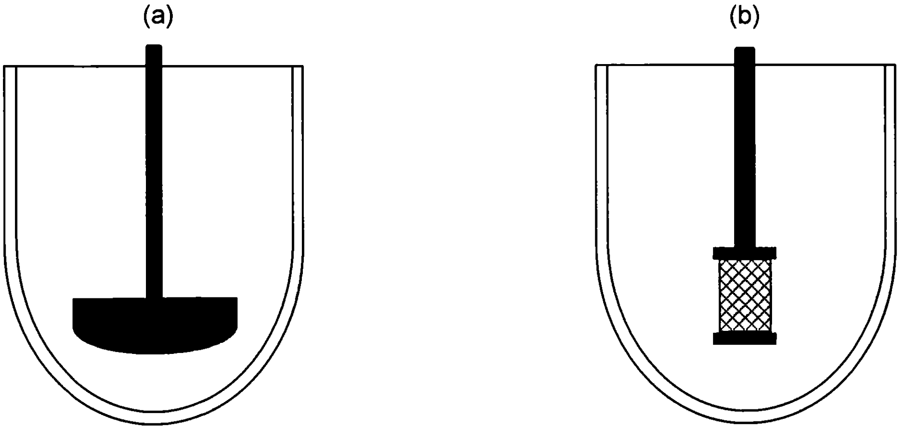

Figure 1-1: Schematic of USP dissolution (a) apparatus 2 and (b) apparatus 1

The USP is currently working to harmonise this chapter with the standards of the Japanese Pharmacopoeia (JP) and the European Pharmacopoeia (EP) and will deal with many areas including equipment dimensions and specifications, automation, use of sinkers and acceptance criteria.

The USP dissolution testing involves three stages, S_1, S_2 and S_3 with the acceptance criteria defined as a function of the quantity Q, which is a percentage of the labelled value that is established in the specified monograph. These acceptance criteria are summarised in Table 1-2. A product failing at S_3 dissolution would typically undergo investigation to find the cause of this major change in performance.

Stage	Number of Units	Acceptance Criteria
S_1	6	Each unit is not less than Q +5%
S_2	6	Average of the 12 (S_1 + S_2) units is ≥ Q and no unit is less than Q – 15%
S_3	12	The average of 24 (S_1 + S_2 + S_3) units is ≥ Q and not more than 2 units are < Q – 15% and no unit is < Q – 25%

Table 1-2: USP dissolution acceptance criteria

1.3.3 Sources of Potential Issues

There are many factors that can affect the dissolution rate of a product, which can be physico-chemical factors which include temperature, pH, degree of agitation, concentration gradient, composition and viscosity of dissolution medium (Arayne and Sultana, 1979). There have been some discussions on the relevance of water as a dissolution medium, due to its lack of buffering ability and lack of representation of the environment within the gastrointestinal tract (Noory *et al.*, 1999; Leeson, 2000). Physical changes in the actual dissolution set-up can also have an effect on the results obtained. These can include improper de-aeration and equilibration of the dissolution medium (Degenhardt *et al.*, 2004; Fliszar *et al.*, 2005), sample position in the vessel (Haystead, 2003; Healy *et al.*, 2002), centring of the spindles, verticality and wobble of the spindles, sources of vibration (Cox *et al.*, 1978), poor hydrodynamics (Haystead, 2003; Healy *et al.*, 2002) and irregularities in the vessel (Scott, 2005). In view of this, care must be taken to minimise the influence of any of these factors on the dissolution results by ensuring that the physical set-up is mechanically calibrated and the vessels are calibrated using the USP dissolution calibrators (Gray, 2006). These calibrators will be discussed in more detail in chapter five. A method for investigating out of specification (OOS) dissolution results was suggested by Scott, which looks into many aspects where sources of error may have occurred, including those beyond the apparatus and method used such as the personnel and the laboratory (Scott, 2002).

One method of improving the hydrodynamics in the vessel with apparatus 2 has been evaluated where the conventional paddle used has been replaced with one that has a crescent shaped spindle. The bottom section consists of a brush that has been shaped to the curve of the vessel and this maintains contact with the inner surface throughout the dissolution. Results have shown that this type of spindle, at a relatively slow 25 rpm, can consistently give a 100% dissolution plateau, which is sometimes not achieved by the conventional paddles. Another finding was that samples with different pharmaceutical properties, such as I-R and extended release (ER) could be analysed using a single set of conditions (Qureshi and Shabnam, 2003; Qureshi, 2004; Qureshi, 2006). Any new apparatus would require the rigorous qualification that was undertaken by the current apparatus. At a time where cost saving is pertinent in the pharmaceutical industry there will be resistance to move away from equipment it already owns and that can do the job as is currently required (Gray, 2006). New technologies such as fibre-optics have added to the effectiveness of the dissolution test.

1.3.4 Fibre-Optic Dissolution Testing

Fibre-optic based analysis for dissolution testing has been the subject of investigation for nearly 20 years and moved beyond the prototype stage 12 years ago (Cho *et al.*, 1995; Gray, 2003). It has the main advantage of being an in-situ measurement system negating the need for any sample extraction, simplifying the analysis and saving labour and resources. It also has the benefit of real-time analysis allowing the acquisition of dissolution profiles which can provide much more information on the dissolution behaviour of a product compared to that gained from time-point measurements. There also exists the possibility to automate the fibre-optic procedure using robots (Rogers *et al.*, 1999).

The system comprises four major parts, the dissolution apparatus, the spectrophotometer, the multiplexer and the probes (Nir *et al.*, 2001). The fibres transfer the light from the deuterium source in the spectrophotometer *via* the multiplexer to the probes immersed in the dissolution media. The light interacts with the solution present in the probe gap and is fed back to the diode array detector via the same light pathway. The fibres comprise a silica core and silica cladding which are selected for transmission in the UV wavelength range. As standard there is a filter present in the spectrophotometer which prevents light <220 nm passing into the fibres, as these wavelengths can cause solarisation of the silica. This leads to the formation of black areas in the fibres and a decrease in the absorptions. The fibres used are solarisation resistant, which means that they withstand the shorter wavelengths to a greater degree than normal fibres, but care must be taken to allow adequate recovery time between measurements.

The probes are specific to dissolution. There are two fibres, one to carry the light from the source to the probe and another to carry the signal back from the probe. There is a quartz lens and a back surface mirror within the stainless steel body of the probe. The light is focused by the lens through the liquid in the sample gap, which then gets reflected by the mirror back through the gap and is refocused into the fibre to the detector. The pathlength is determined by the size of the gap in the probe, which can be varied by using different sized probe tips.

Issues Encountered with Fibre-Optic Dissolution Measurement

There are two potential issues with *in-situ* measurements. One is the possible changes, which may occur to the hydrodynamics in the vessel, by having the probes present and any subsequent changes in the dissolution rate being measured (Martin, 2003). The other is interferences to the measurements by excipients and other particles moving through the sample gap.

There are a number of ways to deal with the first issue of changes in the hydrodynamic behaviour in the vessel. In the majority of situations, the presence of the probes in the solution does not cause any significant changes to the dissolution rate measured, except in the longest time-extended release drugs. For a particular formulation the absence of any effect can be shown, then the method validated with the probes remaining in-situ for the remainder of the measurements. The use of thinner probes as opposed to thicker ones can aid the situation. Immersion probes have a very reproducible effect on the hydrodynamic flow behaviour which it is possible to determine quantitatively, then corrected for (Schatz *et al.*, 2001). It has been shown that the results from dissolution calibration using prednisone calibrator tablets with the presence of rod and arc probe types in the dissolution vessels did not result in any failure to meet USP acceptance range (Lu *et al.*, 2003). The results from the fibre-optic sampling in this study were also compared to those obtained from manual sampling and the difference was ~1%.

For the cases where the change in dissolution rate caused by the probes is deemed statistically significant, there are two ways of compensating. One is to make use of an automated manifold, which can raise and lower the probes to be in the vessel for the measurement time alone (Schatz *et al.*, 2001). This total withdrawal of the probes from the solution has been shown not to be ideal in practice as residue can dry on the mirror and air bubbles can form in the gap when it is re-submerged. The other is to use in-shaft sampling whereby the probe is in the paddle or basket shaft, which would not cause any changes in the hydrodynamics (Lu *et al.*, 2003; Schatz *et al.*, Feb, 2000).

Excipient and other particle interferences are removed in conventional dissolution measurements by filtering the sample that is withdrawn from the vessel, before it is presented to the UV spectrophotometer. For the in-situ probes this is not possible, as the addition of a mesh, for example would change the hydrodynamics to a larger extent and lead to the collection of particles in the filter. Therefore these particles (and/or bubbles) would be present in the sample gap during measurement and these can cause scattering of the light resulting in a false change in absorbance (Lu *et al.*, 2003; Toher *et al.*, 2003). Data correction methods are required to compensate for this scattering effect and there are two correction algorithms in use. The first is a baseline correction. This can be performed using the response at one, two or multiple wavelength(s) outside the absorption band of the drug being measured as a reference, which is then subtracted from the drug band (Bynum *et al.*, 2001; Nir *et al.*, 2001; Lu *et al.*, 2003). The main assumption here is that any particles present would affect the drug and the reference band(s) measurements equally, so that the change in the absorption would be the same for both. Subtracting the offset value from the drug absorption would correct for the particle effects.

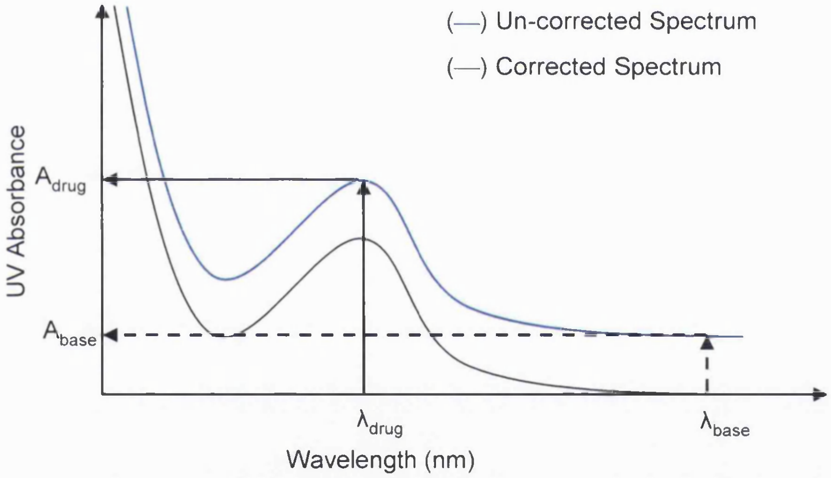

Figure 1-2: Scattering correction by baseline subtraction. Adapted from Bynum *et al.*, 2001.

From Figure 1-2, the A_{drug} must be corrected by the A_{base} to account for the spectral baseline shift due to particulates in the probe gap. This assumption needs verification for each system in use. This baseline correction method seems to be more accepted in the dissolution community. It is based on a physical principle, which if necessary can be directly confirmed so explaining this to the regulatory agencies may seem simpler than for a more indirect dissolution measurement. A Pfizer I-R, capsule product was used to evaluate the baseline correction method, by carrying out probe measurements and withdrawing samples at selected intervals coinciding with the probe measurements times. It was shown that the off-line UV measurements and the *in-situ*, corrected measurements nearly overlaid (Nir *et al.*, 2001). It was reported in the same study that the presence of two probes in the same vessel did not cause a significant change in the dissolution results when compared to the variance in vessel to vessel measurement.

The second method uses a second derivative calculation, to analyse the rate of change of the absorption curve and not the actual value. This data manipulation can be applied to correct for more severe interference which was demonstrated using a sample spiked with a specific amount of caffeine, to be measured, along with the sequential addition of a turbidity standard to mimic the situation that would occur from a disintegrating solid dosage form. In this instance a significant offset in the caffeine measurement remained after a single point baseline correction, but after the second derivative calculation was performed on the data, the amount of caffeine remained constant (Bynum *et al.*, 2001).

A paper in Dissolution Technologies examined the robustness of the *in-situ* measurements when baseline correction was utilised for capsule samples and found that changes in temperature, immersion depth and paddle speed did not change the fibre-optic dissolution results significantly (Schatz *et al.*, 2000). The ability to measure samples which contain two APIs and obtain two separate dissolution profiles has also been reported (Gemperline *et al.*, 1997; Johansson *et al.*, 2002).

1.3.5 Alternative Methods to Dissolution Testing

The FDA's initiatives focussed on Quality by Design and PAT has, to some extent put dissolution testing under investigation due to its potential flaws. The industry is now encouraged to gain more process and product understanding before the point where there are failures in the end-product testing such as dissolution, with the underlying aim of eradicating the requirement for any end-product testing. It is felt that the dissolution test can still provide results which are significant to the industry. Gray stated:

"*the dissolution test's ability to show changes in so many parameters is its power and its frustration. The power of the test outweighs the frustration for one simple reason*"

The reason being that it is the only test that has any degree of clinical relevance with regards to the therapeutic effect of the drug *in vivo* combined with the provision of assay data for the amount of API present (Gray, 2006).

Work has been carried out in an attempt to predict dissolution behaviour from physical parameters of the samples such as the microstructures of tablets, where computer simulation has been utilised in connection with actual sample data for dissolution predictions (Jia and Williams, 2006). Another study showed how the dissolution profile of a suspension formulation could be predicted from the mean of the particle size distribution (Tinke *et al.*, 2005). It has also been shown that the dissolution test can be accelerated by changing the temperature, solvent or paddle speed without any loss of correlation when compared to the results obtained by the "normal" test (Quist and Östling, 2002).

Sections 1.2 gave examples where NIRS had been utlised for the monitoring and/or prediction of dissolution and section 1.6.1 goes on to describe where MIRM imaging with attenuated total reflection (ATR) has also been applied for dissolution studies. The aim of this research is to extend this line of thinking to include NIRM imaging.

1.4 History of Near-infrared Spectroscopy (NIRS)

Herschel first discovered NIR radiation in 1800, when he projected a rainbow onto a bench using a prism and then measured the relative heating of the different colours (Herschel, 1800; Davies, 1998). He observed that on moving from blue to red, the temperature increased, but also that there existed a form of radiation just beyond the visible that could increase the reading on a thermometer significantly (Wheeler, 1929). This was initially named the infrared region, but it is now known as the near-infrared region. In 1881 the first infrared (IR) spectrum of an organic sample was recorded photographically by Abney and Festing between 700-1200 nm and further studies in absorption were mostly restricted to the mid-infrared (MIR) region.

The prevailing use of NIRS generally followed the work carried out by Karl Norris in the 1960's (Norris and Hart 1996). Norris applied NIRS for the determination of analytes in agricultural stocks. It was at this point that mini-computers became more readily available, enabling multiple regression analysis to be made practical (Davies, 1987).

In the early 1980's, the technique was labelled a "*sleeper*" compared to other spectroscopic techniques (Wetzel, 1983) as it was either unknown or not deemed legitimate for use by spectroscopists. This review of NIRS reflectance analysis put forward the potential of the method. Tony Davies stated in 1987 that it was "*Time for the Giant to wake up*" (Davies, 1987) and by 1998 it was believed that it had, but the "Giant" that had been envisaged was a "*pygmy*" compared to the actual potential that existed for the technique (Davies, 1998). The NIR region of the electromagnetic spectrum that had previously been regarded as having little analytical potential has become one of the most promising in molecular spectroscopy.

1.5 Theory of Near-infrared Spectroscopy

The NIR region falls between the visible and MIR regions of the electromagnetic spectrum. It is defined as the wavelength range of approximately 780 nm to 2500 nm (or 4000 cm^{-1} to 12800 cm^{-1}). This in turn can be divided into two regions, from 780 nm - 1100 nm called the Herschel region (short-wave NIR) and 1100 nm – 2500 nm (General Chapter 1119, USP-NF, 2005).

NIR absorption bands occur due to overtones and combinations of the fundamental molecular vibrations, which occur in the MIR region (Dempsey *et al.*, 1997). They are 10-1000 fold less intense, broader and overlap to a greater degree than the parent MIR vibrations, but can provide information which is not available from the MIR region i.e. combinations (MacDonald and Prebble, 1993). For the IR light to be absorbed, it must have sufficient energy to induce vibrational transitions in the molecule of interest. This means that the frequency of the light should be the same as for a fundamental vibration frequency of the molecule, which then causes a change in the dipole moment of the molecule due to this fundamental vibration (Blanco, 1998).

Overtones of polar groups that produce intense fundamental bands are the easiest to detect. Predominantly, the results of vibrations of light atoms, which have strong molecular bonds, are seen because the vibrational frequency is high enough to allow their overtones to be detectable in the NIR region (Wetzel, 1983). These tend to be from X-H bond stretching e.g. C-H, N-H, O-H and S-H.

1.5.1 Principles of Near-infrared Spectroscopy

Harmonic Oscillator

When two atoms form a covalent bond, there is an electronic rearrangement and the atoms finally come to rest at a distance where the energy of the system is at a minimum producing a diatomic molecule. The stretching of this bond is the only vibration that can occur. The potential energy of the molecule changes as any bond distortion occurs, as there will be repulsive forces acting when the atoms are pushed together or attractive forces when the atoms are pulled apart. These effects can be likened to the extension and compression motion of a spring and therefore Hooke's law can be utilised (Barton, 2002). This gives a parabola with the potential energy (V) as a function of internuclear distance.

$$V = \frac{1}{2}k\left(r - r_{eq}\right)^2$$ **Equation 1-1**

Where k is the bonding force constant which describes the rigidity of the bond, r is the internuclear distance and r_{eq} is the bond distance at the point of minimum energy.

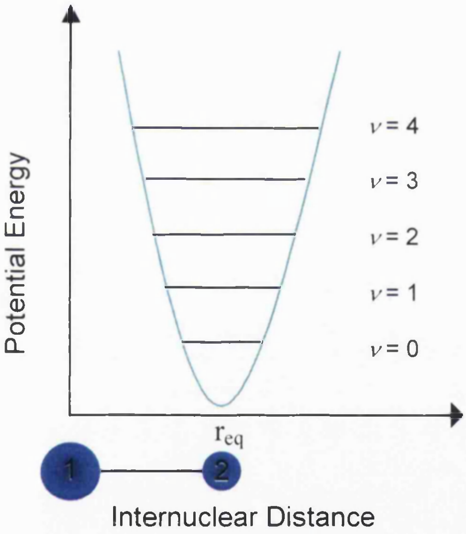

Figure 1-3 Potential energy curve for a diatomic molecule where Hooke's law is obeyed.

This bond distortion is proportional to the force applied. The vibration frequencies (f) for elastic bonds are specific and controlled by the reduced mass (μ) of the two-atom system and the bonding force constant k. The frequency of vibration can be calculated by,

$$f_c = \frac{1}{2\pi c}\sqrt{\frac{k}{\mu}}$$ **Equation 1-2**

Here c is the speed of light and μ is the reduced mass of the diatomic molecule given by,

$$\mu = \frac{m_1 m_2}{m_1 + m_2}$$ **Equation 1-3**

Where m_1 and m_2 represent the masses of each atom in the diatomic molecule. If the reduced mass of the diatomic bonds which contribute to the majority of NIR bands are compared, the values are very similar e.g. C-H has μ = 0.85, N-H has μ = 0.87 and O-H has μ = 0.89.

Equation 1.2 would predict that the vibrational frequencies of these bonds would be alike, but in reality this is not the case for actual molecules. The force constant (k) varies significantly with the electronic nature of the bond, i.e. the presence of neighbouring groups, and this largely governs the vibration frequency (Wheeler, 1929).

Quantum theory dictates that the vibrational energy can only have quantised, discrete energy values described by the Schrödinger equation. These energy levels are equally spaced, Figure 1-3.

There are selection rules that govern which energy level transitions are allowed. Only transitions where the vibrational quantum number changes by 1 are permitted i.e. Δv = ± 1. Transitions such as $v_{0\rightarrow1}$ or $v_{1\rightarrow2}$ are allowed, but any instance where $v_{0\rightarrow2}$ giving a change in the vibrational quantum number of greater than 1 is forbidden. A further condition set by these rules is that there must be a change in the dipole moment. Therefore diatomic molecules must show this change when the internuclear distance changes and the atoms have to be heteronuclear in order for them to be IR active.

At room temperature the majority of molecules will exist in the lowest vibrational energy level, v = 0 which results in the allowed transition from $v_{0\rightarrow1}$ being encountered most frequently. This transition gives rise to the fundamental frequency of the molecule which is detected in the MIR region.

Anharmonic Oscillator

For real molecules, this simple harmonic oscillator model is an over simplification of the situation. If the harmonic selection rules were followed, there would not be any NIR absorptions. For NIR absorptions to occur there have to be transitions where the change in vibrational quantum number is greater than 1. These relate to transitions such as $v_{0\rightarrow2}$ and $v_{0\rightarrow3}$. As a result of this the vibrational energy levels are no longer equally spaced.

The bonds are elastic, but Hooke's law no longer applies and extension or compression is not proportional to the force applied. There will also come a point in the stretching of a bond where the energy input is equal to the dissociation energy and the bond will dissociate into two atoms. This behaviour is not taken into account by the simple harmonic oscillator model. The Morse function is used as a good approximation of the potential energy curve as it accounts for unbound states, anharmonicity, overtone and combination frequencies, Figure 1-4.

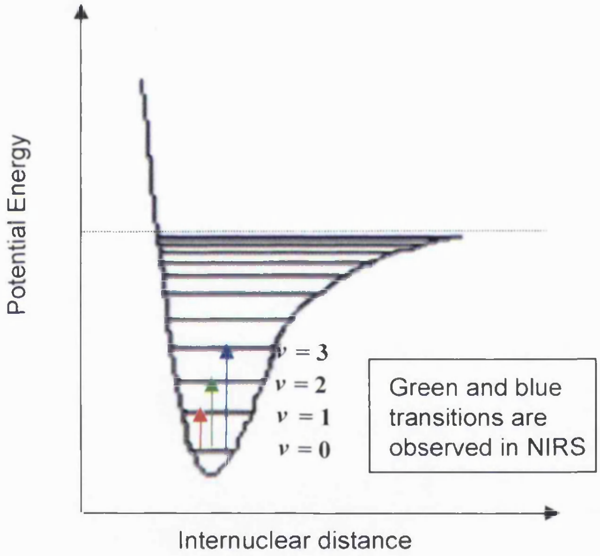

Green and blue transitions are observed in NIRS

Figure 1-4 Energy curves for an anharmonic (Morse function) oscillator

The energy levels are no longer equally spaced, but decrease with increasing v value. For the anharmonic oscillator, the selection rules state that the vibrational change can be $\Delta v = \pm1, \pm2, \pm3, \ldots\pm n$ where "n" is an integer, which gives the possibility of larger vibrational changes than for the harmonic model. In reality only the bands from $\Delta v = \pm 1, \pm 2, \pm 3$ have sufficient intensity to be observed in the spectra. The bands seen at $\Delta v = \pm2, \pm3$ are the first and second overtones respectively, which are the basis of NIRS. The first overtone will be stronger than the second, but the likelihood of either overtone occurring is still much less than for the fundamental transition.

Typically the molecules of interest will not be diatomic, but polyatomic. If the number of nuclei is *N*, there exists 3*N* – 6 energy levels in a non-linear polyatomic molecule. In a typical three component molecule such as water these vibrational modes can include a symmetric stretch, an asymmetric stretch, symmetric in plane bending and asymmetric in plane bending.

The situation can arise where there are energy changes occurring in two or more vibrational modes simultaneously. These can combine via addition ($f_1 + f_2$, $2f_1 + f_2$,....) resulting in a combination band being observed in the spectrum, (Blanco,1998). Combinations can be considered to be the average of two neighbouring molecular motions, where the nearness of the atoms is more important than the closeness of the energy levels. However the probability of this phenomenon is low and only the simple combination bands will be detected easily.

In NIRS the majority of the overtone and combination bands are from bonds to hydrogen (C-H, N-H, O-H and S-H). This is a result of the small reduced mass of such systems and large force constants, which means that the initial few overtones arise in the NIR region, Figure 1-5. Groups such as C=O, C-C, C-F and C-Cl have low fundamental frequencies in the MIR region, resulting in the first couple of overtones also being present at higher frequencies in the MIR region.

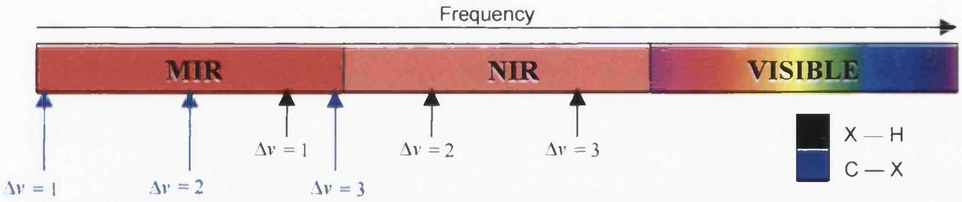

Figure 1-5 Comparison of approximate absorption bands from different bonds

1.5.2 Sample Presentation

Transmission and reflection are commonly used measurement techniques in NIRS, Figure 1-6.

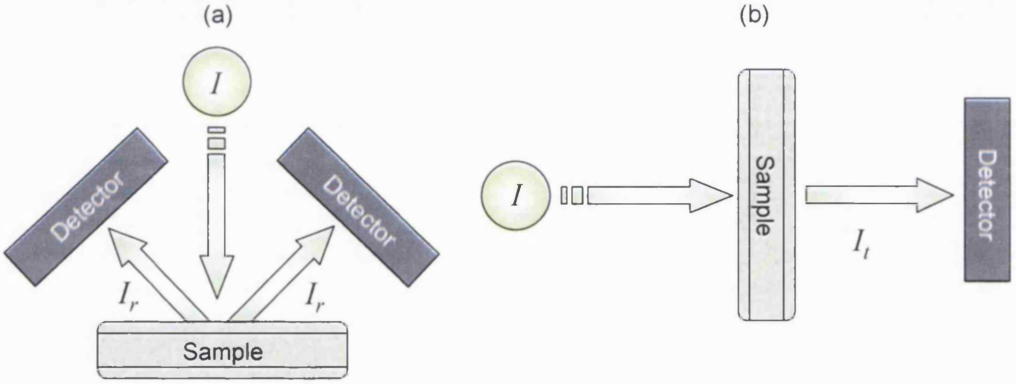

Figure 1-6 Schematic of Data Collection in NIRS (a) reflection and (b) transmission

For reflection, the ratio of the intensity of light reflected by the sample (I_r) to the intensity of light incident on the sample (I) is measured. For transmission, it is the ratio of radiation intensity transmitted by the sample (I_t) to that incident upon it (I) (General Chapter 1119, USP-NF 2005). These measurements would give the absolute reflectance and transmittance of the sample, respectively.

In practice, however, the value of I is not directly utilised and it is replaced by the intensity of radiation reflected by or transmitted through a reference material, I_0, which gives the relative reflectance or transmittance of the sample. The reference material can be a certified standard such as a Spectralon disc for reflectance measurements and air can be used for transmission measurements.

Reflection

As mentioned previously, the low molar absorptivity encountered in NIR absorption bands, typically between 0.01 and 0.1 $l\ mol^{-1}\ cm^{-1}$(Blanco, 1998), allows the reflection mode to be utilised for analysis of solid specimens.

The radiation incident on the sample can interact in a number of ways, Figure 1-7. It can be reflected straight back off the surface without any sample interaction and hence does not contain any compositional information. This is termed specular reflection and detectors are angled to reduce any contribution from this type of reflection. The light can pass into particles in the sample and it may be absorbed, if the frequency is correct for a molecule present, or it can be refracted into another adjacent particle in the sample. This process is repeated until the light is either absorbed or is reflected back from the incident sample surface, which is termed diffuse reflection. It is this type of reflection which can contain chemical and physical sample information as it can emerge in all directions from the incident radiation over a range of angles from the sample surface. It is the basis of measurements by this technique (Blanco *et al.*, 1998). Diffuse reflection only occurs from the first few tenths of a millimetre of the sample surface.

A relationship can be applied, similar to Beer's law, which is described in terms of concentration and relative reflectance.

$$A_0 = \log\frac{1}{R} = a'c$$

Equation 1-4

Where

$$R = \frac{I_r}{I_0}$$

Where A_0 is the relative absorbance, R is the relative reflectance, a' is a proportionality constant and c is the concentration. This can provide acceptable results in various diffuse reflection applications.

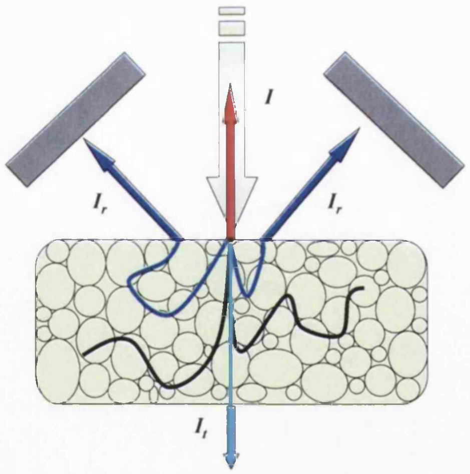

Figure 1-7 Radiation pathways within a solid sample showing specular reflection (—), diffuse reflection (—), transmission (—) and absorption by the sample (—). Adapted from M. R. Smith, PhD Thesis 2004.

Transmission

In comparison to reflection measurements, transmission measurements represent a larger proportion of the sample analysed. This can be advantageous when the homogeneity of a sample cannot be guaranteed. For example if a degradation product was of interest, diffuse reflection results of a small sample volume may be misleading as the distribution may not be homogeneous (Gottfries *et al.*, 1996). Figure 1-7 shows the possible light pathways through a sample. The way the light is scattered through a sample is dependent on the process by which the sample is produced i.e. the manufacturing process. Scattering within a tablet can result in a wide range of photon pathlengths, anything from a few millimeters up to approximately a metre before emerging to be detected (Abrahamsson *et al.*, 2005). When the radiation emerges it can be at many angles compared to the incident light, but from the opposite side of the sample and this is where the detector is positioned. This scattering can effect calibration, but data pre-treatment methods are employed to help compensate for this.

As the light has to pass through the whole depth of the sample to reach the detector, significantly less of the incident radiation arrives there making lower energy measurements compared to reflectance methods.

1.5.3 Exploitation of the NIR Region

The information contained within NIR spectra is not readily accessible as it is with MIR spectra, due to the broad overlapping peaks obtained. Advanced deconvolution techniques are required to extract the data and allow interpretation, combined with calibrations to allow quantitative analyses. The immense growth of NIRS is primarily the result of advancements in powerful computer hardware and chemometric software, allowing the technique to be utilised to its full potential (MacDonald and Prebble,1993). The expansion in the use of NIRS as an analytical tool is also likely to be down to two factors that are advantageous to its application for quality control. The first is the low molar absorptivity of the NIR bands, which permit the analysis of solid samples in reflection mode with minimal, if any prior sample manipulation. Along with a high degree of flexibility with regards to the type of sample which can be handled by the technique, solids through to liquids, and increasing the throughput of samples, there exists a dependence of the spectral signal on the chemical and physical properties of the sample in question. This allows the identification and determination of both these parameters from the spectra, making NIRS an appealing technique for the examination of pharmaceuticals.

1.6 Spectroscopic Microscopy and Imaging Techniques

As an extension to spectroscopy methods, which give information at macro-scale, it is possible to combine a spectrometer with a microscope or microscope optics. This addition still permits the spectroscopic identification of the components present, but also provides invaluable information regarding the two-dimensional distribution enabling visualisation of the sample matrix at a micro-scale. This technique is available for use with visible (Bonifazzi *et al.*, 2006; Exline *et al.*, 2003), X-ray fluorescence (Patterson and Havrilla, 2006), MIR, Raman, and NIR spectroscopies.

1.6.1 Mid-infrared Microscopy

The concept of this spectrometer/microscope union was initially voiced nearly 60 years ago in 1949 when a reflecting microscope was joined with an MIR spectrometer as it was becoming increasingly desirable to be able to analyse very small amounts of material in biological problems (Barer *et al.*, 1949). Later that year, another paper was published on research into the coupling of other reflecting microscopes to a MIR spectrometer (Gore, 1949). The first commercial microscope attachment for MIR spectrometry was provided by Perkin-Elmer in 1953 (Reffner *et al.*, 1987). Since then MIR microscopy (MIRM) has been employed for many applications including geology (Guilhaumou *et al.*, 1998), pharmaceutical blend homogeneity monitoring (Lee and Lin, 2004), identification of silicone in human breast tissue (Centeno and Johnson, 1993), fibre analysis, plastic laminates and forensics (Reffner *et al.*, 1987). The advent of focal plane array (FPA) detectors in the 1970's (Lewis *et al.*, 1997) led to the development of MIRM with the ability to produce chemical images. Initially the MIR-FPA combination was utilised for remote sensing such as in the field of astronomy and for military surveillance applications. In the mid-nineties this technology was made more widely available and was adopted by laboratory spectroscopists (Colarusso *et al.*, 1998). FPAs consist of a grid made up of multiple detection elements called pixels. Each pixel has the ability to measure a spectum and they are all active simultaneously when measurements are collected. The arrays can be made from indium antimonide (InSb), doped silicon and mercury cadmium telluride (MCT) amongst other materials, which can influence the wavelength range available for measurement (Colarusso, 1998; Lewis *et al.*, 1997; Kidder *et al.*, 1997). Due to the semi-conductor nature of these detectors they perform optimally at sub-zero temperatures which are generally achieved by the use of liquid nitrogen.

This MIRM imaging has been harnessed for medical applications, providing images to show the presence of silicone in breast biopsy tissue (Foster, 1997) and to monitor the mechanism of cyanoacrylate tissue adhesion to cartilage (Chenery and Bowring, 2003). Work has also been carried out on polymer systems to characterise the phase morphology of blends (Oh and Koenig, 1998; Kressler *et al.*, 1998). It has also been used to differentiate between samples with "good" and "bad" dissolution behaviour using univariate analysis of each component present (Roggo *et al.*, 2005). The dissolution of polymers under different organic solvent conditions has been studied by the timed acquisition of sequential images in transmission, which provided the means to study solvent penetration, dissolution rate and diffusion profiles (Ribar *et al.*, 2000; Ribar and Koenig, 2001; Miller-Chou and Koenig, 2002; González-Benito and Koenig, 2002). The same timed image method was used to examine drug delivery behaviour during controlled dissolution of a drug from a polymer matrix (Coutts-Lendon *et al.*, 2003) and gave an insight into the effect of crystallinity and molecular weight on the dissolution rate of polyethylene oxide (Coutts-Lendon and Koenig, 2005).

Attenuated Total Reflection

The introduction of an attenuated total reflection (ATR) imaging objective can provide improved spatial resolution for MIRM imaging (Chan *et al.*, 2005). The sample is introduced directly onto the ATR crystal (zinc selenide (ZnSe), Germanium (Ge) or diamond), which has a relatively high refractive index compared with air. Pressure is applied on top of the sample to ensure good contact with the ATR crystal in order to produce a consistent image. The MIR light is totally internally reflected at the crystal-sample interface and it is here that the light enters the sample by up to a few microns as an evanescent wave. This produces attenuated radiation, which is detected and from which a MIR spectrum is obtained (Chan *et al.*, 2003).

In this configuration there have been many studies carried out, mainly by the same basic research team of K. L. A. Chan and S. G. Kazarian, which encompass pharmaceutical systems (Chan *et al.*, 2003; Chan and Kazarian, 2005; Chan and Kazarian, 2006a; Chan and Kazarian, 2006b) along with an investigation into the imaging of a human hair (Chan *et al.*, 2005). As previously mentioned, controlled forms of dissolution have been monitored using MIRM with a FPA and this has also been performed using ATR with MIRM and FPA detection. In these studies, however, it was possible to investigate dissolution in aqueous solution as the evanescent wave does not penetrate far into the sample providing a very small pathlength. Therefore the measurement is not hampered by the strong MIR absorption of water (Kazarian and Chan, 2003). The sample was attached directly onto the ATR crystal, but positioned to cover only half of the total area to allow water to be added to the other half. A number of different drug and excipient/polymer complexes were considered including drug/polyethylene glycol (PEG) (Kazarian and Chan, 2003; Kazarian and Chan, 2006b; Chan and Kazarian, 2006c; Chan and Kazarian, 2004) and drug/hydroxypropyl methylcellulose (HPMC) (van der Weerd and Kazarian, 2005; van der Weerd and Kazarian, 2004b; van der Weerd *et al.*, 2004). This also included a study of the swelling of a HPMC tablet upon dissolution (van der Weerd and Kazarian, 2004a). One of the papers included the calculation of the concentration of the components from the images after calibration, which were then compared to the results from UV detection of the aqueous dissolution solution (van der Weerd and Kazarian, 2004b). Unlike the previous MIRM/FPA studies, there was no attempt to calculate the dissolution rates of the drugs or model the release profiles.

1.6.2 Raman Microscopy

There have been many Raman microscopy (RM) imaging methods developed since the 1970's. It is a complementary method to MIR as vibrational modes which are MIR inactive, such as in symmetrical molecules with no change in dipole moment, will be Raman active. Detectors similar to the FPAs in MIRM are utilised, called charge-coupled devices (CCD) and are made from silicon. High quality CCD detectors are available at a reasonable price and as a result RM imaging approaches were more generally employed in spite of the potential for fluorescence and the inefficiency of the Raman scattering process when compared to MIRS (Lewis *et al.*, 1995). RM imaging can be described in two ways, as mapping and global illumination. Mapping is when spectra are collected either point-by-point or line-by-line, facilitated by stage movement. Global illumination is when the entire sample area is imaged and tuneable filters such as liquid crystal (LCTF) or acoustic optical tuneable filters (AOTF) are used for wavelength selection (Šašić and

Clark, 2006). The global illumination mode provides images directly whereas the mapping data must undergo processing to enable image generation. Even with the extra data manipulation step, mapping instruments are most commonly used and understood. RM imaging has been successfully applied to a wide range of industries. Applications include polymers (Schaeberle *et al.*, 1995), biological samples (Kleine and Treado, 1997; Sheifer-Peltier *et al.*, 2002; Eliasson *et al.*, 2006; Matthäus *et al.*, 2006) and pharmaceutical samples (Brody and Clark, 2003; Šašić and Clark, 2006; Clegg and Everall, 2003; Enculescu and Steiginga, 2002).

1.6.3 Near-infrared Microscopy

MIRM and RM have been seen as the conventional imaging methods for studying micron-sized samples. MIRM as mentioned previously has found much use for biological samples and RM has its footing in pharmaceutical analysis (Hammond and Clarke, 2002). The benefits and use of NIR combined with microscopy and imaging have only really been considered as a possibility within the last decade.

NIRS has a better ability to distinguish between different types of carbohydrates (lactose, cellulose products and starch), which are present in many pharmaceutical formulations to perform certain functions. To gain the maximum imaging information from a pharmaceutical sample it is essential that each carbohydrate can be identified in the presence of others, but due to many similarities in their chemical structures this proves problematic for MIRS and RM.

If the situation occurs where hydration state of certain sample components is of interest then RM cannot be utilized as water does not have an effect on the spectra.

Sample presentation can be more relaxed for NIRM imaging compared to the requirements of the other techniques. RM must have very flat samples as a result of a limited depth-of-field available and MIRM imaging needs samples to be sectioned and flat as most work is carried out using transmission measurements due to signal-to-noise constraints (Koehler *et al.*, 2002).

In contrast, RM can have an advantage over NIRM when inorganic materials are involved. Samples such as dibasic calcium phosphate (DCP) do not give a NIR spectrum, but it is active for RM and gives a response. Another benefit that can be gained by the use of RM is a smaller spatial resolution. Spot sizes of ~1 μm can be obtained in RM due to the laser excitation source, whereas the spatial resolution in NIRS is limited by the wavelength of the light in use and cannot go below ~5 μm (Clarke *et al.*, 2001). The two approaches have been combined in a way where the same sample was analysed on one technique then the other and the spectral information from both was interpreted to give a more comprehensive image of the whole formulation (Clarke *et al.*, 2001). This image fusion technique improved the information gained from the techniques individually, but it is possible to locate the dibasic calcium phosphate (DCP) in NIRM by the absence of its spectrum or through multivariate approaches (Hammond and Clarke, 2002).

Principles of Near-infrared Microscopy and Imaging

The instrumentation requirements for a NIRM imaging system have not changed significantly since the first forays of spectrometer/microscope pairing in 1949. The general set-up requires an illumination source of NIR radiation onto the sample, microscope optics, a method of wavelength separation/filtration, a means to detect the radiation coming back from the sample and a system to record the data with analysis software (Lewis *et al.*, 2005). There are currently three modes of data acquisition available based on this general set-up and similar to those available for RM imaging: point mapping, line mapping and global illumination. In point mapping a single element detector is utilised and an individual spectrum is obtained at a point of fixed dimensions on the sample surface. The sample stage moves to the next point and this is repeated until the total sample area defined has been scanned. Line mapping is based on the same technique of controlled stage movement, but in this case the detector consists of a linear array of elements/pixels. When global illumination is implemented, the whole sample area is measured simultaneously using a FPA and tunable filters, LCTF or AOTF to control the wavelength selection, in a similar way to RM imaging. Figure 1-8 shows the maximum live detector elements during data collection.

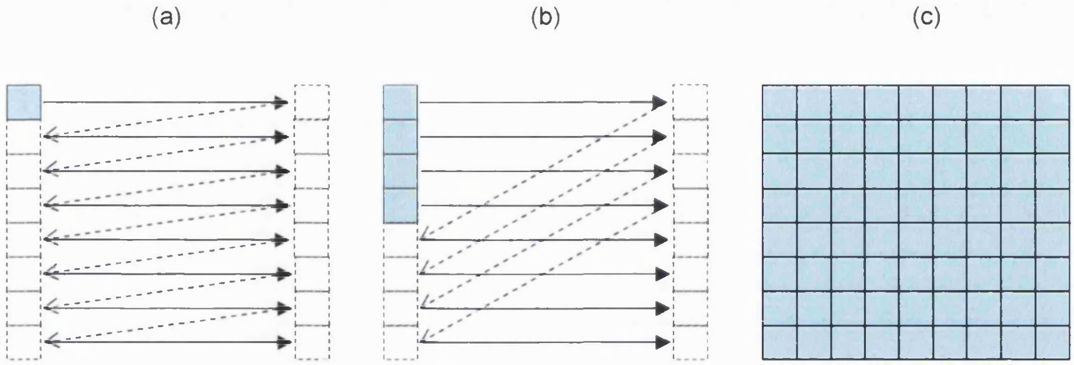

Figure 1-8: Schematic of scan configurations in (a) point mapping, (b) line mapping and (c) global illumination (Colarusso *et al.*, 1998)

Even with this variation in acquisition, the data obtained from NIRM imaging are independent of the method used. There will always be a spatial element from either the combination of the single or line array detector results over the defined sample area or the dimensions of a FPA, combined with spectral information at each pixel measured. This combination provides a three dimensional image cube, often referred to as a hypercube (Lewis *et al.*, 2005) which contains all the information required for the determination of component identification, distribution and quantification, Figure 1-9.

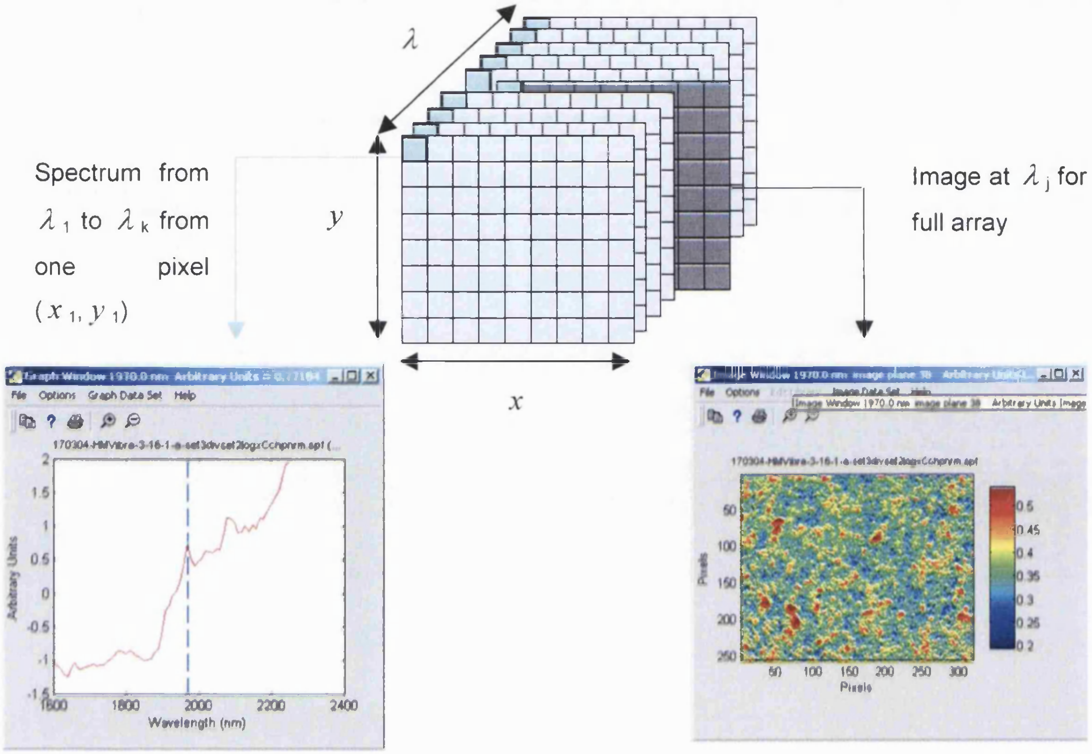

Figure 1-9: Schematic of a hypercube illustrating the spatial and spectral components. *Adapted from Lewis et al., 2005.*

Applications of Near-infrared Microscopy and Imaging

The advent of commercially available de-classified, military FPAs has meant that over the last decade, NIRM imaging has been more readily explored for smaller scale laboratory and industrial applications. Progress has been made in many different fields from food through to forensics.

NIRM imaging has been used for agricultural samples where it showed the ability to produce chemical images of soybean seeds, somatic embryos and single cells at a resolution approaching one micron. This allowed detailed analysis of the oil and protein content and demonstrated a potential for aiding research in genomics and proteomics as a method for the fast and accurate detection of high-content micro-arrays (Baianu *et al.*, 2003). Another study had corn kernels as the sample of interest. In this case, it was possible to predict the oil or oleic acid content from images and spectra of the kernels using chemometrics. The non-destructive measurement of these properties can highlight different genotypes of corn which are important for selective breeding (Weinstock *et al.*, 2006). On a similar thread, NIRM was used for the identification of desirable or undesirable traits in grain kernels to assist the plant breeding of wheat (Samil *et al.*, 2006).

Further examples have been published where NIRM imaging has been able to provide information on properties of food stuffs. The ripening of kiwi fruit is characterised by the conversion of starch into soluble solids comprising glucose, sucrose and fructose. NIRM imaging calibrations were able to predict the concentrations of the soluble solids in ripening fruit and, although the accuracy was not as good as the reference method (refractometry), a benefit was found in the ability to show the spatial distribution of the solids (Martinsen *et al.*, 1998). Similarly the sugar distribution in melons was visualised by NIRM imaging (Tsuta *et al.*, 2002). Pickling cucumbers have also been the subject of NIRM imaging research. Mechanical injury to cucumbers upon harvesting and handling can damage the fruit internally, which is difficult for human inspectors to identify and upon pickling and these bruised fruit represent a major financial loss. NIRM imaging provided a means to differentiate bruised tissue from normal tissue as the former generally had lower reflectance compared to the latter (Ariana *et al.*, 2006). It has also been applied to detect fecal contaminants on apples (Liu *et al.*, 2007). Strawberries were the subject of another NIRM study where the interest was to determine certain physical attributes to describe the quality of the fruit (ElMasry *et al.*, 2007).

Animal feed has also been the subject of investigation. The composition of such feeds is now governed by stricter controls since Bovine Spongiform Encephalopathy (BSE) was discovered to try and stop its spread. An example of cattle feed was used and NIRM imaging showed the potential for identifying particles of feed that contained a poultry by-product from all the other particles (Koehler *et al.*, 2002).

NIRS has been extensively used for the analysis in the polymer industry, but it is known that these types of polymer samples tend to be chemically inhomogeneous. Understanding this inhomogeneity was deemed highly important before the application of any NIRS method, particularly if it only measures one point in the sample. In order to appreciate any inhomogeneity present in a sample it would be necessary to take measurements at several positions of that sample, which is where NIRM imaging was utilised. Samples of ethylene/vinyl acetate copolymers with varying amounts of vinyl acetate have been analysed and chemical inhomogeneity present in all the samples was identified from the images viewed at a single channel (Tran *et al.*, 1998). In a further example, the reaction kinetics of epoxy resin curing were monitored using the epoxy band at 1155 nm. The data from individual pixels at different positions in the chemical images showed a maximum difference of 37% in the degree of epoxy groups, but this variation caused by the inhomogeneity in the sample was lost when the average was taken from a large number of pixels (Fischer and Tran, 1999). The kinetics of sol-gel formation and solid-peptide synthesis were determined in a similar fashion (Tran and Politi, 2002; Fischer and Tran, 1999).

NIRM imaging has extended into the realm of forensic science. It has been applied to the analysis of ball point inks (Payne *et al.*, 2005) and the printing ink used for U.S. currency (Tran *et al.*, 1998). Counterfeiting comes under the same forensic heading and work has been conducted to identify this, mainly within pharmaceutical products. Samples of genuine and counterfeit anti-malarial tablets were evaluated by NIRM imaging and it was relatively simple to split them into various groups related to their APIs using chemometrics (Wolff *et al.*, FACSS, 2005, Dubois *et al.*, 2007).

Just as MIRM imaging can be applied to biological samples, NIRM imaging has found a use in this area. NIRM imaging has been used in stroke research where the analysis of different lipoprotein arterial deposits has been carried out on human samples to gain a better understanding of the processes leading up to a stroke (Dempsey *et al.* 1997). NIR imaging was used for obesity studies in rats where the fat/lipid metabolism was monitored (Buice *et al.*, 1998). Similarly it was also found that surface temperature and lipid composition could be studied in rats that were conscious and free to move around by NIR imaging (Cassis *et al.*, http://kerouac.pharm.uky.edu/ASRG/Wave/Lipo/lipo.htm). Attas *et al.* found that hydration of the skin could be measured with NIRM imaging. This was carried out by the application of a drying agent or a moisturiser to a test subject's skin *in vivo* and comparing the regions in the chemical images to those without any applications (Attas *et al.*, 2002). Recently NIRM has been shown to have an application for the determination of the degree of burns to the skin which can aid the medical profession in selection of the best treatment for the patient (National Research Council Canada, http://www.nrc-cnrc.gc.ca/highlights/2005/0506nir_spectroscopy-print_e.html).

Many of these applications have found extended benefits from using NIRM imaging compared to the standard spectroscopic methods alone, but in just as many instances only a small portion of the imaging data acquired is actually utilized e.g. the response at one wavelength of one component is monitored over a selected number of pixels.

The number of pharmaceutical applications has been increasing in the last few years as the technique has become better known for this purpose. At the beginning of 2006 the breaking news on in-PharmaTechnologist.com was that NIRM imaging *"was emerging as the analytical tool of choice for drug development, analysis and process monitoring"*.

At the American Association of Pharmaceutical Scientists (AAPS) meeting in 2005 NIRM imaging was shown to be able to predict the amount of API and another excipient present in direct compression tablets (Shah *et al.*, 2005). Imaging has also shown potential for layer visualisation in time-release granules (Lewis *et al.*, 2001), distinction between coated and uncoated elements in a granule mixture (Lewis *et al.*, 2005) and for the measurement of the amount and location of moisture in coated and uncoated tablets with different manufacturing processes (Gulian *et al.*, 2005). The degradation of gelatin capsules by the exposure to formaldehyde was investigated using NIR imaging (Hamilton and Lodder, 2002; Hamilton *et al.*, 2002). It was estimated that nearly 1300 tablets could be simultaneously measured inside their blister packaging using a particular set-up (Malik *et al.*, 2001). This high-throughput type of method continues to find applications in the pharmaceutical industry and more recently was used for a quantitative determination of the API concentration in tablets. It was achieved by placing calibrator tablets of known API concentration in the same field of view (FOV) as those of unknown concentration (Lee *et al.*, 2006).

The location and identification of impurities was found to be of interest in another investigation, whereby it was useful to know where to look if further impurity analysis was required on a sample (de Juan *et al.*, 2004; Lyon *et al.*, 2005). Blend homogeneity has been another parameter investigated. It was discovered that the value of the percent standard deviation for the amount of API (calculated from the standard deviation of the pixel distribution from the scores image) increase upon moving from homogeneous to heterogeneous blends (Lyon *et al.*, 2002). NIRM imaging has also been applied to visualise over-the-counter formulations (Lewis *et al.*, 2005; Koehler *et al.*, 2002) as well as prescription pharmaceutical products. Major insights have been gained by the use of NIRM imaging in a troubleshooting capacity (Lewis *et al.*, 2004). Examples have been reported where the distribution of a matrix component, not always the API, was different between "good" and "bad" samples. This difference was subsequently attributed to causing the particular issue such as problems with dissolution, tabletting, process of manufacture (Clarke and Hammond, 2003; Clarke, 2004). Information can also be gained on how the manufacturing process affects the end product e.g. how the roller compaction force used to produce tablets can alter the disintegrant distribution and hence give variations in the dissolution performance (Clarke, 2004). The coating of other powders by magnesium stearate has been studied as this can have a great influence on the successive dissolution performance of the blend (Ellison *et al.*, 2005). In all of the pharmaceutical applications, a much larger amount of the data collected has been utilised than previously reported. This extra information being obtained is being put to good use as it is slowly being realised that the "inert", non-API components of the formulation are possibly more "active" in determining product performance than was previously thought.

In summary dissolution irregularities occur frequently within the pharmaceutical industry and due to the inherent nature of the testing it becomes difficult to investigate these issues further on the same samples. The PAT initiative has urged companies to steer away from problem solving after the event has happened and to focus on process understanding to enable prediction of the products behaviour at a much earlier stage in the manufacturing process. The final goal would be to have the ability to predict certain behaviour from the NIRM images of the blend at an intermediate stage in the process to provide pass or fail criteria and forego the destructive testing.

It has already been established in previous work that there can be correlation between the distintegrant in the NIRM images and dissolution results for one specific pharmaceutical product (Clarke, PhD thesis, 2006). However, further work would be required to evaluate other potential factors that could affect the dissolution behaviour and how/if these differences would present themselves in the NIRM images of the samples.

1.7 Aims and Objectives.

The scope of this work is to extend what has been done previously and to gain more knowledge about what may be causing the dissolution problems within the sample matrices using NIRM imaging. The use of the fibre-optic dissolution set-up will allow a greater amount of information to be extracted from the resultant profile data that will go far beyond the usual set time point measurements used in the specification for conventional dissolution testing. This will allow factors related to the dissolution rate to be available for the eventual comparison to the NIRM images.

Some preliminary experiments will be carried out to determine the factors that cause changes in the NIRM images and the dissolution performance. This will include analysis of samples produced to further the understanding of how certain changes to the physical parameters in the sample production, such as blending time can affect the images and subsequent dissolution behaviour of a number of products. This will provide information as to whether or not there may be any common causes for dissolution variation in pharmaceuticals generally. Features of the NIRM images to be examined will be parameters such as the number and size of the component domains, as well as descriptors of the distribution of the API over the image such as the mean score value (MSV) that gives an indication of the abundance in the image.

The work will then progress onto some “real” examples to evaluate if any effects observed in the laboratory based studies were also seen in actual products. The products chosen were two Pfizer products and the USP prednisone dissolution calibrators. All of the products were known to have experienced variable dissolution at some time in the past, without the source of the changes being known.

With respect to the dissolution results, a number of numerical parameters will be derived from the profiles to allow the evaluation of any correlations with the NIRM parameters. These will include “fixed point” values such as the percentage at a certain time elapsed, to mimic the current situation in dissolution testing, but also some parameters based more on the shape of the curve, hence the rate of dissolution. This will be achieved by the application of certain models to the profile data, such as the Weibull and Korsmeyer-Peppas models, which were cited in literature as suitable for this purpose.

Following this the assessment of the NIRM imaging results as a predictive tool for the dissolution behaviour will be conducted by determining if there are any good correlations between the sets of numerical parameters calculated to describe the imaging and dissolution results. This will highlight if the NIRM imaging may be utilised as a control mechanism for dissolution behaviour within the pharmaceutical production process. If this is the case then implementation within an intermediate stage in the manufacturing process, such as between the blending and the tableting stages of a product, may allow the identification of batches that were not up to specification. This would allow any remedial action to be taken on the blend before the product reached the point where the situation could not be rectified. This has the potential for huge cost savings for the pharmaceutical industry.

2 Processing Methods for NIRM Imaging and Dissolution Data

2.1 Evaluation of Imaging Hypercubes

As discussed in chapter one, the data obtained from NIRM imaging experiments are an amalgamation of both spectral and spatial information about the sample. Each data set can include up to ~82,000 spectra, one from each pixel in the FPA. This combination of size and 3D information can require the use of various approaches in the analysis of the data. As a result of this, the data processing tends to be the rate limiting step for NIRM imaging as the actual data acquisition is relatively fast and simple. This chapter will describe and review the types of data processing available for NIRM imaging and dissolution data. The aim is to evaluate these methods and choose the parameters that will be used in the subsequent work to describe both sets of data.

2.1.1 Data Pre-Processing

The nature of NIRS means that the spectra obtained for NIRM imaging will contain information regarding the physical aspect of the sample resulting from scattering and the chemical features due to absorption of the radiation. Ideally the data would be gathered from a sample with an optically flat surface, but in reality there will be some contribution to the physical component of the NIRS by imperfections on the sample surface, adding to any spectral offsets observed.

There are many data pre-processing techniques available and only the ones applied during this research will be discussed. All of the image processing was carried out using ISys software (Spectral Dimensions Inc., Olney, MD, USA).

Standard Normal Variate

The standard normal variate (SNV) transformation is one data processing method that is used to separate the physical from the chemical information (Barnes *et al.*, 1989). It corrects for interferences resulting from light scattering and particle size. It can lead to an improvement in the final images obtained as SNV helps correct for deviations in the flatness of the sample surface. A comparison of raw data and SNV data showed that the removal of spectral offset allowed improvement in the ability to identify different spectral groupings related to the positions they had originated on the sample surface (Clarke, 2004).

SNV is applied to each wavelength in every spectrum. Firstly the mean spectral response over all the wavelengths is subtracted from each individual wavelength response. This is the mean centring step. Then these mean centred responses are scaled at each wavelength using the standard deviation of each spectrum over the whole wavelength range. This is described by Equation 2-1, where A_j is the original absorbance at wavelength j, $\overline{A}$ is the mean absorbance over the all the wavelengths, J is the number of wavelengths in the range and SNV_j is the corrected response at wavelength j.

$$SNV_j = \frac{\left(A_j - \overline{A}\right)}{\sqrt{\frac{\sum_{j=1}^{J}\left(A_j - \overline{A}\right)^2}{J-1}}}$$

Equation 2-1

Spectral Derivatisation

Derivatives are used to improve spectral resolution and aid the visualisation of overlapping peaks and minor spectral features (O'Haver and Green, 1976). Its application provides some background compensation as it reduces the variable spectral background, seen as a sloping baseline (O'Haver and Begley, 1981).

The derivative of a spectrum is obtained by calculating the change in absorbance by the change in wavelength, i.e. differentiating the absorbance with respect to the wavelength or wavenumber. This can be done any number of times. One disadvantage of derivative use is a reduction in the signal-to-noise ratio (SNR) with increasing order of derivative. It has been found that the use of smoothing is required prior to the derivatisation (O'Haver and Begley, 1981). The most commonly used derivatives in NIRS tend to be the first and second. The first derivative is not affected by baseline offsets and measures the slope of the curve at all points in a spectrum. The second derivative measures the change in the slope of the first derivative curve and is not affected by baseline offsets or slope of the original spectrum. In second derivative spectra the negative peaks relate to the absorbance peaks in the original spectra, which can simplify the interpretation. Second derivative spectra can be advantageous in a situation where the sample contains species with similar structures such as different types of carbohydrate. In these cases any small differences that are seen in the original spectra, or even may not be apparent, can be visualised in the second derivative spectra.

Savitsky-Golay derivatives were utilised in subsequent chapters which required selection of two parameters, filter length and filter order. Filter length determined the length of region that the polynomial had to fit and the filter order governed the order of the polynomial used. The filter order, however, had to be set to one more than the derivative order. For example, if a second derivative was selected, the filter order would have a minimum possible value of three.

2.1.2 Processing Utilising the Spatial and Spectral Information

The pre-processing tends to deal with the spectral aspect of the image hypercube. The next step involves the inclusion of the spatial component of the image cube as well as the spectral component to extract chemical information, i.e. identify the matrix components of the sample and show their distribution. In some cases this can be achieved using univariate means. This type of method is considered to be simple as it is based on the evaluation of the data at individual wavelengths or wavenumbers, unique to the different components in the sample. Within the imaging framework this would relate to the generation of separate images of each of the individual components based on the pixel responses at a wavelength or wavenumber value unique to the particular component. This requires knowledge of the sample composition and the ability of the user to locate unique spectral values for each component present compared to the others. This can be a difficult task due to the broad and overlapping spectra obtained in NIRS. There is also the fact that each pixel in the image will not contain a spectrum relating to a single component, but a spectrum representing a combination of several if not all the entities in the blend.

In these cases, where focussing on single values does not provide relevant discrimination, the focus should be moved to methods where the complete spectrum is evaluated. This type of data analysis is known as a multivariate approach. It can be applied with or without any prior knowledge of the sample composition and removes the user dependence found in univariate approaches. Principal component analysis (PCA) and partial least squares analysis (PLS) were the multivariate methods used in this research.

Principal Component Analysis

PCA is a method with widespread application to NIRS and imaging techniques within pharmaceuticals and many other fields. It is often used as an exploratory technique as it is an unsupervised method, requiring no prior knowledge of the sample composition. PCA is a method of data reduction whereby it looks to describe a large data set by using a smaller number of variables that represent the major variations present. These new variables are called principal components (PC) (Davies and Fearn, 2004). Each of the original spectra used for the PCA can be described using linear combinations of the calculated PCs (Chen and Wang, 2001). Each PC is the combination of a score value and a loading. The score value relates to the contribution of a PC to a particular spectrum in the original data set. The loading represents the spectral contribution of the PC at each wavelength or wavenumber and loadings maintain similar features to actual spectra.

PCA works from a 2D matrix, therefore there needs to be an initial step performed to convert the 3D hypercube into a 2D representation (Huang *et al.*, 2003). For example, if the dimensions of a 3D image cube are $(\mathrm{x},\ \mathrm{y}, \lambda)$ the dimensions of the 2D matrix, X, are given by $((\mathrm{x} \ \mathrm{x} \ \mathrm{y}),\ \lambda)$ where each row represents the spectrum at one pixel. Next PCA is performed on X, which is deconstructed into the product of the scores, T and the loadings, P^T matrices which describe the "structure" of the sample. The variable E represents the residual error, Equation 2-2 (de Juan and Tauler, 2003). There are *s* loading vectors which are orthogonal and relate to the same number of PCs, see Figure 2-1.

$$X = TP^T + E$$ **Equation 2-2**

The first PC represents the direction of maximum variance through the data set, giving p_1^T. The score values relate to p_1^T are found by the projection of the data set, X on p_1^T giving t_1. The second PC represents the next direction of maximum variance through the remainder of the data set and will be orthogonal to PC1. The order of the PC calculation means that the first PC captures the largest amount of variation in the data set and each subsequent PC contains less than the one previous to it. The calculation of PCs continues until all the possible variance has been described, see Equation 2-3 (Geladi and Kowalski, 1986).

$$X = t_1 p_1^T + t_2 p_2^T + \dots\dots\dots t_s p_s^T \qquad \textbf{Equation 2-3}$$

The residual error is assumed to be associated with random noise and hence has no bearing on the description of the "structure" as previously mentioned. The scores matrix is refolded from 2D back to 3D giving a distribution map of the score values, relating to the contributions of each PC loading to each pixel, Figure 2-1.

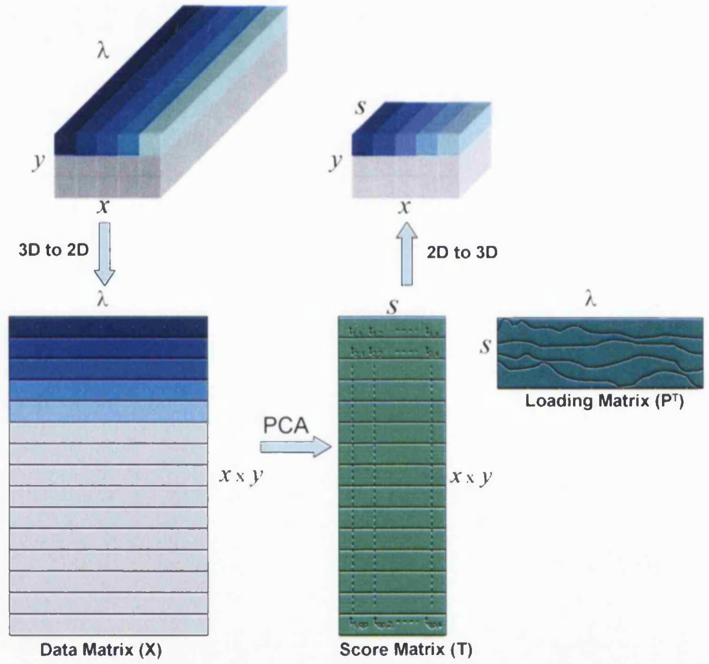

Figure 2-1: Schematic of steps for PCA on a 3D hypercube.

Examples of PCA Applications

PCA has found many applications in spectral and imaging analysis. It has been used on pharmaceutical samples in various situations where it has shown potential for determining the presence of impurities (de Juan *et al.*, 2004), determination of different dosage strengths of tablets (Walczak *et al.*, 1995) and elucidation of a sample matrix using Raman mapping (Šašić and Clark, 2006). It has found a biological application with Raman imaging to monitor the uptake of rhodamine in human lymphocytes in cancer studies (Eliasson *et al.*, 2006). The degradation products of polyvinylchloride (PVC) using x-ray photoelectron spectroscopy (XPS) images were evaluated using PCA (Artyushkova and Fulghum, 2002). Work has been carried out to classify different zones by the pigments found to be present using PCA on NIR and visible images for works of art (Baronti *et al.*, 1997) and similarly PCA was used in the prediction of average coating concentration and distribution on the surface of snackfoods (Yu and MacGregor, 2003). It has also been applied in a study to monitor the moisture content of maize in the drying process (Liu *et al.*, 2006) as well as trying to determine a relationship between the PCs and the oil content of canola seeds (Golebiowski *et al.*, 2005). Internal damage could be detected in pickling cucumbers using PCA on NIRM imaging data (Ariana *et al.*, 2006). The geographical source of crude oil could be distinguished from PCA of data from MIR with ATR, down to the type of rock it came from (Abbas *et al.*, 2006) and on the same theme of geology, the adsorption of water onto zeolite wafers could be monitored using PCA and MIR spectroscopy (Zhang *et al.*, 2005). As NIRM imaging found its way into forensics, so did PCA. It has been used with MIRS and NIRS data to classify different types of paper (Kher *et al.*, 2005) as well as for the detection of counterfeit anti-malarial tablets (Wolff *et al.*, 2005).

Principal Component Analysis: Data Reconstruction

The first PC describes the largest amount of variation in a sample set. For a hypercube of a "real" sample this will equate to the average response from all the components over all the pixels. In cases where there is a high percentage of one component present in a formulation it can sometimes act to mask the responses of other minor components present. The first PC here would have a high degree of association with the spectral features of the major component, so the removal of this PC may aid the resolution of the minor components.

The procedure used deletes the first PC after the PCA has been performed and then the image cube is reconstructed by multiplication of the scores and loadings of the remaining PCs. This produces a hypercube with exactly the same dimensions as the original with the average response subtracted from every pixel. This can lead to the location of minor components that were otherwise spectrally concealed.

Partial Least Squares Analysis

PCA can be used in an unsupervised manner, but when the composition of the sample is well known there is the option of utilising a supervised method such as PLS.

PLS is a technique used to model one or several dependant variables responses by the use of a set of predictor variables (Wold *et al.*, 2001). The predictor variables usually take the form of a library containing spectra of each component in the sample and should where possible contain all the spectral variations possible for that sample. PLS has its basis in PCA, but where PCA is concerned with describing all sources of variation in the data set, PLS is only focused on the sources of variation which are associated with the individual components of the sample (Golebiowski *et al.*, 2005). It can be used for regression and as a method of data reduction, in a similar way to PCA (Liu *et al.*, 2006). PLS takes advantage of any correlation that is inherent in the spectral data and the concentrations of the components in the sample. This co-linearity can be problematic for other methods such as multiple linear regression, but in PLS it acts as a stabilising advantage (Lindgren *et al.*, 1994). Compared with PCA, PLS models usually give better predictions (Setarehdan *et al.*, 2002). PLS can be used in method 1, where a relationship can be obtained between a specific variable, e.g. concentration, and a series of other variables e.g. absorbance values. It can also be applied as method 2, where more than one variable e.g. spectral components present in a sample, are related to a different set of variables, e.g. data matrix from NIRM imaging.

There are many examples where PLS has been applied to various types of data including chromatography (Galera *et al.*, 1997; Gallego and Arroyo, 2003), UV (Goicoechea and Olivieri, 1999; Ferraro *et al.*, 2001), fluorescence (Martos *et al.*, 2000; Pomerleau *et al.*, 2005), MIR (Kornmann *et al.*, 2003; Li *et al.*, 2005) and NIRS (Rutan *et al.*, 1998; Setarehdan *et al.*, 2002; Roggo *et al.*, 2005; Huck *et al.*, 2006; Sohn *et al.*, 2006). The benefits of multivariate analysis such as PLS in PAT applications are fast becoming known and viewed as a necessity (Wold, 2007) However, examples involving PLS applied to imaging data are not as common in the literature.

In an evaluation of NIRM imaging of soluble solid (sugars) distribution in kiwi fruit, PLS was utilised and improved the standard error of prediction for the model (Martinsen *et al.*, 1998). PLS was utilised on NIRM imaging data of maize kernels to predict the oil or oleic acid content (Weinstock *et al.*, 2006). It has also been applied to data from functional magnetic resonance imaging (fMRI) in kinetic studies as a target-directed structure-seeking technique (Rayens and Andersen, 2004). In a pharmaceutical context, it was applied to NIRM imaging data in an investigation into the moisture content and location within film-coated tablets prepared under different conditions (Gulian *et al.*, 2005).

There have been applications of kernel based PLS to image data. This kernel PLS algorithm has been further developed from PLS as a more simplified method to increase the speed of calculation using large data sets (Lindgren *et al.*, 1994). It makes use of smaller matrices based on the number of variables in the data matrix (X) and the concentration matrix (C) and not the number of observations (pixels) (Lied *et al.*, 2000). It also allows for the calculation of the regression coefficient (b) required for the final PLS equation (discussed in the following section) without calculating any scores vector. This method has been utilised for visible, NIR and MIR images from satellites and showed improvement in the prediction compared to the previous model applied (Lindgren *et al.*, 1994). The same technique of kernel PLS has been compared to PCA to highlight the differences in the two multivariate techniques when used on the same image data with varying textural elements (Lied *et al.*, 2000). The kernel PLS scores images contained more detail and looked more focussed than those obtained from PCA.

In a further paper kernel PLS was again the chosen method, but in this study examples had been chosen to illustrate certain image regression cases providing the term image PLS (IPLS) (Lied and Esbensen, 2001). The imaging was performed using a three channel system to mimic many of the industrial systems available, but retained the ability to represent other multivariate imaging cases as the principles remain the same for any number of variables used. The first example showed IPLS used to discriminate between acceptable samples of Scandinavian crispbread and samples which were broken or burnt. The second example was performed to estimate the storage time of fruit using bananas. Images were gathered over set time intervals of the same banana from being raw, green to very ripe and dark brown. It was found to be the case that the deterioration was not just related to the spatial distribution of brown areas, but also by incorporation of a spectral aspect of the fruit.

Definition of PLS

In addition to the decomposition of the 2D matrix representation of the image data set, X into the T and P^T matrices (as with PCA), there is an additional step involving a concentration matrix, C. In a similar fashion this concentration matrix is deconstructed into a scores matrix, U and loading matrix, Q^T. A factor F is given to represent the residual noise as in Equation 2-2.

$$C = UQ^T + F \qquad \textbf{Equation 2-4}$$

In the same way as for PCA, Equation 2-4 can be described as;

$$C = u_1 q_1^T + u_2 q_2^T + \dots\dots\dots u_s q_s^T \qquad \textbf{Equation 2-5}$$

PLS evaluates Equation 2-2 and 2-4 to calculate the outer relations of the individual X and C matrices. The results of these outer relations are used to produce an inner relation between the X and C matrices (Geladi and Kowalski, 1986). The factors for X are estimated using the values of C and *vice versa*. The result of this is that the values of factors in T are not optimal for the prediction of the X columns due to the fact they are also used to describe C, incurring a degree of rotation (Beebe and Kowalski, 1987). Ideally the variation in X would be the same as in C which would make all the factors identical for Equations 2-2 and 2-4, but this is wishful thinking when real samples are involved. X will tend to vary in ways that have no correlation to those in C i.e. $t \neq u$, but there is still an inner relation which is linear in its simplest form (Geladi and Kowalski, 1986).

$$u = bt + \varepsilon \qquad \textbf{Equation 2-6}$$

In Equation 2-6, ε refers to the prediction error and b is a regression coefficient used to calculate subsequent factors. The vectors of t and u will be alike and ε will be small if there is a good association between X and C. If X has dimensionality greater than one, additional factors are determined and then C can be described using Equation 2-4 with substitution of U from Equation 2-6.

$$C = bTQ^T + G \qquad \textbf{Equation 2-7}$$

Equation 2-7 makes it possible to calculate the scores of C from the scores of X.

The model used to determine the scores for X and C and the relationship b can be used to carry out the concentration prediction of an unknown sample. Firstly the responses of the unknown sample, y_{un} are taken through the calibration model to give a score vector t_{un}, this in turn is used in Equation 2-6 to predict a scores vector for the predicted concentration matrix, u_{un}. This vector u_{un} is used in the calibration model for C to give predictions of concentration.

The application of PLS to predict component concentrations quantitatively as described from NIRM imaging data poses some problems. The data set may contain a large number of spectra, which suits these multivariate techniques, but as the spectra represent the responses at different pixels in a distribution, some may contain a higher response for one of the components due to heterogeneity in the sample. This would relate to a higher concentration of that component, which may or may not be the API. This means that suitable reference methods would be needed for each component present and standard reference methods usually focus on the API. Also, the concentration reference standards required for imaging would need to be highly homogeneous in order to obtain the same response at every pixel in the images obtained. To this end, PLS has been adopted as a method to classify the components present in a sample, as opposed to quantifying them (Ståhle and Wold, 1987).

PLS Classification

With PLS, quantitative analysis can be achieved without the knowledge of the concentrations of all species present in a system. As described previously, a set of data is required to function as a reference or training set, which takes the form of a library of pure spectra from all the components representing the sample being analysed. An assumption is made that individually the purity of the components are equal to 1, so when the PLS is performed and utilises the library, the concentration is presumed to be equivalent. The results from the PLS calculation comprise a matrix of ones and zeros for each factor. For example, an image file is constructed from three pure components and a library was also made up of the same three components. PLS is then performed on the pure component image file and the number of factors required to describe the data matrix should be equal to the number of individual components in the library. The scores image cube will subsequently have the same number of image planes as library components, which will each show score values of either one and zero to describe whether that particular component has been located at that factor (one) or not (zero). Figure 2-2 shows the score results of a PLS calculation of a three pure component image file Figure 2-2 (a) against a library of the same components. As predicted, the number of factors (steps) required to describe the data set is equivalent to the number of components present, in this case three. Figure 2-2 (b) shows the score image planes for each of the three factors and the pixel distributions relating to those images. For each separate factor the area related to that component has score values of one in the data set, while the other two components have score values of zero, giving a bimodal distribution centred around one and zero in the pixel distribution. This illustrates the classification ability of PLS.

(a)

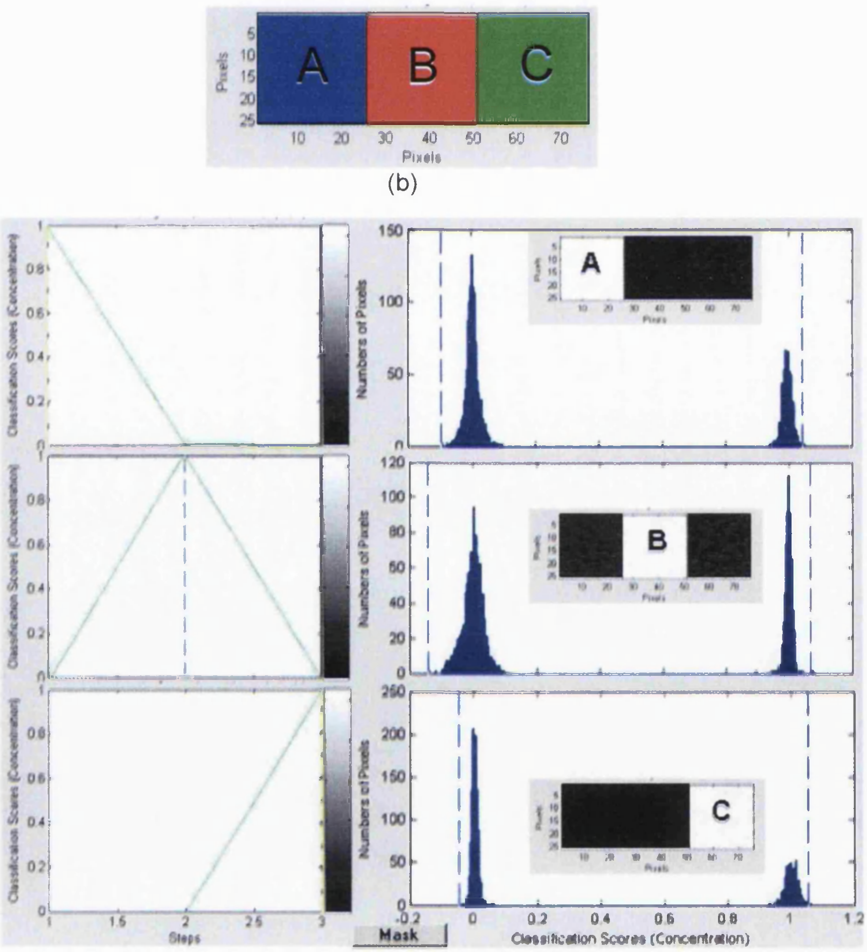

(b)

Figure 2-2: Example of a PLS classification using a library file showing (a) the three pure component image file and (b) the score images and pixel distributions of all three PLS factors from that image file.

However, in the case of an actual pharmaceutical sample, each component is rarely as discretely separated as they are in the above example. Here the pixel distributions seen for the image planes at each factor after PLS in the majority of cases will be unimodal and centred around a score value between one and zero, Figure 2-3(b). This is the result of spectral mixing at each pixel from all the components present due to blend homogeneity, particle size and sampling depth of measurements.

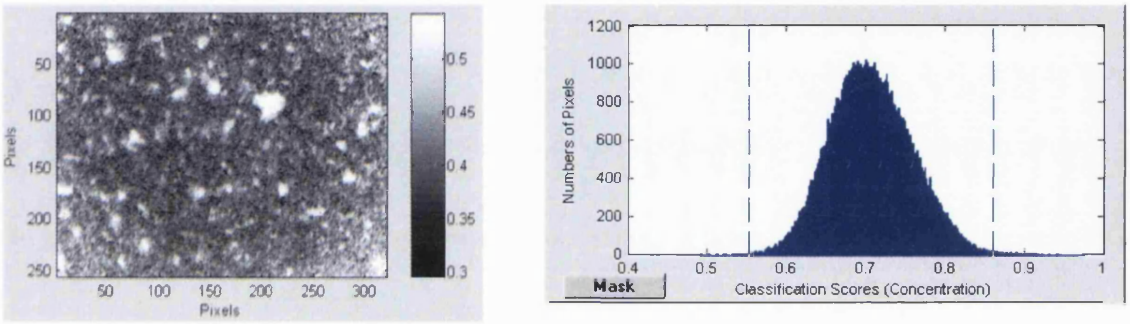
(a)

(b)

Figure 2-3: Example of a PLS classification using a "real" file showing (a) the score image plane and (b) the pixel distribution.

Comparing Figure 2-3(a) with Figure 2-2 (a) the overall colour is grey, with occasionally more defined areas of that particular component related to factor two. Using the results from Figure 2-2 (b) there would be high degree of confidence that choosing the part of the distribution centred around the score value of one would correlate to only that particular component related to factor two in the image. This in turn would provide a good representation of its distribution within the sample i.e. the area shown in Figure 2-2 (a). With the "real" sample however there would be no confidence that including the whole distribution obtained in Figure 2-3(b) would only result in that particular component being selected in the image plane. The distribution in Figure 2-3(b) represents the contribution of that component to every pixel in the image plane. The higher the score value of the pixel, the greater the contribution for that particular component.

This results in the requirement of a cut-off point for the score values or region of the pixel distribution where anything above that point or within that area will be accepted as that component for the interpretation of the image files.

Classification of Components in a Scores Image

There are a number of ways available to accomplish this classification, but in all cases it will be related to the amount of the component in the formulation. The methods used in this research will be discussed.

Percentage of Pixels

This system assumes the known percentage of each component from the formulation to calculate the equivalent number of pixels that would represent that percentage of the total pixels in the image. For example, if the API was in the formulation at 10% m/m and the total pixels in the image was 82,000 then 8,200 pixels would be included for the PLS pixel distribution for the factor related to the API. The pixels of the distribution would be from the higher end of the score values. Figure 2-4 shows the selection of 10% of the total pixels from the higher end of the distribution. This is repeated for each of the individual factors/components.

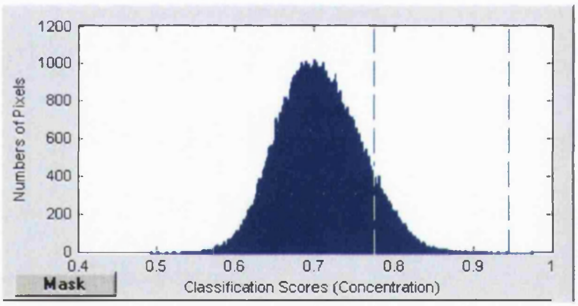

Figure 2-4: Selection of high score end of pixel distribution.

Area Selection of the Pixel Distribution

Another technique is the selection of certain areas of the pixel distributions depending on the amount of the components present in the sample. The limits of these regions are not fixed score values, but they give an estimate of which area to include, Figure 2-5.

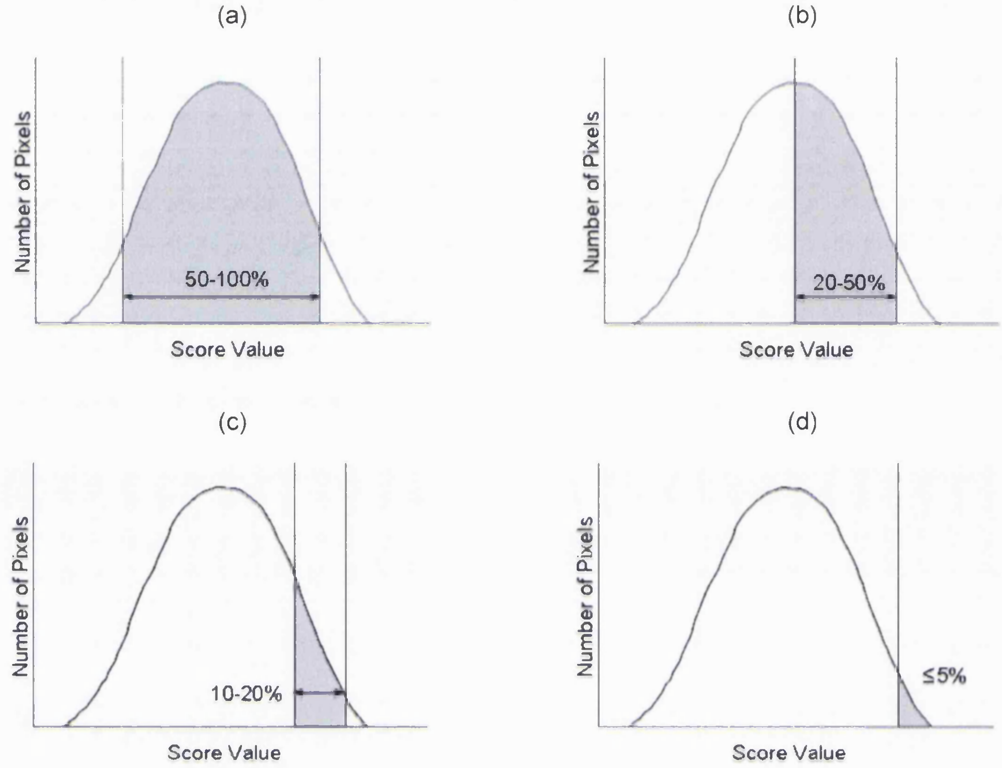

Figure 2-5: Areas of pixel distributions used.

The technique applied for each system or product will be stated.

2.1.3 Alternative Approaches to Multivariate Analysis

In addition to the techniques of PCA and PLS that have been applied to the data in this research, there are a number of other approaches that can be applied to imaging data.

Euclidean and Mahalanobis distances have been utilised for image analysis (Spectral Dimensions, ISys User Manual, version 3.1.1). The Euclidean distance is distance between two points, irrelevant of any correlations in the data (Buice *et al.*, 1998). The Mahalanobis distance is a distance with its measurement based on correlations between variables by which different patterns can be identified and analysed (Tsuchikawa *et al.*, 2003). It can show the similarity of an unknown sample set to one that is known.

A study into imaging secondary ion mass spectroscopy (SIMS) found that visual interpretation, which is usually not possible due to peak interferences between atomic and molecular ions, was viable using classification by a Kohonen network (Wolkenstein *et al.*, 1997). A Kohonen network is a type of neural network, which is a form of unsupervised learning called a self-organising map. Data from higher dimensions are mapped by a 2D neuron array. There is a weighting to each node, initially determined at random, but then an input vector is selected and compared to these weighting values by calculation of the Euclidean distance. The weight vector closest in value to the input vector gets selected and this neuron and its neighbours are updated with the values. This iterative process continues until convergence occurs.

In another paper, NIRM imaging was being evaluated for the determination of the main chemical constituents in wheat (namely bran), gluten and starch (Robert *et al.*, 1992). An attempt to directly study the images at fixed wavelengths only resulted in the discrimination of starch, the other two components did not have unique wavelengths for comparison. This lead to the use of step-wise discriminant analysis to identify the wavelengths for identification of all the components present, then canonical discriminant analysis was applied to linearly combine the images at these wavelengths. The discriminant factors obtained were used to classify the unknown pixels in the image into qualitative groups by comparing them to the score values. This allowed the identification of the three individual components.

The use of wavelets has been described for spectroscopic data. One of the main elements of using wavelets is that it can decompose a signal directly related to the frequency. It can then represent the signal in the frequency domain distribution state in the time domain. The time domain can be replaced by other domains such as wavelength if required (Leung *et al.*, 1998). Performing wavelet analysis produces a vector of wavelet coefficients which are assigned to different frequency bands. Each of these bands expands over the total wavelength range and are associated with a different frequency range of the signal. Regression of appropriately selected wavelet coefficients against concentrations can establish a spectral model (Chen and Wang, 2001). Wavelets have been applied for pattern recognition in NIRS (Walczak *et al.*, 1996) which improved the classification ability. It has also been applied as a method to aid de-noising and smoothing of electrospray mass spectra (Barclay and Bonner, 1997). This de-noising technique has been applied to SIMS images, where image processing and classification are difficult (Nikolov *et al.*, 1996). More recently wavelet filters have been applied to NIRM imaging data for the approximation of texture descriptors that would facilitate a more automated means of describing features of the surface matrix in a pharmaceutical dosage form such as homogeneity or particle density (Josefson *et al.*, 2006).

Another method widely used is multivariate curve resolution (MCR). In a similar fashion to PCA, MCR involves a bilinear decomposition of the data matrix (X) providing a matrix describing the contribution of each species across the data set (T), another matrix describing how the responses of the species changes (P^T) as well as a matrix to account for unexplained variance (E) (Larrechi *et al.*, 2006). MCR is usually combined with alternating least squares (ALS). ALS is a iterative method that calculates new T and P^T matrices on every cycle which include a number of conditions based on the chemical information available in order to minimize E. The iteration stops when the convergence criteria are met when X is reconstructed using the new values of T and P^T.

MCR-ALS is viewed as a soft modeling technique due to the ability of obtaining the spectral and concentration profiles without explicitly using the underlying chemical model associated with it. For example MCR-ALS was used with a kinetic modeling strategy to calculate the rate constants for the curing reaction of epoxy resins. The kinetic information was not directly available form the MCR-ALS results but the results could be used in a hard modeling method, in this case non-linear least squares fitting of the kinetics parameters (Larrechi *et al.*, 2006). It has also been applied to Raman imaging data (Hancewicz and Andrew, 1998) and for the analysis of Raman and MIRS data (Schoonover *et al.*, 2003).

Single value decomposition (SVD) is another multivariate method available for imaging data. It works to the same principles as PCA, but in this situation the scores matrix, T is the product of two matrices. Only one of these two matrices is used for the score plot, the other matrix is associated with scaling and has no effect on the plot. In these plots clusters can form but only when the information is preserved in the data, so the choice of variables is important for cluster discrimination. SVD has been applied to the improvement of images by removal of spectral artifacts in the identification of plastics by NIRM imaging (Buydens *et al.*, 1995).

Fuzzy C-means clustering has also been applied to NIRM imaging data (Mansfield *et al.*, 1997). It made it possible to detect sub-regions of the image containing unexpected and unique spectral features and did not need any prior knowledge of the sample composition. There had been an increase in the amount of information obtained from NIRM images by using fuzzy C-means analysis. It separated spectra based on their shape, resulting in regions with distinct spectral features being separated into discrete clusters. It has been used in a biological application for the classification of different tissue types in human prostate biopsies (Haka *et al.*, 2001).

2.2 Analysis of Dissolution Data

The dissolution procedures associated with quality control (QC) within the pharmaceutical industry have specifications based on the amount of a product API dissolved at one or multiple time points in the dissolution process e.g. Q = 90% dissolved at 90 minutes. This requires some form of sampling from the dissolution vessels, either manually or automated for the analysis to quantify the amount of API dissolved by HPLC or UV detection for example. The acceptance criteria set by the pharmacopoeias (section 1.3.2) are followed.

The results of these tests allow the pass or fail of the dissolution test for a product, but when failures occur, it is the only information available regarding the dissolution behaviour. It may not give much insight into what may have caused the failure and due to the destructive nature of the test, the samples cannot be re-analysed *via* alternative investigative methods.

Fibre-optic dissolution testing has been discussed in section 1.3.4 and via this method of dissolution monitoring there are measurements acquired at regular time intervals e.g. every minute which accumulate into a dissolution profile, Figure 2-6.

These profiles show the whole dissolution process, making it possible to calculate the amount of API dissolved at any time point, not just those defined by the QC specifications. This also opens the door to evaluation of the dissolution kinetics and calculation of dissolution rates and other parameters to describe the process. Application of kinetic models would enable the description of the profile using a set of parameters/constants which could be used for a comparison (Schatz *et al.*, 2003).

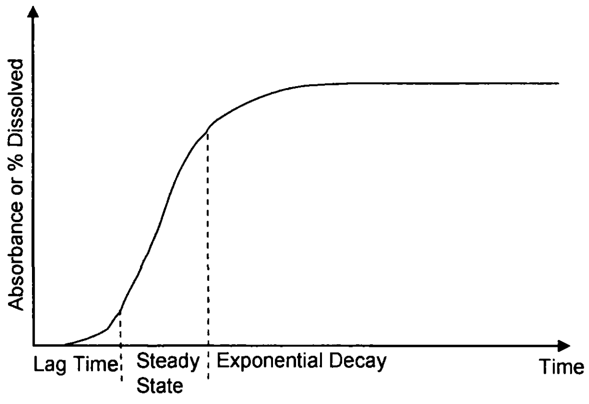

Figure 2-6: General shape of a dissolution profile. Adapted from Wilberg and Hutlin, 2006.

In the research for this thesis the amount dissolved at a time point was utilised, to represent the current QC situation combined with the application of selected kinetics models to obtain parameter values, all of which will be discussed in section 2.2.2.

2.2.1 Dissolution Profile Comparison Techniques

The FDA acknowledges that the use of dissolution profiles as opposed to time point measurements can lead to improved characterisation of a product. This requires some means to compare dissolution profiles before and after any changes implemented to a product or for different strengths. It should be able to indicate similarity and, if present, should also signal any bioinequivalence (Shah *et al.,* 1999). The FDA concluded that calculation of the f_2 similarity factor was the simplest method for profile comparison and this is the suggested method to use in the FDA guidelines, Equation 2-8. An equation also exists describing a difference factor, f_1, but the regulatory interest was more focused on identifying the similarities between profiles, which incorporates the ability to highlight large differences at any time point resulting in the focus on the f_2 calculation.

$$f_2 = 50\log_{10}\left\{100\left[1+\frac{1}{t}\sum_{j=1}^{t}\left(R_j - T_j\right)^2\right]^{-0.5}\right\}$$

Equation 2-8

Where R_j and T_j are the average percent API dissolved at time j for a reference and test, respectively with t as the number of time points tested. It can be seen that if the average dissolution of the API of R and T is the same at each time point i.e. $\sum_{j=1}^{t}(R_j - T_j)^2 = 0$, then $f_2 = 100$. The FDA states that an f_2 value between 50 and 100 will allow the similarity of the two dissolution profiles to be claimed. When $f_2 = 50$, this relates to $\frac{1}{t}\sum_{j=1}^{t}(R_j - T_j)^2 = 99$.

There are also a number of stipulations stated that need to be applied to the profile comparison, mainly indicating that the same test conditions should be used for all of the dissolution profiles to be compared. They also suggest that only one measurement is taken after 85% has dissolved and that rapidly dissolving products (BCS, where > 85% is dissolved in 15 minutes or less) do not require profile comparison (Shah *et al.*, 1999). It has been suggested that although this test is easy to apply, it does not necessarily have any scientific justification (Ju and Liaw, 1997).

A number of different applications exist for dissolution profile comparison in addition to (and including) the f_2 calculation. These fall under the headings of statistical, model-independent and model-dependant methods, Table 2-1.

Application	Method
Statistically based	Multivariate ANOVA
	Multiple univariate ANOVA
Model-independent	Ratio test procedures
	Pairwise procedures
Model-dependent	Zero-order
	First order
	Weibull
	Higuchi
	Hixson-Crowell
	Baker-Lonsdale

Table 2-1: Different applications available for dissolution profile comparison. Adapted from Polli *et al.*, 1997.

The f_2 calculation falls under the model-independent methods as these ratio the test results with the results of a reference sample. Comparison of the dissolution equivalence (DE) of different profiles falls under the same heading as the f_2 calculation (Anderson *et al.*, 1998), but depending on the method used to calculate the area under the curve (AUC) it may be viewed as model-dependent (Adams *et al.*, 2001).

In certain cases the Analysis Of Variance (ANOVA) based methods can be regarded as model-independent. These methods investigate statistical equivalence as opposed to pharmaceutical equivalence in the samples and have been found to be overly discriminative and not very useful (Polli *et al.*, 1997). In the same study, different methods of model-independent methods were used and compared including the ratio of AUC, ratio of percentage API dissolved and the pairwise calculation of f_2 similarity factor and f_1 difference factor. All the methods applying ratios give satisfactory results for profile comparison and the formulation of dissolution specifications. For the pairwise procedures all the methods could be viable for comparison of dissolution profiles, although they all undergo the same issues relating to the length of profile used, the sampling and the pairing of the individual profiles. However the f_2 similarity factor has the feature where its value increases with increasing similarity. The final investigation of the model-dependent procedures shows that a certain selection of those stated in Table 2-1 could be applied in the example utilised, but none of the models could be chosen as the ideal one to use. The overall conclusion is that there are many feasible methodologies that can be applied for dissolution profile comparison and no single procedure stands out as the best one to employ.

An alternative approach for profile comparison that can be used is PCA. In work carried out comparing the profiles from various reference and test batches of tablets and capsules, the PCA scores could provide information on the variation between and within the different batches. The PC1 and PC2 contained information regarding the level or overall percentage API dissolved once the profile reached a plateau and the shape of the profile, respectively (Adams *et al.*, 2001; Adams *et al.*, 2002)

In the research for this thesis, the parameters obtained through the various techniques applied are listed in section 2.2.2.

2.2.2 Methods Used to Obtain Dissolution Parameters

The techniques outlined in this section were utilised to obtain dissolution parameters that could be used to describe the profiles in a concise way. These parameters were directly compared to values acquired from the NIRM imaging data.

Time to Specific Percentage Dissolved

This is the time (*t*) taken for a set percentage of API (P) to dissolve. The P value was evaluated for each different product used. The dissolution profiles were acquired, converted to percentage of stated amount of API dissolved, corrected for the mass of the dosage form, vs. time then assessed for an appropriate value to set for the parameter. The value selected represented a point which provided a good spread in the subsequent time values, Figure 2-7.

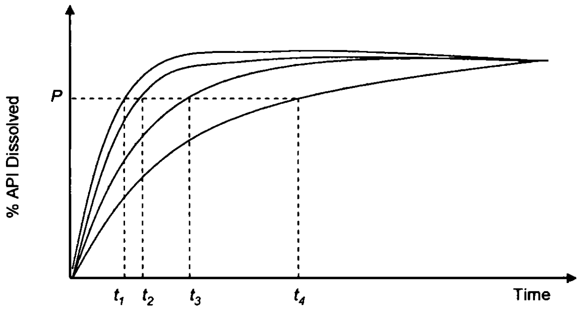

Figure 2-7: Diagram showing the selection of percentage value dissolution parameter.

In the cases where there was apparently less than 100% of the stated amount of API dissolved at the plateau region, the profiles were taken as they were measured and were not normalised in any way to make them appear more uniform. This was because dissolution testing in the pharmaceutical industry does not perform any type of normalisation on results obtained. They require the exact information for the amount of API dissolved from the dosage forms. It is, however, corrected for the individual weights of the dosage forms being dissolved.

Percentage Dissolved at a Specific Time

This is the P value at a specific time in minutes. The time point used was evaluated for each different product used. The dissolution profiles were acquired, converted to percentage API dissolved vs. time then assessed for an appropriate value to set for the parameter. The value selected represented a point which provided a good spread in the subsequent P values,

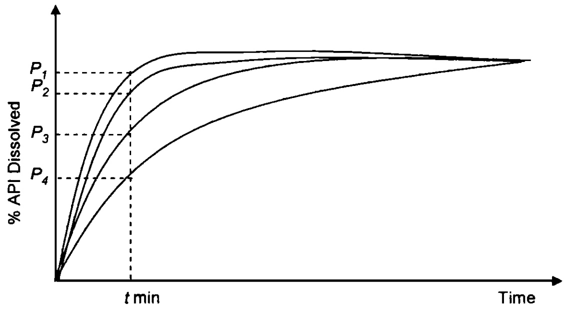

Figure 2-8: Diagram showing the selection of time point dissolution parameter.

Initial Dissolution Rate: Zero-Order

This was taken as the rate of change of P with time taken from the steady state part of the dissolution profiles shown in Figure 2-6, which is closest to linearity and gives zero-order kinetics.

$$\frac{dP}{dt} = k_0 t \qquad \textbf{Equation 2-9}$$

Here k_0 is the initial rate.

Exponential Curve: First Order

The general shape of the dissolution profiles is comparable to that of an exponential curve. The exponential function shown in Equation 2-10 was utilised to fit the dissolution profile data using a non-linear fitting programme, NLReg.

$$D = ce^{-k_e t} + f \qquad \textbf{Equation 2-10}$$

However this was not a typical form of an exponential equation and it could be expressed in a more familiar way as,

$$D = a\left(1 - e^{-k_e t}\right) + b \qquad \textbf{Equation 2-11}$$

Where D corresponds to the absorbance of the solution in the dissolution vessel or P value, t is the time and k_e shows the rate constant for both Equations 2-10 and 2-11. The other terms in Equation 2-11 related to the dissolution profile as shown in Figure 2-9 where the values of a represents the amplitude and b shows the offset from zero.

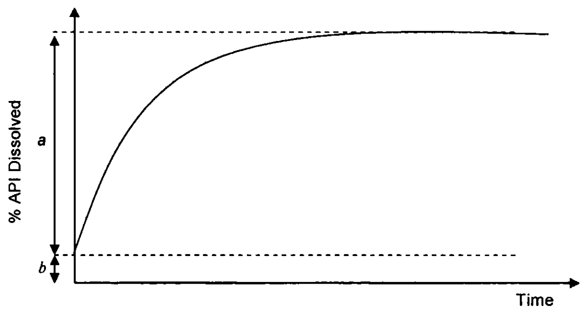

Figure 2-9: Definition of terms in an exponential model for a curve.

The constants in Equation 2-10 relate to a and b where $-c$ is the amplitude of the profile on the y-axis (a) and f is the offset of the data from zero plus the amplitude ($a+b$).

Weibull Model

When it is not possible to deduce an equation to represent the dissolution profile from theoretical fundamentals, as in zero order systems, empirical equations can be utilised. The Weibull model uses a general empirical equation, described in 1951 as a statistical distribution function with a wide applicability (Weibull, 1951). In the 1970's it was applied to the modelling of dissolution profiles (Langenbucher, 1972; Langenbucher, 1976) and has subsequently been commonly used for this purpose (Lánský and Weiss, 2003; Yuksel *et al*, 2000; Anderson *et al.*, 1998; Polli *et al.*, 1997). The equation is not derived directly from kinetic parameters, but analysis of the resulting Weibull parameters can provide information about the dissolution event. The equation takes the form of Equation 2-11 when applied to drug dissolution or release from pharmaceutical dosage forms.

$$D = D_{inf}\left(1-\mathrm{e}^{\left(-\frac{(t-t_L)^{\beta}}{T_d}\right)}\right)$$ **Equation 2-12**

Where D is the value of P, t is time and the other terms are the Weibull parameters. D_{inf} is the value of P at infinite time which gives an insight into API and excipient interactions. T_d is the time scale parameter (or the time to reach 63.2% dissolution of the

API) which provides information about the rate of the dissolution. t_L is the dissolution lag time and describes the processes taking place before the onset of dissolution e.g. the time taken for a capsule or a coating to dissolve (Rubino *et al.*, 1985). β is the shape parameter and can give information about the effect of disintegration and diffusion processes on the dissolution rate. When $\beta = 1$ the curve is a first order exponential. If $\beta > 1$ the curve becomes a sigmoid S-shape, where disintegration and de-aggregation processes cause an inflection at the base of the profile. When $\beta < 1$ the profile shows burst behaviour followed by an asymptotic approach to the dissolution end point. In this latter case there is virtually no lag time, which indicates that de-aggregation and disintegration processes are very fast relating to an I-R formulation (Costa and Lobo, 2001).

Higuchi Model

Higuchi worked on many theoretical models to explain the drug release into a solvent. This included dissolution studies from wax and solid matrices (Higuchi *et al.*, 1966; Higuchi *et al.*, 1968). Various equations were formulated for different situations such as one for the dissolution from a planar system with a homogeneous matrix (drugs in suspension from ointment bases) and another for when there is a tablet matrix dissolving. It is possible to simplify the Higuchi model in a general way.

$$f_t = \mathrm{K_H} t^{1/2}$$ **Equation 2-13**

Where $\mathrm{K_H}$ is the Higuchi dissolution constant and f_t is the amount of API released at time t. This describes the dissolution/drug release as a process based on Ficks law (steady state diffusion) relating to diffusion with square root time dependence, which can be used to describe the dissolution from several types of pharmaceutical dosage forms (Yuksel *et al.*, 2000; Koenig *et al.*, 2003; Gohel *et al.*, 2000) including transdermal film (Reza *et al.*, 2004).

Korsmeyer-Peppas Model

A simple model relating the fraction of API released exponentially to time was developed by Korsmeyer *et al.* (1983).

$f_t = at^n$ **Equation 2-14**

It is semi-empirical equation where a is a constant relating to the physical characteristics of the dosage form, n is indicative of the release mechanism and f_t is the fraction of API that has been released. If the main release mechanism is diffusion, then a plot showing f_t vs. $t^{0.5}$ should produce a straight line, similar to the Higuchi model. It is also known as the Power Law and it has been applied to the dissolution of drugs from polymer matrices and modified release pharmaceutical dosage forms (Koenig *et al.*, 2003; Kim and Fassihi, 1997). The value of n can be used to describe different release mechanisms.

The tabular values relate to the dissolution when the sample is in the form of a slab. So n = 0.5 describes Fickian diffusion and the higher values between 0.5 and/or equal to 1.0 account for mass transfer following a non-Fickian release. These values change if the sample is in the form of a cylinder to n = 0.45 in place of 0.5 and 0.89 replacing 1.0. In order to calculate this exponent value, the part of the dissolution profile relating to $f_t = 0.6$ should be the only values utilised.

Release Exponent (n)	**Drug Release Mechanism**	**Rate as function of time**
0.5	Fickian diffusion	$t^{-0.5}$
0.5<n<1.0	Anomalous transport	t^{n-1}
1.0	Case-II transport	Zero order release
Higher than 1.0	Super Case-II transport	t^{n-1}

Table 2-2: Diffusional release mechanisms characterized from values of n. Adapted from Costa and Lobo, 2001.

2.2.3 Interrelationships and Limitations of Selected Models

The methods and models selected to obtain parameters to describe the dissolution process were based on the current measurements taken for dissolution testing and those found on multiple occasions in the literature. The exponential, Weibull, Higuchi and Korsmeyer-Peppas models provided numerous parameters between them, some of which could be interrelated and others that did not really have any relevance to the dissolution rate.

If a first-order process was considered where there was relatively simple kinetics, it could be described as,

$$D_t = D_\infty\left[1 - e^{-kt}\right] \qquad \textbf{Equation 2-15}$$

Where D_t represented the absorbance or amount of API dissolved, D_∞ was the absorbance or amount of API dissolved at infinite time and k was the rate constant. Rearranging for the rate constant parameter gave,

$$-kt = \ln\left[1 - \frac{D_t}{D_\infty}\right] \qquad \textbf{Equation 2-16}$$

Therefore at a fixed time, the rate constant, k would be proportional to $\ln\left[1 - \frac{D_t}{D_\infty}\right]$. Due to the fact that the Weibull β = 1 and there would be no lag, t_L = 0 for first-order kinetics, $k = \frac{1}{T_d}$. T_d would also be directly related to the t_P as it represented the time to reach 63.2% dissolution of the API.

The Weibull model could be applied to fit a profile that limits at infinite time, but the Higuchi and Korsmeyer-Peppas models could not. Therefore, theoretically, if a profile fitted the Weibull equation it would not fit the Korsmeyer-Peppas or Higuchi models. In the case where a profile fitted the Higuchi model, it would also fit the Korsmeyer-Peppas, when n = 0.5 as they became the same equation.

Figure 2-10 shows some simulations performed for this thesis for the Korsmeyer-Peppas model to illustrate this. It also shows that the parameter a does not relate to the dissolution rate and is just a scaling factor relating to the separation between the profiles, Figure 2-10(a). The factor of K_H in the Higuchi model also contributes as a scaling parameter due to the similarity to the Korsmeyer-Peppas equation.

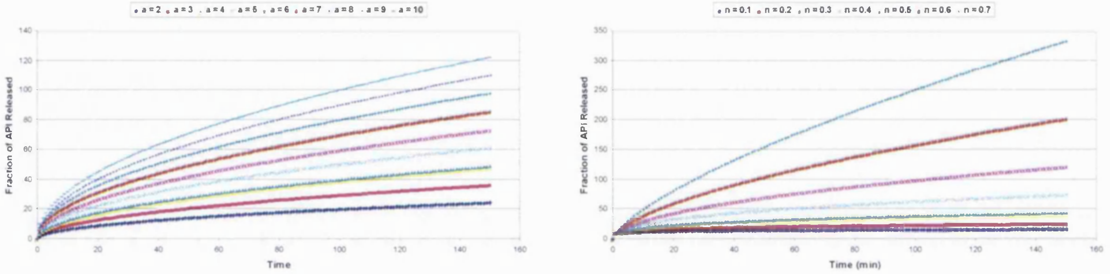
(a)

(b)

Figure 2-10: Korsmeyer-Peppas model (a) the effect of changing a with n = 0.5 and (b) the effect of changing n with a = 10.

Profiles that fit the exponential model should fit the Weibull model resulting in β = 1 and a t_L = 0, but this would not be the case in reverse if $\beta \neq$ 1 and a $t_L \neq$ 0. Figure 2-11 shows some simulations performed for the Weibull model to show the effect of the changing the different parameters. It is seen that variations in the D_{inf} value give a similar result to that of the a parameter for the Korsmeyer-Peppas model, see Figure 2-11(a). However changing the T_d and the β parameters relates more to changes in the dissolution rate.

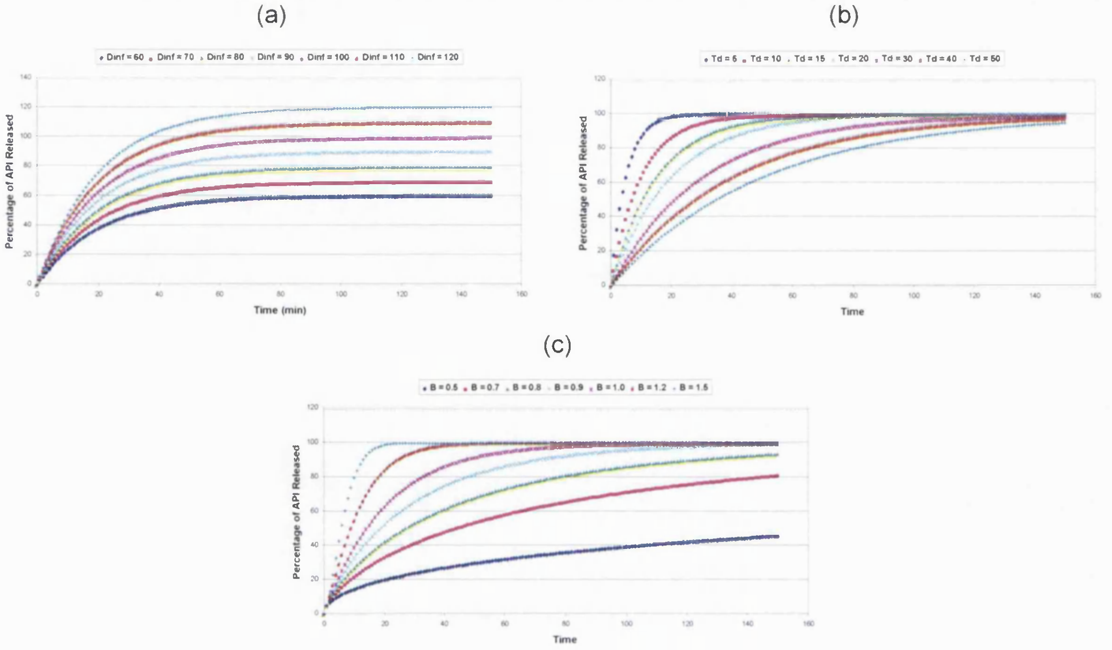
(a)

(b)

(c)

Figure 2-11: Weibull model (a) the effect of changing D_{inf} with β = 1, t_L = 0 and T_d = 20 min, (b) the effect of changing T_d with D_{inf} = 100, β = 1 and t_L = 0 and (c) the effect of changing β with D_{inf} = 100, t_L = 0 and T_d = 20 min.

The time range of experimental data used for the Weibull model is also important with respect to the lag time, t_L. Figure 2-12(a) gives an example of where positive values of t_L would give negative results for the amount of API dissolved at time points prior to the onset of dissolution when ($t - t_L$) was negative and β = 1.

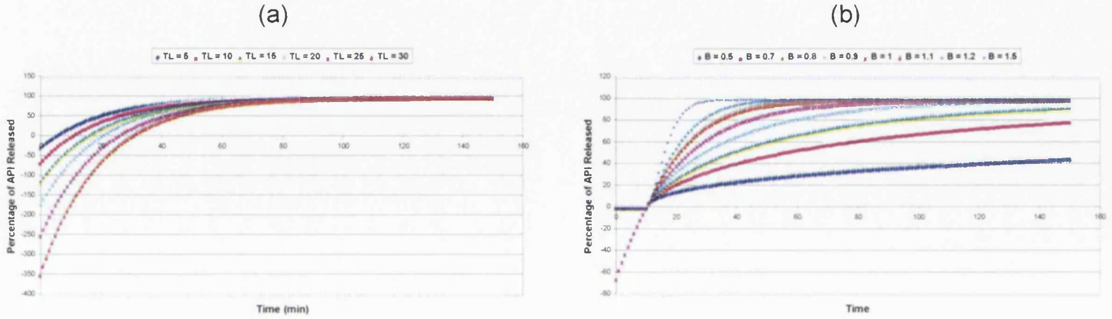
(a)

(b)

Figure 2-12: Weibull model (a) effect of a positive t_L for β = 1 and (b) the effect of a positive t_L with non-integer values of β.

Figure 2-12(b) illustrated how non-integer values of β combined with a negative value of $(t - t_L)$ result in the equation becoming non-defined in that region.

2.2.4 Other Methods Used to Model Dissolution Profiles

Hixson-Crowell Model

Work performed to investigate the "dependence of reaction velocity upon surface and agitation" in 1931 resulted in a theoretical equation that described the particle regular area as proportional to the cubic root of its volume (Hixson and Crowell, 1931; Hixson and Crowell, 1931a).

$$W_0^{\frac{1}{3}} - W_t^{\frac{1}{3}} = \mathrm{K}_s t \qquad \textbf{Equation 2-17}$$

Where W_0 is the amount of API present in the sample initially, W_t is the amount left at time t and K_s is a constant representing the surface-volume relationship (Coata and Lobo, 2001) also called the dissolving constant (Schatz *et al.*, 2003). It can be used to describe API release profile bearing in mind the effect of the dissolution causing a decrease of the surface for the API particles. The model can be rewritten and simplified when applied for samples where dissolution takes place in planes that are parallel to the drug surface upon proportional reduction of the sample dimensions retaining the sample geometry; such is the case for tablets. However it appears that generally the model is applied in the form of Equation 2-17 (Polli *et al.*, 1997; Schatz *et al.*, 2003). When this model is employed the assumption is made that the API release rate is unaffected by any diffusion processes that may occur through the sample matrix and that the only limitation is the dissolution of the drug particles.

Baker-Lonsdale Model

This method was derived from the Higuchi model. It was developed to illustrate the controlled release of API from a spherical dosage form.

$$\frac{3}{2}\left[1-\left(1-\frac{M_t}{M_\infty}\right)^{\frac{2}{3}}\right]-\frac{M_t}{M_\infty}=\frac{3\mathrm{D}_\mathrm{m}C_{ms}}{r_0^2C_0} \qquad \textbf{Equation 2-18}$$

Where M_t is the amount of API released at time t, M_∞ is the infinite amount of API released, C_{ms} is the solubility and C_0 is the initial concentration of the API in the sample matrix, r_0 is the radius of the sample and $\mathrm{D_m}$ is the diffusion coefficient (Costa and Lobo, 2001).

Dissolution Efficiency

The *DE* is calculated by the area under the dissolution profile/curve (AUC) up to a specific time as a percentage of the rectangle that represents complete dissolution i.e. 100% at the same time point, Figure 2-13 and Equation 2-17 (Costa and Lobo, 2001; Anderson *et al.*, 1998).

$$DE = \frac{\int_{t_1}^{t_2} D\,dt}{D_{100} \times (t_2 - t_1)} \times 100\% \qquad \textbf{Equation 2-19}$$

Where D is the percentage of API dissolved at time t.

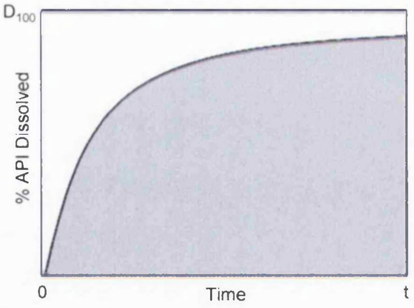

Figure 2-13: Calculation of dissolution efficiency by AUC.

2.3 Comparison of Dissolution and Image Parameters

The main objective of this work is the correlation of NIRM images of the dosage forms to their dissolution performance. This requires that there must be numerical values to describe the images that can be compared to the dissolution parameters calculated from the methods used in section 2.2.2. Chapter three will investigate one of these image parameters called the mean score value (MSV). The pixel distributions that can be obtained for a component from the scores image is described earlier in this chapter, section 2.1.2 in Figure 2-3(b). The values calculated for these distributions are called sample statistics. This is the source of the MSV along with other parameters that describe different features of the pixel distribution including the skew, kurtosis and standard deviation.

The skew value describes any asymmetry of the distribution with an ideal value of zero. A negative skew value relates to asymmetry to the left hand side of the distribution which would relate to "holes" in the image where there might be none of that particular component. Alternatively a positive skew value relates to asymmetry to the right hand side of the distribution that would relate to "hot spots" which are regions with a very high abundance of that particular component.

The kurtosis value describes any deviations of the distribution i.e. any tailing present. A negative kurtosis value means the distribution does not have any tailing, whereas a positive kurtosis shows that it does.

In work carried out investigating the powder blend homogeneity from NIRM images of tablets, it was found that calculation of a percentage standard deviation value (% STD), also known as the normalised standard deviation, could provide an indication of the extent of blending whereby the value would decrease with increased blending/homogeneity of the sample (Lyon *et al.*, 2002).

In total the parameters that would be taken from the sample statistics for comparison would be the MSV, skew, kurtosis and the % STD values.

It is also possible to obtain domain statistics about the components in an image. These relate to the areas of the components on the sample surface, which tend to form clusters or domains. These domains can be quantified by calculating the number, average size and distance from each other in the image, which will be described in chapter three. The domain statistics that would be selected and added to the ones from the sample statistics to describe the images are the number of domains, the mean equivalent diameter (MED) and the nearest neighbour (NN) values. The imaging parameters that were used are summarised in Table 2-3.

However, the specific image parameters used may, in reality, only apply to the initial dissolution process as the particular of the wafer image would effectively change as the dissolution process progresses (Aaltonen *et al.*, 2006).

	Imaging Parameters
Particle Statistics	MSV
	skew
	kurtosis
	% STD
Domain Statistics	number of domains
	MED
	NN

Table 2-3: Imaging parameters selected for comparison to dissolution parameters.

The dissolution parameters that were selected for use are shown in Table 2-4. The t_p and P_t values were model independent which allowed their measurement for all dissolution profiles irrelevant of shape. The initial rate, k_0, was also a parameter that could be calculated for dissolution profiles independent of shape as it was not particularly tied to any overall kinetic model.

Many of the parameters present in the models that could have been used to fit the dissolution curves were not really related to the dissolution rate, see section 2.2.3. They were more dependent on the units used and would not be a good choice for the comparison to the imaging parameters. Only the parameters related to the dissolution rate would be used for any correlations, Table 2-4. As the Higuchi model was the same as the Korsmeyer-Peppas model with $n = 0.5$, only the Korsmeyer-Peppas would be included.

Table 2-3 and Table 2-4 show the numerical parameters that have been selected to be used for the evaluation and eventual correlation (chapter seven) of the NIRM imaging and dissolution profile data.

Method	Dissolution Parameters
Time to Percentage Dissolved	t_p
Percentage at Specific Time	P_t
Initial Rate	k_0
Exponential Function	k_e
Weibull Model	t_L, T_d, β
Korsmeyer-Peppas Model	n

Table 2-4: Dissolution parameters selected for comparison to image parameters.

3 Evaluation of NIRM Chemical Images: Mean Score Value

3.1 Introduction

In the majority of spectroscopic imaging performed, only one or two components of the sample are focused on using selected wavelengths or PCA. This tends to be in a qualitative situation, such as the detection of an impurity or degradation product (Koehler *et al.*, 2002). As the field of NIRM imaging expands into pharmaceuticals, there is the need for a more comprehensive understanding of the chemical images being produced. The mind set is shifting away from the traditional QC approach of focusing on the API as more and more examples are coming to light that problems with finished products can be due to the other "inert" components present in the formulation (Clarke and Hammond, 2003; Clarke, 2004). Currently, the analysis of images tends to be dependent on the ability of the user to identify the differences between the images. As the situation is changing, and the whole sample matrix comes under scrutiny with comparisons of the chemical images required between samples as well as to other physical parameters associated with the sample, improvements would be made if there was a way of translating and displaying the results of the NIRM imaging in a more standardised and simplified form. This in turn could be used to establish limits on a pass or fail basis for the parameter of interest.

Investigations are required into image parameters that can be used to describe the data in this reduced form. One of the possible parameters to use is the mean score value (MSV). This value is obtained after PLS has been performed on the image and the score matrix has been refolded to create the score images for each factor (representing each component in the sample) calculated, see section 2.1.2 for an example in Figure 2-3. There are a set of sample statistics for the pixel distribution of each factor's score image including the mean score value. This is the average value of the score values of every pixel in the distribution and it has been reported that the MSV is directly related to the percentage of that component in the sample formulation (Clarke, 2004). This chapter aims to investigate this relationship and evaluate the MSV as a viable parameter for the simplified description of the NIRM images.

3.2 Experimental

3.2.1 Materials

A three-component system based on a Pfizer product (V) was selected for the initial work to be carried out, assessing the suitability of producing blends in the laboratory. This would be important as further work will involve changing various physical input parameters of the excipients and API, which would not be possible at plant scale to obtain the blends necessary. V is a product that has been known to have experienced some dissolution issues in the past.

Table 3-1 shows the percentage m/m (% m/m) concentration for the formulation of interest. Due to delays in the sourcing of larger quantities of the API and excipients, existing laboratory samples were used, but there were only small quantities available.

Ingredient	**% (m/m) V Formulation**
D (API)	46.5
Microcrystalline Cellulose (MCC)	52.0
Magnesium Stearate/Sodium Lauryl Sulphate 90:10 Blend	1.5

Table 3-1: % m/m in V formulation.

The lubricant blend was regarded as one component for all the imaging techniques utilised because in the production of pharmaceuticals it gets added as one component[1]. Also there was only the equivalent of 0.15% of the sodium lauryl sulphate (SLS) present in the formulation therefore the spatial constraints of the imaging systems would have prevented this from being detected.

The blend wafers for the concentration investigation into the formulation information that could be obtained from the NIR images, section 3.3.5 were made using materials from a different source as there were not enough of the components in Table 3-1 left to allow production of all the blends required.

---

[1] The lubricant blend may also be referred to as magst or magst/SLS in subsequent figures throughout the work performed on Product V.

3.2.2 Methods

Particle Sizing- PharmaVision System

The excipients and API were analysed using the PharmaVision 830 particle size instrument (PVS) (Malvern Instruments, Worcs, UK) to gain some information about their particle size distributions. In this method the dry samples are dispersed onto a glass slide by a sample preparation device (SPD) using compressed air. The conditions used have been developed to maximise the number of primary particles of the substance and to minimise agglomerates by breaking them up. The instrument then scans the dispersion, whereby the particles are illuminated from beneath and a set of optics above the slide collects the size information from the particle silhouettes produced. It can cover the range 0.5 μm - 2000 μm using various different optical settings. The images obtained are manually inspected and anything that is not a primary particle can be removed, for example a smudge on the glass sample plate. The software then provides histograms of the size distribution by number and by volume. These also include other size statistics such as the mean particle size.

Blending and Wafer Production

A blend of ~25 g was calculated to be the maximum size possible taking into account the quantities of excipients and API available, from Table 3-1. This was weighed out and mixed using a Turbula blender (Glen Mills, NJ, USA) for five minutes at 96 rpm.

The blend was pressed into wafers to emulate a solid dosage form and to provide a more optically flat surface for spectroscopic analysis. This was also carried out to ensure reproducibility of the sample form available for dissolution within the studies to ensure consistency. For this 300 mg of the blend was weighed then compressed in a punch and dye using a hydraulic press at 2000 psi for three seconds. Ten wafers were made from both the laboratory produced and the commercial blend, for comparison. The weight and thickness of the wafers were measured.

For the investigation into MSV using a two component blend of D and MCC, the % m/m was weighed out of each ingredient to make up 300 mg for each wafer. This was then mixed by hand for approximately two minutes and pressed into a wafer using the same conditions as above.

Near-infrared Spectroscopy

Reflectance NIRS

Initially for all the studies, powder samples were run at the macro-scale to evaluate any differences in the bulk of the samples. Five replicates of the each of the excipients and API (~1 g) were placed into glass vials and analysed using the Foss NIRSystems 6500 monochromator (Foss NIRSystems Inc., Silver Springs, MD, USA) with a vial module attachment as shown in Figure 3-1 which was controlled using Delight software (DSquared Development, LaGrande, OR, USA). This was to aid the characterisation of the blend ingredients. The wavelength range was truncated at 1150 nm to remove any colour peaks present as well as a detector changeover at ~1100 nm, so the range used was 1150 - 2400 nm.

This method was used for the commercial and laboratory made blends with three replicates performed and the average of all three spectra was used.

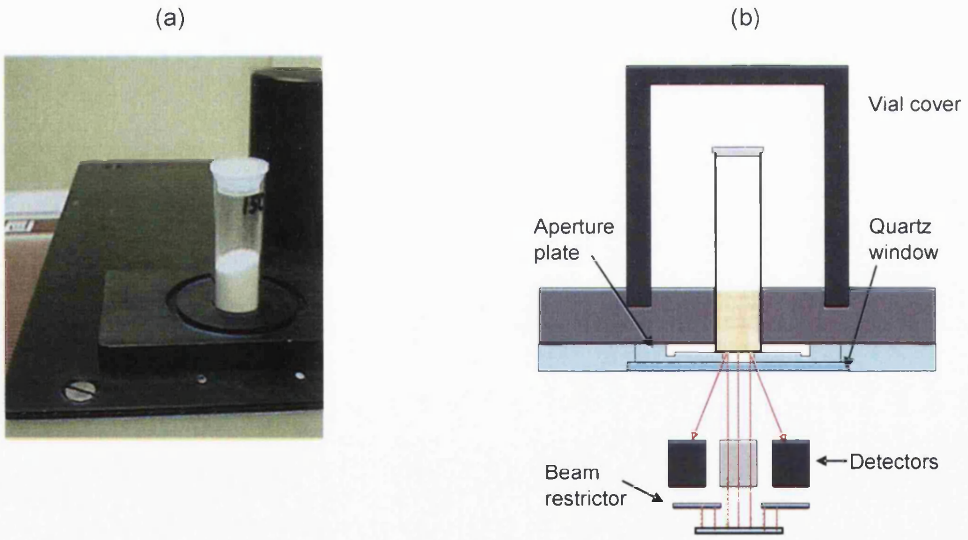

Figure 3-1: (a) Foss Vial Module for powder samples with (b) schematic of data collection method.

The instrument passed all the manufacturer's performance tests including wavelength accuracy, photometric noise and accuracy and repeatability. The instrument was considered to be operating correctly.

Transmission NIRS

Ten wafers of the laboratory made and ten wafers of the commercial blend were analysed using the Foss NIRSystems 6500 monochromator (Foss NIRSystems Inc., Silver Springs, MD, USA) with an InTact tablet transmission analyser. In this analysis the NIR light is incident on one side of the tablet/wafer and the detector is on the other side, which allows the light that has passed through the sample to be detected. The spectra obtained are representative of the whole sample, see Figure 3-2. The wavelength range used was 850 - 1450 nm as the responses at higher wavelengths had a reduced signal-to-noise ratio due to sample thickness. The thickness, hardness and weight of tablets can cause variation in the spectra.

The instrument passed all the manufacturers performance tests including wavelength accuracy, photometric noise and accuracy and repeatability. The instrument was considered to be operating correctly.

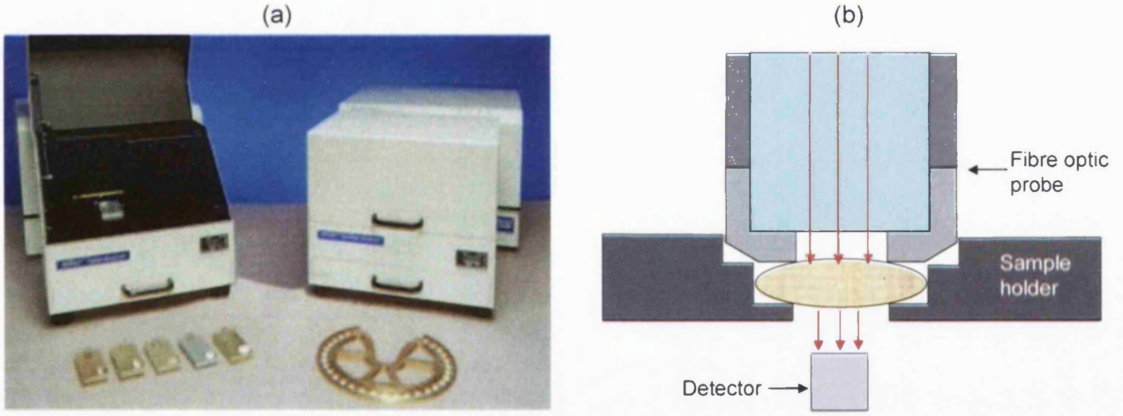

Figure 3-2: (a) Foss NIRSystems monochromator with InTact tablet transmission analyser (source: Foss website www.foss-nirsystems.com) and (b) a schematic of data collection method.

Near-infrared Microscopy Imaging

Spectrum Spotlight 350-Line Mapping

In this method, a PerkinElmer Spectrum Spotlight FT-NIR 350 (PerkinElmer, Wellesley, MA, USA) was used. The Spotlight used a liquid nitrogen cooled, 16 pixel indium gallium arsenide (InGaAs) linear array detector which gave a wavenumber range of 7800 to 3600 cm^{-1} (approximately 1280 to 2700 nm). The sample was mounted onto a microscope slide and placed on a stage then moved under the detector to enable the 2D image of a defined area to be built up line by line. Steps of 25 μm in the x and 400 μm (16 × 25 μm) in the y direction were made, resulting in a spectrum from each 25 by 25 μm area (pixel). The third dimension was added as the spectral information was collected. Figure 1-8(b) shows a schematic of line mapping. Spectra were collected over the spectral range 3600 – 7800 cm^{-1}, with 16 cm^{-1} data intervals and an average of 4 scans per pixel. An area of 5 x 5 mm was scanned for each of the blend wafers and an area of 1 x 1 mm was scanned on wafers made of the excipients and API for the library images.

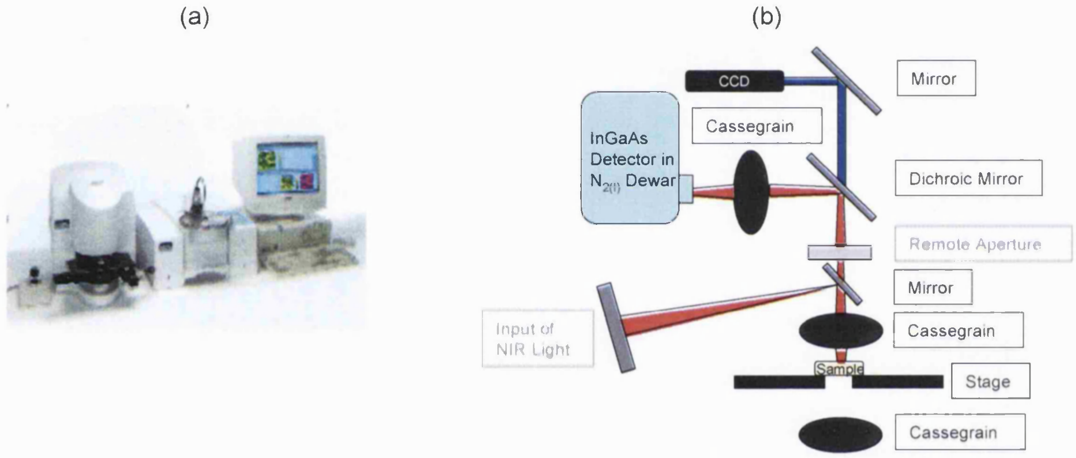

Figure 3-3: (a) Image of the PerkinElmer Spectrum Spotlight 350(source: PerkinElmer website http://las.perkinelmer.com) and (b) schematic of the system.

Data Processing

The blends could not be compared in a univariate manner as utilised for the pure components as the light penetrated the sample and would probably have interacted with more than one component. This was the result of particle size, spatial resolution and sampling depth. Therefore each pixel contained information relating to more than one component and hence multivariate analysis was required.

All data processing was carried out using the Spectral Dimensions ISys chemical imaging software version 3.1.1.14 (Spectral Dimensions, Olney, MD, USA).

The range used was 7600 - 3800 cm^{-1}. Pre-processing of the sample data files were carried out before the chemometrics were performed. The sample spectra were collected in % reflectance (% *R*) therefore they were divided by a constant of 100 to convert them into reflectance (*R*). Then to convert to absorbance, the inverse of the reflectance spectra was taken (1/*R*) and finally $\log_{10}(1/R)$. The spectra were normalised using a standard normal variate (SNV) transform to remove any offsets, which may have been present in the data due to physical variations and also to correct for sample surfaces that were not optically flat, therefore improving the image produced, see section 2.1.1.

Next a PLS-2 calculation was performed. This was used as a classification model and allowed the identification of the individual ingredients within the sample matrix. Initially a library was built using all three ingredients giving three classes. This was then compared to the sample data in order to describe it in terms of a spectral (loading) and a numerical (score) contribution. The model used four factors as this was where the minimum error was observed from the predicted residual error sum of squares (PRESS) plot, indicating the minimum number of factors required to describe the data set.

Every pixel in the image had a score value for each of the loadings contributing to that pixel. RGB three channel colour images could then be produced whereby limits were set (see below) for the score values of each factor to determine which pixel would be assigned to which component. This resulted in a single channel image for each component. These were then given an individual colour (red, green or blue) then overlaid to give the RGB image.

Each score image was produced by selecting the percentage of pixels or area of the pixel distribution related to the amount present, see section 2.1.2. For this chapter the percentage method was applied. Here the upper limit remained stationary, the lower limit was moved to allow the calculated number of pixels to be included, or a value as close as possible to the ideal, due to the bar width of the histogram, see Figure 3-4. Next a single channel image with colour limit clipping was created for each of the three factors and these were overlaid using the RGB image tool to create the chemical image.

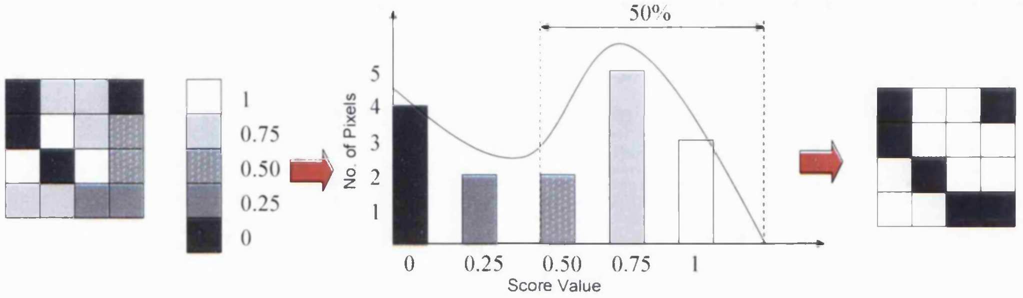

1. Score image for whole sample

2. Plot of pixel distribution with 50% selected for an example component with 50% m/m in the formulation

3. Score image for the component of interest (white pixels)

Figure 3-4: Production of score images for the individual components in a blend.

Domain size information could also be produced after the PLS calculation had been performed. As with the production of RGB images, the lower limit was moved to allow the calculated number of pixels to be equal or as close to the percentage m/m in the formulation of the component as possible. Then the contour tool was selected and a value was used as the contour level that represented the point where all the areas deemed to be that particular component were enclosed in the contours. For consistency, the ideal contour level value was compared to the values for the pixel distribution and mostly they would be the same as the mean value or the lower limit, otherwise some form of calculation would be used involving these values. In this case the value of the lower limit was entered into the contour level box, a single channel binary image was created and the particle statistics option selected. This provided information on the number of domains, their size and area covered.

3.3 Results

3.3.1 Particle Sizing

Vision particle size analysis was performed in triplicate for each excipient in V. This was done to gain more information on the input materials going into the blend as particle size may have had an effect on the images produced.

The resultant particle size distributions are shown in Figure 3-5. The particle size ranges of the input materials of the blend are defined in Table 3-2.

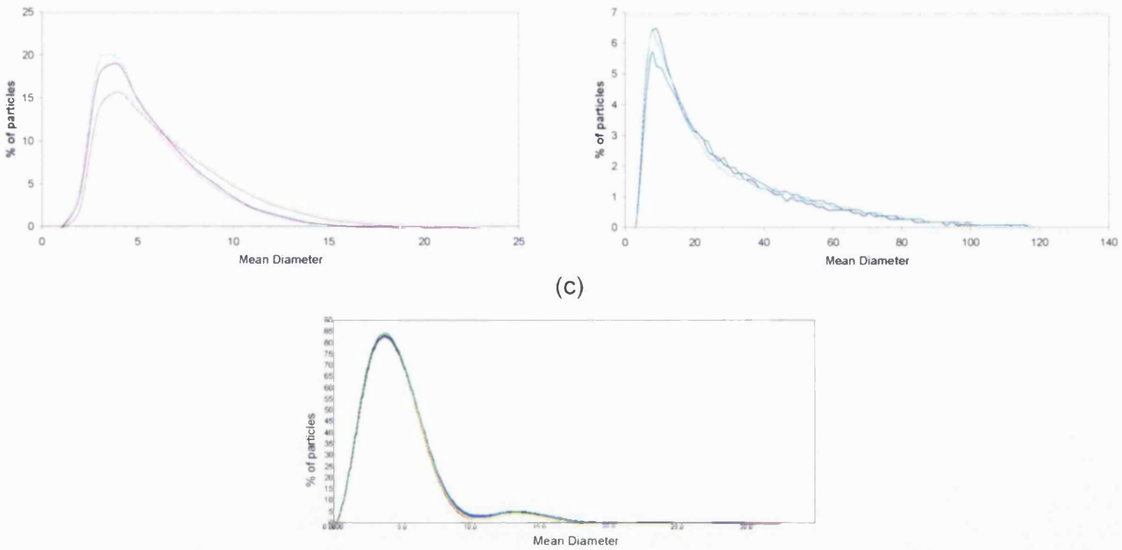
(a) (b) (c)

Figure 3-5: Particle size distributions by number for (a) lubricant blend, (b) MCC and (c) D.

The full size ranges were taken from volume distributions as these gave a good indication of the larger particles present. The number distributions showed that the mean particle size of all three substituents did not fall above 20 μm. Any differences seen in the results of the multiple samples were due to the sampling of the powder and distribution by the SPD.

Sample	Size Range (μm)
Lubricant blend	0 - 65
MCC	0 - 180
D	0 - 95

Table 3-2: Particle sizes for input materials.

The lubricant blend had the smallest mean particle size of ~4.5 μm. When compared to the pixel size in use for the NIR imaging instrument being 25 x 25 μm, it could be predicted that there may be some difficulty assigning areas of lubricant blend present. MCC had the largest mean particle size at ~15 μm, therefore no identification problems would be foreseen. D had a mean particle size of ~4.5 μm so; depending on how it associated with itself in the blend, there may be some problems in pixel assignment.

3.3.2 Wafer Production

The weight and thickness of each wafer made from the commercial and the laboratory made blend were measured, see Table 3-3.

Sample	Mass (g)	RSD	Thickness (mm)	RSD
Commercial	0.3050	1.672	1.57	1.3
Laboratory	0.3019	0.596	1.53	2.0

Table 3-3: Average physical parameters of commercial and laboratory V wafers.

There were no significant differences between the wafers produced from each blend with respect to mass and thickness.

3.3.3 Near-infrared Spectroscopy (NIRS)

Reflectance NIRS

Reflectance NIRS analysis performed for five samples of each excipient in the V blend showed the spectra of the excipients and API to be significantly different. Therefore, this should allow adequate discrimination between them with the possibility to monitor unique wavelengths e.g. ~1720 nm for lubricant blend, see Figure 3-6.

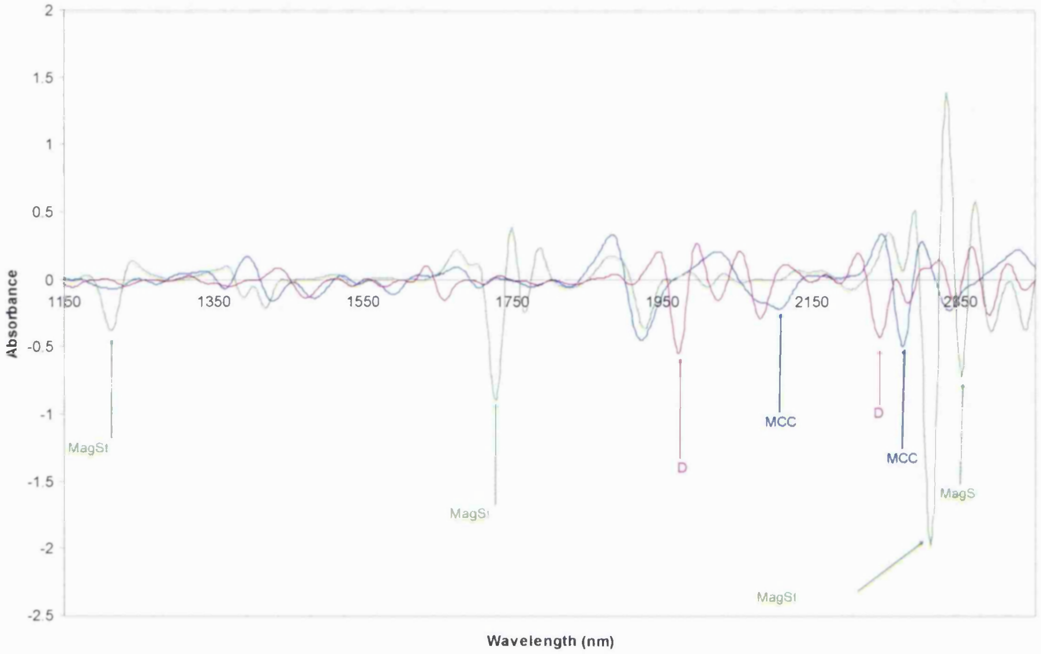

Figure 3-6: Second derivative of the average NIR spectra of five replicates for the MCC (—), D (—) and lubricant blend (—).

Reflectance NIRS was also performed in triplicate on both commercial and laboratory blends. The raw spectra showed that the laboratory blend had a slightly larger particle size than the commercial blend. Upon performing a standard normal variate (SNV) and derivatisation there were still some variations present in the intensity at certain wavelengths, see Figure 3-7.

There was a peak shape variation at ~1742 nm and intensity differences at 2276 nm and 2310 nm between the two blends, which were related to the magnesium stearate. It was not known if the lubricant blend used in the laboratory blend was the same as was used for the commercial blend. Commercial samples of magnesium stearate exist as a compound of magnesium with a mixture of solid organic acids that consists mainly of variable proportions of magnesium stearate and magnesium palmitate. This can vary between suppliers so, if the supplier of the magnesium stearate was different between the blends, this could affect the proportion of the stearate/palmitate and hence the NIR spectra. There were also intensity differences between the blends at 1972 nm, 2026 nm, 2082 nm and

2238 nm, which were related to the D, Figure 3-7. This API can decompose on exposure to light and the sample container was a glass jar, therefore some decomposition may have occurred leading to the differences in the spectra. However, the peaks were still in the same position. Therefore, it may have been an effect of moisture or particle size.

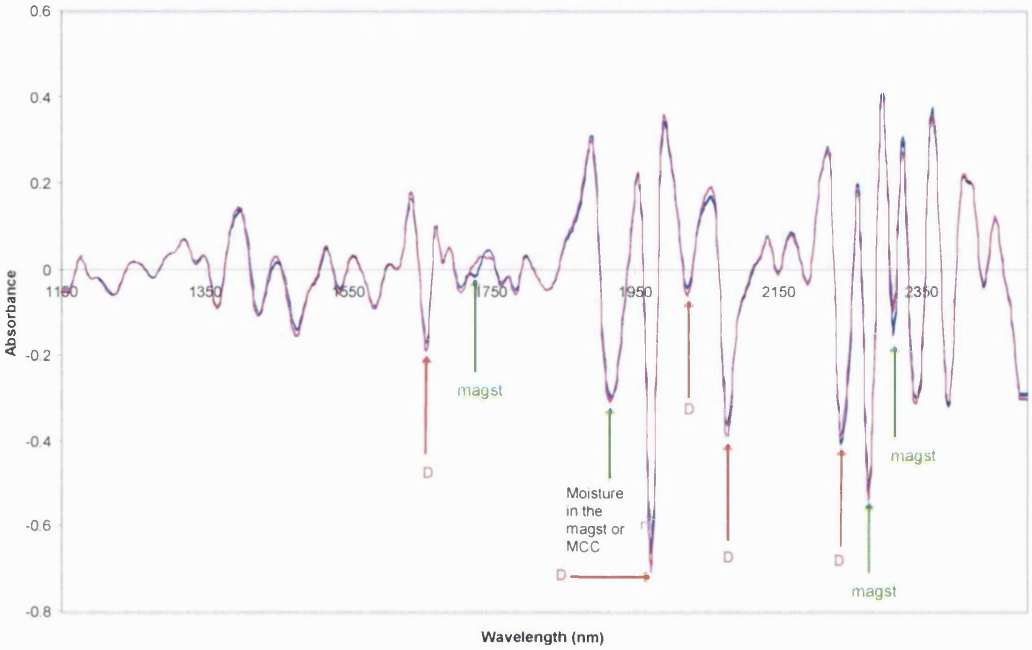

Figure 3-7: Second derivatised NIRS reflectance data of three replicates of commercial (—) and laboratory (—) samples.

PCA was performed on the derivatised data (whereby physical effects had been removed) and the score values produced were plotted against each other to look for any separation between the blends.

In the score 2 vs. score 1 plot the data separated into two distinct blend clusters by the score 1 values, Figure 3-8. The commercial blend was more variable with respect to the score 2 values than the laboratory blend. A similar relationship was seen for score 3 vs. score 1, but the plot of score 3 vs. score 2 gave a random distribution of points. The difference seen along score 1 would most likely have been related to a variation in the ingredients used in the two blends. The mixing of the results for the other score values indicated that the two blends were similar.

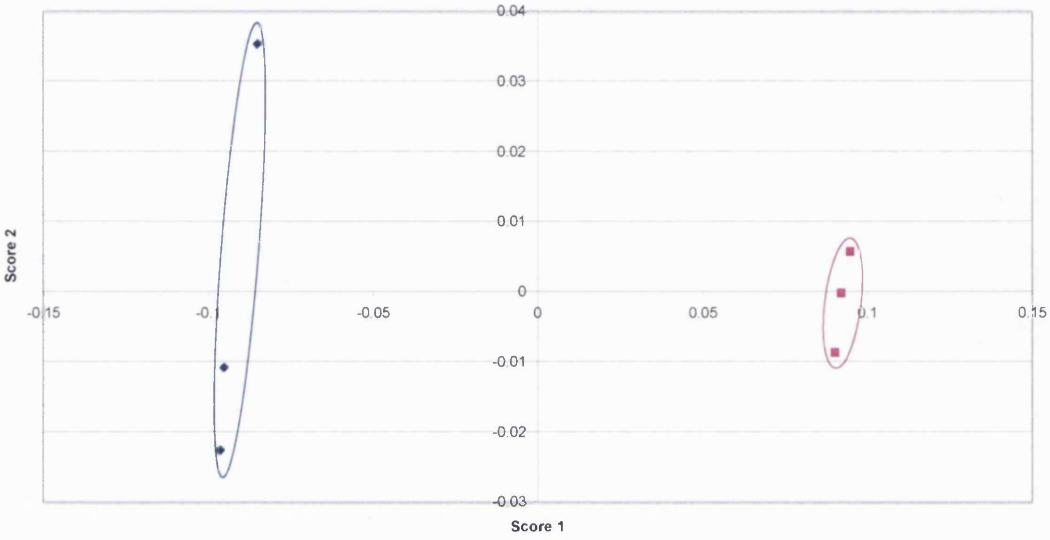

Figure 3-8: Comparison of PCA score 2 vs. score 1 for reflectance NIRS of three replicates of commercial (◆) and laboratory (■) samples[2,3].

Transmission NIRS

Transmission NIRS measurements were carried out for ten wafers of each the commercial and laboratory blends. Transmission measurements on the Intact instrument can lose reproducibility at the higher end of the wavelength range, >1400 nm, due to the depth of penetration being greatly reduced and poor signal to noise, therefore spectra were truncated at 1425 nm.

On comparison of the commercial and laboratory blend wafers, there did not seem to be any significant differences between the average raw or derivatised spectra.

---

[2] Note that the ellipses drawn around data points in this scatter plot and any subsequent plots are there as a visual aid and do not have any statistical meaning.

[3] The score plots shown for this study and subsequent studies are meaningful as they account for >~40% variance.

PCA was performed on the derivatised data (whereby physical effects had been removed) and the score values produced were plotted against each other to look for any separation between the blends.

The same separation was observed along score 1 in the score plots as for the reflectance data, Figure 3-9. Again this could have been due to the lot of lubricant blend being different for each blend, but in general the two sample sets were similar.

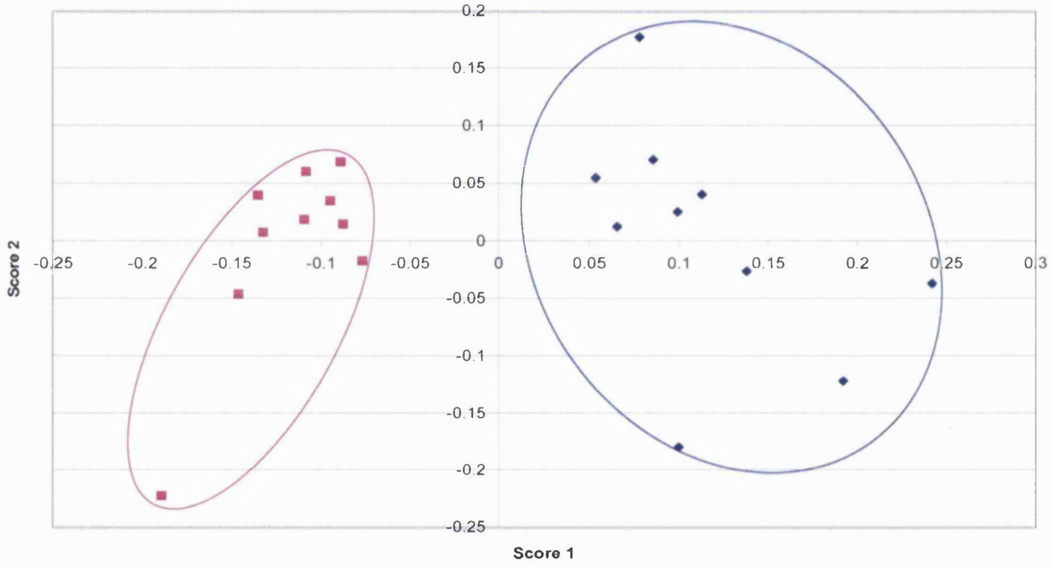

Figure 3-9: Comparison of score 2 vs. score 1 for transmission NIRS of three replicates of commercial (◆) and laboratory (■) samples.

3.3.4 Near-infrared Microscopy Imaging

Spectrum Spotlight 350-Line Mapping

Initially RGB images were produced for all the wafers of both blends to evaluate if there were any visual differences in the component matrix. Figure 3-10 shows an example of each.

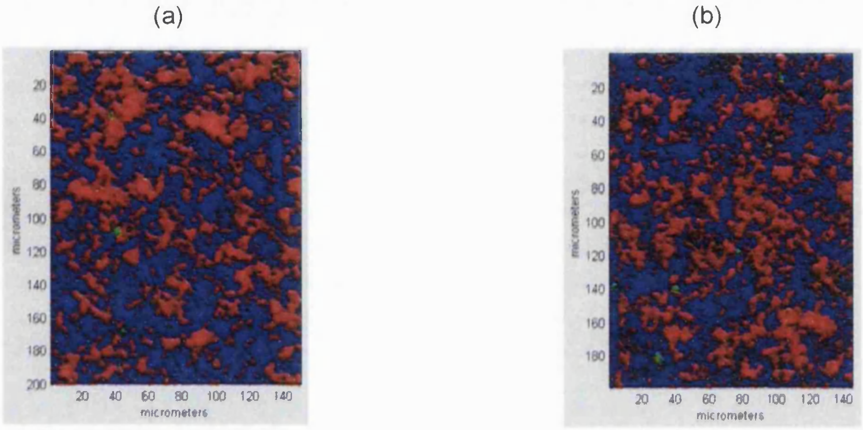

Figure 3-10: Comparison of Spotlight RGB images of (a) laboratory and (b) commercial blend wafers with MCC (—), lubricant blend (—) and D (—).

Visual comparison of the two blends does not show any major differences. The laboratory blend appears to have larger regions of D and MCC compared to the commercial blend, which may be due to the differences in the mixing between the plant production method and the scaled down version used in the laboratory.

The domain statistics were calculated, which relate to the areas of the different components present in the image. This showed the lubricant blend to be fairly consistent in both blends, with an average mean equivalent diameter (MED) of 36.25 μm ± 1.77 μm for the laboratory and 40.75 μm ± 2.80 μm for the commercial blends.

The D was shown to have a slightly higher domain size in the laboratory blend with an average MED of 243.25 μm ± 11.67 μm vs. 218.75 μm ± 12.60 μm for the commercial blend, which led to a reduced number of domains, 189.7 ± 18.51 vs. 236.8 ± 24.54 for the commercial blend. A similar difference was observed for MCC, with an average mean equivalent diameter of 370.5 ± 17.15 μm vs. 305.75 ± 18.78 μm, which in turn resulted in fewer domains being present, 91.4 ± 7.89 vs. 135.6 ± 20.26 for the commercial blend.

Overall, in the laboratory blend, the MCC domains were ~21% larger, the D domains were ~11% larger and the lubricant blend domains were ~11% smaller. A Student's *t*-test was performed on the domain statistics for both of the sample sets. The number and MED of domains for MCC and D were found to be significantly different between the two blend types, with values of $p < 0.05$. The MED of the lubricant blend domains also showed a significant difference however, the number of domains did not, Table 3-4.

	p Value	
Component	**Number of Domains**	**MED**
MCC	3.26×10^{-5}	2.24×10^{-7}
D	1.52×10^{-4}	2.70×10^{-4}
lubricant blend	7.42×10^{-2}	7.87×10^{-4}

Table 3-4: Student's *t*-test results for domain statistics for laboratory versus commercial blend samples.

These differences could have been attributed to the scaled down method of blend production. Therefore it was concluded that the laboratory blends would be comparable to the commercial blend, given the available information.

Input Particle Size versus Domain Size

There is the possibility that confusion can arise in the discussion of NIR chemical images. This is mainly due to the choice of descriptive words used by the instrument manufacturers. For example, the statistics used to describe the regions of one component within an RGB image was labeled as particle statistics in the software. This would result in the naming of these regions as particles of that component. However, a comparison of the mean domain size results from the Spotlight data for each component with the measured mean input particle sizes, Table 3-2 clearly indicated that this nomenclature does not reflect the actual situation. The regions identified related to an agglomeration of that specific component as opposed to a particle, therefore in this work, these regions have been designated as domains of a particular component to minimize misinterpretation of the results.

3.3.5 Mean Score Value and Formulation Concentration Percentage m/m for Laboratory vs. Commercial Blends

It has been presented that the MSV found in the sample statistics showed some correlation to the percentage m/m (% m/m) of that component in the formulation (Clarke, 2004). When these values from the wafers were compared to the V formulation, the results did not show a direct correlation. This was the case for the commercial and the laboratory blends. Therefore it was not due to a variation in the mixing of the components between methods, Figure 3-11.

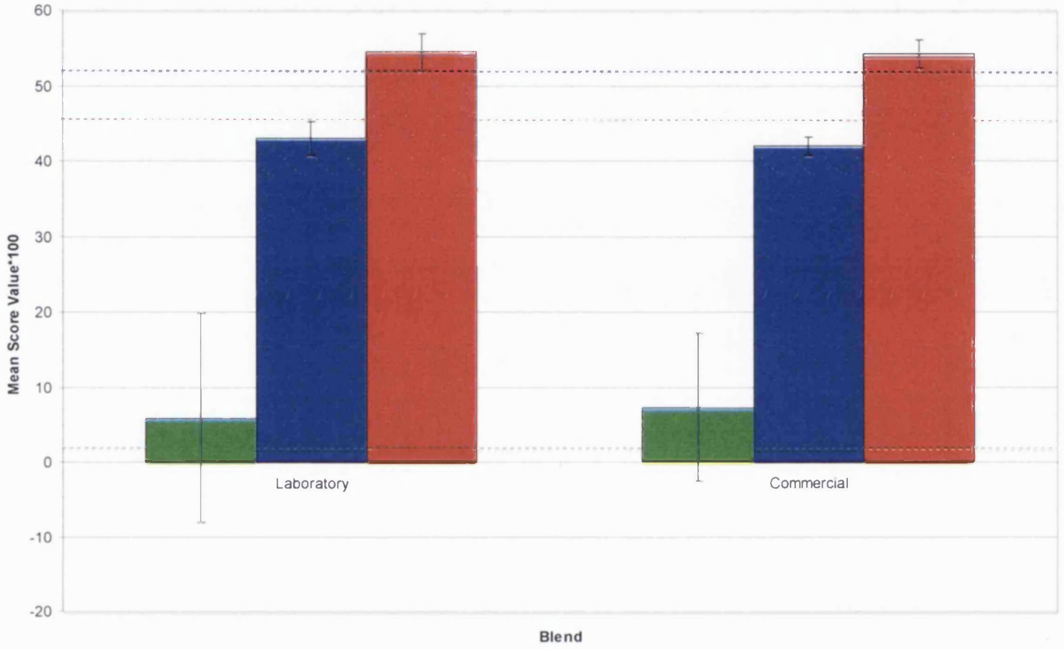

Figure 3-11: Comparison of mean score values for laboratory and commercial V blends with MCC (—), lubricant blend (—), D (—) and RSD error bars. The dashed lines represent the % of the three components in the formulation.

Therefore this method appears to be underestimating the amount of MCC and overestimating the amount of D present in the blend.

In this case the data were normalised prior to the PLS processing and score image generation, subsequently other pre-processing methods were utilised on the data from three of the commercial blend wafers to determine if another model described the blends more accurately. After the data normalisation, a number of Savitsky-Golay derivatives were carried out with varying parameters. The filter length, which determines how many data points are included, and the filter order, which represents the polynomial fitted to the data, were both varied and the results are shown below, Figure 3-12 to Figure 3-14. The

normalised data included was the average result for the same three wafers that were used for the derivatised data.
For the lubricant blend, the derivatised data up to a filter length of 19 gave a better indication of the formulation concentration than the normalised data alone, but these values were still at least 1% more than the formulation concentration, Figure 3-12.

The normalised result gave the highest mean score value for the MCC, but this was still approximately 10% below the formulation % m/m of 52%. The derivatised data at its best was ~16% below the formulation amount, Figure 3-13.

Using a second derivative produced the results closest to the actual value of 46.5% for the D, but these were still overestimated by ~6%, Figure 3-14.

Overall, using a second derivative with a filter length of 11 and a filter order of 3 would seem to give the best results for the lubricant blend mix and the D, but the value for the MCC is greatly underestimated when compared to simply pre-processing with normalisation.

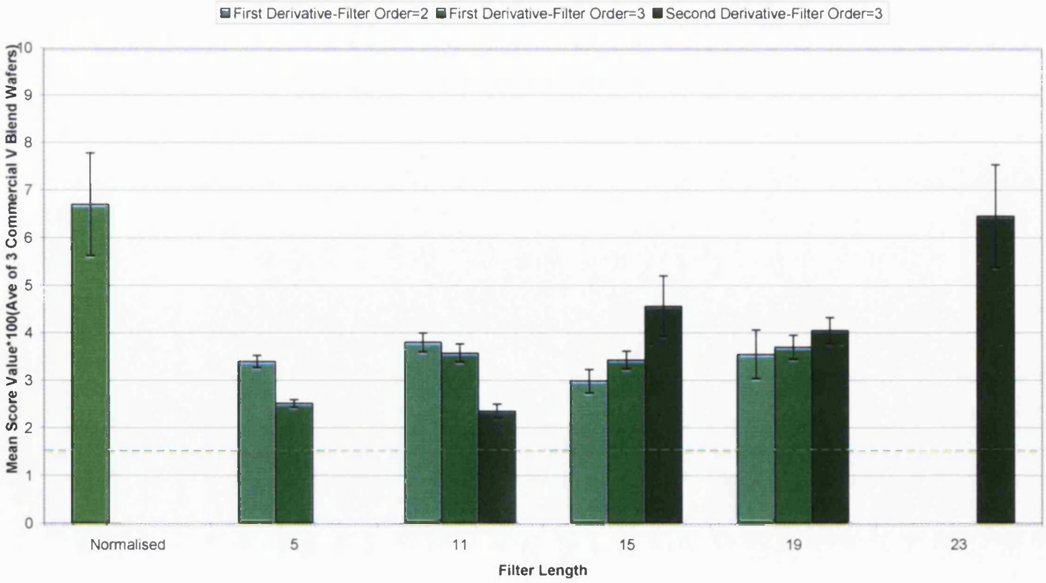

Figure 3-12: Comparison of mean score values for different pre-processing lubricant blend.

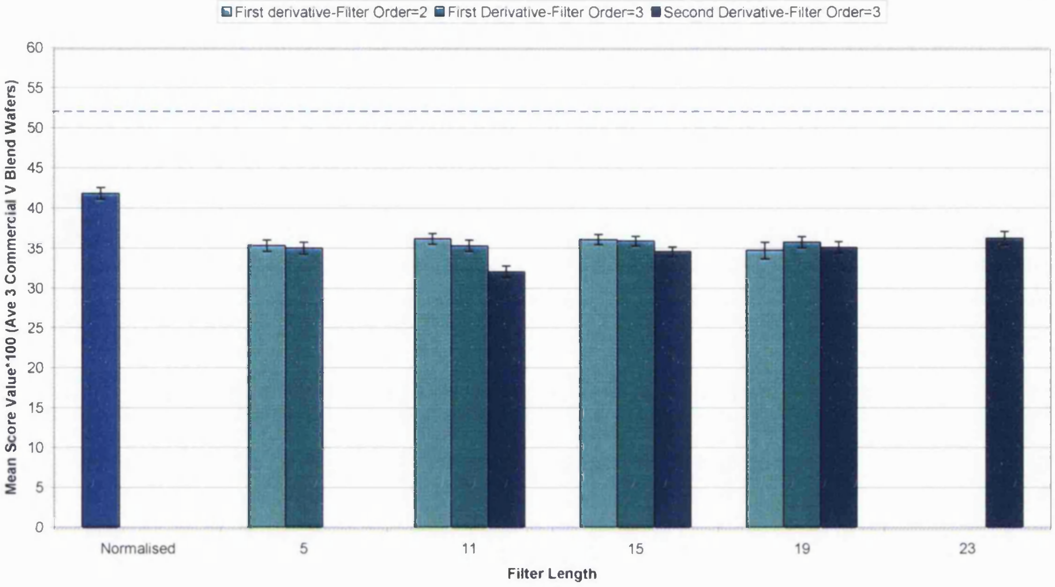

Figure 3-13: Comparison of mean score values for different pre-processing MCC

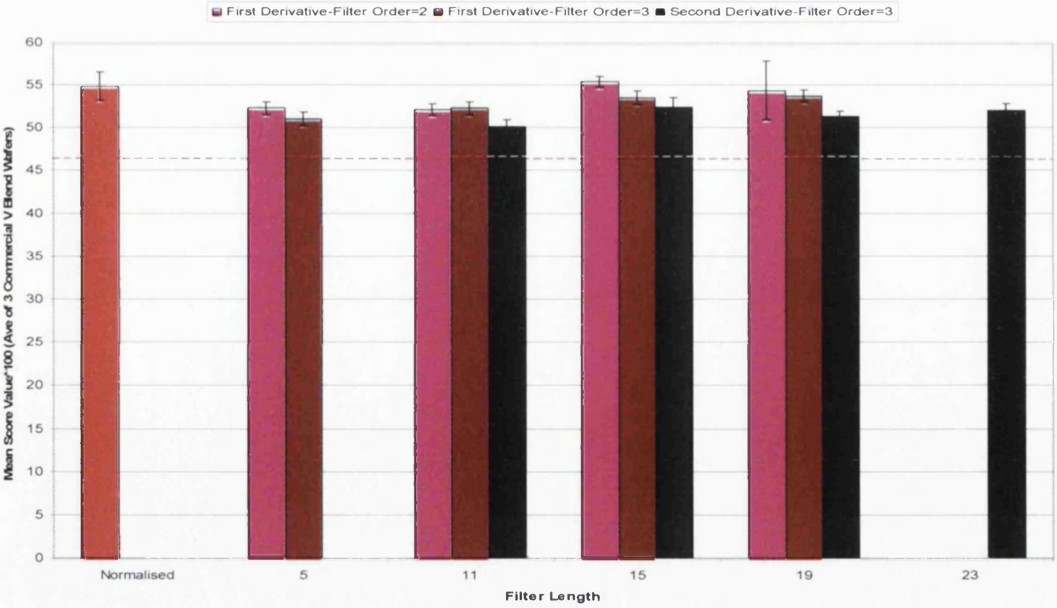

Figure 3-14: Comparison of mean score values for different pre-processing D.

Figure 3-15 shows the RSD of the scaled MSV relative to the actual % m/m in the formulation. From this plot it was seen that normalisation gave the best results for MCC and similar % RSD results to the derivatives for D, but it gave the highest RSD value for the lubricant blend. All the error in lubricant blend was much greater than for the MCC and D, with the smallest % RSD of ~56% observed for the second derivative with a filter length of 11 and a filter order of 3. The error was much larger for the lubricant blend because it was such a small component in the formulation, so 50% % RSD equates to 2.25% m/m vs. 1.5% m/m.

Of the derivatives, the first derivatives with a filter length of 11 and filter orders 2 and 3 seemed to give results that had reasonable % RSD for all the components, relative to each other. Although the % RSD for these came out at ~150, ~30 and ~12 for lubricant blend, MCC and D respectively, this value would ideally be less than five. Taking into account all the information, the values from the normalised data would be utilised for further investigations involving Spotlight data.

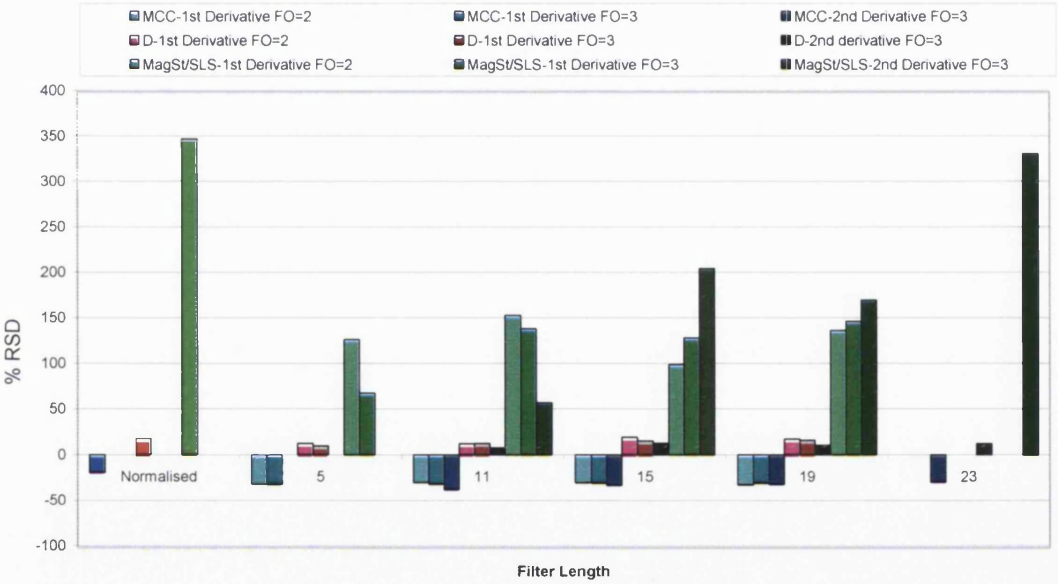

Figure 3-15: Comparison of the RSD of the average MSV to the actual % m/m in the formulation.

Construction of Calibration Equations for % m/m Prediction

In order to gain a better understanding of any relationship that might be present, blend wafers were made with varying concentrations of the two components covering the whole range of 10-90% m/m. Each component was weighed out to make up 300 mg in the total blend then pressed into a wafer using 2000 psi for three seconds. The blend wafers made are given in Table 3-5 and three were made for each % m/m combination.

% m/m MCC	% m/m D
90	10
80	20
70	30
60	40
50	50
40	60
30	70
20	80
10	90

Table 3-5: Composition of two component blend wafers for the calibration set.

The files were normalised[4] and the MSV*100 from the scores images were plotted against the % m/m in the formulation, Figure 3-16.

---

[4] The data had a 1st derivative, filter length 11 and filter order 3 applied and the calculations were carried out using this and the normalised files. Here the normalised provided MSV values closer to the actual % m/m.

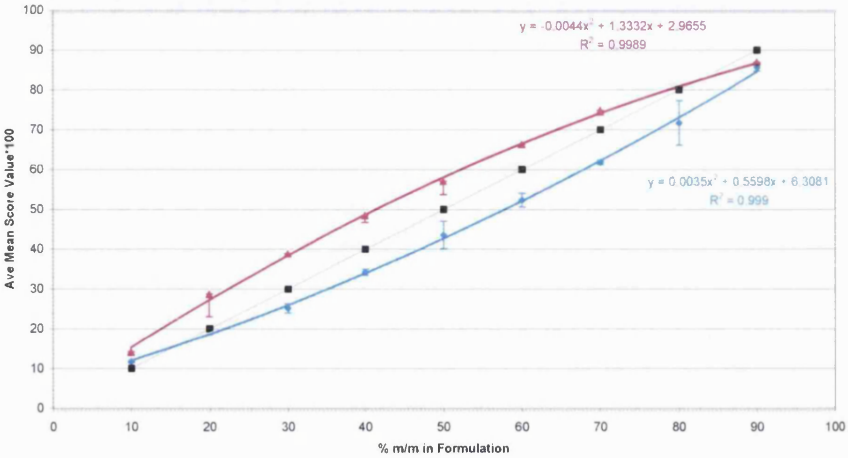

Figure 3-16: Plot of MSV*100 vs. % m/m in formulation for Spotlight images of two component blends, normalised with factor 1 (MCC) (—), factor 2 (D) (—) and the ideal (—).

Trend lines with quadratic functions were fitted to the data, Table 3-6.

Factor 1 (MCC)	$y = 0.0035x^2 + 0.5598x + 6.3081$
Factor 2 (D)	$y = -0.0044x^2 + 1.3332x + 2.9655$

Table 3-6: Calibration equations for the two component system from normalised Spotlight images.

In order to validate the prediction equations, three wafers were produced for each of the combinations in Table 3-7.

% m/m MCC	% m/m D
15	85
25	75
35	65
45	55
55	45
65	35
75	25
85	15

Table 3-7: Composition of the two component blend wafers for the validation set.

The validation set Table 3-7 was scanned and the % m/m of the components were calculated using the MSV*100 from the score images in the calibration equations and solving for x.

Factor 1 (MCC)			Factor 2 (D)		
Actual % m/m	**Ave Calculated % m/m**	**RSD**	**Actual % m/m**	**Ave Calculated % m/m**	**RSD**
15	13.35	6.29	85	91.12	1.13
25	24.19	2.04	75	78.87	0.46
35	34.24	1.70	65	68.27	0.94
45	43.81	6.97	55	58.51	5.17
55	52.03	2.22	45	50.13	2.24
65	64.42	0.78	35	37.60	1.31
75	74.62	1.54	25	27.23	4.35
85	84.68	1.21	15	16.99	6.11

Table 3-8: Predicted vs. actual % m/m values the validation two component blends from Spotlight images, normalised.

These calculated values were plotted against the actual values, which again demonstrated the possibility for the calculation of the % m/m in a formulation from the MSVs of the scores images, Figure 3-17(a) and (b). The % RSD values all fell within the analytical ideal of less than 5% error.

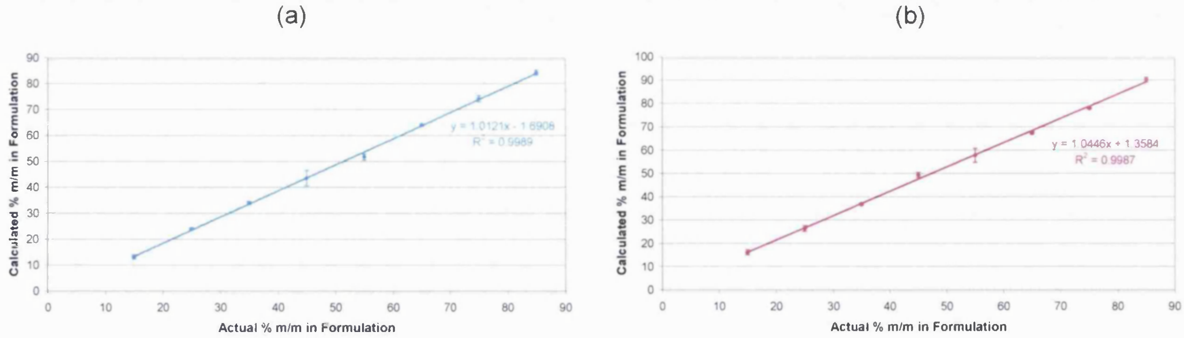

Figure 3-17: Calculated % m/m vs. actual % m/m for (a) factor 1/MCC (—) and (b) factor 2/D (—) from the Spotlight data for the validation two component blends.

Further Investigation into the Quadratic Nature of the Prediction Equations

It had been assumed that the MSV was linearly related to the number of pixels (area) assigned to the particular component. In reality, factors such as the density of each material would have affected this relationship. Differences in the molar absorptivites may have also played a part in any non-linearity observed in the relationship. For example, an API might be expected to have an increased absorptivity due to any aromaticity present in the compound, whereas excipients do not tend to contain aromatic groups.

A simple evaluation was conducted into the effect of different material densities. The absorptivities were assumed to be equal and a binary mixture of materials A and B, with densities (ρ) of 1 and 10 (mass per unit volume) was considered.

Component A has $\rho = 1$
Component B has $\rho = 10$

For a mixture with 50% m/m B, then the mixture would need to be made with the volume ratio 1 of B to 10 of A.

Figure 3-18: Unit representation of a 50% m/m mixture of components A and B.

The % m/m of B would be,

$$\%\text{m/m of B} = \frac{\text{Mass of B}}{\text{Mass of A + B}} \times 100$$

$$\%\text{m/m of B} = \frac{10}{10 + (10 \times 1)} \times 100$$

$$\%\text{m/m of B} = \underline{\underline{50\%}}$$

It was known that the depth of penetration of the NIR light into a sample was variable with respect to a number of factors including wavelength and density. Therefore, for this example, a unit depth was assumed to limit the calculations to areas as this would relate to the number of pixels.

Then the % area for B would be,

$$\%\text{Area of B} = \frac{\text{Area of B}}{\text{Area of A + B}} \times 100$$

$$\%\text{Area of B} = \frac{1}{1 + 10} \times 100$$

$$\%\text{Area of B} = \underline{\underline{9.09\%}}$$

Therefore 50% m/m of B would be represented by only 9.09% of the total area of the sample surface.

The general case for a binary mixture could be represented as follows:

Let $x_1 = \text{Mass fraction for component 1}$

$\rho_1 = \text{Density for component 1}$

$y_1 = \text{Area fraction for component 1}$

x_2, ρ_2 and y_2 were the corresponding values for component 2.

Let the surface area be A_1 for component 1 and A_2 for component 2.

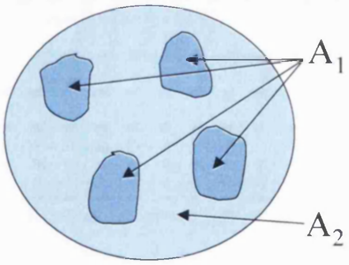

Figure 3-19: Example representation of the area assignment for a general binary mixture.

Now $x_1 = \dfrac{A_1\rho_1}{A_1\rho_1 + A_2\rho_2}$ i.e. $\dfrac{\text{Mass of component 1}}{\text{Total mass}}$

and $x_2 = \dfrac{A_2\rho_2}{A_1\rho_1 + A_2\rho_2}$

This assumes that the sample matrix looked the same no matter how the sample had been cut (if it had been cut) and also that the areas of components 1 and 2 represent the same volumes of the components.

Now $y_1 = \dfrac{A_1}{A_1 + A_2}$ and $y_2 = \dfrac{A_2}{A_1 + A_2}$

Rearranging and substituting for A_1 and A_2:

$$x_1 = \frac{y_1(A_1 + A_2)\rho_1}{y_1(A_1 + A_2)\rho_1 + y_2(A_1 + A_2)\rho_2}$$

$$x_1 = \frac{y_1\rho_1}{y_1\rho_1 + y_2\rho_2}$$

Similarly for component 2:

$$x_2 = \frac{y_2\rho_2}{y_1\rho_1 + y_2\rho_2}$$

Now $y_1 + y_2 = 1 \quad \therefore \quad y_2 = 1 - y_1$

So in terms of y_1:

$$x_1 = \frac{y_1\rho_1}{y_1\rho_1 + (1 - y_1)\rho_2}$$

$$x_1\left(y_1\rho_1 + (1 - y_1)\rho_2\right) = y_1\rho_1$$

$$x_1 y_1 \rho_1 + x_1 \rho_2 - x_1 y_1 \rho_2 = y_1 \rho_1$$

Move all y_1 terms to one side:

$$x_1 y_1 \rho_1 - y_1 \rho_1 - x_1 y_1 \rho_2 = -x_1 \rho_2$$

$$y_1 (x_1 \rho_1 - \rho_2 - x_1 \rho_2) = -x_1 \rho_2$$

$$\therefore \qquad y_1 = \frac{-x_1 \rho_2}{x_1 \rho_1 - \rho_1 - x_1 \rho_2}$$

or $$y_1 = \frac{x_1 \rho_2}{x_1 \rho_2 + \rho_1 - x_1 \rho_1}$$

$$y_1 = \frac{x_1 \rho_2}{x_1 \rho_2 + \rho_1 (1 - x_1)}$$

Similarly an equation could be derived for y_2 whereby,

$$y_2 = \frac{x_2 \rho_1}{x_2 \rho_1 + \rho_2 (1 - x_2)}$$

The absolute density values would not be important in this case, but the ratio of the two values.

Let $r = {}^{\rho_1}\!/_{\rho_2}$ so $\rho_2 = {}^{\rho_1}\!/_{r}$

Substituting into the area fraction equation for component 1;

$$\therefore \qquad y_1 = \frac{x_1 \, {}^{\rho_1}\!/_{r}}{x_1 \, {}^{\rho_1}\!/_{r} + \rho_1 (1 - x_1)}$$

$$y_1 = \frac{\rho_1 \left({}^{x_1}\!/_{r} \right)}{\rho_1 \left({}^{x_1}\!/_{r} + (1 - x_1) \right)}$$

$$y_1 = \frac{{}^{x_1}\!/_{r}}{{}^{x_1}\!/_{r} + (1 - x_1)}$$

And similarly for y_2 substituting $\rho_1 = r \rho_2$ gives;

$$y_2 = \frac{x_2 r}{x_2 r + (1 - x_2)}$$

Therefore $y_1 = x_1$ and $y_2 = x_2$ only when $r = 1$ i.e. when both material densities are the same.

E.g.

$$y_1 = \frac{x_1/1}{x_1/1 + (1 - x_1)}$$

$$y_1 = \frac{x_1}{x_1 + 1 - x_1}$$

$$y_1 = \underline{\underline{x_1}}$$

This provided a possible explanation for the % m/m not being proportional to the number of pixels in the image, as was determined from the experimental results.

The plot below shows the area fraction, y vs. the mass fraction, x for various r values from 0 to 10.

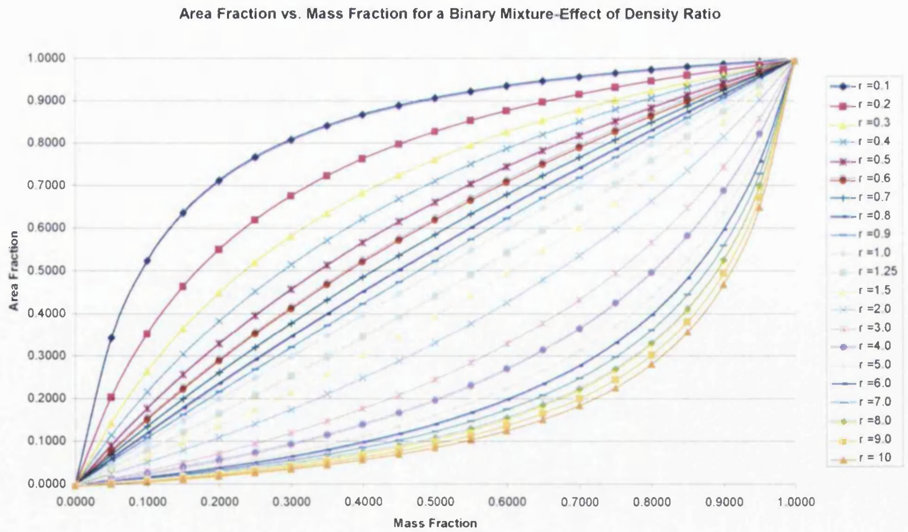

Figure 3-20: Effect of density ratio "r" on the area fraction for a binary mixture.

Using the data from the calibration set of MCC and D wafers and rearranging the above equations for y_1 and y_2 to give;

$$r = \frac{x_1(1-y_1)}{y_1(1-x_1)} \quad \text{and} \quad r = \frac{y_2(1-x_2)}{x_2(1-y_2)}$$

Estimates for the r values for the MCC and D were obtained, respectively.

	Average r value	
	Spotlight	**RSD**
Factor 1 (MCC)	1.28	17.97
Factor 2 (D)	1.34	20.15

Table 3-9: Average r values for MCC and D from Spotlight data.

Therefore the density of the MCC would be estimated as one and a third times D from the Spotlight data.

A plot of area fraction vs. mass fraction for the density ratios calculated using the inverse of the D values giving 0.75 for factor 2 the Spotlight overlaid with the actual MSVs from the calibration set showed some correlation.

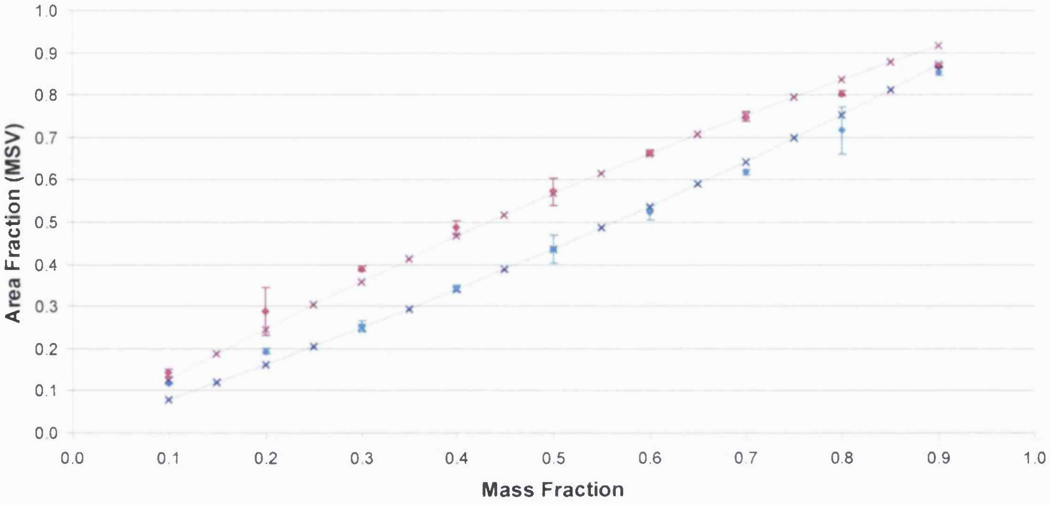

Figure 3-21: Overlay of the density ratio plots with the actual MSVs from the calibration set from Spotlight data with factor 1 (MCC) (◆), factor 2 (D) (◆), r = 0.75 (×) and r = 1.28 (×).

The actual r values were evaluated by producing three wafers of each component using the same pressure each time. These were weighed, the dimensions measured and the densities calculated, Table 3-10 and Table 3-11.

Component	Mass (g)	Thickness (cm)	Radius(cm)	Volume (cm^3)	Density (g/cm^3)
MCC-1	0.2992	0.287	0.5015	0.2268	1.3192
MCC-2	0.2976	0.284	0.5020	0.2248	1.3238
MCC-3	0.2990	0.285	0.5020	0.2256	1.3254
				Average	**1.3228**

Table 3-10: Calculating the density of MCC.

Component	Mass (g)	Thickness (cm)	Radius(cm)	Volume (cm^3)	Density (g/cm^3)
D -1	0.2908	0.306	0.5035	0.2437	1.1933
D -2	0.3018	0.309	0.5025	0.2451	1.2300
D -3	0.2996	0.307	0.5035	0.2445	1.2253
				Average	**1.2162**

Table 3-11: Calculating the density of D.

From these average values r = 1.088, therefore the results from the wafers were not consistent with the calculated ratio results from the imaging data[5]. This indicates that there may still be other factors involved that contribute to the quadratic nature of the MSV with % m/m, such as variations in particle size or molar absorptivities.

3.4 Conclusion

The initial work carried out on the comparison of the commercial and laboratory made V blends concluded that it was viable to use the non-production blends for further studies. There were differences observed in the spectra and domain statistics for the two blend types, but these inconsistencies could be accounted for by the possibility of dissimilarities in the components namely the lubricant blend as well as potential moisture differences and the simplified manufacturing process employed in contrast to the one used commercially (two stages vs. >eight stages), respectively.

Evaluation of the relationship between the MSVs from the pixel distribution of the score images and the % m/m in the sample formulation demonstrated that it was not a simple linear correlation for this particular system, but showed a quadratic association for the results. The RSDs for the % m/m prediction from the calibration equations for both components varied from ~0.5% to a maximum of ~7% depending on the % m/m in the sample. The quadratic nature of the relationship could theoretically be related to the differences in the densities of the two materials, using density ratio values calculated from the area fraction (MSV) and the mass fraction (% m/m in the formulation divided by 100) assuming unit sample depth. However the theoretical ratio calculated from the images did not match the experimentally determined value therefore there must be other factors contributing to the outcome e.g. particle size and/or absorptivity differences.

Although the MSV was not found to be a direct indicator of the % m/m in this case, it does serve as a fairly constant sample statistic where the value can indicate differences in the components between samples. The MSV will change with the amount of each substance present as it gives an indication of the average pixel purity or the abundance of a particular factor (representing one of the components) in the image e.g. a MSV of 0.5 would relate to

---

[5] The density of D could not be established from the literature so only the calculated values were utilised.

the majority of the pixel responses in the image being comprised of approximately half of this component's loading spectrum.

For subsequent investigation into the relationship between NIRM chemical images and dissolution performance, the MSV will be one of the values used as a numerical descriptor of the images.

4 Correlation of NIRM Chemical Images from Laboratory Produced Wafers with Varying Physical Characteristics to Dissolution Properties

4.1 Introduction

It is well known that the dissolution testing of a product can be influenced by a wide range of factors, including differences or changes in the physical properties of the dosage forms.

This chapter will explore the influence of changing certain physical parameters of a blend on the subsequent dissolution profiles obtained for that product. The blending time, input particle size and compression force used to produce the samples will be varied in an effort to induce changes in the resulting NIRM images and dissolution profiles obtained. Any differences observed will be correlated and prediction equations constructed.

4.2 Experimental

4.2.1 Materials

The use of the three-component system (V) based on a Pfizer product was continued in this chapter as there had been no unexplained changes encountered between the commercial and laboratory produced blends in the assessment conducted in the previous chapter.

Changing Blending Time

The first five wafers produced from the laboratory V blend made using the Turbula blender (Glen Mills, NJ, USA) for five minutes at 96 rpm were used as the five minute blend samples for this blending study. The remainder of the five minute blend was split into two. Half was blended for a further five minutes and the rest for a further ten minutes, producing a ten and 15 minute blend respectively for comparison.

The blends were pressed into wafers to emulate a solid dosage form and to provide a more optically flat surface for spectroscopic analysis. For this, 300 mg of the blend was weighed then compressed in a punch and dye using a hydraulic press at 2000 psi for three seconds. Five wafers were produced for each of the ten and 15 minute blends using a die with a 10 mm diameter, resulting in a thickness of ~2.85 mm.

Changing Input Particle Size

For this part of the investigation, two component blends of major components MCC and D were utilised. A range of Fisher sieves was used to alter the size fractions available for the blend production. The lubricant blend was omitted in this case as it only contributed to 1.5% of the formulation and due to a mean particle size of < five microns, there were no sieves available that would be of a sufficiently small mesh size for this material.

The results from a previous investigation into the relationship between the MSV and the % m/m in the formulation had shown that 45% MCC and 55% D gave good results for the wafers. Therefore this ratio was selected for the production of these two component blends. Wafers were made for the sieved fraction of one component with the unsieved fraction of the other and then *vice versa* Table 4-1. The % m/m was weighed out of each ingredient to make up 300 mg for each wafer. This was then mixed by hand for approximately two minutes, as the quantity was not sufficient to utilise the Turbula blender, then pressed into a wafer using the same conditions as for the wafer production previously.

	Wafers Produced	
Sieved Size Fraction	**Sieved MCC + unsieved D**	**Sieved D + unsieved MCC**
≤ 25 μm	✓	-
25-53 μm	✓	✓
53-75 μm	✓	✓
75-125 μm	✓	✓
≥ 125 μm	✓	✓

Table 4-1: Two component wafers produced from sieved fractions of MCC and D.

There was very little of the smaller fraction for the D, partly due to the fact that it was hand sieved and also there was not very much of the sample to start with. Overall there were three wafers produced for each size fraction, except for the D 25 - 53 μm where there was only enough D for one wafer.

When preparing the wafers one of the MCC 25 µm and all of the D wafers, except one of the D 75 - 125 µm, became stuck in the wafer press, which meant that one of the surfaces was roughened and part of the wafer sheared off. This deteriorated further when the sieved D was used, but was an obvious side effect of omitting the lubricant blend.

Changing Compression Force

Wafers were produced from the same commercial V blend used in chapter 3. Various different compression forces were applied using an Atlas T25 wafer press (Specac Inc., Woodstock, GA, USA), Table 4-2. The press was held at the individual pressures for approximately three seconds to form the wafers using a ten mm punch and die system.

Compression Force (tons)	Number of Wafers
4	3
6	3
8	3
10	3
12	3

Table 4-2: Compression forces used to produce V wafers for imaging and dissolution.

As a result of practical constraints the wafers from Table 4-2 could not be used for the transmission measurements. Therefore another set of wafers were produced to demonstrate how increased compression force affected the NIRS transmission spectra of a sample, see Table 4-3. One wafer was produced at each force.

Compression Force (tons)	Wafer Thickness (mm)
1	2.0
2	1.6
4	1.2
6	1.0
8	0.9

Table 4-3: Compression forces used to produce V wafers for NIRS.

4.2.2 Near-infrared Spectroscopic Analysis

Reflectance NIRS

Samples of each of the blends prepared for blending and particle size studies (~1 g of each or what was available) were placed into glass vials and analysed using the Foss NIRSystems 6500 monochromator (Foss NIRSystems Inc., Silver Springs, MD, USA) with a vial module attachment as shown in section 3.2.3, which was controlled using Delight software (DSquared Development, LaGrande, OR, USA). Three replicates of the each sample were obtained and the average spectra were used.

Transmission NIRS

The wafer samples produced for the compression study, Table 4-3 were analysed using the Foss NIRSystems 6500 monochromator (Foss NIRSystems Inc., Silver Springs, MD, USA) with an InTact tablet transmission analyser, shown in section 3.2.2. A customised sample holder was used to ensure reproducible measurements of the wafers. Five replicates were performed for each wafer, with the sample being turned over between measurements. The average of the spectra was used over the range 850 nm - 1450 nm.

Both of the Foss instruments used passed all the manufacturer's performance tests including wavelength accuracy, photometric noise and accuracy and repeatability and were therefore considered to be operating correctly.

4.2.3 Near-infrared Microscopy Imaging

Spectrum Spotlight 350-Line Mapping

The wafers produced for all three studies were analysed on the Spotlight as described in section 3.2.2, except for the ones in Table 4-3 as these were produced for transmission NIRS only. An area of 5 x 5 mm was scanned for each of the blend wafers and an area of 1 x 1 mm was scanned on wafers made of the excipients and API for the library images.

The data processing varied slightly between the three studies for the Spotlight data, which is summarised in Table 4-4. In all cases the files from the Spotlight (.fsm) were converted into a format (.spc) that could be recognised by the image analysis software, ISys.

Study	Final Pre-Processing	Selection Method of Pixel Distribution	Contour Value
Blending	Normalisation	% Pixels	Lower limit of selected region
Particle Size	Normalisation	% Pixels	MSV of selected region
Compression	Normalisation	% Pixels	MSV of selected region for MCC and D with the result of (((upper limit – lower limit) ÷ 3) + lower limit) for lubricant blend

Table 4-4: Summary of the data processing for the Spotlight results.

The explanation and method for the pixel selection can be found in section 2.1.2. In each case the components used in the complementary library file reflected the components present in each blend i.e. MCC, D and lubricant blend for the blending and compression studies, but only MCC and D for the particle size study.

4.2.4 Dissolution

The USP dissolution apparatus 2 (paddle) was used for the wafer dissolution using a VanKel VK7000 dissolution system (Varian Inc., Palo Alto, CA, USA) which had eight glass vessels suspended in a water bath, which was set to heat the vessels to 37.0 ^{0}C ± 0.5 ^{0}C. A Zeiss UV spectrometer (Carl Zeiss, Thornwood, NY, USA) was set-up with eight transflectance UV probes connected to a multiplexer by SiO_2 fibres. Every fibre carried the light from the source (deuterium lamp) individually to the dissolution media in the vessel then back to the diode array detector. Each probe had a removable probe tip that could be changed depending on the pathlength required. All the probes were fixed into a manifold on the dissolution bath which could be raised and lowered to allow movement in and out of the media in the vessels.

Data Acquisition

The software used was ProcyOn, which was a beta version. Parameter files were set-up individually within the software for each product dissolved and multiples of each when a different number of vessels were employed for different dissolutions. Within each parameter file a measurement sequence for the probes in use was created. The minimum interval required for one probe measurement was approximately seven seconds, but this was just enough time for all the mechanical movement to complete, i.e. the multiplexer to change channels. A minimum of ten seconds per probe was actually required to allow for any minor timing variations within the system as well as the mechanical movement of the multiplexer. As the data collection was staggered at each probe, the addition of the samples to the vessels were also done to coincide with the first data measurement ensuring the correct timing for all the profiles in that run.

The number of dissolution vessels in use depended on a number of factors. In instances where there was a limited sample set, attempting to dissolve all the same sample type in one run was not advised and therefore multiple runs were used.

The wavelength monitored for the API in the particular product (276 nm) was identified in the parameter file along with the calculation of a baseline correction at another wavelength away from any responses of the system of interest. The baseline correction was carried out in order to correct for any particulates that may have been present in the probe gap upon measurement and also for any fluctuations in the lamp intensity over the dissolution period. A change would have been seen over the entire wavelength range so subtracting the response of a wavelength on the baseline from the value of interest would correct for any of these types of variation.

Each parameter file was loaded at the beginning of the dissolution with the probes lowered into the equilibrated media and references were taken for each of the probes. These reference spectra were automatically subtracted from the resulting spectra along with any processing stipulated.

In this chapter the conditions for the dissolution of V for each study were as follows: The paddles were positioned at 45 mm ± 2 mm from the base of the vessel and set to 75 rpm, as was stated in the procedure from Pfizer for the product. The wavelength monitored was 276 nm which was characteristic for the API, D. Baseline correction was performed using the response at 420 nm. The media used was 900 ml of de-gassed, de-ionised water, which had been prepared using a Caleva Degasser system (G.B. Caleva Ltd., Sturminster Newton, Dorset, UK) with a media pre-heating attachment. The degasser used a vacuum pump for the degassing and was in accordance with the USP. Table 4-5 shows the dissolution parameters used.

Study	**Vessels Used**	**Measurement Interval (sec)**	**Pathlength (mm)**
Blending	2	30	2
Particle Size	4	40	2
Compression	4	40	2

Table 4-5: Dissolution parameter conditions for V blends.

Standard solutions of the API were used to assess the linearity of the spectrometer. This also gave an absorbance value equivalent to 100% of dissolved API. The amount of API was calculated for each wafer from the mass and the % m/m used in the blend, which was used to correct for any differences between samples on the conversion to percentage (%) API dissolved.

4.3 Results and Discussion

The results from all the methods used will be discussed together in three sections relating to the three studies performed.

4.3.1 Changing Blending Time

Wafer Production

The masses of the wafers were measured as this would be important for the subsequent dissolution experiments for the conversion of the profiles from absorbance to the % API dissolved, Table 4-6

Sample Wafer	**Average Mass of Wafer (mg)**	**RSD**	**Average Mass of API (46.5%) (mg)**
5 min	302.5	0.73	140.7
10 min	301.3	0.38	140.1
15 min	301.6	0.30	140.3

Table 4-6: Average physical parameters of blending study wafers.

Reflectance NIRS

The results for the average of three scans showed an offset in the raw spectra that could relate to an increase in mean particle size going from 5 to 15 minutes blending, Figure 4-1(a). The second derivative data showed a difference at ~1920 nm whereby the amplitude of the peak increased with blending time. This is in the region related to the combination band for OH bonds and therefore could be related to differences in the moisture content of the blends whereby the extra blending time allowed the pick up of more water into the sample, Figure 4-1 (b). A comparison of the excipient and API spectra to the blends show this change at 1920 nm may be related to the MCC as the same pattern with blending time is seen at ~1884 nm as well, which fits well with the MCC derivative spectrum. Another trend was seen with blend time at ~1970 nm relating to the API, but in this case the peak amplitude decreased with blending time. This, in combination with the MCC peak changes, would suggest that as the blending time increased, the response from the MCC became stronger, while the API became weaker as it presumably became more mixed into the matrix.

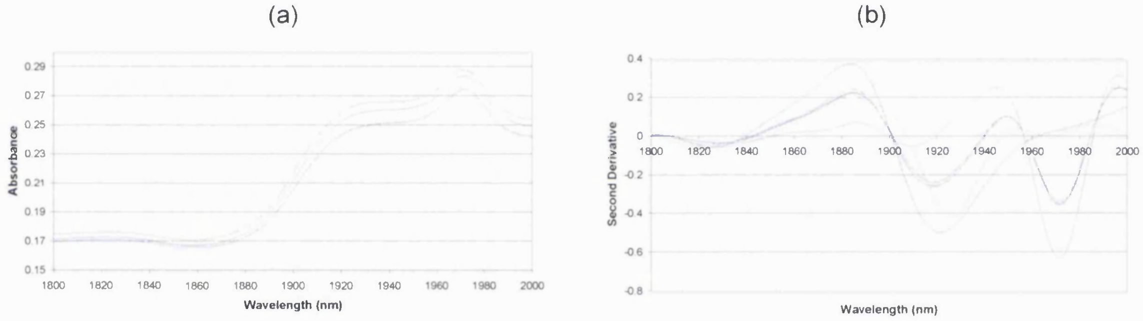
(a)

(b)

Figure 4-1: (a) Raw and (b) second derivative NIRS reflectance data, average of three replicates for blending study blends with (—) 5 min, (—) 10 min, (—) 15 min, (—) D, (—) MCC and (—) lubricant blend.

PCA was performed on the second derivative spectra (whereby physical effects had been removed) and the score values produced were plotted against each other to look for any separation between the blends. In the score 2 vs. score 1 plot the data separated into three distinct blend clusters by the score 1 values, Figure 4-2. It was apparent that the move towards a more negative value along score 1 was due to the increased blending time applied, hence the possible uptake of water, as mentioned above. A degree of separation was also seen for score 2, where the five and 15 minutes blends had negative score values, but the ten minute blends had positive values. The samples may not have been completely homogenous and there may have been some differences encountered due to the sampling of the NIRS.

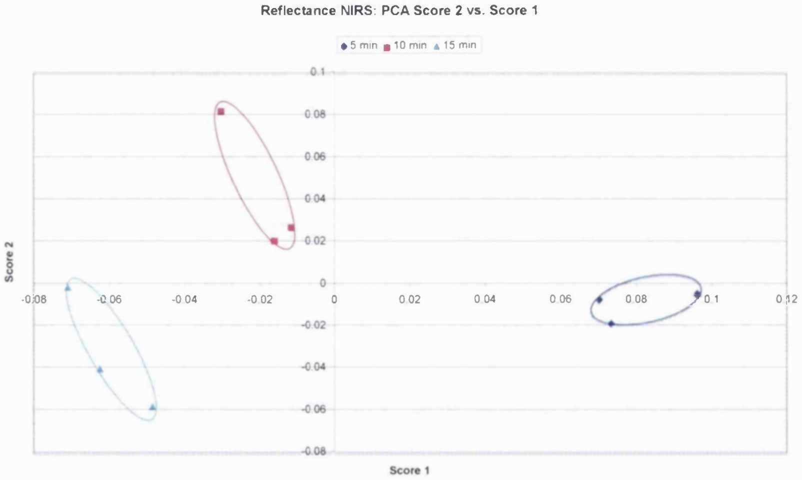

Figure 4-2: Comparison of PCA score 2 vs. score 1 for reflectance NIRS of blending study blends with (◆) 5 min, (■) 10 min, (▲) 15 min.

Spectrum Spotlight 350-Line Mapping

In order to evaluate any changes between the three blend types before any of the manipulation required for the production of RGB images or calculation of the domain statistics, the pixel distributions for each of the components were overlaid and compared, Figure 4-3.

As the blend time was increased from 5 to 10 minutes the distributions for the MCC and the D became more separated from each other. This would have been the result of the blend becoming more homogenous, with any larger areas being reduced. In this case the pixel distributions were low, spread out and overlapping when there were large areas of one of the major components. This was because there were more pixels with higher score contributions from the component with the larger areas e.g. from the pixels situated in the centre of a large domain, hence the distribution spread out to the right. In turn this caused these same pixels to have a lower score contribution from the other major component, resulting in its distribution to spread out to the left and to flatten out. This happened for both the MCC and D. As the domains were reduced in size by the increased blending, there were less pixels with high score contributions as there were more interactions with the other major component being that they were closer together. This caused the distributions to be pulled in and become more centred around the mean score value of all the pixels. On increasing the time to 15 minutes, the distributions stayed very similar to those for the 10 minute data.

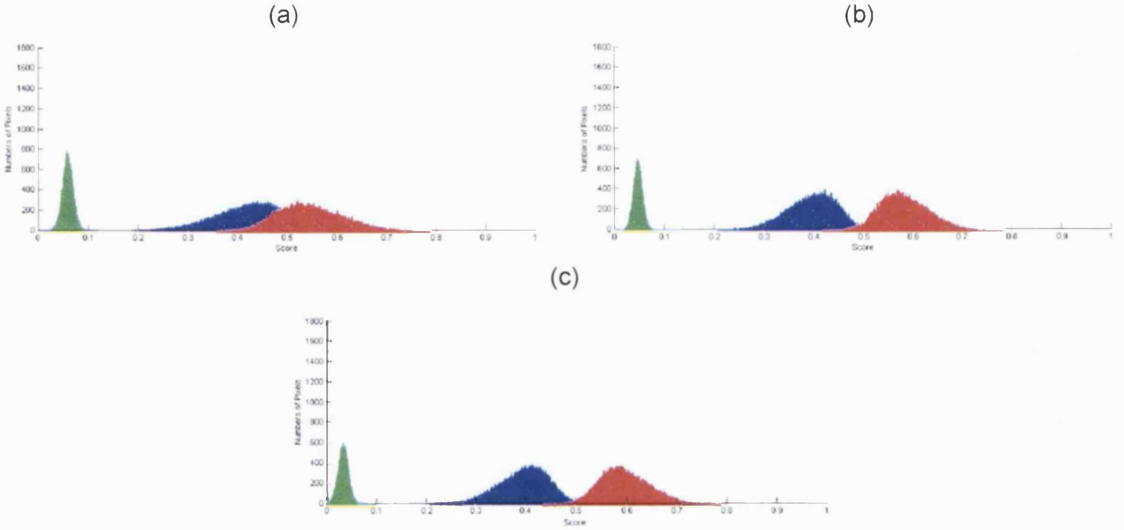
(a)

(b)

(c)

Figure 4-3: Pixel distributions of all three components at (a) 5 min, (b) 10 min and (c) 15 min with MCC(—), D (—) and lubricant blend (—) from Spotlight data.

The average MSV for each component, shown in Table 4-7 should have stayed approximately the same value as the composition of the blends did not change. The shape of the distribution could have changed due to domain size, but each pixel had to equate to a value of one and there were approximately the same number of pixels for each analysis.

For all three components the average MSV differed for the five minute blend compared to those for the 10 and 15 minute blends, which were similar. This was the same pattern observed in the pixel distribution overlays. This was also seen for all the components % STD values and for the skew values of MCC and D. These imaging parameters describe the spread and tailing of the pixel distribution of the components. The kurtosis values were higher for all the 10 minute blend results for all the components, with the other two values being relatively similar. The lubricant blend values were the most variable as this was present at such a low concentration.

Component	MSV	% STD	Skew	Kurtosis
lubricant blend – 5 mins	0.064	17.804	0.023	0.954
lubricant blend – 10 mins	0.042	24.621	0.147	1.485
lubricant blend – 15 mins	0.039	27.132	0.011	0.656
MCC – 5 mins	0.431	14.249	-0.314	-0.211
MCC – 10 mins	0.404	12.677	-0.264	0.063
MCC – 15 mins	0.401	12.093	-0.263	-0.164
D – 5 mins	0.539	11.810	0.343	-0.189
D – 10 mins	0.583	8.925	0.265	0.050
D – 15 mins	0.589	8.441	0.257	-0.161

Table 4-7: Average sample statistics for blending study from Spotlight data.

The domain size statistics were calculated for the different blends, which related to the areas of the different components that were present on the surface analysed. This provided a more quantitative approach for the description of the component distribution in the images, as the RGB images produced did not show any significant differences between the blend time samples, Table 4-8.

For all three components the number of domains increased upon going from 5 to 15 minutes blending. Both the MCC and the D had an increase from five to 10 minutes of ~21% and ~7% respectively, then the values for the 15 minute stayed approximately the same as for the 10 minute. This tied in with the previous findings for the pixel distributions. The number of lubricant blend domains also increased from five minute to 10 minute by ~28%, but in this case it did not level off in value for the 15 minute result, instead it increased by another ~11%.

The MED would typically be expected to decrease with an increase in the number of domains, but for both the MCC and D the opposite is true. The MED increased by ~4% for MCC and ~11% for the D on going from 5 to 10 minutes, but again the 15 minute value was similar to the 10 minute one.

Component	Number of Domains	MED (µm)	Nearest Neighbour (µm)
lubricant blend - 5 mins	268.3	36.3	8.1
lubricant blend - 10 mins	343.0	38.0	8.2
lubricant blend - 15 mins	380.2	36.5	7.7
MCC - 5 mins	91.4	370.5	13.9
MCC - 10 mins	110.2	386.5	14.2
MCC - 15 mins	107.4	393.5	14.1
D - 5 mins	189.7	243.3	10.1
D - 10 mins	201.2	270.0	10.8
D - 15 mins	202.8	269.0	10.7

Table 4-8: Average domain statistics for blending study from Spotlight data.

The MED of the lubricant blend did not vary significantly with the differing blend times and stayed relatively similar between 36 µm and 38 µm, which would probably be the result of the spatial resolution of the technique. The MED would equate to just over one pixel in width and as the input particle size range for the majority of the lubricant blend fell in the region up to ~20 µm, Figure 3.6 (a), it would have resulted in small domains which may have only occupied a single pixel. The nearest neighbour (NN) values remained relatively similar between the different blending times. The NN value relates to the average of the distances between the centroids of each domain of that component relative to their closest neighbour.

Overall, the 10 and 15 minute blends were relatively similar with respect to the major components. There was a difference in the lubricant blend domains, but otherwise the main differences were seen between the 5 minute and the 10 and 15 minute blends.

4.3.2 Dissolution Profiles

Initially standard solutions of D were made up covering the range of 20% - 120% dissolved API in the dissolution vessels to test the linearity of the system. The absorbance value for each solution was measured through the fibre-optic probe and baseline correction was applied as was done for the actual dissolutions for a fair comparison. The results showed the response of the spectrometer was linear over the absorbance range to be used, Figure 4-4(a).

All of the blending study wafers were then dissolved to see if there were any differences in the profiles. The average profiles showed a distinction between the five minute blend and the other two blends. The five minute wafers had a higher dissolution rate than the 10 and 15 minute samples, which were nearly inseparable although the 10 minute had a slight edge on the 15 minute blend at points, Figure 4-4(b). This would fit with the separation seen in the shapes of the pixel distributions in Figure 4-3 and the patterns seen in the sample and domain statistics.

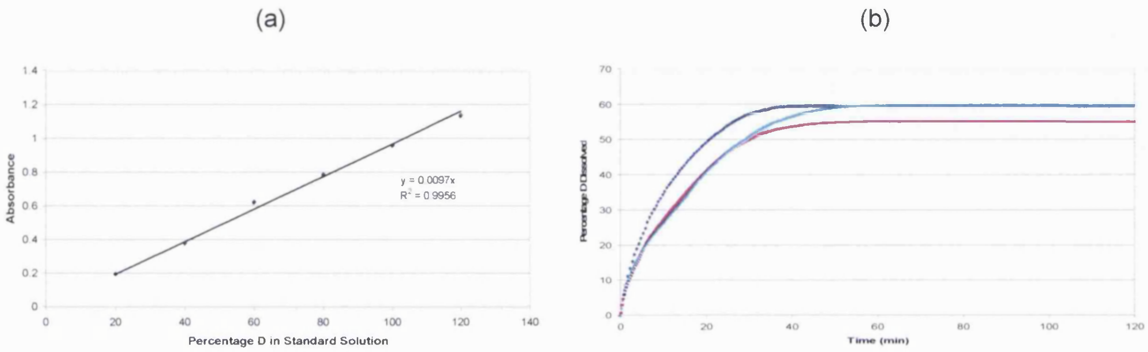

Figure 4-4: (a) A linearity plot for UV spectrometer using standard solutions of D and (b) the average D dissolution profiles for blending study wafers (◆) 5 min, (■) 10 min, (▲) 15 min.

Within the domain statistics from the NIRM imaging, the average number of domains seen would be greatly influenced by the appearance of smaller regions than larger ones as there would be a higher proportion. In the same manner, the average MED would be influenced mainly by any larger domains present as these would skew the value to a greater extent than the small domains. Following on from this, the number of domains increased for the Spotlight data and the domain size also increased. This could mean that there were smaller domains being produced with the extra blending, but some of the domains were increasing in size at the same time. The size of the domains increased the most for the API and these larger domains would take longer to completely dissolve due to the reduced surface area. The similar initial dissolution profiles seen may have been due to the smaller domains dissolving first in each blend, leaving the progressively larger ones to go to completion.

The increase in the number of lubricant blend domains with blending time seen could also explain the change in the average dissolution profiles. As the blending time increased, the lubricant blend became more dispersed within and around the particles of the major components in the blend therefore more were detected by the domain statistics. The size of the lubricant blend domains remained fairly consistent, which may have been the result of the limited spatial distribution of each technique compared to input particle size.

All the methods described in section 2.2.2. were applied to the profile data and the resultant values are shown in Table 4-9.

Blending Study	t_{45} **(min)**	P_{25} **(%)**	k_0 **(%/min)**	k_e **(min^{-1})**	β	T_d **(min)**	t_L **(min)**	n
5 min	16.40	54.08	1.747	0.089	1.12	12.21	-0.74	0.49
10 min	25.50	46.81	1.487	0.069	1.33	17.90	-3.29	0.54
15 min	24.47	46.97	1.474	0.058	1.49	23.18	-5.93	0.50

Table 4-9: Dissolution parameters for blending study wafer profiles.

The goodness-of-fit of the models was compared to the actual data used by calculating the residual sum of squares (RSS) and overlaying the data, see Table 4-10 and Figure 4-5.

RSS	**Exponential**	**Weibull**	**Korsmeyer-Peppas**
5 min	0.72	0.65	2.09
10 min	1.18	0.59	1.74
15 min	1.12	0.68	1.42

Table 4-10: RSS for blending study dissolution models.

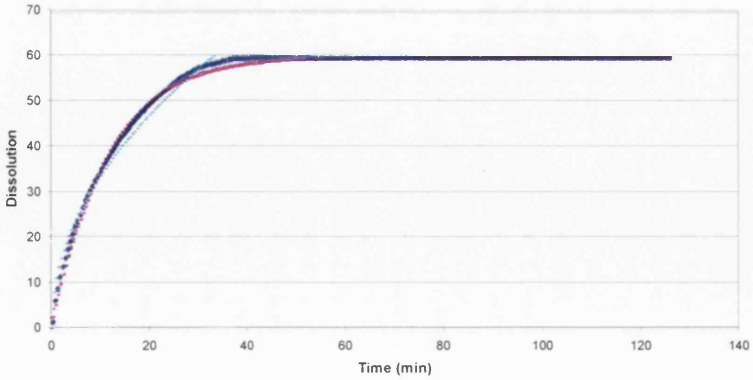

Figure 4-5: Overlay of dissolution profile and model profiles for five minute blending with (•) actual dissolution profile, (–) exponential, (–) Weibull and (–) Korsmeyer-Peppas model values.

The smaller the RSS value, the better the fit of the data so here only the parameters for the exponential and the Weibull models were retained for correlation (see chapter 7).

4.3.3 Changing Input Particle Size

Wafer Production

The masses of the wafers produced were measured as this would be important for the subsequent dissolution experiments as mentioned for the blending study wafers.

Sample	**Average Mass of Wafer (mg)**	**RSD**	**Average Mass of API (46.5%)**
Average MCC < 25 µm	301.6	0.3	140.2
Average MCC 25 – 53 µm	299.6	1.1	139.3
Average MCC 53 - 75 µm	310.6	0.3	140.3
Average MCC 75 - 125 µm	301.4	0.1	140.2
Average MCC > 125 µm	300.6	0.2	139.8
Average D 25 - 53 µm	301.7	0	140.3
Average D 53 - 75 µm	301.8	0.4	140.3
Average D 75 - 125 µm	302.2	0.6	140.5
Average D > 125 µm	300.9	0.6	139.9

Table 4-11: Average physical parameters for particle size study wafers.

Reflectance NIRS

The results for the average of three scans for the blends comprising sieved MCC showed an offset in the raw spectra that relate to the increase in mean particle size of the total blend as the size fraction utilised increased, which would be expected, Figure 4-6(a). This offset was relatively large at the higher wavelength end of the range. The average raw spectra for the blends containing sieved D did not show the same pattern with increasing size fraction. There was an offset observed but not to the same extent as for the sieved MCC blends, Figure 4-7(a). These offsets were observed in the derivative spectra of both blend types and as for the raw spectra, the offset was greater for the sieved MCC blends, Figure 4-6(b) and Figure 4-7(b). As the size fraction of MCC increased in the blend there was less of the MCC and more of the D, but this was not seen for the blends with sieved API. This indicated that the size fraction of the MCC had much more of an influence on the blend produced than that of the API. As the MCC size fraction decreased, the blend might have become progressively more homogeneous with the D. This might have resulted in the sampled blend volume for the smallest size fraction giving a spectrum that would have more of a MCC contribution as opposed to that from the blend of the largest size fraction, where lack of mixing may have given the impression of an increase in the D contribution.

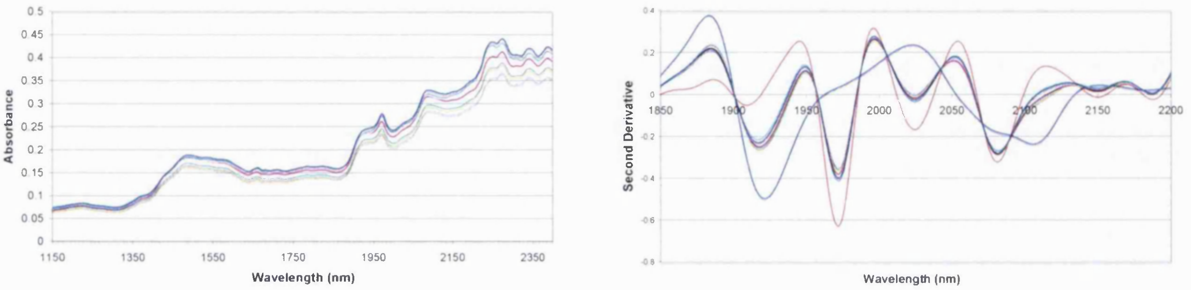
(a) (b)

Figure 4-6: (a) Average raw and (b) second derivative reflectance spectra for particle size study sieved MCC blends with (—) < 25 µm, (—) 25 - 53 µm, (—)53 - 75 µm, (—) 75 - 125 µm, (—) > 125 µm, (—) D and (—) MCC.

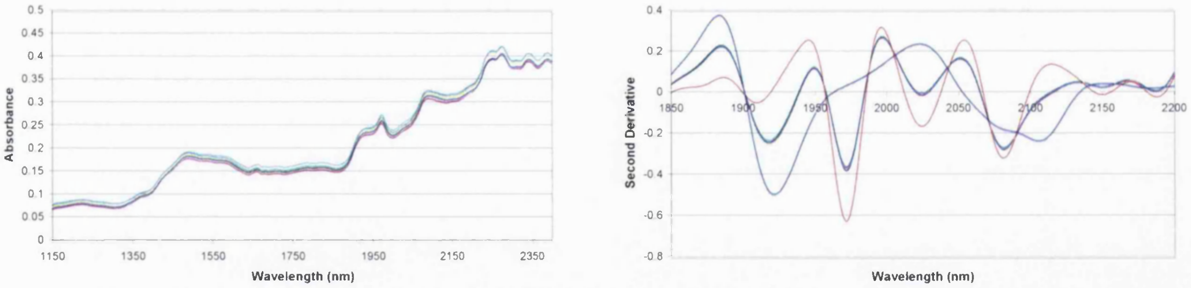
(a) (b)

Figure 4-7: (a) Average raw and (b) second derivative reflectance spectra for particle size study sieved D blends with (—) 25 - 53 µm, (—)53 - 75 µm, (—) 75 - 125 µm, (—) > 125 µm, (—) D and (—) MCC.

PCA was performed on the derivatised data (whereby physical effects had been removed) and the score values produced were plotted against each other to look for any separation between the blends. In the score 2 vs. score 1 plot for the sieved MCC blends the data separated into five distinct blend clusters by the score 1 values, Figure 4-8(a). The major separation occurred along the score 1 axis and would have been related in some way to the size fraction used, although the largest two fractions were reversed. There was also a degree of separation by score 2 where the MCC 53 - 75 μm and MCC > 125 μm both grouped with values and the remaining three had negative values. For the PCA results of the sieved D spectra the only separation was into four distinct groups as a combination of score 2 and 3, Figure 4-8(b). Score 2 picked out the blends containing the lower two fractions from those with the larger ones, then score 3 separated the blends containing the larger fractions.

From the PCA comparisons it could be concluded that all the different size fraction blends could be grouped by certain score values. This related to variation within the spectra, which seemed to follow the increase in size fraction used.

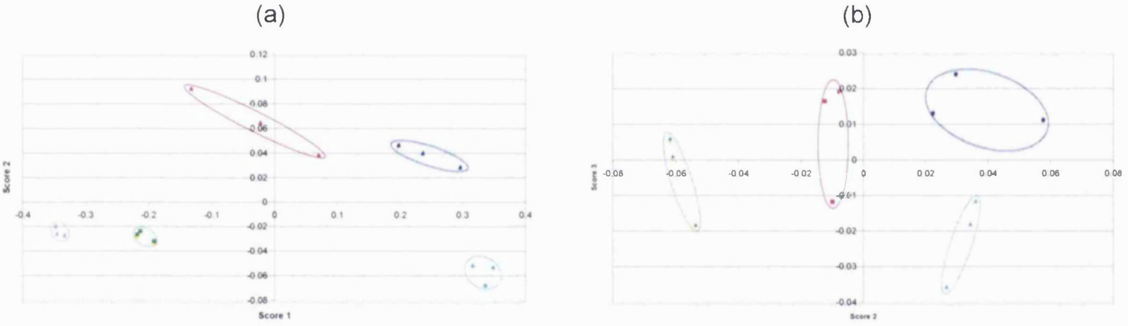
(a)

(b)

Figure 4-8: Comparison of PCA results of derivatised reflectance data (a) score 2 vs. score 1 for sieved MCC blends and (b) score 3 vs. score 2 for sieved D blends with (◆) < 25 μm, (■ ◆) 25 - 53 μm, (▲ ■)53 - 75 μm, (● ▲) 75 - 125 μm, (▲ ●) > 125 μm.

Spectrum Spotlight 350-Line Mapping

Initially the pixel distributions were overlaid for each component from the scores images to evaluate any changes prior to the selection required to produce the domain statistics, Figure 4-9.

When the sieved MCC was used in the wafers, there was a marked change when the size fraction was increased. The distributions of both components started out fairly well separated with only a small amount of pixel overlap at MCC< 25 μm,, and then as the size fraction gets larger the distributions flatten out and spread up and down into the regions of high and low score values respectively causing a greater amount of overlap, see Figure

4-9. This was the result of the domain size increasing and allowing the presence of pixels with higher score contributions from both components, e.g. from pixels in the centre of a large domain of one component with limited interaction with the other component. As each pixel has a total score contribution of one, the high score pixels for one components will result in low score pixels for the other and the same is true in reverse. This results in mirror image distributions for the two component system.

When the sieved D was used in the wafers, again there was a change in the pixel distributions upon increasing the size fraction, but not to the same extent as for the sieved MCC. Initially the distributions were separated as with the sieved MCC, but as the fraction size increased up to D > 125 µm the overlap of the distributions only increased and flattened very slightly.

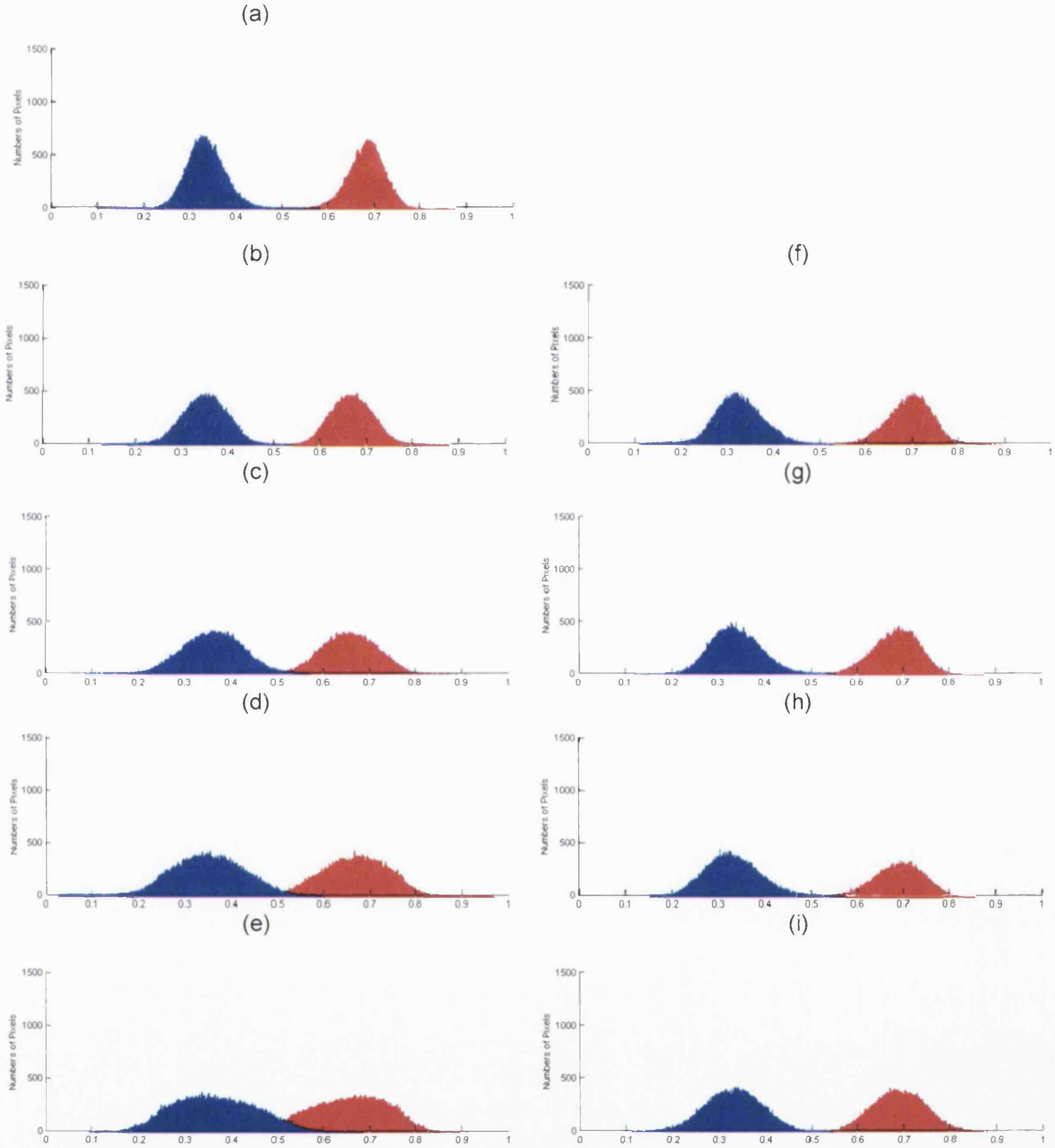

Figure 4-9: Pixel distributions for MCC(—) and D (—) for sieved MCC (a) < 25 µm, (b) 25 - 53 µm, (c) 53 - 75 µm, (d) 75 -125 µm, (e) > 125 µm and sieved D (f) 25 - 53 µm, (g) 53 - 75 µm, (h) 75 -125 µm and (i) > 125 µm.

The average sample statistics of the distributions were evaluated, Table 4-12 and Table 4-13.

The wafers with sieved MCC had similar results for both the MCC and D components in the blend. There was an increase in the % STD with size fraction used, which would indicate a decrease in homogeneity in the samples (Lyons *et al.*, 2002) as was seen in the pixel distributions. In addition, the values of the kurtosis value decreased from positive through to negative values as the size fraction increased, which also described the changes seen in the pixel distributions. The remaining sample statistics did not show any trends with the size fraction of MCC used.

The blend wafers involving the sieved D again showed similar result for both components present in the blends. The only change observed in the sample statistics was in the values of the % STD, which increased with size fraction, but this difference was only a value of one at its maximum. All the other values showed no trends with size fraction.

RGB images produced did not show any obvious visual differences in the distribution of the two components therefore the domain size statistics were calculated for the different blends as a more quantitative means to describe the images.

The number of D domains for the unsieved D combined with the sieved MCC appeared to decrease with increasing MCC size fraction used in the wafers. The wafers with MCC < 25 µm and MCC 25-53 µm gave results with similar values. The average MED of the D domains increased ~47% as the number of domains present decreased, which would be expected, Table 4-12.

When the D was sieved, the number of API domains present was relatively similar for all four of the different wafer types. The average MED for the D domains were again relatively consistent compared to the wafers containing the unsieved D at a value of ~153 µm.

D	MSV	% STD	Skew	Kurtosis	Number of Domains	MED (µm)	NN (µm)
MCC < 25	0.678	6.273	-0.118	0.899	503.0	122.5	7.0
MCC 25-53	0.670	6.926	0.190	0.261	519.0	122.5	7.2
MCC 53-75	0.644	9.850	0.031	-0.125	392.5	141.3	8.1
MCC 75-125	0.657	11.695	0.090	-0.178	335.3	152.5	8.8
MCC > 125	0.668	12.871	-0.299	-0.451	260.3	180.0	10.2
D 25-53	0.696	7.196	0.043	0.717	336.0	150.0	8.8
D 53-75	0.693	7.401	-0.205	0.142	352.3	149.2	8.5
D 75-125	0.706	7.564	-0.131	0.250	331.0	153.8	8.9
D > 125	0.689	7.958	-0.038	-0.044	317.3	158.3	9.2

Table 4-12: Average sample and domain statistics for D from both sieved MCC and sieved D blends.

MCC	MSV	% STD	Skew	Kurtosis	Number of Domains	MED (µm)	NN (µm)
MCC < 25	0.344	12.786	0.072	0.874	469.0	113.3	7.3
MCC 25-53	0.352	13.632	-0.227	0.293	554.0	107.5	7.2
MCC 53-75	0.378	17.295	-0.075	-0.111	458.5	117.5	7.4
MCC 75-125	0.365	21.690	-0.137	-0.148	385.7	130.0	8.3
MCC > 125	0.353	25.154	0.256	-0.378	373.0	132.5	8.6
D 25-53	0.325	16.023	-0.089	0.752	368.0	127.5	8.8
D 53-75	0.328	16.212	0.167	0.121	411.0	123.3	8.0
D 75-125	0.330	16.424	0.090	0.243	392.5	125.0	8.4
D > 125	0.332	17.153	-0.001	-0.045	385.0	129.2	8.6

Table 4-13: Average sample and domain statistics for MCC from both sieved MCC and sieved D blends.

For the sieved MCC wafers the pattern of the MCC domain results was comparable to that of the D, but there was more overlap of the individual data values between the different types of wafer. This resulted in average values that did not show such a large decrease compared to the D upon increasing the MCC size fraction, with a change of ~180 domains. The average MED of the sieved MCC increased, as before with the D, but the difference was ~20 µm as opposed to ~60 µm making an increase of only ~20% compared to ~47% for the D, Table 4-13.

The number of unsieved MCC domains varied between the different wafers, but there was no real pattern related to the size fraction. The average MED for the MCC domains in the sieved D wafers were similar at ~126 µm as was seen for the D.

It appeared that the use of sieved D and unsieved MCC did not contribute to significant variation in the domain statistics for the different size fraction wafers produced, whereas there were more considerable changes observed when sieved MCC was combined with unsieved D. The smaller particles of MCC in the lower size fractions may have been more capable of flowing and moulding around the D than those in the larger fractions, which resulted in the formation of more domains of decreased size in the matrix upon compression.

4.3.4 Dissolution Profiles

All the wafers produced from the sieved fractions of D and MCC were dissolved after being scanned on the Spotlight and the average dissolution profiles are shown in Figure 4-10(a) for sieved MCC and (b) for sieved D.

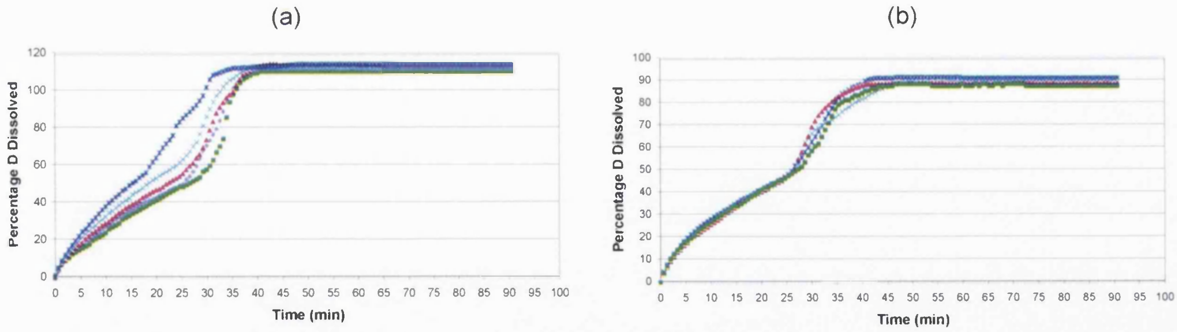

Figure 4-10: Average dissolution profiles for (a) sieved MCC and (b) sieved D blend wafers with (•) < 25 µm, (■) 25 - 53 µm, (▲)53 - 75 µm, (×) 75 - 125 µm, (×) > 125 µm.

The average dissolution profiles show that sieving D did not cause much of a difference to be seen in the subsequent dissolution profiles for the wafers. However, when the MCC was sieved prior to wafer production, the average dissolution profiles appear to change with the size fraction used for the wafer. The MCC < 25 µm and MCC 25-53 µm were relatively similar, but as the size fraction increased above these values, the wafers dissolved faster.

This effect may have been the result of the increasing MCC particle sizes not interacting to the same extent with the API in the blend. The larger particles of MCC may not have been able to mould around the API upon compression as substantially as it would if the particles were a smaller size. This would make the API more freely available for the dissolution.

The dissolution parameters were calculated for the profiles as was shown in sections 2.2.2. In this case, however, the exponential and the Weibull model were calculated on the initial part of the dissolution curve, up to 18 minutes and then again separately on the second part of the profile, from 26 minutes to 60 minutes as it appeared to be a two stage dissolution process[1].

Particle Size Study (μm)	**t_{60} (min)**	**P_{20} (%)**	**k_0 (%/min)**	**k_e (min^{-1})**	**β**	**T_d (min)**	**t_L (min)**	**n**
MCC < 25	28.22	43.05	1.936	0.048	0.72	1866.56	-1.71 E-02	0.680
MCC 25-53	30.66	41.34	1.828	0.025	0.78	546771.35	-5.81 E-01	0.728
MCC 53-75	27.00	47.46	1.990	0.055	0.68	5052.50	-4.11 E-21	0.673
MCC 75-125	23.77	53.08	2.259	0.054	0.80	45.93	-5.21 E-20	0.698
MCC > 125	18.88	64.18	2.589	0.057	0.77	79.88	-3.69 E-15	0.702
D 25-53	30.01	41.45	1.568	0.087	0.67	86.77	3.12 E-04	0.608
D 53-75	28.67	40.97	1.625	0.072	0.61	1605.26	-2.96 E-05	0.627
D 75-125	31.34	40.20	1.610	0.050	0.70	72.25	4.45 E-04	0.626
D > 125	29.78	41.43	1.550	0.097	0.71	31.16	8.48 E-04	0.577

Table 4-14: Dissolution parameters for the particle size study wafers.

The sieved MCC wafers showed a general decrease in the t_{60} value accompanied with increases in the P_{20}, k_0 and k_e values. This was related to an increase in the rate at which the wafers were dissolving with the increase in the size fraction of the MCC. The Weibull values were calculated using only the initial part of the dissolution profile for this study where they were still increasing and had not reached a plateau. The values for the T_d and t_L appear to be slightly irregular on occasion due to this, however, the resulting Weibull models fit the profile data very well.

---

[1] This two stage dissolution process had been observed for the commercial V tablets and was not due to the lack of lubricant blend in the blends.

The Wafers containing sieved D on the other hand, showed more consistent values for the fixed point terms, t_{60} and P_{20}. The k_0 values were also very similar for these profiles, however, the k_e was more variable. The β values also showed consistency and this indicated that there was little variation in the dissolution of the wafers with increasing size fraction of the API.

The results for the different models were overlaid with the actual dissolution profiles and the RSSs were calculated, Table 4-15.

RSS	Exponential	Weibull 18 min	Weibull 26-90 min	Korsmeyer-Peppas
MCC 25	0.61	0.39	4.03	4.70
MCC 25-53	0.83	0.64	7.51	2.98
MCC 53-75	0.79	0.28	6.30	1.49
MCC 75-125	0.78	0.40	2.90	25.60
MCC 125	0.66	0.24	3.35	0.41
D 25-53	0.88	0.36	2.89	8.42
D 53-75	0.89	1.21	2.85	10.68
D 75-125	0.91	0.29	12.62	8.49
D 125	0.76	0.25	2.52	10.32

Table 4-15: RSS for particle size study dissolution models.

All the values were high for the second part of the dissolution and the Korsmeyer-Peppas, so only the exponential and Weibull model for the initial part of the dissolution (0 to 18 minutes) were progressed for correlation to the imaging parameters.

(a)

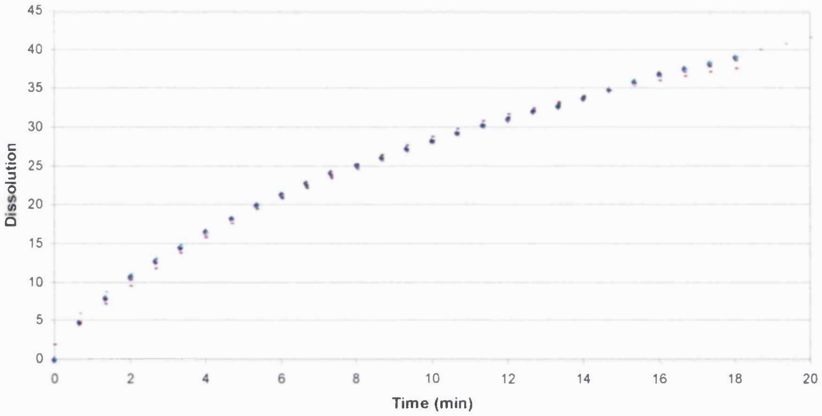

(b)

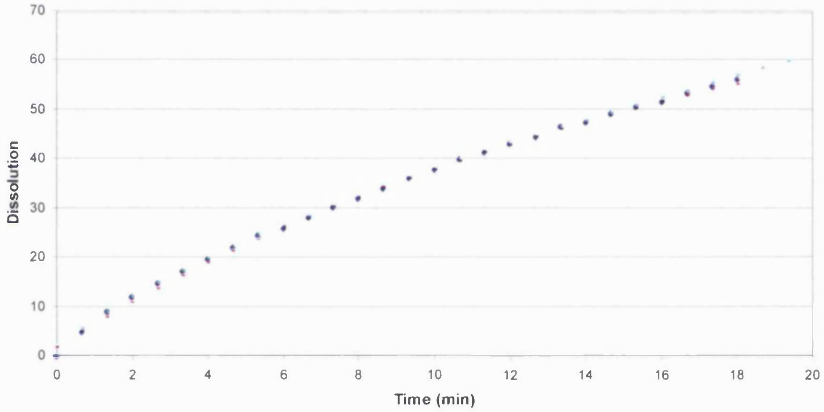

Figure 4-11: Overlay of dissolution profile and model profiles for particle size study (a) D >125 µm 0 -18 min and (b) MCC >125 µm 0 -18 min with (•) actual dissolution profile, (–) exponential, (–) Weibull and (–) Korsmeyer-Peppas model values.

4.3.5 Changing Compression Force

Wafer Production

The masses of the wafers produced in section 4.2.1 were measured as this would be important for the subsequent dissolution experiments as mentioned for the blending and particle size study wafers. The averages of these values are shown in Table 4-16.

Sample	Average Mass of Wafer (mg)	RSD	Average Amount of API (mg)
4 ton	301.4	1.2	140.2
6 ton	300.6	0.8	139.8
8 ton	299.5	0.7	139.3
10 ton	303.8	0.9	141.3
12 ton	304.3	0.3	141.5

Table 4-16: Average physical parameters for compression study wafers.

Transmission NIRS

The sample wafers produced were all scanned as described in section 4.2.1 to investigate the effect of increasing the compression force on the NIR spectra.

As the compression force was increased, the wafers became more compacted therefore reducing any inter-particle spacing present and increasing the density of the wafer. This in turn made the wafer thinner so the pathlength for the light was decreased, reducing the interaction with the sample and therefore reducing the absorbance value, Figure 4-12.

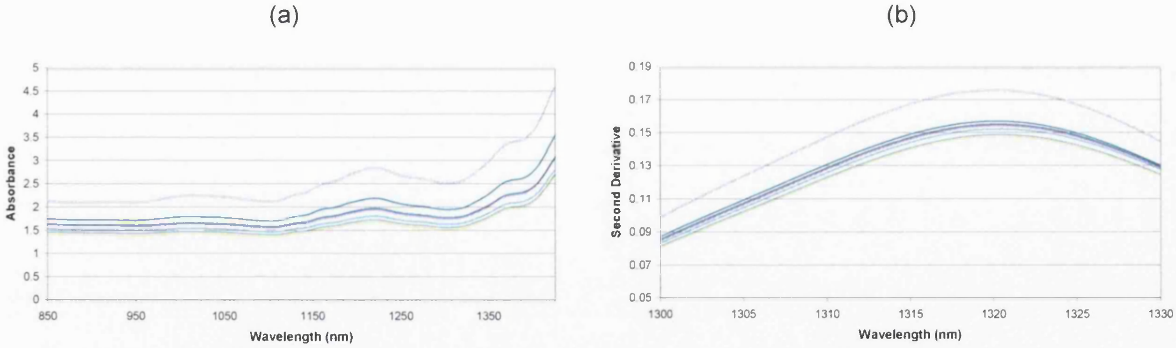

Figure 4-12: (a) Average raw and (b) second derivative transmission spectra for compression study blends with (—) 1 ton, (—) 2 ton, (—) 4 ton, (—) 6 ton and (—) 8 ton compression force.

PCA was performed on the derivatised data and the score values produced were plotted against each other to look for any separation between the blends. In the score 3 vs. score 1 plot the data separated into five distinct blend clusters,

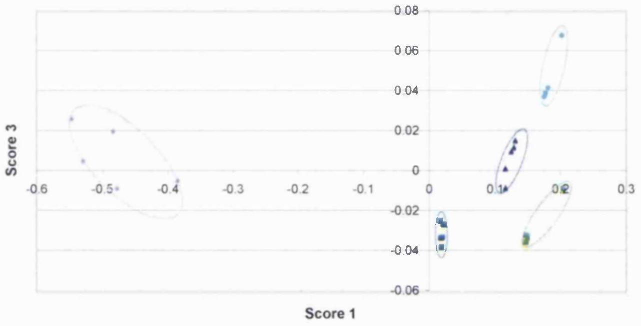

Figure 4-13: Comparison of PCA results of derivatised transmission data for compression study wafers, score 3 vs. score 1 with (◆) 1 ton, (■) 2 ton, (▲) 4 ton, (●) 6 ton and (■) 8 ton compression force.

Score 1 appeared to be related to the compression force used or the thickness of the wafer produced as it increased from one ton to six and eight tons. There was some degree of overlap with the score one values for the six and eight ton wafers. The average thicknesses of these wafers only varied by 0.1 mm therefore overlap in the individual thickness values may be the cause of the score value similarities.

Spectrum Spotlight 350-Line Mapping

All of the wafers from Table 4-2 were scanned on the Spotlight to evaluate whether the changes in the wafer compression force had any effect on the wafer matrix. Initially the pixel distributions were overlaid for each component from the scores images to evaluate any changes prior to the selection required to produce the domain statistics, Figure 4-14.

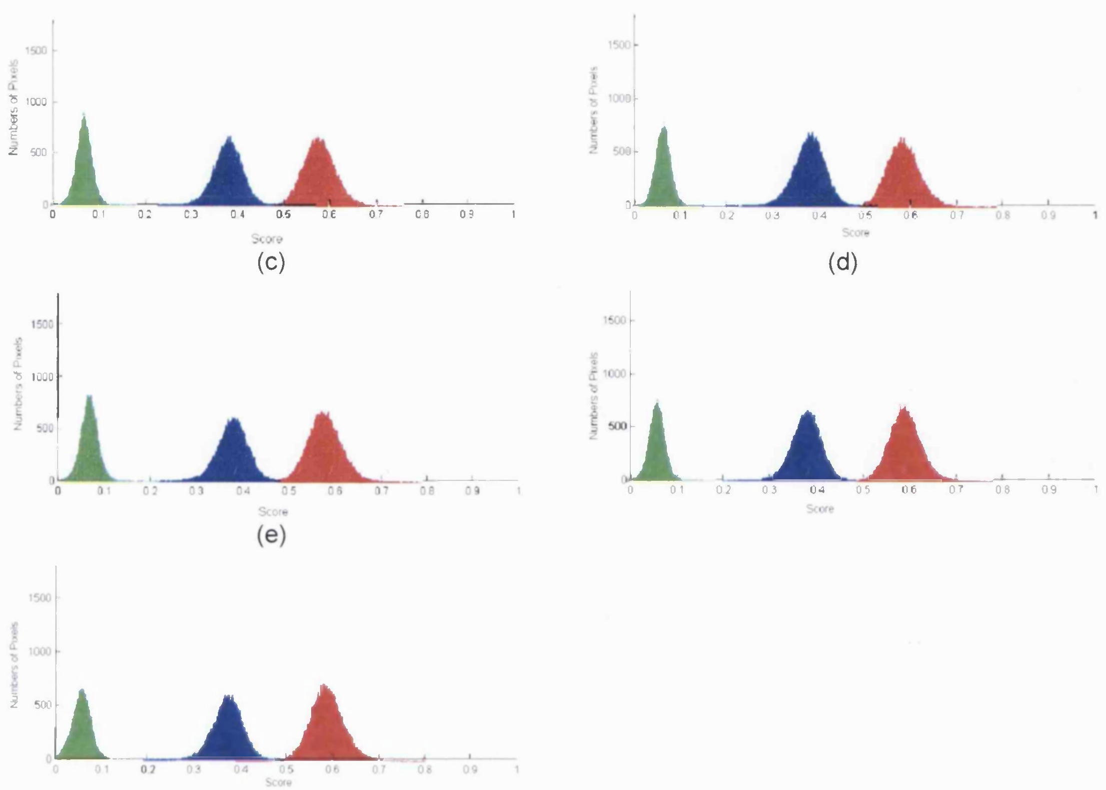

(a) (b) (c) (d) (e)

Figure 4-14: Pixel distributions for MCC (—), D (—) and lubricant blend (—) for compression study blends (a) 4, (b) 6, (c) 8, (d) 10 and (e) 12 tons.

Upon comparing the pixel distribution of the all the components it was concluded that increasing the compression pressure did not affect the homogeneity of the blend in the wafers as the pixel distributions all remained approximately the same shape. A small difference was noted between the four ton and six ton compared to the eight, ten and 12 ton forces whereby the MCC pixel distribution was slightly higher than the D distribution for the lower compression forces, which was then reversed for the higher ones. This was interpreted as the MCC becoming more integrated into the matrix with increased force, moulding around the D domains. The lubricant blend appeared very similar throughout the different compression forces used.

The sample statistics for all the pixel distributions were noted and the average values did not show any trends that were correlated to the changes in the compression force used for any of the components, Table 4-17.

Sample	MSV	% STD	Skew	Kurtosis	Number of Domains	MED (µm)	NN (µm)
lubricant blend-4 tons	0.035	25.641	0.195	4.679	95.0	35.0	19.6
lubricant blend-6 tons	0.015	-13.560	-0.125	0.309	34.5	35.0	27.8
lubricant blend-8 tons	0.064	28.418	-0.053	1.546	64.7	30.0	20.0
lubricant blend-10 tons	0.058	28.791	-0.010	0.740	30.5	30.0	26.5
lubricant blend-12 tons	0.057	31.937	-0.047	0.906	39.3	31.7	27.3
MCC-4 tons	0.363	7.978	-0.217	0.589	517.0	168.3	6.5
MCC-6 tons	0.367	9.109	-0.255	0.416	571.5	147.5	6.2
MCC-8 tons	0.381	8.168	-0.191	1.499	648.0	140.0	5.9
MCC-10 tons	0.378	8.413	-0.247	0.519	744.5	123.8	5.7
MCC-12 tons	0.375	8.022	-0.222	0.462	825.3	112.5	5.5
D-4 tons	0.623	5.959	0.200	0.473	1059.3	89.2	5.0
D-6 tons	0.622	5.424	0.277	0.509	925.5	83.8	5.3
D-8 tons	0.583	6.091	0.177	1.538	954.7	103.3	5.1
D-10 tons	0.590	5.762	0.257	0.672	791.5	123.8	5.6
D-12 tons	0.592	5.680	0.251	0.632	802.7	125.8	5.4

Table 4-17: Average sample and domain statistics for the compression study data.

The RGB images produced did not show any significant visual differences between the wafers, which was expected from the lack of differences observed in the pixel distributions. The domain statistics were calculated for the three components at the different compression forces, Table 4-17.

The domain statistics for the lubricant blend component did not show any patterns with the change of compression force.

The MCC data, however, showed a trend whereby the number of domains increased and the MED decreased with an increase in force applied. This may have been the result of the MCC being forced to spread out more within the matrix causing it to form slightly smaller domains. This was accompanied by a slight reduction in the distance between the domains, NN, so as more domains were formed they would be more spread within the matrix and move closer to one another.

The D values showed a general decrease in the number of domains, with an increase in the MED which would imply that there were some large areas of D being formed upon increased compaction. This may have been due to the MCC spreading through the matrix, encompassing various D domains and reducing the number of small ones present.

4.3.6 Dissolution Profiles

After the NIRM imaging was performed, the changing compression study wafers were dissolved and the dissolution solution profiles are shown in Figure 4-15.

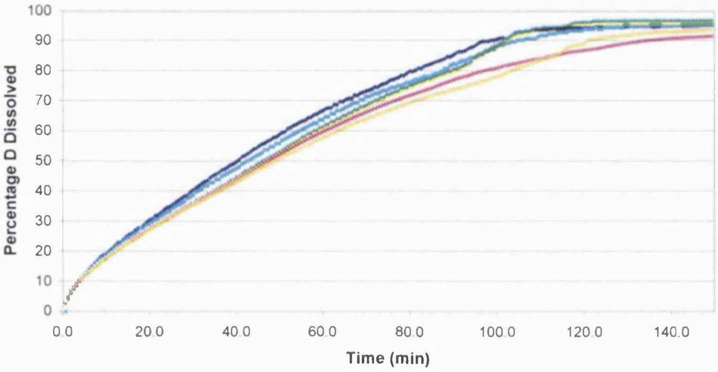

Figure 4-15: Average dissolution profiles for compression study blends with (◆) four, (■) six, (▲) eight, (●) ten and (·) 12 tons.

Initially the average dissolution profiles overlaid till approximately ten minutes when they began to separate into two groups, one with four and six tons and the other with the remaining three compression forces. The average profiles for the four and six ton wafers continued to overlay until ~20 minutes when they started to separate again. For the other group, containing eight, ten and 12 tons, they remained very similar until ~50 minutes before dividing. Subsequently at ~50 minutes into the dissolution all the average profiles were separated and in the order of successive compression forces used, with the four ton dissolving the fastest down to the 12 ton dissolving the slowest. This was the case until ~95 minutes when the average profiles began to cross over each other as they neared completion of the dissolution.

This would be an expected result as the higher the force used to make the wafer, the more compacted the material would become therefore making it harder for the water to penetrate and decreasing the release of the D into solution. The increase in the MED of the D domains and the moulding of the MCC around these domains would also have contributed to retarding the dissolution process.

The dissolution parameters were calculated for the average profiles as was shown in sections 2.2.2.

Compression Study	t_{70} (min)	P_{60} (%)	k_0 (%/min)	k_e (min^{-1})	β	T_d (min)	t_L (min)	n
4 Ton	64.21	66.89	0.92	0.021	1.98	75.79	-25.13	0.694
6 Ton	67.99	64.85	0.87	0.019	1.84	78.50	-24.22	0.667
8 Ton	71.10	61.63	0.85	0.017	2.72	112.10	-52.87	0.685
10 Ton	78.21	60.24	0.81	0.017	1.64	77.58	-19.44	0.671
12 Ton	81.10	58.51	0.76	0.015	1.82	90.56	-28.10	0.658

Table 4-18: Dissolution parameters for compression study blends.

The fit of the models to the data was compared, see Table 4-19 and Figure 4-16. The Weibull and Korsmeyer-Peppas parameters were selected for use in the correlation with the imaging parameters due to their low RSS values for the fit to the actual dissolution data.

RSS	Exponential	Weibull	Korsmeyer-Peppas
4 ton	1.19	0.26	0.55
6 ton	1.21	0.26	0.81
8 ton	1.39	0.29	0.91
10 ton	1.03	0.20	0.62
12 ton	1.12	0.39	0.88

Table 4-19: RSS for compression study.

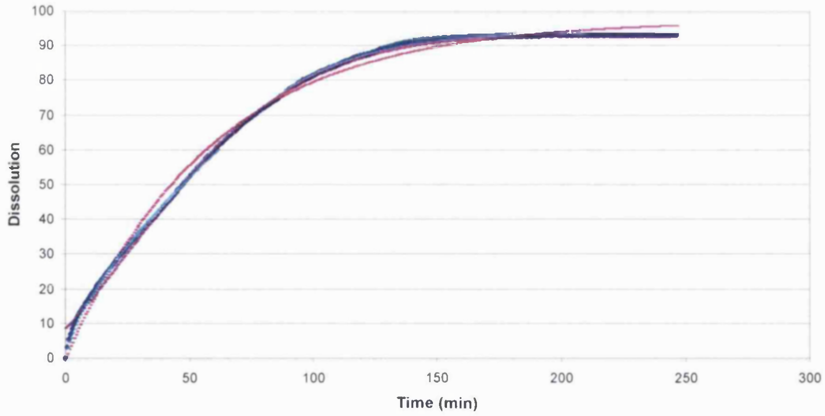

Figure 4-16: Overlay of actual dissolution profile and model values for ten ton compression with (•) actual dissolution profile, (–) exponential, (–) Weibull and (–) Korsmeyer-Peppas model values.

4.4 Conclusions

Variation of physical parameters such as blending time, input particle size and compression force used in the manufacture of blends and solid dosage forms have been found to cause changes in the sample matrix, which in turn can produce variation in the dissolution profiles of those samples. This chapter has shown examples of these physical variations applied to a pharmaceutical system based on a Pfizer product where parameters describing changes in the NIRM images of the samples provided values that showed trends relating to the subsequent dissolution profiles of the same samples.

Changing the blending time of product V resulted in an increase in the number of lubricant blend domains combined with a decrease in the MSV, related to the abundance of that component in the images. This would have been related to the lubricant blend becoming more dispersed within the matrix, resulting in each pixel containing a lower score for it and hence the abundance value dropping e.g. it cannot "see" it as accurately when it was very well mixed. This in turn showed a decrease in the rate parameters for the dissolution profiles as the blending increased, such as the initial rate and the Weibull beta value. This would have been expected as the extent of lubricant blend mixing was known to be related to changes in dissolution, i.e. the more dispersed within a blend, the more the other domains could become coated and the harder it was for the water to penetrate the blend.

When the size fraction of the blends was varied, the increasing size fractions of MCC used caused more changes in the NIR images than those of the API. As the MCC size fraction increased in the blends, both the number and size of the API and MCC domains generally decreased and increased, respectively. This was accompanied by an increase in the % STD, which gave an indication of the overall homogeneity of the image. Therefore, this increased with the MCC size fraction. However, the values for both components remained approximately the same for the two components and gave little variation when the API size fraction was varied. Deviations were echoed in the dissolution behaviour. The samples that contained the increasing size fractions of MCC appeared to dissolve progressively quicker. However, those containing the sieved D gave average dissolution profiles which overlaid to the extent that they looked like they were from different dissolutions of the same sample. This resulted in limited variations for the sieved D data, both from dissolution and imaging as the blends were all very similar. The reason for the difference was thought to be that the large MCC could not mould around the API as well as the smaller fractions, resulting in the larger domains and the faster dissolution as the water could reach the API quicker and take it into solution.

Variations in the compression force used to produce wafers of the commercial V blend provided variations in both imaging and dissolution results. The increase in compression appeared to spread the MCC around the D in the matrix to a greater extent and slow the dissolution. This was observed as an increase in the number of domains accompanied by a decrease in the size for the MCC with increased force as it became more distributed within the matrix.

This investigation has shown the potential of using NIRM images to give an insight to changes in the dissolution behaviour for samples of a particular product system. It has highlighted probable reasons for the change in performance such as the lubricant blend in the blending and the MCC in the compression and particle size studies.

5 Investigation of the Relationship between the Dissolution Properties of USP Prednisone Dissolution Calibrator Tablets and their NIRM Images

5.1 Introduction

This chapter will examine current and expired lots of the prednisone calibrator tablets to evaluate any changes in the dissolution performance with the age of the samples and show instances where certain features of the tablet matrix could be related to dissolution parameters providing the possibility of performance prediction.

5.1.1 History of Dissolution Calibrators

The dissolution test remains one of the most important evaluations performed as part of an oral drug product specification providing information regarding the quality of the manufacturing process. However, the test distinguishes itself from any other performed as it can provide a means for the surrogate assessment of *in vivo* performance of the product. With this in mind the apparatus must be shown to function in a standard and reproducible manner to guarantee confidence in the dissolution results obtained, as dissolution failure remains a primary cause of product recalls, contributing to > 10% of the total (FDA, 2005, www.fda.gov/ohrms/dockets/ac/05/briefing/2005_4137BI_05_Dissolution-summary.doc). This leads to the requirement for some form of dissolution apparatus calibration procedure.

The approach taken by the USP to assess the suitability of the apparatus is a combination of detailed descriptions of the testing apparatuses listed in the pharmacopoeia chapter <711> including dimensional and operational tolerances, e.g. the paddle should be 25 ± 2 mm above the inside bottom of the vessel, along with a method to show suitable performance using a standard reference material. These describe the mechanical (physical parameters) and chemical (dissolution calibrators) calibrations respectively (Foster and Brown, 2005). These relate to apparatuses 1 and 2, baskets and paddles. The physical parameters involved in the mechanical calibration include vessel, basket and paddle dimensions, shaft vertical alignment, shaft wobble, vessel/shaft centring, basket/paddle depth, vibration, rotational speed and vessel medium temperature. Suggestions have been made to the extent of removing the chemical calibration altogether and focussing in on the mechanical aspect of the calibration. This would be achieved by tightening the apparatus tolerances set out in the pharmacopoeias, but initial discussions have raised concerns about the possible worldwide impact of the proposed changes and as such they were put on hold pending further investigation (Gray *et al.*, 2005; Shah, 2004). However a USP bulletin in November 2006 stated some changes to the nomenclature and definitions of the tests performed on dissolution apparatuses. The term calibrator would no longer be used to describe the USP reference standard tablets, i.e. the prednisone tablets, and the title "Apparatus Suitability Test" as stated in <711> that used the calibrators would be changed to "Performance Verification Test". The mechanical calibration would still need to be performed as neither alone had been deemed sufficient (USP, 2006).

Currently the chemical calibration is recommended every six months, or on any occasion when a unit has been moved or undergone a major alteration. The first official USP dissolution calibrators were adopted in 1978 and comprised a disintegrating 50 mg prednisone tablet manufactured by Upjohn and a non-disintegrating 300 mg salicylic acid tablet made by Hoffman LaRoche. However the Division of Pharmaceutical Analysis (DPA, formerly the National Centre for Drug Analysis, NCDA) within the FDA discovered a commercially available 10 mg prednisone tablet called the NCDA #2 that was sensitive to vessel centring for apparatus 2 and to dissolved gases in the medium, but was not suitable for apparatus 1 (Moore *et al.*, 1996). This type of tablet remained the in-house calibrator in the DPA for approximately 20 years until the cessation of their commercial production. In 1994 the DPA provided the University of Maryland at Baltimore (UMAB) with a tablet formulation that was thought would produce similar tablet characteristics to the NCDA #2 lots. In 1995 the NCDA #2 tablets had remained stable since their adoption by the DPA in 1979 with the expectation of the lots of tablets prepared at the UMAB to do the same. Following the discontinuation of the 50 mg prednisone calibrator production by Upjohn in 1999, the USP replaced it with the 10 mg tablets produced at UMAB, but unlike the original NCDA #2 tablets they did not remain stable as expected and tended to give lower dissolution results with paddles over time (FDA, 2005). As a result of this, the design of an "ideal" calibrator tablet has been high on the list of priorities for the USP. Discussions have lead to the suggestion to re-evaluate the 50 mg formulation (acquired from Upjohn) as well as the current USP formulation and a copy of the NCDA #2 tablets to see which comes out with the best sensitivity to changes in the dissolution system and may fall under the heading of "ideal" or as close to it as is reasonably possible. A summary of the prednisone history is given in Table 5-1.

USP	NDCA (DPA)
50 mg formulation distributed from 1978 (lot F) up to 1999 (lot L).	NCDA #1 tablets were a 5 mg formulation used in early dissolution studies for reproducibility by the NDCA now DPA.
Current 10 mg formulation developed by Ralph Shangraw at the UMAB, supported by the USP and the DPA, intended to imitate the NCDA #2 tablets, the first lot produced in 1999 was lot M followed by N, O with P in the process of manufacture.	NCDA #2 tablets were a 10 mg formulation that replaced the NCDA #1 when the supplies ran out. Used as the in-house calibrator for paddles for ~20 years.

Table 5-1: Prednisone calibrator history. Adapted from Foster and Brown, 2005.

The salicylic acid calibrators have also experienced their own issues including fused or chipped tablets found in distributed bottles of samples, but as the focus of this work was on the prednisone tablets, there will be no further discussion on the non-disintegrating type.

A point of continuing concern is the situation where a dissolution apparatus fails the calibration. A means to verify any failing result by a retest was considered by the USP project team on dissolution (Brown, 2002). The acceptance criteria set for the calibrators are the result of a collaborative study and tend to be wide so that they have the capacity to include data from multiple laboratories, but they are calculated for the individual vessel positions. This dependence on the individual results has been in question prior to the USP investigation (Qureshi and McGilveray, 1999). A failure at one position in a multi-position test (the majority of dissolution testing carried out will be at ≥ 6 vessels) would mean that whole system would require a retest (Gray *et al*, 2005). Statistical analysis was applied to some test dissolution data and the findings showed retesting gave some benefits for the basket apparatus and none for the paddles. This resulted in the USP reanalysing the method used to calculate the acceptance ranges and a change was made that recognised the reliance of the whole system passing on the individual vessel results. The first result of this new calculation method was observed for the lot O prednisone tablets where the acceptance range was altered on the 6th of December 2004.

5.1.2 Sources of Error in Chemical Calibration Testing

This suitability testing of dissolution apparatus utilising the calibrator tablets has lead to many discussions relating to the quality of the tablets and even the relevance of the test altogether. There are many areas that can contribute to error in the calibration results which should be carefully monitored to prevent failures (Burmicz, 2005). Some have been previously mentioned in chapter one section 1.5.3., but these will be discussed in more detail here with relevance to the calibration procedure.

Initially the calibrator tablets should be checked for quality, e.g. is the correct number present or do any of the tablets show evidence of moisture damage? The storage of the tablets is another factor and ideally they should be kept in dry conditions such as in a desiccator. They should be taken out as required for the test and not left out on the bench while waiting for the test to start.

Another problem area is the insufficient deaeration/degassing of the medium. The USP recommends to heat the medium to ~41 °C then vacuum filter through a 0.45 µm porosity membrane into a flask whilst being stirred magnetically and remain under the vacuum whilst stirring for a further five minutes. Although now it is possible to use other techniques for this purpose as long as they have been validated and show no negative reaction. The 10 mg lots of prednisone are very sensitive to degassing whereby if done excessively the results will be low and *vice versa* for inadequate degassing. Care should be taken with the transfer of the degassed media into the vessel so air is not folded-in. In any circumstance the media will in most cases re-aerate after approximately an hour, but it is this initial time window that will have the greatest bearing on the dissolution rate and subsequent profile (Pharmatest, USP Dissolution Calibration PQ SOP).

The physical condition of the apparatus can also contribute to problems in the calibrator dissolution results. The vessels should be free from scratches and spherical in the base. Vibration near the apparatus should be kept to a minimum and the mechanism for dropping the paddle/basket shafts down should be maintained to avoid then hitting the media suddenly. The quality of the baskets should be monitored, making sure breather holes are clear and they remain vertical with no bend in the sides or blocked mesh.

The correct filter size should be used when sampling is involved as the results from a sample containing excipients or active that has found its way through the filter can be the difference between a pass and a fail. Absorption of the drug can also occur on the filter and any tubing in use for sampling which should be checked.

Finally the current lot of USP reference standard should be used, any drying instructions provided should be followed and the standard solution should be prepared on the day it is required.

5.1.3 Calibrator Variability

There have been a number of reports regarding the variability of the results obtained from the USP calibrators in collaborative studies between and within many laboratories worldwide (Qureshi and McGilveray, 1999; Cox and Furman, 1984; Ashanta *et al.*, 1995; Qureshi *et al.*, 1995). This was the 50 mg prednisone formulation in the papers pre-1999, but the experiments tended to make a comparison of these to the NCDA #2 tablets which are among the candidates for the title of "ideal" calibrator. The results of these comparisons generally concluded that the USP 50 mg tablets were either insensitive to the critical parameters of the test and/or the NCDA #2 tablets made them look totally inadequate for the purpose of calibration (Moore *et al.*, 1995). However, results from another comparison study four years later than Moore *et al.* showed the opposite to be true. They found that the results from the NCDA #2 tablets gave results that were more variable than the USP calibrators at the time (Qureshi and McGilveray, 1999), but this may not be the case currently as the formulation has been altered. It is also understood that the formulation can vary slightly between lots such as lot N to lot O. It has been suggested that the current 10 mg prednisone formulation contains two different fractions of particles, one with small and the other with large particles, based on the shape of dissolution profiles obtained (Quist and Röst, 2003). This was put forward as a possible explanation for the variability seen between different lots of the calibrators, whereby there may be varying fractions or sizes of the large and small particle contributions.

Another study involving dissolution calibrators involved NIRS. Here the aim was to predict the dissolution profile of salicylic acid calibrators using PLS calculations based on data from reflectance and transmission NIRS to correlate to the fractions dissolved at seven time points over three hours. The results published show that this was possible with an f_2 (see section 2.2.1) value of ~90 (the closer to 100, the more similar the profiles) for both the reflectance and transmission results when compared to the reference profile, but there was no indication of how many calibrators were evaluated by NIRS or dissolution (Voytilla and Drennan, 2004). In this case, however, prednisone calibrators were not evaluated.

5.2 Experimental

5.2.1 Materials

The prednisone dissolution calibrator tablets were bought directly from the USP store for the current lot available, lot O. The other samples were sourced from G.B. Caleva (G.B. Caleva Ltd., Sturminster Newton, Dorset, UK) as they were no longer commercially available, Table 5-2.

Calibrator Lot	Number of Tablets	Prednisone (mg)	Valid Use Date
M	25	10	09/02
N (2001)	29	10	06/04
N (2003)	30	10	06/04
O (2004)	10	10	07/06
O (2005)	27	10	07/06

Table 5-2: Samples of USP prednisone calibrator tablets.

Prednisone reference standard was also purchased directly from the USP. It was not possible to obtain the full formulation information or acquire samples of the actual excipients that were used for the calibrator tablets. The partial formulation information that was available with the tablets is shown in Table 5-3.

Component	% m/m in Tablet
Prednisone	4.5
Dibasic Calcium Phosphate (DCP)	38.5
Stearic Acid	1.4

Table 5-3: Partial tablet formulation given in prednisone tablets material safety data sheet.

In order to complete the formulation, PCA was performed on a Spotlight image file of a calibrator tablet from the current lot and the first PC illustrated that a cellulose was contributing to the remainder of the tablet. This was the case for tablets from the other lots obtained. MCC was found to be a very good match to the PC loading and as such was used to complete the formulation excipients at 55.6% m/m, Figure 5-1.

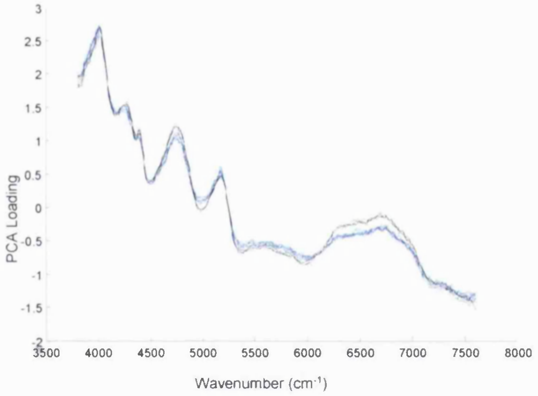

Figure 5-1: Elucidation of tablet formulation using PCA on a Spotlight data with PC 1 (—) and MCC spectra (—).

Laboratory excipient samples were utilised for the purpose of library construction for image analysis.

All the tablets were weighed and their thickness measured. Based on these values, six tablets of each lot were selected for dissolution and another six for imaging.

Accelerated Conditions (AC)

Further to the initial selection for dissolution and imaging samples, eight more of the lot N (2001) tablets were chosen for an experiment devised to accelerate any processes that may occur upon storage of the tablets over time. The conditions for pharmaceutical storage are set out in the guidance on stability testing from the International Conference on Harmonisation (ICH, 2005). However, due to time constraints, it was advised in this case that a very short study be undertaken. All eight tablets were placed in an oven set at 100 ^{0}C for 24 hours and then allowed to cool for approximately one hour prior to the dissolution of six and imaging of the remaining two samples. The thought behind using a much higher temperature than stated by the ICH was that it would push the calibrators into changing in the much abbreviated time frame. The tablets used for dissolution were weighed and measured.

Sample Preparation

Unlike the blend wafers utilised in chapters three and four, the calibrator tablets did not have a flat sample surface, they were curved. To optimise the surface presentation for NIRM imaging on the Spotlight all the tablets for this purpose were milled using a Leica EM Trim (Leica Microsystems GmbH, Wetzler, Germany). This was done by gluing the tablet onto a microscope slide then gradually milling thin layers off the curved surface.

5.2.2 Near-infrared Spectroscopic Analysis

Transmission NIRS

All the available dissolution calibrators from Table 5-2 were scanned using the Foss NIRSystems 6500 monochromator (Foss NIRSystems Inc., Silver Springs, MD, USA) with an InTact tablet transmission analyser, shown in section 3.2.3. A customised sample holder was used to ensure reproducible measurements of the wafers. The spectra were used over the range 850 - 1450 nm and three replicates were performed per tablet.

Reflectance NIRS

All the available dissolution calibrators from Table 5-2 were also scanned using the Foss NIRSystems 6500 monochromator (Foss NIRSystems Inc., Silver Springs, MD, USA) with a Rapid Content Analyser attachment, Figure 5-2. Each tablet was placed on the sample window, positioned using the centring mechanism then the lid was closed and the sample scanned. This signal was obtained from approximately the top one to five mm of the sample. Three replicates were performed per tablet. Both of the Foss instruments used passed all the manufacturer's performance tests including wavelength accuracy, photometric noise and accuracy and repeatability and were therefore considered to be operating correctly.

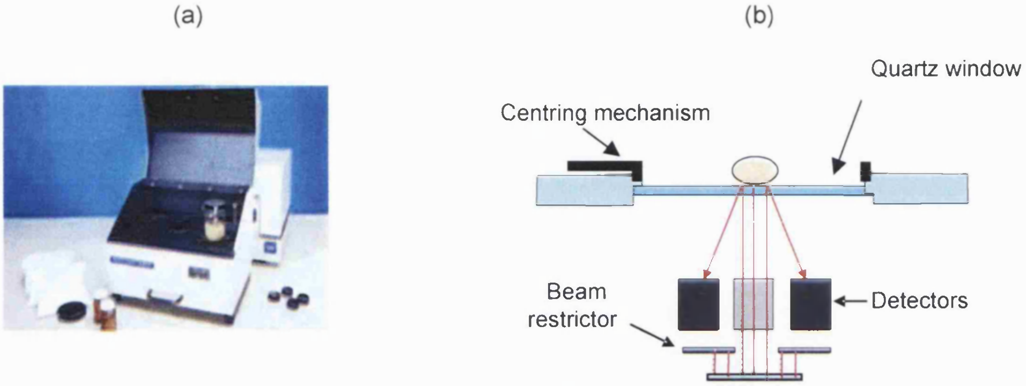

Figure 5-2: (a) Foss NIRSystems monochromator with Rapid Content Analyser (source: Foss website www.foss-nirsystems.com) with (b) a schematic of data collection method.

5.2.3 Near-infrared Microscopy Imaging

Spectrum Spotlight 350-Line Mapping

The calibrator tablets selected for NIRM imaging were prepared and analysed on the Spotlight as described in section 3.2.4.

Data Processing

In all cases, the files from the Spotlight (.fsm) were converted into a format (.spc) that could be imported into the image analysis software, ISys.

The data processing described in section 3.2.2. was also applied to the calibrator results using the selection of specific areas of the pixel distribution, section 2.1.2., and using the mean value for the contour tool. Further to this processing, it was found necessary to use PCA reconstruction on the normalised data, section 2.1.2. This was due to difficulties locating the API within the matrix using PLS calculations due to the large contribution of the MCC component. The removal of the first PC removed the mean spectral response over all the pixels, which had its main contribution from the MCC. A library was constructed using the reconstructed data cube by sitting at univariate wavelengths which related to the four components and selecting the reconstructed spectra for the pixels with the highest absorbance i.e. the brightest pixels when working in greyscale. PLS analysis was then performed using the reconstructed library then sample statistics, RGB images and domain statistics were calculated from the resulting scores images.

5.2.4 Dissolution

The dissolution apparatus was the same as for section 4.2.4. The data acquisition was done from six vessels, to mimic the USP dissolution testing using 900 ml of pre-warmed, degassed water as the dissolution medium. The paddles were positioned at 25 mm ± 2 mm from the base of the vessel. The wavelength of 242 nm was monitored for the prednisone, as specified in the experimental conditions for the calibrator dissolution.

RPM	Pathlength (mm)	UV λ Monitored (nm)	Baseline Correction Wavelength
50	10	242	320

Table 5-4: Dissolution conditions applied for prednisone calibrator tablets.

A standard solution of the API was used to give an absorbance value equivalent to 100% of dissolved API. The amount of API was calculated for each tablet from the mass and the % m/m used in the blend, which was used to correct for any differences between samples on the conversion to percentage (%) API dissolved.

5.3 Results and Discussion

5.3.1 Sample Selection

The calibrator tablets were selected for dissolution and imaging in a way that all the possible variations observed in the physical parameters were covered so that the mean values would be representative of the lot being examined, Table 5-5.

5.3.2 Transmission NIRS

The average results of the three scans were averaged again for calibrator lot. There was an offset in the raw spectra which related to the differences in the average tablet thicknesses. Lot M had the lowest average tablet thickness of ~3.30 mm, then lot O 2005 at ~3.55 mm and the other three lots had similar values at ~3.57 mm, Figure 5-3(a).

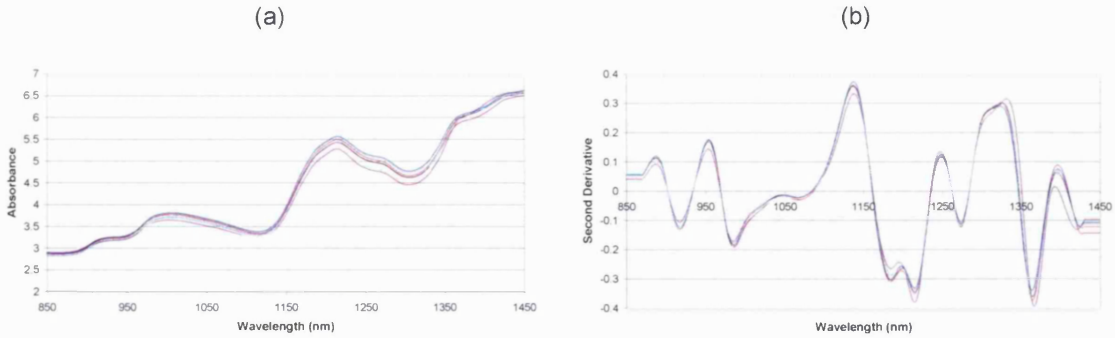

Figure 5-3: (a) Average raw and (b) second derivative absorbance spectra for dissolution calibrators with (—) lot M, (—) lot N 2001, (—) lot N 2003, (—) lot O 2004 and (—) lot O 2005.

The second derivative absorbance spectra showed a similar pattern to the raw spectra. Lot M particularly stood out as different, with the others grouping relatively close to each other, Figure 5-3(b). There were differences in peak amplitude at the wavelengths associated with prednisone showing that there was more of a response for this component in lot M accompanied by a peak shift at ~1334 nm and ~1370 nm.

PCA scores were calculated for the normalised data, but this did not show much separation between the different lots. PCA was subsequently performed on the derivatised data[1] (whereby physical effects had been removed) and the score values produced were plotted against each other to look for any separation between the different lots analysed. Score two showed some separation of lot M from the other lots, but scores one and three did not, Figure 5-4(a). This may have been related to the differences observed in the spectra for the prednisone in lot M. Score four versus score two helped to separate the lots N and O from each other, Figure 5-4(b), but there was always a slight overlap between the score values of the three groups.

---

[1] In addition, the PCA was performed on the non-derivatised data to see if there was any increase in the separation of the calibrator lots. However it was found that the derivatised data provided the greatest discrimination.

	Dissolution		Imaging			Dissolution		Imaging	
	Mass (mg)	Thickness (mm)	Mass (mg)	Thickness (mm)		Mass (mg)	Thickness (mm)	Mass (mg)	Thickness (mm)
Lot M	210.7	3.25	209.8	3.26	Lot O (2005)	210.3	3.49	203.8	3.49
	213.4	3.27	212.6	3.27		214.7	3.50	214.8	3.50
	218.2	3.29	217.8	3.29		215.5	3.52	214.3	3.52
	217.0	3.30	218.0	3.30		219.8	3.55	215.2	3.55
	220.2	3.32	221.5	3.32		229.7	3.58	219.4	3.57
	221.7	3.34	222.5	3.32		233.7	3.67	238.6	3.62
Average	*216.9*	*3.30*	*217.0*	*3.29*	*Average*	*220.6*	*3.55*	*217.7*	*3.54*
Lot N (2001)	210.0	3.48	247.4	3.53	Lot O (2004)	220.0	3.58	217.5	3.54
	218.3	3.55	222.6	3.56		233.5	3.60	220.1	3.56
	220.4	3.58	223.0	3.58		222.1	3.55	223.5	3.59
	221.4	3.59	223.3	3.59		217.7	3.56	231.9	3.61
	221.3	3.61	226.9	3.61		218.2	3.55	219.1	3.55
	222.1	3.65	224.1	3.66					
Average	*218.9*	*3.58*	*227.9*	*3.59*	*Average*	*222.3*	*3.57*	*222.4*	*3.57*
Lot N (2003)	213.4	3.47	213.8	3.50	Lot N (2001) AC	225.8	3.59		
	217.3	3.53	217.3	3.53		227.0	3.59		
	222.0	3.55	221.0	3.55		222.1	3.59		
	221.6	3.58	217.9	3.58		220.1	3.60		
	223.3	3.60	221.4	3.60		225.7	3.59		
	226.6	3.63	214.1	3.63		224.5	3.60		
Average	*220.7*	*3.56*	*217.6*	*3.57*	*Average*	*224.2*	*3.59*		

Table 5-5: Physical parameters for calibrator tablets selected for dissolution and imaging.

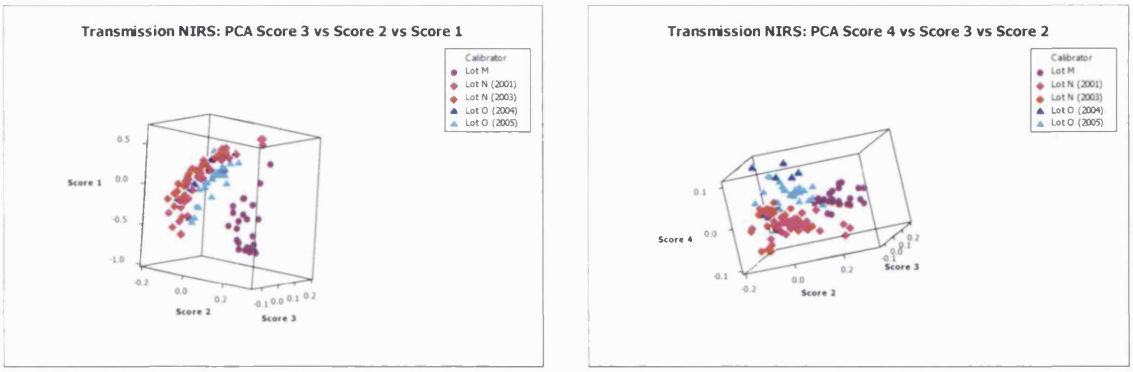
(a) (b)

Figure 5-4: Comparison of PCA results of derivatised transmission data (a) score 3 vs. score 2 vs. score 1 and (b) score 4 vs. score 3 vs. score 2 for calibrator tablets.

5.3.3 Reflectance NIRS

The results for the average of three scans for the calibrators were again averaged for each calibrator lot. The raw spectra showed an offset of lot M from the other calibrators, which may have been related to a difference in the mean particle size, with M having a higher value than the other lots, Figure 5-5(a). The lot N 2001 spectrum sat just above the other lot N and O spectra, which may have been related to the same parameter as for lot M.

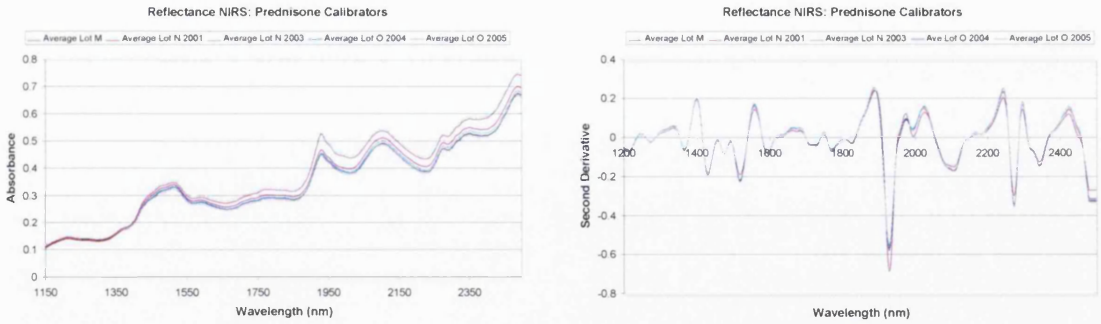
(a) (b)

Figure 5-5: (a) Average raw and (b) second derivative reflectance spectra for dissolution calibrators with (—) lot M, (—) lot N 2001, (—) lot N 2003, (—) lot O 2004 and (—) lot O 2005.

A second derivative was applied to remove any features caused by physical differences in the tablets. This showed lot M to be different from the others where there was an increased response at ~1930 nm, which could relate to an increase in moisture content,

Figure 5-5(b). There was an increase in the peak amplitude and hence the amount of that component observed at ~1970 nm and ~2000 nm, which were associated with the prednisone.

PCA was performed on the derivatised data, as the raw data scores did not show any enhancement in the data separation. The score values produced were plotted against each other to look for any grouping within the different lots analysed.

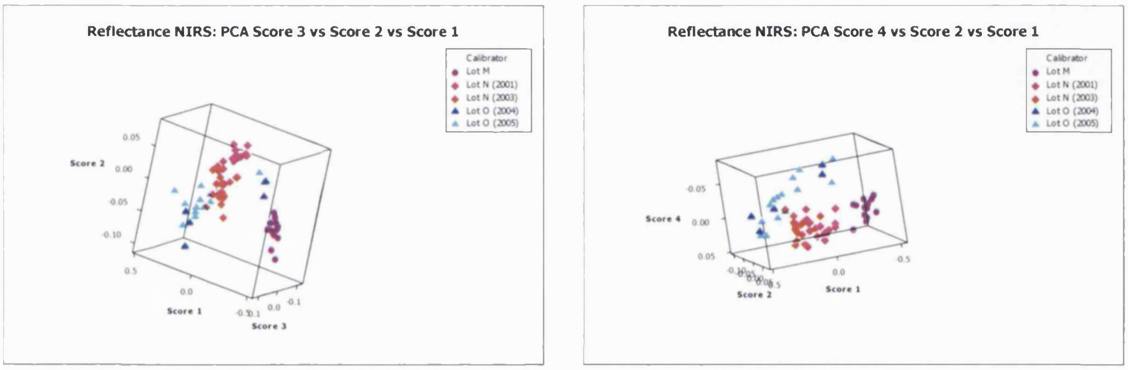
(a)

(b)

Figure 5-6: Comparison of PCA results of derivitised reflectance data (a) score 3 vs. score 2 vs. score 1 and (b) score 4 vs. score 2 vs. score 1 for calibrator tablets.

Lot M was separated from the other two by score one. The lot N and O data did not completely separate from each other along any of the score values, but a combination of score four and score one gave the best separation, Figure 5-6(b). Lot O appeared to be slightly more variable than lot N as there was more of a spread within the score values for O.

5.3.4 Spectrum Spotlight 350-Line Mapping

The samples from each calibrator lot were prepared and analysed on the Spotlight to gain information on the component matrix. Initial data processing highlighted an issue where it was not possible to distinguish the API from the other excipients present. Subsequently, PCA reconstruction was applied to the normalised data and the scores file from the PLS calculation performed on the reconstructed data cube was used to overlay the pixel distributions, as was done in the last chapter to evaluate any changes between the lots before any of the manipulation required for the production of RGB images or calculation of the domain statistics. This did not provide a lot of information regarding variations between the lots, but a difference was observed for the DCP distribution.

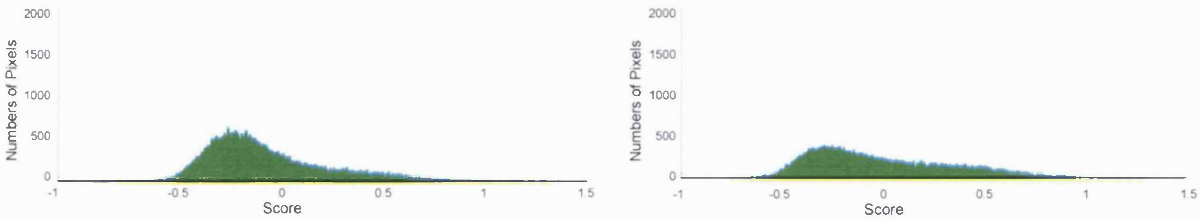
(a)

(b)

Figure 5-7: Pixel distributions for DCP from PLS score file from PCA reconstructed data for (a) lot M and (b) lot O 2005 calibrators.

It could be seen that the DCP distribution was slightly more flattened for the current lot of calibrators compared to the distribution from the oldest lot analysed. This could have indicated the formation of smaller domains of DCP which would result in the height of the pixel distribution increasing accompanied by a narrowing, as the MSV shifted to accommodate the changes in the pixel purity, i.e. if the domains were smaller there would be less pixels with the higher score contributions.


(a)

(b)

Figure 5-8: Single channel images for DCP from PLS score file from PCA reconstructed data for (a) lot M and (b) lot O 2005 calibrators with (—) DCP and (—) remainder of matrix components.

The images in Figure 5-8 show the distribution of the DCP in a sample from lot M and lot O and it could be clearly seen that there were a higher number of much smaller domains present in the lot M sample.

The sample statistics for each component for all the samples were examined, Table 5-6. The values for the DCP backed up the observations in the pixel distributions and the single channel images showing the MSV to decrease with the age of the calibrator tablet lot. However, it may be the case that the amounts of DCP used in each different formulation for released lot may have been varied slightly compared to the previous lot available. The % STD values showed a trend with age also, but in this case there was an increase as the tablet lot matured. The kurtosis value for the API decreased in value from lot O to lot M which indicated a reduction in the amount of tailing on the distribution. In this case the skew is positive so the tailing must have been on the right hand side of the pixel distribution, so a reduction here would have related to a reduced amount of pixels with a high contribution from the API as the calibrator aged. It should be noted that the values for the MCC came out negative for the MSV due to the nature of the PCA reconstruction. The first PC response contained the mean spectral response over all the pixels in the image and in this case the mean spectral response took the shape of the MCC spectrum (see Figure 5-1) as this was the main component present in the samples. The removal of this PC and the subsequent reconstruction of the image cube would have eliminated a huge amount of the MCC character from the data. Therefore the sample and domain statistics for all the components were affected, but particularly the MCC.

Component	MSV	%STD	Skew	Kurtosis
Stearic Acid-Lot M	1.26×10^{-5}	1263216.37	4.07	31.60
Stearic Acid-Lot N (2001)	3.89×10^{-5}	167341.38	5.20	44.53
Stearic Acid-Lot N (2003)	3.30×10^{-5}	165445.68	4.60	38.22
Stearic Acid-Lot O (2004)	3.77×10^{-5}	196105.95	4.66	32.36
Stearic Acid-Lot O (2005)	3.36×10^{-5}	183351.22	4.73	37.20
DCP-Lot M	3.56×10^{-4}	84474.42	0.93	0.45
DCP-Lot N (2001)	4.27×10^{-4}	79832.02	0.82	0.06
DCP-Lot N (2003)	4.21×10^{-4}	76545.35	0.94	0.42
DCP-Lot O (2004)	7.89×10^{-4}	48642.76	1.02	0.17
DCP-Lot O (2005)	7.25×10^{-4}	57911.56	0.98	0.23
Prednisone-Lot M	8.80×10^{-5}	265725.16	0.58	1.27
Prednisone -Lot N (2001)	3.10×10^{-4}	107803.74	0.92	1.55
Prednisone -Lot N (2003)	4.22×10^{-4}	82162.91	1.12	1.80
Prednisone -Lot O (2004)	3.56×10^{-4}	75202.01	1.06	1.98
Prednisone -Lot O (2005)	4.04×10^{-4}	82666.21	1.18	2.50
MCC-Lot M	-9.73×10^{-5}	-226144.29	0.15	0.49
MCC -Lot N (2001)	-7.61×10^{-5}	1536869.57	0.03	0.04
MCC -Lot N (2003)	-1.07×10^{-4}	-232726.28	0.06	0.13
MCC -Lot O (2004)	-1.91×10^{-4}	-122139.44	-0.12	-0.01
MCC -Lot O (2005)	-1.06×10^{-4}	-274975.21	0.06	0.16

Table 5-6: Average sample statistics for dissolution calibrators from Spotlight data.

Following on from the sample statistics, the domain statistics were calculated to describe the size and distribution of the component areas in the image, Table 5-7.

Component	Number of Domains	MED (μm)	NN (μm)
Stearic Acid-Lot M	84.2	85.4	16.8
Stearic Acid-Lot N (2001)	45.2	92.1	24.2
Stearic Acid-Lot N (2003)	43.0	87.1	25.4
Stearic Acid-Lot O (2004)	55.8	86.0	21.6
Stearic Acid-Lot O (2005)	45.8	85.4	24.1
DCP-Lot M	337.5	125.4	9.0
DCP-Lot N (2001)	296.2	150.4	10.1
DCP-Lot N (2003)	304.3	148.3	9.6
DCP-Lot O (2004)	243.2	146.0	11.2
DCP-Lot O (2005)	261.7	146.7	10.7
Prednisone-Lot M	233.8	67.9	9.1
Prednisone -Lot N (2001)	63.3	97.1	19.5
Prednisone -Lot N (2003)	64.3	99.2	20.1
Prednisone -Lot O (2004)	65.6	98.0	17.8
Prednisone -Lot O (2005)	72.5	104.6	18.3
MCC-Lot M	545.5	145.4	6.2
MCC -Lot N (2001)	538.8	150.4	6.3
MCC -Lot N (2003)	640.2	136.7	5.6
MCC -Lot O (2004)	459.8	155.0	6.6
MCC -Lot O (2005)	543.3	142.1	6.3

Table 5-7: Average domain statistics for dissolution calibrators from Spotlight data.

The DCP showed an increase in the number of domains with age of calibrator and the MED of lot M was smaller than that of the newer lots. The prednisone component had significantly more domains present in lot M with a lower MED compared to the other four lots examined. This confirmed the observations seen for the reflectance and transmission NIRS, where lot M had increased peak amplitude related to prednisone. A similar situation was observed with the stearic acid, but the MED did not vary with the number of domains observed.

Accelerated Conditions

In the same manner as for the other calibrators analysed, the normalised data had PCA reconstruction applied to it and the scores file from the PLS calculation performed on the reconstructed data cube was used. The pixel distributions were overlaid and the most significant change was seen for the stearic acid component.

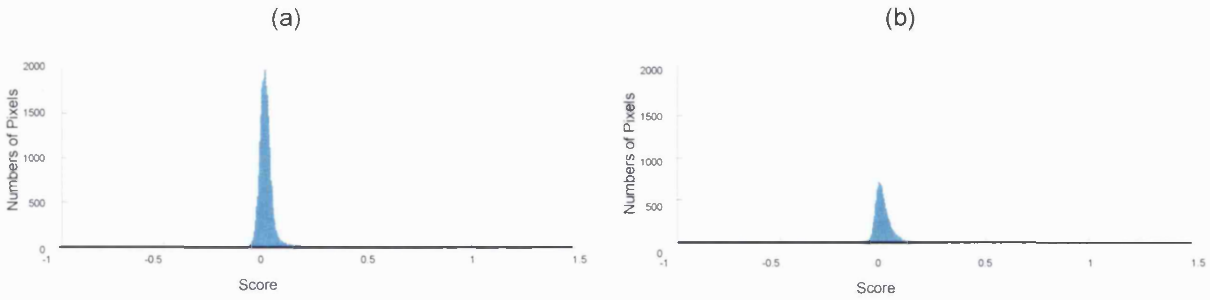
(a)

(b)

Figure 5-9: Pixel distributions for stearic acid from PLS score file from PCA reconstructed data for (a) lot N (2001) and (b) lot N (2001) with accelerated conditions.

The loss of the tailing to the right hand side of the distribution would indicate the formation of smaller domains. This was indicated by the reduction in the number of pixels with high score contributions, which would usually be associated with the response from an area in the centre of a component domain for example where the domain was large enough that the total composition of the pixel would be mainly that single component. The RGB images were built for the stearic acid, DCP and API, Figure 5-10.


(a)

(b)

Figure 5-10: RGB images for stearic acid (—), DCP (—) and prednisone (—) from PLS score file from PCA reconstructed data for (a) lot N (2001) and (b) lot N (2001) with accelerated conditions.

It was clear that the distribution of the stearic acid had changed significantly with the heating. It appeared to have become further combined within the matrix, specifically associating with the API, compared to the discrete, separated domains observed prior to the heating.

The sample and domain statistics for the heated samples were compared to those for the lot N (2001) samples and as with the pixel distributions the main changes were seen in the stearic acid component.

Lot N (2001) Stearic Acid	MSV	% STD	Skew	Kurtosis	Number of Domains	MED (µm)	NN (µm)
No heating	3.88×10^{-5}	167341.38	5.20	44.53	45.2	92.1	24.2
Heating	6.47×10^{-5}	54867.71	0.88	1.35	68.5	56.3	17.6

Table 5-8: Average sample and domain statistics for stearic acid for lot N (2001) before and after heating.

The reduction in the skew and kurtosis values after the heating represented the loss of the right hand tailing seen in the pixel distributions. The smaller %STD would have related to the stearic acid becoming more integrated into the matrix, which was supported by the domain statistics showing an increase in domains complimented by a decrease in the MED and NN.

It was subsequently discovered that the melting point for the stearic acid was actually 69.6 ^{0}C which could have explained the changes observed in the matrix.

5.3.5 Dissolution Profiles

All of the samples allotted for dissolution in Table 5-5 were dissolved to see if there were any differences in the profiles for the different calibrator lots. The average profiles in Figure 5-11 showed lot M to have the slowest dissolution rate, followed by lot O then lot N as the quickest to dissolve. It appeared that the variation in the profiles was not related to the age of the calibrator tablet lot. However it may have been the result of changes in the sample matrices.

The distinctly different dissolution of lot M could have been a result of a combination of the increased amount of practically insoluble DCP and stearic acid domains through the tablet matrices, seen from the imaging parameters, which led to a reduction in the rate of dissolution. If the average was taken for the number of domains of stearic acid for each lot, i.e. providing three parameter values, then the order of magnitude decreased from lot M to O to N, which echoed the increase in the dissolution rate observed in the average profiles. In this respect the stearic acid may have been behaving as a means to retard the dissolution in a similar fashion to its relation magnesium stearate.

The average values for the number of API domains provided a pattern analogous to the stearic acid and the dissolution and as such may have influenced the profile differences.

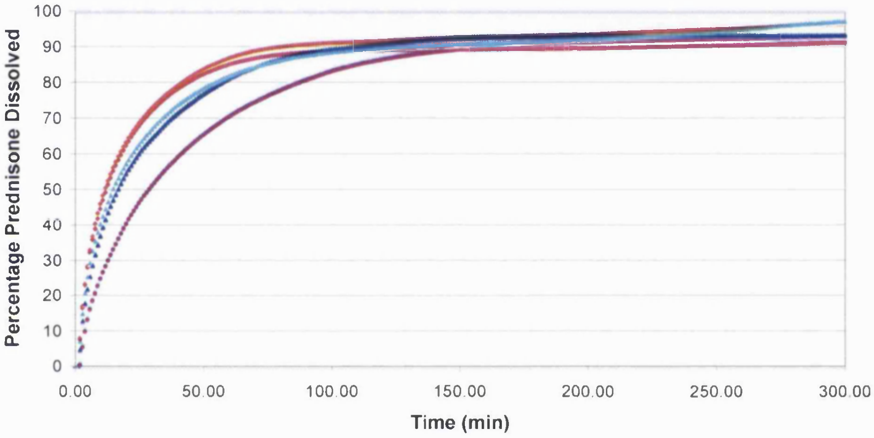

Figure 5-11: The average dissolution profiles for the different lots of prednisone calibrator tablets with (●) lot M, (◆) lot N 2001, (◆) lot N 2003, (▲) lot O 2004 and (▲) lot O 2005.

Another feature of the average profiles showed that the two for lot O did not overlay to the same extent as the two for lot N. This increase in variation for lot O was observed previously in the PCA score plot comparisons from the NIRS data, whereby the data points for lot N samples appeared to group together to a greater extent than those related to lot O, Figure 5-6.

All the methods described in section 2.2.2. were applied to the average profile data and the resultant values are shown in Table 5-9.

Lot	t_{60} (min)	P_{20} (%)	P_{30} (%)	k_0 (%/min)	k_e (min^{-1})	β	T_d (min)	t_L (min)	n
M	42.6	42.17	52.43	1.262	0.024	0.827	38.313	-3.160E-07	0.591
N (2001)	45.8	64.15	73.39	1.250	0.051	0.751	15.082	-5.920E-05	0.557
N (2003)	27.8	65.10	74.26	1.228	0.046	0.693	16.397	-6.326E-08	0.562
O (2004)	29.8	55.98	65.44	1.262	0.034	0.757	23.190	-4.989E-13	0.572
O (2005)	44.6	58.64	68.05	1.227	0.035	0.658	21.362	-6.620E-10	0.534

Table 5-9: Dissolution parameters for dissolution calibrator profiles.

The goodness-of-fit of the models applied was estimated by calculating the RSS of the predicted values versus the actual dissolution data as well as overlaying the values, Table 5-10 and Figure 5-12.

RSS	Exponential	Weibull	Korsmeyer-Peppas
M	1.15	0.40	1.66
N (2001)	9.67	0.50	1.53
N (2003)	1.98	0.89	1.86
O (2004)	1.62	0.43	1.64
O (2005)	1.83	0.88	1.61

Table 5-10: RSS values for calibrator dissolution profiles.

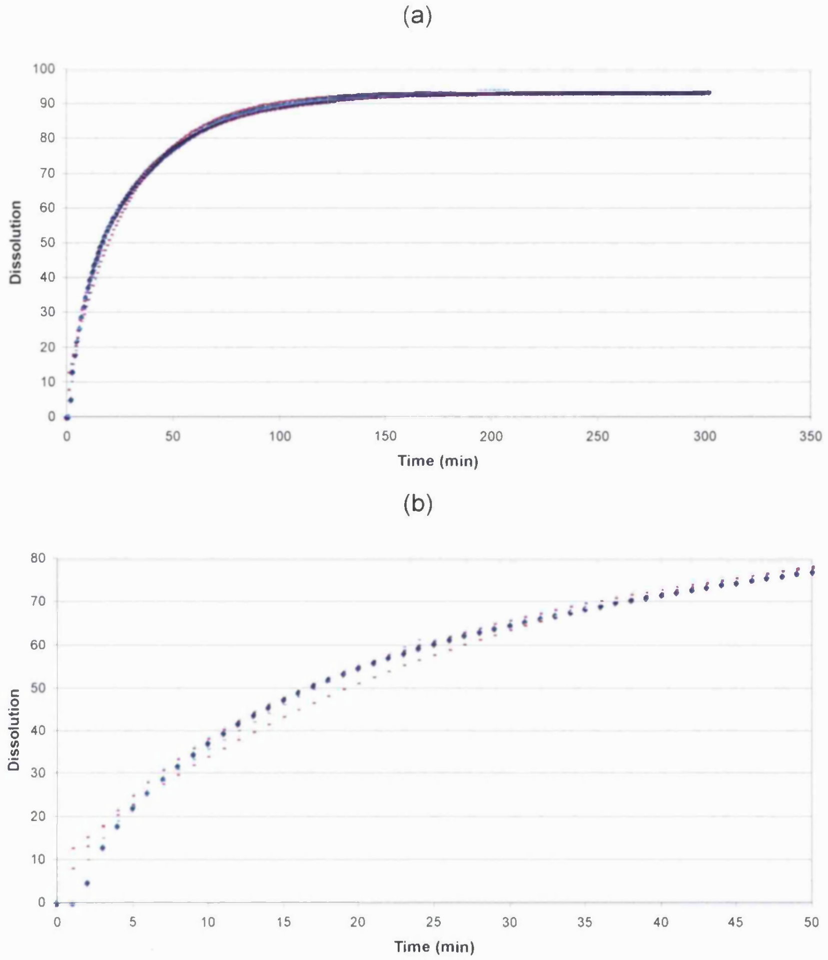

Figure 5-12: Overlay of actual dissolution profile with model values for lot O 2004 (a) full time range and (b) initial dissolution with (•) actual dissolution profile, (–) exponential, (–) Weibull and (–) Korsmeyer-Peppas model values.

In this case the best RSS values were observed for the Weibull model and as such these dissolution parameters were selected for continuation and the correlation to the imaging parameters in a subsequent chapter.

Accelerated Conditions

The six remaining lot N (2001) accelerated condition tablets were dissolved and the average profile is shown in Figure 5-13 compared to the average lot N (2001) profile before the heating were applied. It was decided to perform the dissolution on the tablets even though the probable cause of the differences seen in the imaging results was the melting of the stearic acid. Regardless of how they occurred, there were still differences between the calibrators before and after the heating was applied.

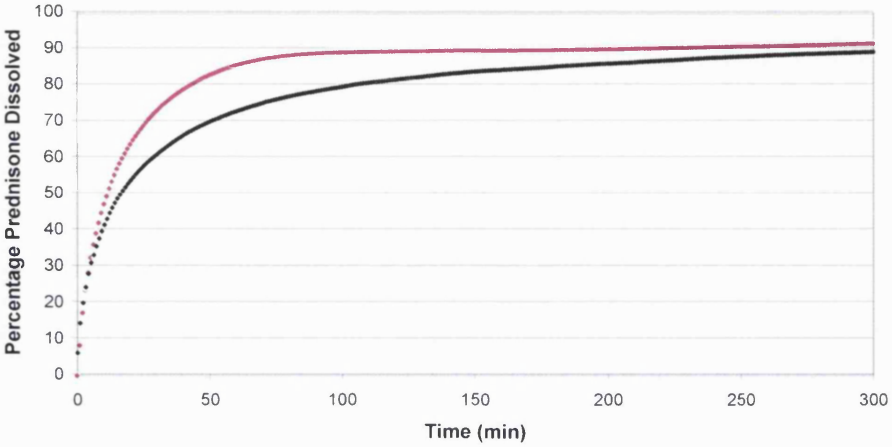

Figure 5-13: The average dissolution profiles for prednisone dissolution calibrators lot N (2001) (—) before and (—) after heating.

The average profile for the heated tablets had a much slower dissolution than those analysed before the accelerated conditions. The dissolution parameters were calculated for comparison.

Lot N (2001)	t_{60} (min)	P_{20} (%)	P_{30} (%)	k_0 (%/min)	k_e (min^{-1})	β	T_d (min)	t_L (min)	n
No heating	45.8	64.15	73.39	1.25	0.051	0.751	15.082	-5.920E-05	0.557
Heating	59.4	52.52	60.08	1.00	0.028	0.582	25.443	-2.539E-12	0.459

Table 5-11: Average dissolution parameters for average dissolution profiles from lot N (2001) before and after heating.

This comparison emphasised that the number and integration of stearic acid domains within the calibrator tablet matrix exerted a large influence upon the dissolution of the tablets, which was observed in the previous section 5.3.5. Here the increase of the stearic acid integration within the matrix caused a slowing in the dissolution rate, in a similar way as was observed for the blending study in the previous chapter.

5.4 Conclusion

The USP prednisone 10 mg dissolution calibrator tablets have acquired a bad reputation over the seven years they have been implemented with some users of dissolution testing, including the FDA, with regards to the variability of inter and intra lot performance. These variations are also known to occur over time i.e. the dissolution changes with the age of the tablet used (FDA, 2005). This chapter has shown examples of these variations between calibrator lots from the results of NIRS, NIRM imaging and dissolution testing.

Initially a comparison of the PCA results for the reflectance NIRS of all the available samples indicated that lot O showed the greatest variability, as the data points had the largest spread with regards to lot N and lot M. This finding was highlighted in the dissolution profiles whereby the two average lot N profiles practically overlaid, but the two from lot O did not.

Elucidation of the calibrator matrices by NIRM imaging uncovered changes in the diluent, DCP occurring with the age of the calibrator lot. Moving from the current lot O to the oldest lot M there was an increase in the number of domains accompanied by a decrease in the MED. It appeared that the DCP became more integrated within the matrix over time, which may have produced an effect in the dissolution as DCP is practically insoluble in water. This was not the case however as the average dissolution profiles did not follow any pattern with calibrator age. Re-evaluation of the imaging parameters revealed a probable relationship with the lubricant, stearic acid. The number of API domains provided a pattern analogous to the stearic acid and as such may have also had an influence on the profiles, but served mainly to distinguish lot M as different to the other two.

The relationship between the stearic acid component in the matrix and the dissolution was reiterated by the outcome of the heating study.

The main outcome from this study was the lack of a dissolution trend related to the age of the tablets, which was somewhat unexpected, even when there were variations present in the tablet matrices to this effect.

6 Dissolution Investigations Based on a "Real" Product

6.1 Introduction

In the USA it is the responsibility of the FDA to ensure that pharmaceutical companies conform to current good manufacturing practices (CGMPs). Audits and inspections of the companies manufacturing facilities are carried out for this purpose. If the case arises when there has been continual non-conformance observed in several of these audits regarding deficiencies in the CGMPs, then further action is taken. The company involved can enter into litigation or choose the option of a consent decree with the FDA. A consent decree includes solutions to correct the non-conformance and set up systems to prevent it occurring again. It is a means used by the FDA to try and bring the company up to the current standards as the company has to commit to performing any corrective actions required in a sensible timeframe throughout the length of the decree. It can be likened to a court order under which manufacturing and provision of the products can recommence under conditions closely monitored by the FDA. In 1993 Warner-Lambert entered into a consent decree with the FDA as a result of inspections at its two manufacturing plants in Puerto Rico. The decree was set to cover all the products manufactured at the sites. The production of certain drugs was authorised under the approval of the FDA as they were deemed medically necessary with no equivalent available elsewhere on the market. Included in the list was the product W.

From 1990 to 1992 there had been a total of seven recalls of Warner-Lambert products. After the consent decree was established, there was an increase in the number of recalls in the next few years, 24 in 1993, 13 in 1994 and 20 in 1995. The product W contributed to 12 of the total recalls between 1990 and 1995 and nine of these were the result of dissolution issues (Wolfe, 1995).

In 2000 Pfizer acquired Warner-Lambert along with the consent decree. It has been estimated that the changes implemented for compliance as a result of the decree has cost nearly one billion dollars from 1993 to 2002 (Chrai, 2004).

Product W continues to present dissolution issues and a great deal of work has been carried out within Pfizer and with external collaborations to gain a better product understanding. Identification of the critical-to-quality attributes for the products dissolution behaviour is the main aim of the investigations performed.

This chapter will examine product W and investigations on the factors affecting the resultant dissolution including variations in component age, blending time, compaction of blend into the capsules and interaction of particular components in the blend and show how changes seen in NIRM imaging results for certain components in the matrix can be correlated to variations in the dissolution profiles acquired.

6.2 Experimental

6.2.1 Materials

Product W is a five component capsule formulation. The API, lactose and sucrose make up the majority of the blend combined with magnesium stearate and talc as the minor, lubricating components, Table 6-1.

Component	% m/m in Formulation
API	43
Sucrose	25
Lactose Monohydrate (LM)	25
Magnesium stearate	4
Talc	3

Table 6-1: Approximate % m/m of components in W formulation.

The compliance specification for the dissolution testing of W is that the percentage of labelled amount of API is between 25% and 60% at 30 minutes and is not less than 70% in 120 minutes.

There have been a number of investigations where designs of experiments have been used to aid the investigation of changing certain process parameters in order to observe the subsequent dissolution effects induced. Three of these types of investigations will be included in this chapter accompanied by work carried out on an actual out-of-specification (OOS) dissolution issue experienced with product W at a foreign manufacturing site.

The samples for all of the studies performed on product W were provided by Pfizer, except for the three component study, where the blends were produced in the laboratory.

Aging Study

The age of the API and the lactose used in the production of the W capsule product was one of the parameters identified as a possibly contribution to the variable dissolution observed. Seven different runs were performed to produce capsules based on a partial factorial design. Limited samples of six of the W capsule runs were obtained consisting of filled capsules and excipient samples. Within the blends manufactured the age of the API, LM, magnesium stearate and empty capsules were varied i.e. they were classed as fresh or aged samples and the sucrose and talc were kept constant throughout all the blends, Table 6-2. There was no lot 6 provided.

Capsule Run	API	Magnesium stearate	Lactose	Empty Capsules	Dissolution Performance
1	Fresh	Fresh	Fresh	Fresh	Steady API release, but too fast to be in-specification
2	Aged	Aged	Aged	Aged	Acceptable
3	Fresh	Aged	Aged	Fresh	OOS > 90% at 30 minutes
4	Fresh	Fresh	Fresh	Aged	OOS > 90% at 30 minutes
5	Aged	Fresh	Fresh	Fresh	OOS > 90% at 30 minutes
7	Aged	Fresh	Aged	Aged	Acceptable

Table 6-2: Age of components used in W capsule runs for aging study.

Samples of each capsule run had been analysed using traditional, time point measurement dissolutions performed on them and the results of these were available for comparison.

Wafers of the blends after encapsulation were utilised for the NIRM imaging analysis, which had been made using a punch and dye system and compression with a hydraulic press at 2000 psi for three seconds on blend emptied out of the capsules.

Two Component Study

Another one of the parameters identified by internal investigation within Pfizer as a possible influence to the variable dissolution observed was the degree of mixing associated with the API and the magnesium stearate. This came after the results of a previous study that examined the effects of blending time and milling (particle size distribution) of the API on the dissolution showed that the longer the blending time, the more the magnesium stearate was incorporated into the blend and the slower the dissolution and also that milling gave the opposite effect. As a feasibility step before a major investigation into a fuller examination of the influence of API particle size and distribution, combined with an investigation into the role of magnesium stearate, small laboratory scale binary blends of these two components were produced for dissolution, NIRS and NIRM imaging. There were nine different blends received in total containing 96% m/m API and 4% m/m magnesium stearate. Each blend had been blended for ten minutes in a laboratory scale V-blender then some were transferred to a Turbula blender (Glen Mills, NJ, USA) and blended further to introduce more shear force in the blending thought to be required for the magnesium stearate to coat the API. The compression used to manually force the blend into the capsule shells was also varied.

Run	Compression	Turbula (hours)
1	None	0
2	Mild	0
3	Hard	0
4	None	1
5	Mild	1
6	Hard	1
7	None	10
8	Mild	10
9	Hard	10

Table 6-3: Manufacturing variations applied to the two component binary blends based on W.

There were only filled capsules available for analysis and as for the aging study samples, the contents were pressed into wafers for the NIRM imaging analysis.

Three Component Study

Following on from the two component and the aging studies, it was noted that the sucrose component may also be contributing to the dissolution variation. Blends containing API (50% m/m), magnesium stearate (4% m/m) and either sucrose or lactose (46% m/m) were prepared with blending times of 7, 15, 30, 45 (production blending time) and 60 minutes using a Turbula blender at 46 rpm. Five wafers were produced for each of the ten blends for NIRM imaging by the same method as described in the aging study. Capsules of the blends were prepared using a manual capsule filler for dissolution along with wafers.

Actual Dissolution Performance Study

An issue arose at a Pfizer site where they had experienced dissolution of W that was not meeting specification. A certain lot of the product was dissolving too rapidly giving 98% at the 30 minute time point when the value should be between 25% and 60%. The issue was thought to be related to the API granule size as remilling and blending the problem lot resulted in a subsequent pass in the dissolution test. Samples of the problem blend before and after the re-working along with a blend that gave satisfactory dissolution performance, were available for analysis. Five wafers of each blend lot were made into wafers for the NIRM imaging and dissolution, as no capsules were available.

6.2.2 Near-infrared Spectroscopic Analysis

There were limited capsule samples available for the aging and two component studies, which were insufficient in number to permit NIRS analysis of the contents in reflectance or transmission (the wafers produced were too thin). Reflectance NIRS had been performed on the aging blend samples before and after encapsulation in the full design of experiment (DOE) study undertaken by Pfizer, to which this work was performed as an addition. The findings of the NIRS for aging study will be summarised as they showed trends with the dissolution performance.

Reflectance NIRS

The eight wafers made from the three component blends for dissolution were scanned using the Foss NIRSystems 6500 monochromator (Foss NIRSystems Inc., Silver Springs, MD, USA) with a Rapid Content Analyser attachment, shown in section 5.2.2. Each wafer was placed on the sample window, positioned using the centring mechanism then the lid was closed and the sample scanned. Three replicates were performed per wafer.

Transmission NIRS

Wafers from the three component and actual dissolution performance studies were analysed using the Foss NIRSystems 6500 monochromator (Foss NIRSystems Inc., Silver Springs, MD, USA) with an InTact tablet transmission analyser, shown in section 3.2.3. A customised sample holder was used to ensure reproducible measurements of the wafers. Three replicates were performed for each wafer, with the sample being turned over between measurements. The average of the spectra was used over the range 850 - 1450 nm.

Both of the Foss instruments used passed all the manufacturer's performance tests including wavelength accuracy, photometric noise and accuracy and repeatability and were therefore considered to be operating correctly.

6.2.3 Near-infrared Microscopy Imaging

Spectrum Spotlight 350-Line Mapping

The wafers produced for all four studies were analysed on the Spotlight. An area of 5 x 5 mm was scanned for each of the blend wafers and an area of 1 x 1 mm was scanned on wafers made of the pure excipients and API for the library images.

The processing varied slightly between the studies for the Spotlight data, which is summarised in Table 6-4. In all cases the files from the Spotlight (.fsm) were converted into a format (.spc) that could be recognised by the image analysis software, ISys.

The explanation and method for the pixel selection can be found in section 2.1.2. In each case the components used in the complementary library file reflected the components present in each blend i.e. all five components for the actual dissolution and aging study, API and magnesium stearate for the two component study then API, magnesium stearate and lactose/sucrose for the three component study.

Study	Final Pre-Processing	Selection Method of Pixel Distribution	Contour Value
Aging	Second derivative, filter length 11, filter order 3	% Pixels	Lower limit of selected region
2 Component	Normalisation	Area selection	MSV of selected region
3 Component	Normalisation	Area selection	MSV of selected region
Actual Dissolution	Second derivative, filter length 11, filter order 3	% Pixels	MSV of selected region

Table 6-4: Summary of the data processing for the Spotlight results.

6.2.4 Dissolution

The dissolution apparatus was the same as for section 4.2.4 for the dissolution of the wafers produced from the three component and actual dissolution studies with USP apparatus 1 (baskets) used for dissolving the capsules from the aging, two and three component studies. The USP apparatus 2 (paddles) was used for the wafers from the three component and actual dissolution studies. The dissolution medium was 900 ml of pre-warmed, degassed water. The paddles or baskets were positioned at 25 mm ± 2 mm from the base of the vessel at 50 rpm. Table 6-5 shows the dissolution parameters used. The API was monitored at 254 nm using 300 nm as the baseline correction wavelength and a pathlength of ten mm. A coil of stainless steel wire was required as a sinker for the capsules, as without this they floated up to the top of the basket when immersed in the dissolution medium and did not dissolve.

Study	Vessels Used	Measurement Interval (sec)
Aging	3	30
Two Component	3	30
Three Component	8	80
Actual Dissolution	5	50

Table 6-5: Dissolution parameters for W blends.

Fewer vessels were utilised for the aging and two component studies as the available number of samples was very limited, in some instances there were only three capsules. A standard solution of the API was used to give an absorbance value equivalent to 100% of dissolved API. The amount of API was calculated for each wafer/capsule from the mass and the % m/m used in the blend, which was used to correct for any differences between samples on the conversion to percentage (%) API dissolved.

6.3 Results and Discussion

The results from all the methods used will be discussed together in four sections relating to the four studies performed.

6.3.1 Aging Study

Reflectance NIRS

There was a full study performed internally at Pfizer on runs 1 to 7 in the aging study[1] and it was determined from the NIRS reflectance results that runs two and seven, acceptable dissolution, were different from the remaining runs analysed in the pre-encapsulated blends. This was observed as a mean particle size difference which resulted in an offset in the raw spectra of run two and seven from the others, Figure 6-1(a) and then at six different wavelength positions in the second derivative spectra related to the API (2078 nm) and sucrose (1672, 1984 and 2106 nm) where these offsets were again apparent, Figure 6-1(b). The API signal was weaker and the sucrose was stronger in the runs with acceptable dissolution compared to those which were OOS (Parnell and Clarke, 2005). This pointed to the API and the sucrose as having the main influence on the dissolution.

The blends from inside the capsules were also analysed which found that the encapsulation process caused an increase in the moisture content compared to the pre-encapsulated blends. This moisture increase masked any spectral variations that were observed between the blends for the different capsule runs prior to the processing.

---

[1] There were no samples provided for run 6.

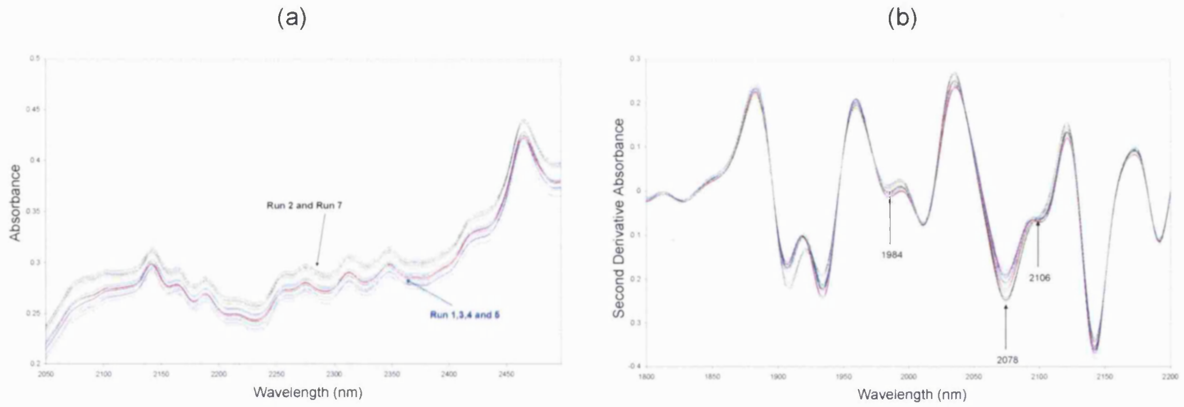

Figure 6-1: Reflectance NIRS of runs one to seven showing (a) the offset related to mean particle size in the raw spectra and (b) some of the differences observed in the second derivative spectra for the pre-encapsulation blends with run 1 (—), run 2 (—), run 3 (—), run 4 (—), run 5 (—) and run 7 (—).

Spectrum Spotlight 350-Line Mapping

NIRM imaging was performed on wafers of the blends made from the contents of the capsules available for analysis for runs one to seven and the data were processed as outlined in 6.2.3. A visual comparison of the RGB images highlighted an obvious difference between the capsule runs. This was not affected by the apparent water uptake during the process of encapsulation found to mask any differences in the NIRS results as imaging does not rely on the mean response, but rather the discrete responses from individual regions.

Large clumps of sucrose were observed in the runs classed with very rapid dissolution e.g. run one, three, four and five whereas the two runs with acceptable dissolution (runs two and seven) did not contain these lumps. Figure 6-2 shows examples of run seven (a) and run three (b).

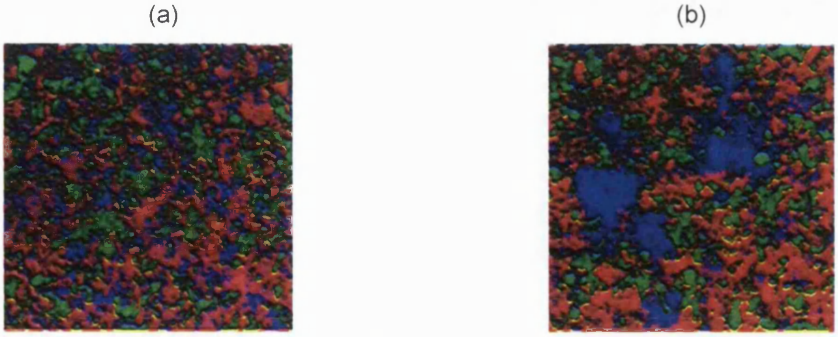

Figure 6-2: RGB images for (a) run seven and (b) run three for aging study blends with API (—), sucrose (—) and lactose (—).

A further comparison of the images in Figure 6-2 revealed a less pronounced variation in the API component. The API domains in run three RGB image appeared to be larger than those present in the run seven image. Following the results for the NIRS for the pre-encapsulated blends, both the sucrose and the API would be predicted to differ between the specified runs, which seemed to be apparent from the RGBs alone. The sample and domain statistics were calculated for all the runs and are given in Table 6-6. As would be expected from the RGB images, the majority of the statistics for the sucrose component showed a trend with the dissolution performance denoted in Table 6-2, whereby the values for run three, four and five were similar to each other but different from the others. Run two and seven were also similar in value to one another and run one sat somewhere between the two groupings but had a bias towards the group with the rapid dissolution rate in some cases. The number of sucrose domains decreased from ~700 for run two and seven to ~500 for the three OOS runs, along with an increase in the MED from ~110 μm to ~130 μm respectively. The values for the domain statistics and the % STD for the API also followed the same trend, where the number of domains decreased from the acceptable to the OOS runs, ~300 to ~260 respectively, accompanied with an increase in the MED from ~220 μm to ~240 μm respectively. This again would have been expected from the RGB comparison. It seemed that an increase in the mean domain size of sucrose and/or the API was related to an increase in the dissolution rate of the sample.

The statistics for the minor components did not mirror those seen for the sucrose and API, but the same trend was observed in the values of the skew for the third major component, lactose. The decrease in the skew value from runs two and seven to one then three, four and five would relate to a decrease in pixels with higher score values in the images i.e. those relating to central areas within domains. This could have been interpreted as the lactose becoming more homogenously blended in the matrices of the samples with faster dissolution. This was not apparent from the RGB images.

Component	MSV	% STD	Skew	Kurtosis	Number of Domains	MED (µm)	NN (µm)
API Run 2	0.391	16.191	-0.009	0.070	303.8	219.0	8.6
API Run 7	0.397	15.749	-0.054	0.230	306.2	216.0	8.4
API Run 1	0.366	16.960	-0.212	0.427	301.0	219.0	8.6
API Run 3	0.408	18.976	-0.306	0.285	262.0	233.0	9.1
API Run 4	0.394	17.706	0.018	0.397	279.2	227.5	8.8
API Run 5	0.396	18.340	-0.277	0.540	255.8	236.0	9.3
Sucrose Run 2	0.392	12.900	0.518	1.401	740.2	110.0	6.0
Sucrose Run 7	0.402	12.890	0.609	1.977	679.4	109.5	6.0
Sucrose Run 1	0.399	16.751	1.323	4.240	616.8	114.5	6.3
Sucrose Run 3	0.399	19.904	1.640	5.000	501.4	127.5	6.7
Sucrose Run 4	0.377	19.266	1.460	4.180	519.0	127.5	6.7
Sucrose Run 5	0.384	19.382	1.446	4.060	513.8	126.0	6.7
Lactose Run 2	0.155	40.913	0.670	0.433	411.4	142.0	7.9
Lactose Run 7	0.158	37.574	0.660	0.522	428.0	138.0	7.8
Lactose Run 1	0.267	25.154	0.486	0.941	413.0	142.0	7.9
Lactose Run 3	0.207	33.157	0.284	0.443	363.0	156.0	8.3
Lactose Run 4	0.210	28.922	0.293	0.591	422.0	140.0	7.8
Lactose Run 5	0.218	29.471	0.267	0.713	396.2	143.0	8.0
Talc Run 2	0.038	21.087	-0.109	0.125	790.6	36.0	5.1
Talc Run 7	0.038	20.679	-0.095	0.290	694.4	35.5	5.5
Talc Run 1	0.036	21.403	-0.099	0.237	737.0	35.0	5.4
Talc Run 3	0.037	23.695	-0.154	0.121	662.8	36.5	5.4
Talc Run 4	0.037	22.022	-0.151	0.160	732.8	35.5	5.4
Talc Run 5	0.036	22.424	-0.244	0.353	736.4	35.0	5.4
magst Run 2	0.054	32.597	0.043	0.715	1128.8	34.5	4.6
magst Run 7	0.053	30.854	0.017	0.193	1201.2	32.5	4.4
magst Run 1	0.062	28.630	-0.042	0.636	1154.2	33.5	4.5
magst Run 3	0.058	25.234	-0.029	0.129	1137.0	33.5	4.5
magst Run 4	0.056	30.110	-0.001	0.478	1158.6	33.5	4.5
magst Run 5	0.054	32.802	-0.096	0.224	1104.0	35.0	4.6

Table 6-6: Sample and domain statistics for the aging study blends.

Dissolution Profiles

The available filled capsule samples for the six runs were dissolved using USP apparatus 1 and the conditions specified in section 6.2.4. The subsequent absorbance vs. time profiles were converted into % API dissolved vs. time and the average profiles are given in Figure 6-3.

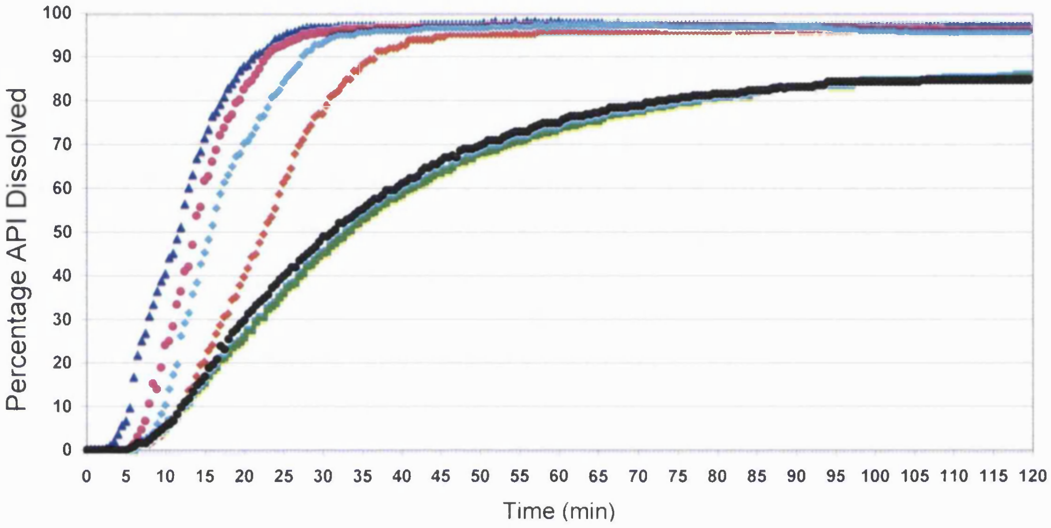

Figure 6-3: Average dissolution profiles for capsule runs 1 to 7 for the aging study with run 1 (◆), run 2 (■), run 3 (▲), run 4 (●), run 5 (●), run 7 (●).

The profiles fit the description of the dissolution performance for the particular capsule runs and the results from the fibre-optic (FO) dissolution monitoring corresponded well to those produced from the traditional (T) time point evaluation of the test, Table 6-7. The largest differences were seen for run two and seven at the 60 minute measurement point.

Run		% API at 30 min	% API at 60 min	% API at 120 min
1	T	76	94	97
	FO	77	96	96
2	T	41	63	79
	FO	45	74	86
3	T	96	99	99
	FO	97	98	98
4	T	91	94	95
	FO	96	97	97
5	T	92	96	97
	FO	93	98	98
7	T	43	65	82
	FO	49	75	85

Table 6-7: Fibre-optic (FO) dissolution results compared to the traditional time point measurements (T) for aging study capsule runs.

The sucrose used in the blends was kept consistent through all the capsule runs, but there were obvious differences in its interactions with the other variations in components observed in the RGB images and statistics. It can play the role of the binder or a diluent in a formulation. The type of sucrose used was confectioner's sugar, which is a very fine grade of the material with a mean particle size of ~7 µm which is known to act as a cohesive solid in contrast to its free flowing crystalline counterpart. The runs with rapid dissolution could have been the result of the large domains of sucrose present in the blend, which in turn lead to insufficient blending of the API causing the increase in domain size and subsequent dissolution rate as more API was available at any given time once the capsule dissolved.

The dissolution parameters were calculated for the average profiles as discussed in section 2.2.2 and shown in Table 6-8.

Aging Study	t_{80} (min)	P_{15} (%)	k_0 (%/min)	k_e (min^{-1})	β	T_d (min)	t_L (min)	n
Run 2	73.90	15.68	1.988	0.028	1.32	31.31	4.99	1.348
Run 7	69.69	16.85	2.166	0.031	1.31	29.10	4.99	1.316
Run 1	30.65	20.84	4.023	0.048	2.35	21.40	3.39	2.265
Run 3	16.82	71.68	4.876	0.095	2.11	13.29	-9.58E-16	1.728
Run 4	18.19	62.32	6.244	0.081	1.90	10.85	4.49	2.682
Run 5	22.39	45.53	6.182	0.070	1.80	12.60	5.49	2.858

Table 6-8: Dissolution parameters for aging study capsule runs.

The values of dissolution parameters relating to t_{80}, P_{15} and T_d followed the pattern seen in the profiles as would be expected. The parameters related to the rate also showed their values to group into runs two and seven, then three, four and five, with run one sitting somewhere in between.

The variations observed in the NIRM images and the dissolution appeared to have been the result of differences in the association of the other components, both aged and fresh, with the constant component of sucrose causing large lumps in certain cases. In runs two and seven, the majority of the blend comprised aged components and the sucrose formed the large domains. However, run one comprised fresh components combined with the sucrose and there were still the presence of some larger domains. There was no clear distinction as to whether the age of the components was directly affecting the dissolution or the images.

The fit of the models applied to the data was tested by calculation of the RSS for the predicted values compared tob the actual dissolution values used, see Table 6-9 and Figure 6-4.

RSS	Exponential	Weibull	Korsmeyer-Peppas
Run 2	2.41	0.77	2.46
Run 7	3.19	0.89	3.25
Run 1	124.76	0.49	1.77
Run 3	4.66	0.86	3.59
Run 4	6.91	0.39	2.02
Run 5	7.34	1.04	2.59

Table 6-9: RSS values for aging study dissolution profiles.

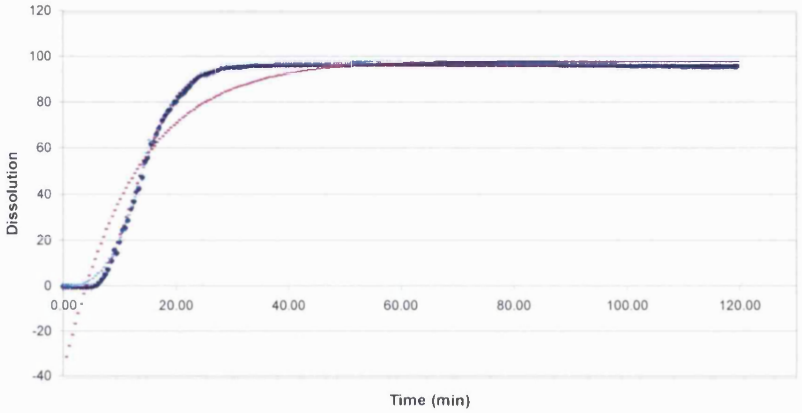

Figure 6-4: Overlay of actual dissolution profile and model values for run 4 with (♦) actual dissolution profile, (–) exponential, (–) Weibull and (–) Korsmeyer-Peppas model values.

The values for the Weibull model results gave the lowest calculated RSS and as such only these model parameters provided the best fit to the data. Hence, these values were selected for the correlation to the imaging parameters along with the initial rate and single point values in chapter 7.

6.3.2 Two Component Study

There were insufficient capsule samples available to permit the NIRS analysis of the encapsulated blends for the two component study and the blend wafers produced were not of an inadequate thickness to allow transmission or reflectance measurements to be taken.

The imaging and dissolution results were sorted and grouped in terms of blending time to show the effect of the compression applied during capsule filling and *vice versa*.

6.3.3 Blending Order

Spectrum Spotlight 350-Line Mapping

The wafers made from the contents of the different capsule samples available were scanned on the Spotlight. Unlike the previous aging study, the processing for the two component images was terminated at the normalisation step due to samples consisting of only two components of the five components, which did not possess similar spectra.

The results for the capsule runs were grouped as shown in Table 6-3 in order to show the effect of the compression used for each of the three blending times.

The RGB images for the blend with no Turbula use did not show any obvious changes with increased compression, although the blends with one and ten hours showed an increase and a decrease in the number of magnesium stearate domains, respectively, Figure 6-5.

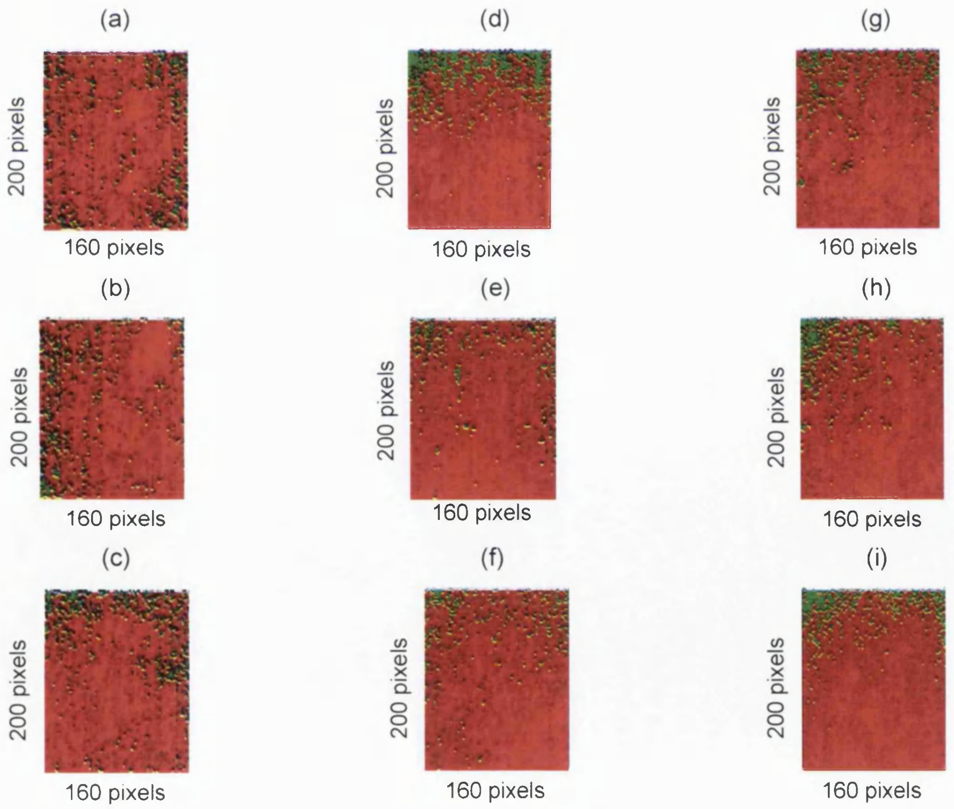

Figure 6-5: RGB images for two component study in Turbula blending order: no Turbula with (a) no to (c) hard compression, one hour Turbula with (d) no to (f) hard compression and ten hours Turbula with (g) no to (i) hard compression with API (—) and magnesium stearate (—).

The sample and domain statistics for the images were determined for the two components, Table 6-10 and Table 6-11. The samples without the extra Turbula blending (runs 1 – 3) showed a small increase in the MSV for the API with increased compression. The number of domains of API for the samples with mild compression had the highest value, 135, with similar values for the other two, ~115, which was reflected in an opposite trend for the MED values. The samples which were exposed to an additional one hour of Turbula blending (runs 4 – 6) showed the % STD to decrease slightly, the number of domains increased and the MED decreased with compression applied. The ten hour blended samples (runs 7 – 9) showed a similar trend to the one hour API domain results, but in this case there was the opposite effect of a decrease in domains, with an increase in size, Table 6-10.

The magnesium stearate results for the samples without the extra Turbula blending (runs 1 – 3) showed a slight increase in the MSV, as was seen for the API and the % STD decreased with compression. The number of magnesium stearate domains also decreased, but the size remained constant. The one hour Turbula blended samples (runs 4 – 6) gave an increase in the number of magnesium stearate domains from no compression to mild, which then stayed at a similar value for the hard compression sample. The MED however showed a decrease in domain size with increase in compression. The samples with an extra ten hours blending (runs 7 – 9) presented the same trend as the one hour samples for the number of magnesium stearate domains, but in reverse, i.e. a decrease in number from no compression to mild compression with a similar value for hard compression and a consistent increase in the MED, Table 6-11.

The change in compression appeared to cause a decrease in the magnesium stearate domains in the samples with no extra Turbula blending. It seemed to result in the formation of smaller domains of both components for the one hour blending time samples then bring about the opposite effect on the ten hour blending time samples.

API	MSV	% STD	Skew	Kurtosis	Number of Domains	MED (µm)	NN (µm)
Run 1	0.886	12.750	0.050	0.048	115.0	165.0	6.5
Run 2	0.877	1.379	0.172	0.234	135.0	155.0	5.7
Run 3	0.871	1.339	-1537.000	0.080	118.0	165.0	6.2
Run 4	0.888	1.953	-0.243	-0.248	84.0	197.5	5.6
Run 5	0.827	1.732	0.011	0.000	125.0	157.5	5.4
Run 6	0.866	1.540	-0.008	-0.078	139.0	150.0	5.2
Run 7	0.891	1.449	-0.128	0.024	108.0	172.5	5.6
Run 8	0.869	1.531	-0.357	0.259	94.0	185.0	6.0
Run 9	0.880	1.791	-0.367	-0.112	92.0	187.5	5.8

Table 6-10: Average sample and domain statistics for the two component study in order of blending time for API.

Magnesium stearate	MSV	%STD	Skew	Kurtosis	Number of Domains	MED (µm)	NN (µm)
Run 1	0.118	10.754	-0.179	0.101	98.0	37.5	7.3
Run 2	0.126	10.467	-0.298	0.286	93.0	37.5	7.0
Run 3	0.131	9.367	-0.047	0.163	82.0	37.5	7.1
Run 4	0.117	14.140	0.042	-0.038	62.0	47.5	4.9
Run 5	0.169	7.991	0.001	0.169	84.0	40.0	7.1
Run 6	0.139	9.134	0.010	0.048	81.0	37.5	6.5
Run 7	0.116	11.549	0.012	0.072	75.0	40.0	5.9
Run 8	0.136	9.419	0.124	0.199	47.0	50.0	8.0
Run 9	0.126	11.967	0.166	0.013	48.0	52.5	5.2

Table 6-11: Average sample and domain statistics for the two component study in order of blending time for magnesium stearate.

Dissolution Profiles

The remaining capsules from each of the nine runs were dissolved using USP apparatus 1 and the conditions specified in section 6.2.4. The average % dissolved vs. time profiles are shown in Figure 6-6. The dissolution for all the capsules was very rapid with the majority of the samples being completely dissolved by about ten minutes, which would have been related to the lack of diluents and binders in the blend that would have served to extend the API release.

The profile for the samples with no extra blending and hard compression appeared to commence dissolution just before the others, which gave very similar profiles, Figure

6-6(a). It had been noted that the run three capsules were observed to contain more of an air space above the compacted blend than for run two, which may have been the result of the larger half of the capsule not having been fixed onto the other half with sufficient force. This could have allowed the capsule to dissolve slightly quicker or even burst and hence the onset of dissolution would occur rapidly.

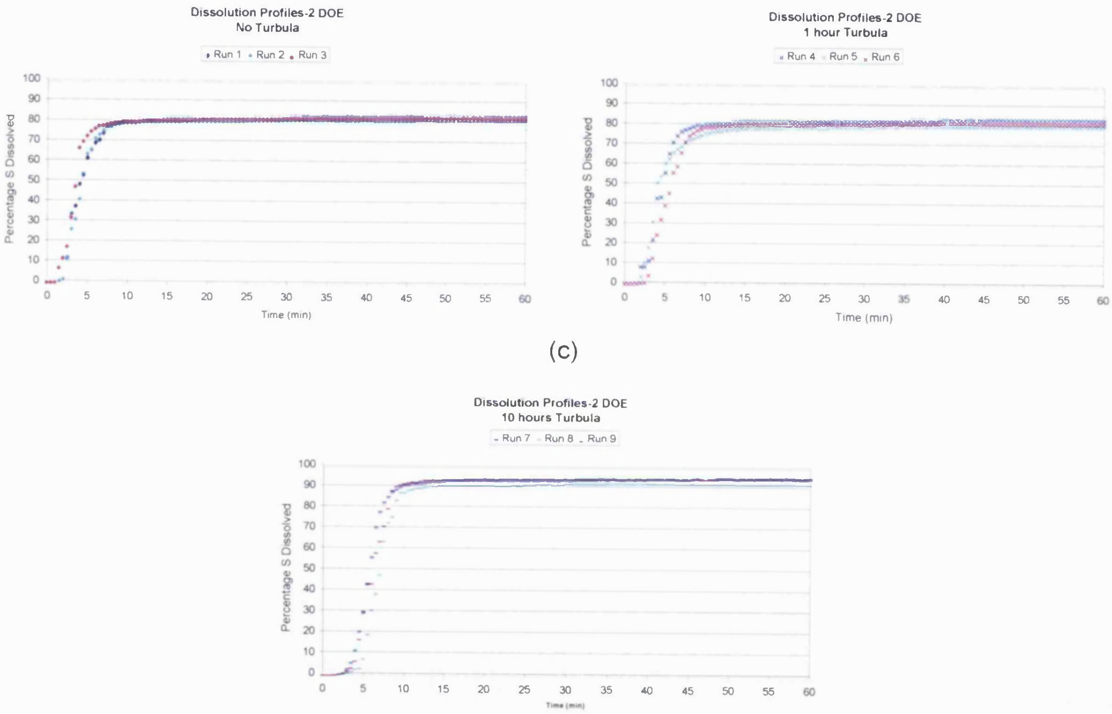
(a)

(b)

(c)

Figure 6-6: Average dissolution profiles for the two component study in order of blending time with no (—), mild (—) and hard (—) compression.

The average dissolution profiles did not always reach 100% dissolved API, which would have mainly been due to the fact that the capsules provided were the product of a small laboratory scale DOE. The blending scale used could have experienced variation in the API uniformity; hence each capsule may not have had the exact % API as expected and hence provided a variation in the dissolution results.

The profiles produced for runs four to six showed the onset of dissolution in compression order, but the remainder of the profiles were very similar although the hard compression profile did appear slightly slower than the other two, Figure 6-6(b). The samples with the maximum Turbula blending again gave similar profiles, but in this case the capsules with mild compression had a slightly longer onset than the other two, but in terms of time this only related to approximately one minute difference, Figure 6-6(c). Overall the compression applied to the blend when filling the capsules did not give any significant changes in the dissolution behaviour for each of the different blending times utilised. The results may have been different if the full blend formulation was used as other components that were absent in the samples for this study may have had an increased reaction to the compression, e.g. the confectioner sugar which is a cohesive solid.

The dissolution parameters were calculated for the average profiles as discussed in section 2.2.2 and are shown in Table 6-12. The lag time was not included in the calculations.

Two Component Study	t_{45} **(min)**	P_5 **(%)**	k_0 **(%/min)**	k_e **(min^{-1})**	β	T_d **(min)**	t_L **(min)**	n
Run 1	3.75	61.43	24.025	0.266	1.349	2.95	1.5	1.952
Run 2	4.10	63.50	19.761	0.273	1.748	3.45	1.0	2.310
Run 3	3.25	72.90	27.875	0.323	1.694	2.69	1.0	2.583
Run 4	4.50	55.70	22.092	0.250	1.997	3.41	1.4	2.309
Run 5	3.75	60.29	21.680	0.255	1.385	3.11	1.5	2.296
Run 6	5.50	39.66	18.014	0.211	2.414	4.84	1.0	2.136
Run 7	5.40	29.57	24.674	0.198	2.671	4.18	2.0	3.830
Run 8	6.60	7.34	19.905	0.168	3.443	5.38	2.0	4.240
Run 9	5.50	30.72	16.373	0.187	3.095	5.69	1.0	4.412

Table 6-12: Dissolution parameters for two component study in order of blending time.

The fit of the models applied to the data was tested by calculation of the RSS for the predicted values compared to the actual dissolution values used.

The values for the Weibull model results gave the lowest calculated RSS and as such only these model parameters provided the best fit to the data. Hence, these values were selected for the correlation to the imaging parameters along with the initial rate and single point values, see Table 6-13 and Figure 6-7.

RSS	Exponential	Weibull	Korsmeyer-Peppas
Run 1	6.66	1.11	6.07
Run 2	4.79	0.98	3.66
Run 3	17.45	1.21	1.47
Run 4	6.80	1.11	8.82
Run 5	6.23	1.31	4.82
Run 6	4.85	0.91	4.41
Run 7	10.95	0.90	1.31
Run 8	10.15	0.79	2.55
Run 9	6.45	0.89	6.18

Table 6-13: RSS values for two component study dissolution profiles.

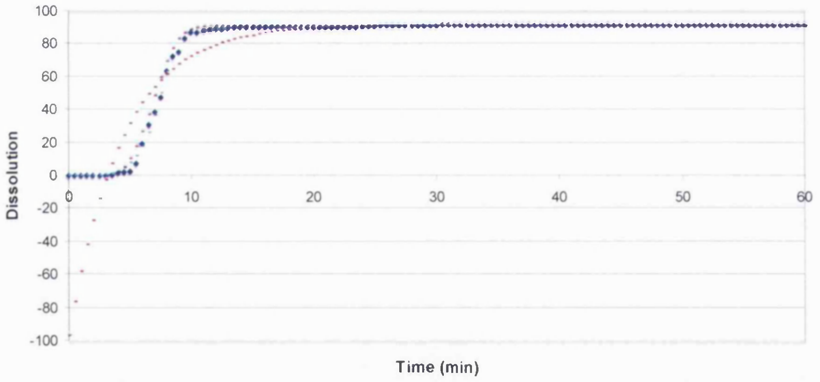

Figure 6-7: Overlay of actual dissolution profile and model values for run 8 with (•) actual dissolution profile, (–) exponential, (–) Weibull and (–) Korsmeyer-Peppas model values.

6.3.4 Compression Order

Spectrum Spotlight 350-Line Mapping

The results for the capsule runs were re-grouped in order to show the effect of the extra blending time used for each of the three compressions applied in the production of all the capsules.

Figure 6-5 showed the RGB images for all the runs. Looking across the rows, e.g. Figure 6-5(a) no extra blending to (g) ten hours in the Turbula for the blends with no compression, illustrated any differences induced by the different Turbula blending times utilised.

A visual comparison of the RGB images for the mild and hard compression appeared to show an increase in the size of the magnesium stearate domains with the increase in blending time used, Figure 6-5(b) to (h) and Figure 6-5(c) to (i) respectively. The samples that had no compression applied to the blend, showed the domain size of magnesium stearate increase with the one hour Turbula blending, Figure 6-5(d) then decrease again after ten hours blending, Figure 6-5(g).

The sample statistics from the pixel distributions and the domain statistics from the areas of the components were calculated and shown in Table 6-14 and Table 6-15. The API domains only appeared to give a trend with the blending for the mild compression images showing an increase in domain size with the accompanying decrease in the number viewed. The patterns observed in the values for the API domains in the samples with no and hard compression were similar but the opposite of each other i.e. the number went down from no to one hour blending then increased again in the ten hour blend for the samples with no compression and the hard compression values went up to the one hour then down again to the ten hour.

API	MSV	%STD	Skew	Kurtosis	Number of Domains	MED (µm)	NN (µm)
Run 1	0.886	12.750	0.050	0.048	115.0	165.0	6.5
Run 4	0.888	1.953	-0.243	-0.248	84.0	197.5	5.6
Run 7	0.891	1.449	-0.128	0.024	108.0	172.5	5.6
Run 2	0.877	1.379	0.172	0.234	135.0	155.0	5.7
Run 5	0.827	1.732	0.011	0.000	125.0	157.5	5.4
Run 8	0.869	1.531	-0.357	0.259	94.0	185.0	6.0
Run 3	0.871	1.339	-1537.000	0.080	118.0	165.0	6.2
Run 6	0.866	1.540	-0.008	-0.078	139.0	150.0	5.2
Run 9	0.880	1.791	-0.367	-0.112	92.0	187.5	5.8

Table 6-14: Average sample and domain statistics for the two component study in order of compression for API.

Magnesium stearate	MSV	%STD	Skew	Kurtosis	Number of Domains	MED (µm)	NN (µm)
Run 1	0.118	10.754	-0.179	0.101	98.0	37.5	7.3
Run 4	0.117	14.140	0.042	-0.038	62.0	47.5	4.9
Run 7	0.116	11.549	0.012	0.072	75.0	40.0	5.9
Run 2	0.126	10.467	-0.298	0.286	93.0	37.5	7.0
Run 5	0.169	7.991	0.001	0.169	84.0	40.0	7.1
Run 8	0.136	9.419	0.124	0.199	47.0	50.0	8.0
Run 3	0.131	9.367	-0.047	0.163	82.0	37.5	7.1
Run 6	0.139	9.134	0.010	0.048	81.0	37.5	6.5
Run 9	0.126	11.967	0.166	0.013	48.0	52.5	5.2

Table 6-15: Average sample and domain statistics for the two component study in order of compression for magnesium stearate.

The number and MED of the magnesium stearate domains for the mild and hard compression samples supported the visual results from the RGB images, where there was an increase in size and decrease in number upon going from no Turbula blending to ten hours in the blender. This was also the case for the samples with no compression where the largest domains of magnesium stearate were present in the one hour blend.

Overall an increase in the extra Turbula blending from none to ten hours caused an increase in size of the magnesium stearate domains with a decrease in the number of domains present in the samples with mild and hard compression. The samples with no compression however had the largest domains in the one hour Turbula blend for both the magnesium stearate and API and the opposite effect was seen for the API in the hard compression samples.

Dissolution Profiles

The average % dissolved vs. time profiles were re-ordered for compression and are given in Figure 6-8.

The profiles viewed in compression order showed more variation with blending than when they were arranged in order of blending time. The samples with no compression applied seemed to show a dissolution order that matched with the increase in the blending time, Figure 6-8(a). The profiles for the mild compression wafers demonstrated an increase in the lag time for run 8, with ten hours blending and the other two profiles overlaid each other Figure 6-8(b). Finally run three, no blending, from the hard compression samples started dissolving first followed by the other two runs, which had similar lag times and profiles Figure 6-8(c).

The dissolution parameters were re-arranged for the average profiles into the compression order and are shown in Table 6-16 with the exponential and Korsmeyer-Peppas values removed as they had been shown to be a poor fit to the data.

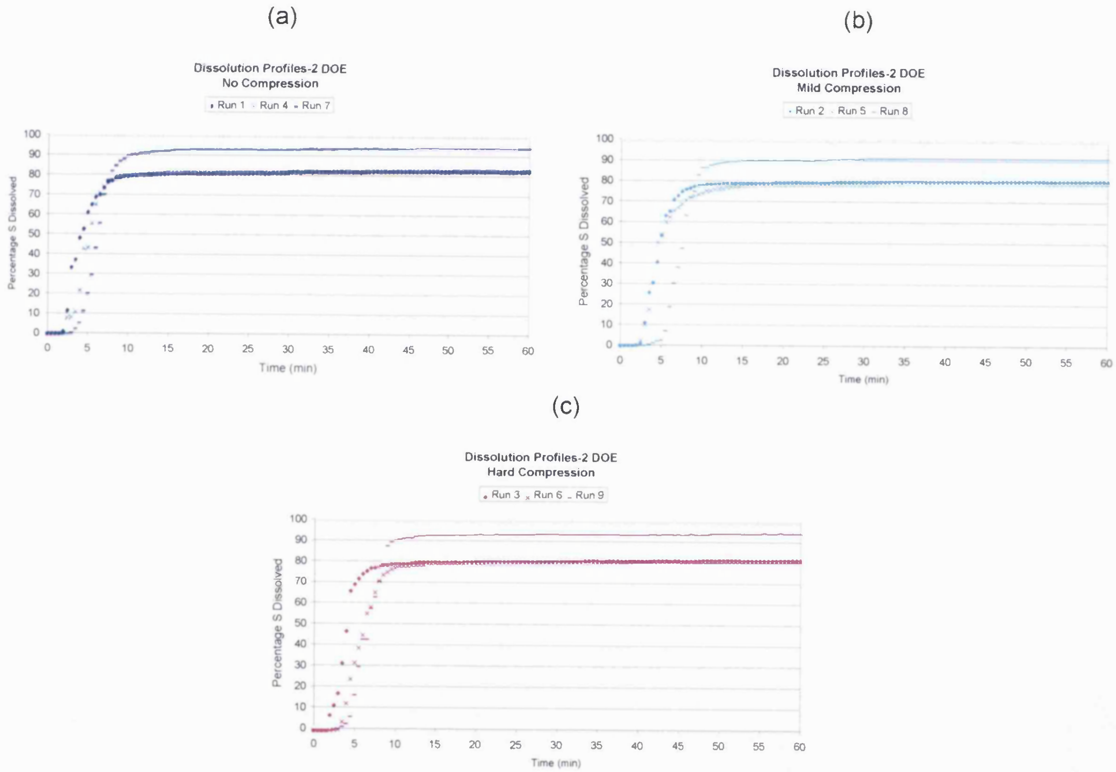
(a)

(b)

(c)

Figure 6-8: Average dissolution profiles for the two component study in order of compression with no (•), one hour (x) and ten hours (-) Turbula blending for (a) no compression, (b) mild compression and (c) hard compression.

Two Component Study	t_{45} (min)	P_5 (%)	k_0 (%/min)	β	T_d (min)	t_L (min)
Run 1	3.75	61.43	24.025	1.349	2.954	1.50
Run 4	4.50	55.70	22.092	1.997	3.405	1.42
Run 7	5.40	29.57	24.674	2.671	4.181	2.00
Run 2	4.10	63.50	19.761	1.748	3.454	1.00
Run 5	3.75	60.29	21.680	1.385	3.111	1.50
Run 8	6.60	7.34	19.905	3.443	5.382	2.00
Run 3	3.25	72.90	27.875	1.694	2.694	1.00
Run 6	5.50	39.66	18.014	2.414	4.844	1.00
Run 9	5.50	30.72	16.373	3.095	5.69	1.00

Table 6-16: Dissolution parameters for the two component study in order of compression.

6.3.5 Three Component Study

Reflectance NIRS

The results for the average of three scans of the three component blend wafers were averaged for each blending time. The raw spectra showed slightly more offset in the sucrose data, specifically at ~1910 nm for the 60 minute blend which relates to the API. The average seven minute lactose blend spectrum sat just above the others, which would indicate a larger mean particle size for that blend.

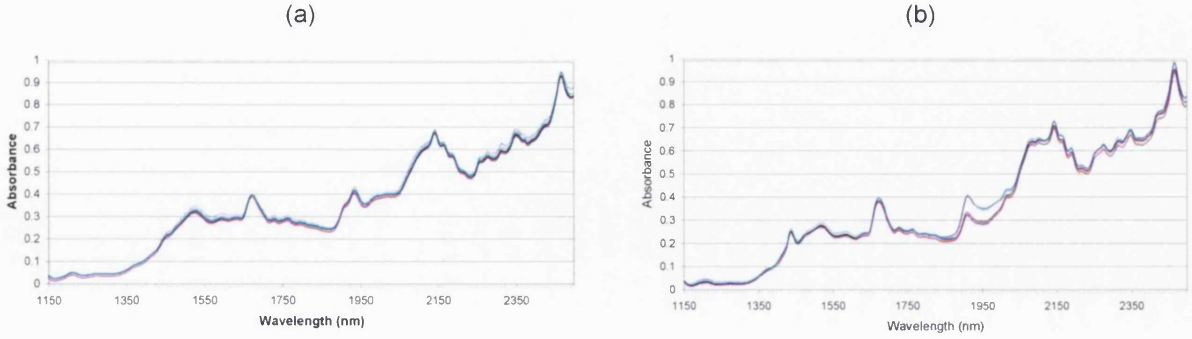

Figure 6-9: Raw reflectance NIRS for (a) lactose blends and (b) sucrose blends in the three component study with (—) 7 min, (—) 15 min, (—) 30 min, (—) 45 min and (—) 60 min.

A second derivative transformation was applied to remove any features caused by physical differences in the wafers. Compared to the other blends the lactose seven minute blend showed decreases in the second derivative absorbances at 1912 nm and 1676 nm, which were associated with the API accompanied by an increase at 1936 nm related to lactose Figure 6-10(a). The sucrose 60 minute blend had a decreased peak amplitude at ~1436 nm related to the sucrose and an increase in the peak at ~1912 nm associated with the API compared to the other four blends.

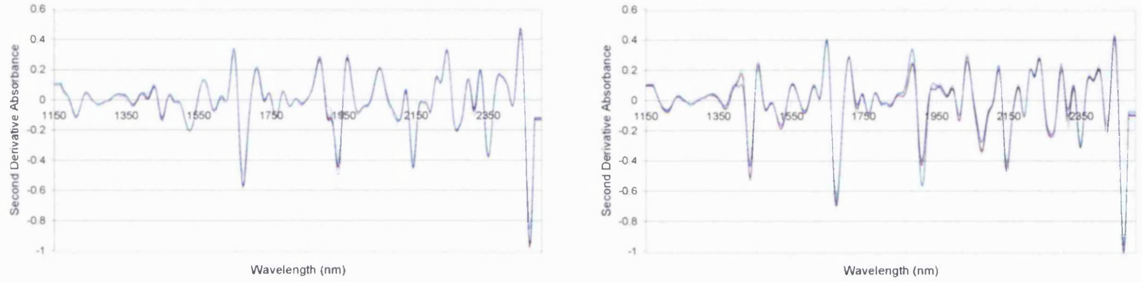
(a)

(b)

Figure 6-10: Derivatised reflectance NIRS for (a) lactose blends and (b) sucrose blends in the three component study with (—) 7 min, (—) 15 min, (—) 30 min, (—) 45 min and (—) 60 min.

PCA was performed on the derivatised data and the score values produced were plotted against each other to look for any separation between the different lots analysed.

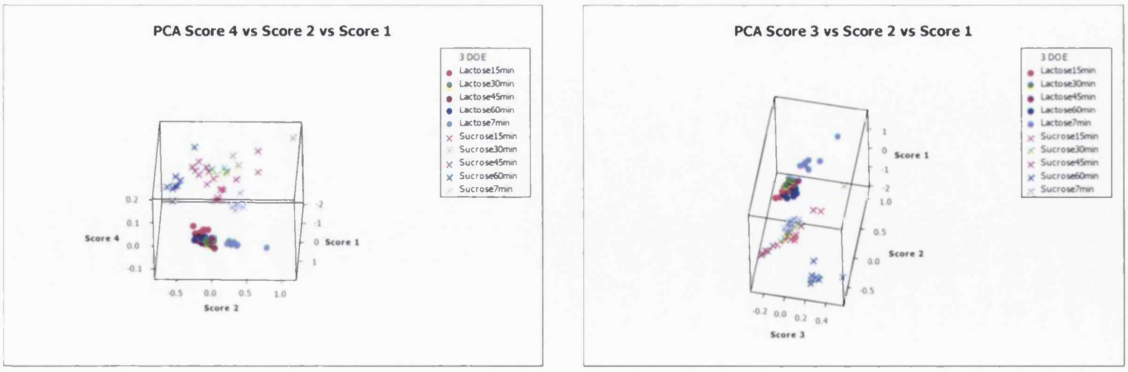
(a)

(b)

Figure 6-11: Comparison of PCA results of derivatised reflectance data (a) score 4 vs. score 2 vs. score 1 and (b) score 3 vs. score 2 vs. score 1 for the three component study blends with (—) 7 min, (—) 15 min, (—) 30 min, (—) 45 min and (—) 60 min.

The scores for the reflectance data showed the main separation of lactose from sucrose blends by score one. The score two values for the sucrose blends were more variable than the lactose blends. The lactose 7 minute and sucrose 60 minute data points were also separated into groups by the score two values, Figure 6-11(a) and (b). Score two may have been related to the spectral contribution of API measured in the wafers. These PCA results reiterated those observed in the raw and derivatised spectra for the two different blend types.

Transmission NIRS

The average of the three spectra was utlised for all the blends and blending time samples. The raw transmission spectra mainly highlighted the physical differences associated with sample thickness due to the nature of the data acquisition. In this way the lactose samples were found to be relatively similar with good overlay of the spectra, although the 7 minute blend was positioned slightly lower which would indicate a longer pathlength, i.e. thicker average sample. A similar situation was encountered for the sucrose blends, but the spectra were more separated with respect to the blending times applied and in this case the 60 minute blend spectra showed the lowest absorbance values. This was consistent with the raw NIR spectra.

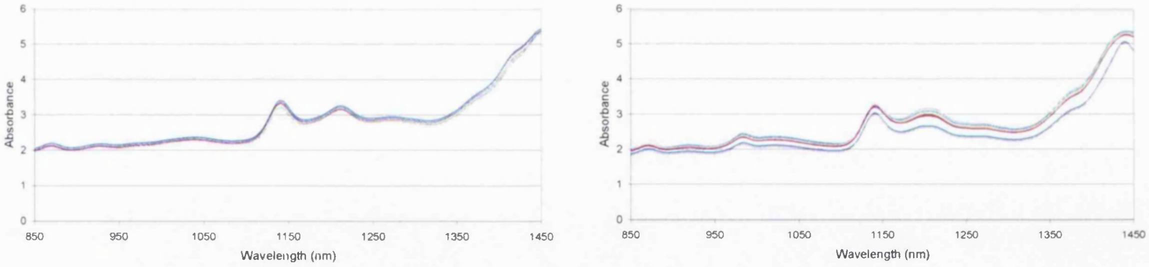
(a)
(b)

Figure 6-12: Raw transmission NIRS for (a) lactose blends and (b) sucrose blends in the three component study with (—) 7 min, (—) 15 min, (—) 30 min, (—) 45 min and (—) 60 min.

The second derivative was performed on the data and the resulting spectra showed the lactose blends to be relatively consistent although there did appear to be an increase in the response at 1416 nm related to the API with blending time, Figure 6-13.

An increase in absorbances of wavelengths associated with the API at 1116, 1140 and 1166 nm and a decrease with those related to the sucrose at 984 and 1370 nm with blending time was observed for the blend containing sucrose. These results followed those gained from the derivatised reflectance NIRS data.

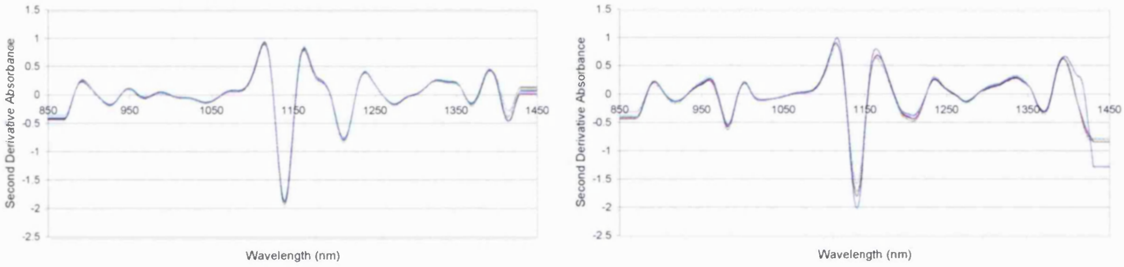
(a) (b)

Figure 6-13: Derivatised transmission NIRS for (a) lactose blends and (b) sucrose blends in the three component study with (—) 7 min, (—) 15 min, (—) 30 min, (—) 45 min and (—) 60 min.

PCA was performed on the derivatised data and the score values produced were plotted against each other to look for any separation between the different lots analysed, Figure 6-14.

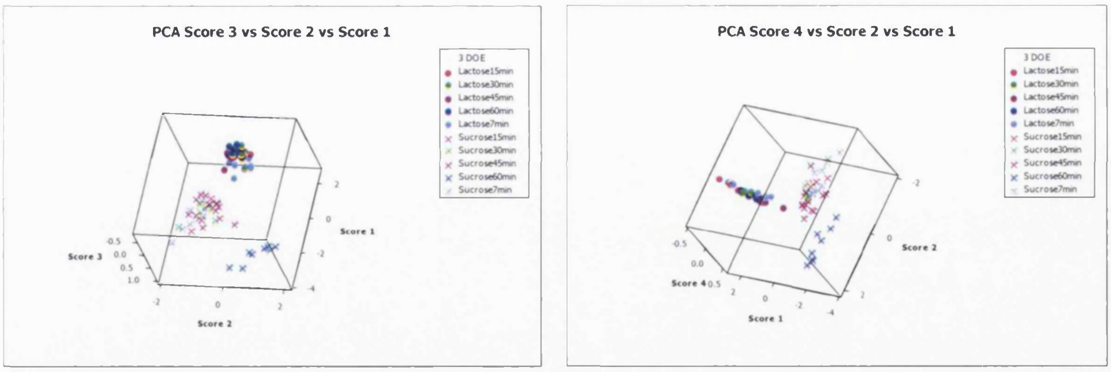
(a) (b)

Figure 6-14: Comparison of PCA results of derivatised transmission data (a) score 3 vs. score 2 vs. score 1 and (b) score 4 vs. score 2 vs. score 1 for three component study with 7 min (●×), 15 min (●×), 30 min(●×), 45 min (●×) and 60 min (●×).

The scores for the transmittance data showed the main separation of lactose from sucrose blends by score one. The score two values for the sucrose blends were much more variable than those for the lactose blends which were clustered quite closely together. The sucrose 60 minute data points also separated into groups by these score two values, Figure 6-14(a) and (b). Score two may have been related to the spectral contribution of API measured in the wafers as in the reflectance results. The lactose 7 minute data points pulled away from the lactose grouping slightly by the score three values, but there was still overlap of the groupings. These PCA results reiterated those observed in the raw and derivatised spectra for the two different blend types as well as being similar to those calculated for the reflectance data.

The results from both the reflectance and transmission NIRS showed a general increase in the API response with blending time. This could be attributed to increased distribution or homogeneity of the API within the blend or possibly the formation of larger, purer areas that contributed to a greater extent to the averaged spectrum of the single point measurements. The 60 minute sucrose blend was highlighted as quite separated from the other sucrose blends with respect to an increase in the API, as was the 7 minute lactose blend to a lesser extent, but here it was due to a decrease in the API compared to the other four samples. This showed that there were changes in the distribution of the API and/or the lactose or sucrose with increased blending time.

Spectrum Spotlight 350-Line Mapping

The wafers made from the ten blends were scanned on the Spotlight. The processing used was the same as for the two component study images, whereby it was terminated at the normalisation step due to samples consisting of three components of the five components, which did not possess similar spectra.

Lactose Blends

RGB images were constructed after PLS was performed on the data, Figure 6-15. A visual comparison of the different blending time samples showed the 15 minute blend, Figure 6-15(b) to have the largest domains of API with the domains in the other blends remaining relatively similar.

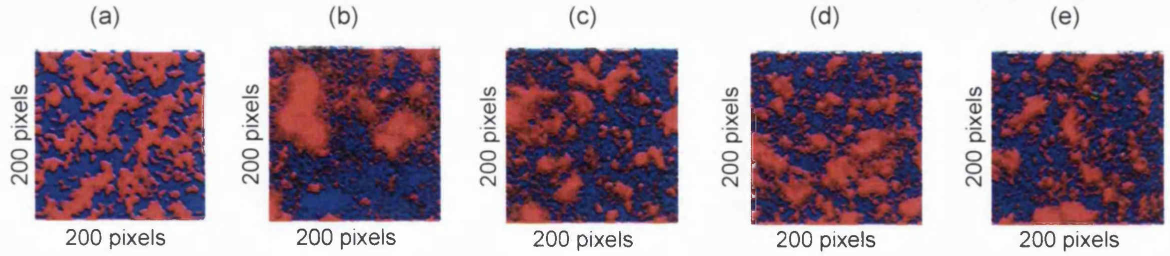

Figure 6-15: RGB images for the three component study lactose blends (a) 7, (b) 15, (c) 30, (d) 45 and (e) 60 minutes blending with API (—), sucrose (—) and magnesium stearate (—).

The sample and domain statistics were calculated, which describe the component distributions within the image and give a means to quantify the areas of each material present, Table 6-17 to Table 6-19.

The sample statistics for the API show the % STD to be the highest at the 15 minute blending time, which related to the homogeneity of the sample with higher values indicating heterogeneity (Lyon *et al.*, 2002). This was consistent with the RGB image comparison where this time point demonstrated the largest areas of API. The % STD value was lowest at 7 minutes blending implying a relatively consistent distribution compared to the other samples and this was observed in the RGB image, Figure 6-15(a). The majority of the statistics values indicated that the samples with 7 minutes blending time were separated from the remaining blends. The 7 minute had the lowest kurtosis value meaning less tailing which would normally have been associated with large domains, but the MED value was the highest and this would normally indicate the presence of large areas. This could be explained by looking at the RGB images, Figure 6-15 where the 7 minute blend had API domains that were fairly consistent in size over the image. The remaining four images for the higher blending times showed the presence of large domains of API, but there were also a greater number of much smaller domains visible compared to the 7 minute sample. As there was a higher ratio of the small domains to the larger ones, this would have lowered the MED values for the API in these images. The number of domains was the lowest for the 7 minute samples for the same reason as the MED values was the highest.

API	MSV	%STD	Skew	Kurtosis	Number of Domains	MED (µm)	NN (µm)
7 minutes	0.398	19.816	0.851	1.713	176.8	262.5	11.7
15 minutes	0.077	119.900	2.900	11.400	574.0	141.0	6.6
30 minutes	0.113	53.836	2.960	13.980	458.4	139.0	7.6
45 minutes	0.133	42.298	2.120	6.860	384.2	153.0	7.9
60 minutes	0.103	52.527	3.140	15.300	519.0	126.5	6.8

Table 6-17: Sample and domain statistics for API in the three component study lactose blends.

Lactose	MSV	%STD	Skew	Kurtosis	Number of Domains	MED (µm)	NN (µm)
7 minutes	0.597	13.635	-0.699	1.543	260.0	189.0	9.8
15 minutes	0.851	10.381	-2.381	8.780	768.8	97.0	5.5
30 minutes	0.833	7.321	-2.332	10.720	713.0	98.0	5.9
45 minutes	0.818	6.802	-1.554	4.780	647.2	101.5	6.1
60 minutes	0.838	6.486	-2.178	10.040	782.4	94.0	5.7

Table 6-18: Sample and domain statistics for lactose in the three component study lactose blends.

Magnesium stearate	MSV	%STD	Skew	Kurtosis	Number of Domains	MED (µm)	NN (µm)
7 minutes	0.039	49.799	-0.203	0.838	47.2	33.0	22.8
15 minutes	0.094	27.525	-0.353	1.674	33.2	47.0	26.1
30 minutes	0.078	26.970	-0.367	1.446	36.4	31.0	27.7
45 minutes	0.074	28.990	-0.354	1.680	35.0	31.5	26.3
60 minutes	0.084	26.370	-0.479	3.480	21.6	43.0	29.6

Table 6-19: Sample and domain statistics for magnesium stearate in the three component study lactose blends.

The same pattern was observed for the lactose statistics, highlighting the 7 minute blend as different to the others, although the % STD decreased with increased blending time utilised, which would be associated with increased homogeneity. The magnesium stearate statistics also pointed towards the 7 minute blend as distinct from the other samples analysed, but in this case the % STD was higher implying the homogeneity increased with blending.

Sucrose Blends

RGB images were constructed for the sucrose blends after PLS was performed on the data, Figure 6-16.

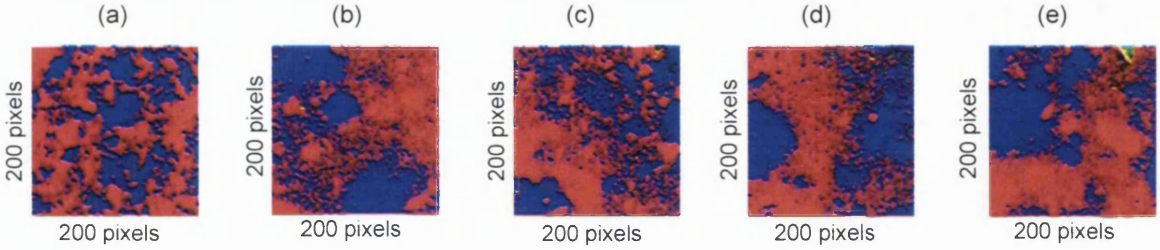

Figure 6-16: RGB images for the three component study sucrose blends (a) 7, (b) 15, (c) 30, (d) 45 and (e) 60 minutes blending with API (—), sucrose (—) and magnesium stearate (—).

The images showed a similar situation as was illustrated for the lactose blends, where the 7 minute blend did not contain as wide a distribution of domain sizes as the other four blend types, i.e. there were fewer very small domains present. The 15, 45 and 60 minute images comprised a number of very large domains of sucrose where the API appeared to fill in the surrounding area, whereas in the lactose RGB images the API appeared to form discrete areas with the lactose behaving as the filler, Figure 6-15. In order to describe these images in a more quantifiable manner the sample and domain statistics were determined, Table 6-20 to Table 6-22.

The statistics for the API showed similar trends for the number of domains, MED and % STD to those seen for the API in the lactose blends and this was for the same reason as was expected from the visual comparison of the RGB images. It was very clear in this instance that the domains of API were spreading out over a larger area to fill the space between the larger domains of sucrose formed with the increasing blending time, which would be anticipated to cause an increase in the % STD value as it would contribute to an increase in heterogeneity in the image. Again the number of domains was higher for the 15 minute blends upward due to the increased number of small areas observed, which in turn meant that the MED was lower due to an averaging effect in the calculation of the values. The same association between blending time and the values of the number and MED of the API domains was observed for the sucrose component.

Even though the presence of the very large domains was obvious from the RGB images, the average nature of the domain statistics did not reflect it as such. The magnesium stearate statistics did not show much of a difference with blending time, although there was a general decrease in the % STD values which would relate to the component being more evenly distributed within the image. However it was apparent from the 60 minute image shown in Figure 6-16(e) and the increase in the MED that there was the presence of some larger domains of magnesium stearate at this blending time point.

It was clear from the comparison of the RGB images in Figure 6-15 and Figure 6-16 that the sucrose would preferentially associate with itself to form very large domains as the blending time was increased, whereas the lactose did not appear to show this type of behaviour and remained to function as a filler or binder around the subsequent API domains produced.

API	MSV	% STD	Skew	Kurtosis	Number of Domains	MED (µm)	NN (µm)
7 minutes	0.431	19.220	-0.257	1.887	159.2	278.0	11.9
15 minutes	0.035	68.127	1.466	10.020	574.6	133.5	6.0
30 minutes	0.060	71.409	1.609	7.800	441.8	162.0	6.4
45 minutes	0.045	60.072	-0.279	1.256	527.6	148.5	5.7
60 minutes	0.063	55.260	1.600	9.500	537.0	151.0	5.9

Table 6-20: Sample and domain statistics for API in the three component study sucrose blends.

Sucrose	MSV	% STD	Skew	Kurtosis	Number of Domains	MED (µm)	NN (µm)
7 minutes	0.840	6.247	-0.385	3.744	228.6	205.5	10.0
15 minutes	0.885	4.006	0.206	2.660	589.6	134.5	5.9
30 minutes	0.862	6.007	-0.193	2.920	405.4	175.0	7.9
45 minutes	0.823	4.914	1.240	2.501	518.0	145.5	6.5
60 minutes	0.839	5.169	0.163	3.320	533.0	137.5	6.3

Table 6-21: Sample and domain statistics for sucrose in the three component study sucrose blends.

Magnesium stearate	MSV	% STD	Skew	Kurtosis	Number of Domains	MED (µm)	NN (µm)
7 minutes	0.136	29.558	-0.596	0.983	44.0	32.5	22.0
15 minutes	0.101	22.441	-0.968	1.940	51.4	31.5	17.8
30 minutes	0.102	26.866	-0.959	1.361	44.2	34.5	19.4
45 minutes	0.161	18.566	-1.047	1.966	43.2	35.5	15.7
60 minutes	0.125	19.997	-0.648	1.990	25.2	63.5	18.4

Table 6-22: Sample and domain statistics for magnesium stearate in the three component study sucrose blends.

Dissolution Profiles

It was aimed that filled capsule samples would be produced for the ten blends in the three component study in order to simulate the actual dissolution conditions for the product as in the two component study. Capsules for one of the ten blends were prepared manually using a capsule filler where half of a capsule shell was positioned in a holder and the blend was moved around over the top of the empty shell halves until they were full. The blend was manually compacted into the half shell then the other half was pushed on top completing the capsule. Eight of these were dissolved and the individual profiles were clearly variable, Figure 6-17(a).

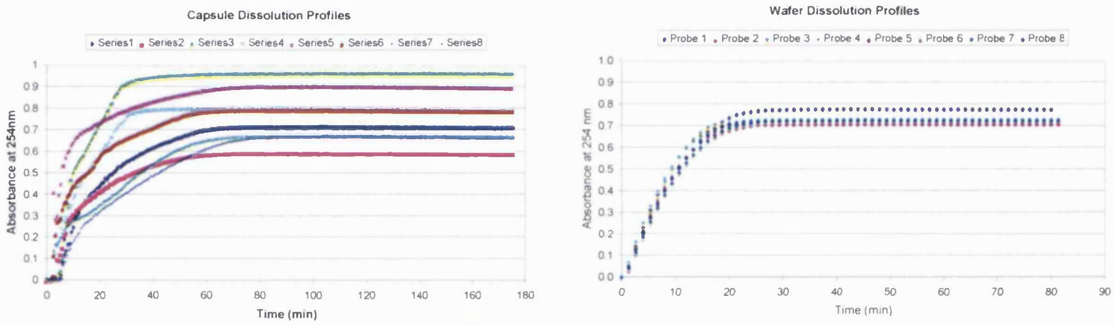
(a)

(b)

Figure 6-17: Dissolution capsule profiles for the three component study (a) capsules and (b) wafers.

Wafers of the same blend were produced for comparison and the dissolution profiles showed them to produce more consistent dissolution performance than the capsules. The production of the capsules using the manual filler introduced intra-blend variation including differences in the amount of blend in each capsule. Therefore, it was decided to continue using wafers which remained relatively constant in comparison to the capsules with regards to the dissolution results.

Eight wafers were produced for each of the ten blends. They were all analysed by NIRS then dissolved using the USP apparatus 2 and the conditions stated in section 6.2.4.

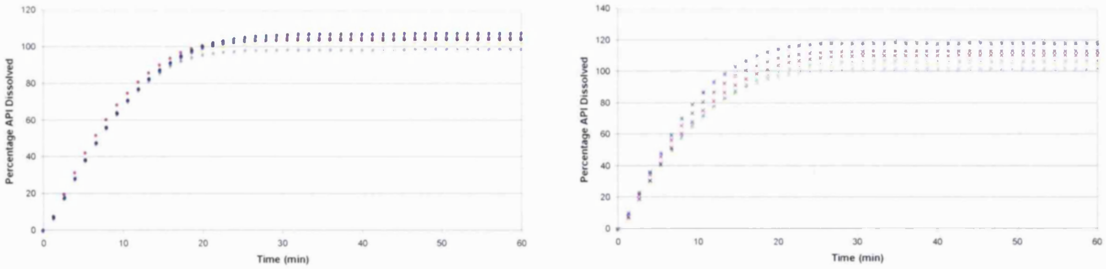
(a)

(b)

Figure 6-18: Average dissolution profiles for three component study (a) lactose and (b) sucrose blends with 7 min (•×), 15 min (•×), 30 min(•×), 45 min (•×) and 60 min (•×).

The average profiles for the lactose blends were very similar and overlaid in the steady state region of the dissolution. The only variation was due to a slightly lower average proportion of API present in the 7 minute blend compared to the others, which was one of the observations from the PCA scores comparison from the reflectance NIRS, Figure 6-11. The average profiles produced for the sucrose blends showed a slight spread in the steady state portion of the dissolution as well as variation in the position of the plateau related to the average amount of API present.

The range of % API dissolved for both sets of profiles was thought to be a homogeneity effect due to the small blend size used causing hot and cold concentration spots when blending in the Turbula and the possibility of aggregation, specifically with the type of sucrose used that was known to be cohesive combined with the apparent tendency to form large clusters.

The dissolution parameters were calculated for the average profiles as discussed in section 2.2.2 and shown in Table 6-23 and Table 6-24.

The parameters from the lactose data illustrate that the different blending times did not have a significant effect on the dissolution as the average values were very similar. The P_{15} value was the highest for the 15 minute lactose blend, which was the blend that had the largest domains of API from the RGB image comparison Figure 6-15(b). The k_e, rate constant for the exponential model, values showed a general increase with blending time and the T_d, time to 63.2% dissolution values generally increased. The sucrose results showed a general increase in the P_{15} and k_0 parameters with blending time. The k_0 increase meant the dissolution experienced for the samples with larger sucrose lumps was slightly faster than that for the samples with smaller domains present.

The main outcome from the three component study was that an increase in blending time had a larger effect on the blends containing the sucrose whereby large domains were formed and this resulted in slightly faster, more variable dissolution rates.

Lactose	t_{90} **(min)**	P_{15} **(%)**	k_0 **(%/min)**	k_e **(min^{-1})**	β	T_d **(min)**	t_L **(min)**	n
7 minutes	16.38	86.15	5.956	0.126	1.47	9.25	-0.38	1.04
15 minutes	14.29	91.44	6.166	0.124	1.38	9.13	-0.28	1.04
30 minutes	15.81	87.08	6.003	0.116	1.43	9.87	-0.37	1.03
45 minutes	15.24	88.35	6.152	0.117	1.47	9.90	-0.41	1.05
60 minutes	15.62	87.21	6.094	0.110	1.42	10.34	-0.34	1.05

Table 6-23: Average dissolution parameters for three component study lactose blends

Sucrose	t_{90} **(min)**	P_{15} **(%)**	k_0 **(%/min)**	k_e **(min^{-1})**	β	T_d **(min)**	t_L **(min)**	n
7 minutes	15.62	87.47	5.930	0.123	1.32	8.93	-0.04	1.02
15 minutes	14.48	92.73	6.298	0.115	1.35	9.66	-0.19	1.08
30 minutes	21.33	88.32	5.940	0.113	1.35	9.86	-0.24	1.01
45 minutes	12.95	98.46	6.580	0.124	1.35	9.04	-0.22	1.04
60 minutes	11.24	103.49	7.175	0.128	1.42	8.92	-0.31	1.1

Table 6-24: Average dissolution parameters for three component study sucrose blends.

The fit of the models applied to the data was tested by calculation of the RSS for the predicted values compared to the actual dissolution values used, see Table 6-25, Table 6-26, Figure 6-19 and Figure 6-20.

The values for the Weibull model results gave the lowest calculated RSS and as such only these model parameters provided the best fit to the data for both the lactose and sucrose blends. These values were selected for the correlation to the imaging parameters along with the initial rate and single point values.

RSS- Lactose	Exponential	Weibull	Korsmeyer-Peppas
7 minutes	2.87	0.49	4.01
15 minutes	2.61	0.47	1.12
30 minutes	2.85	0.55	1.64
45 minutes	3.06	0.57	1.27
60 minutes	2.90	0.49	1.08

Table 6-25: RSS values for three component study dissolution profiles with lactose.

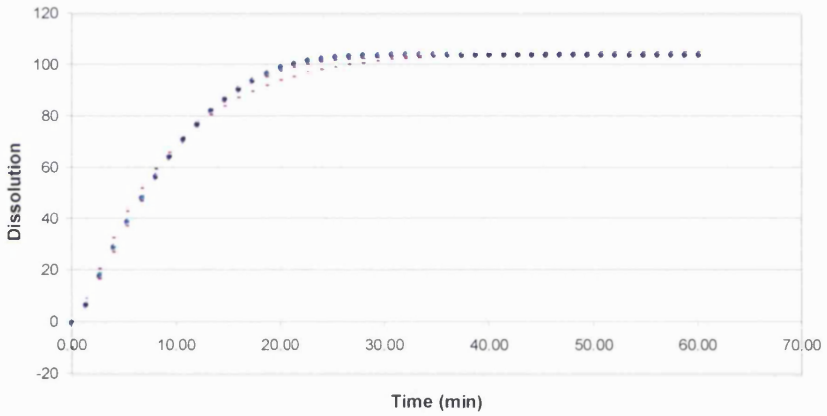

Figure 6-19: Overlay of actual dissolution profile and model values for three component study with lactose 45 minute blending with (•) actual dissolution profile, (–) exponential, (–) Weibull and (–) Korsmeyer-Peppas model values.

RSS- Sucrose	Exponential	Weibull	Korsmeyer-Peppas
7 minutes	2.35	0.38	1.46
15 minutes	2.69	0.56	1.13
30 minutes	2.54	0.58	1.36
45 minutes	2.70	0.55	1.30
60 minutes	3.10	0.47	0.64

Table 6-26: RSS values for three component study dissolution profiles with sucrose.

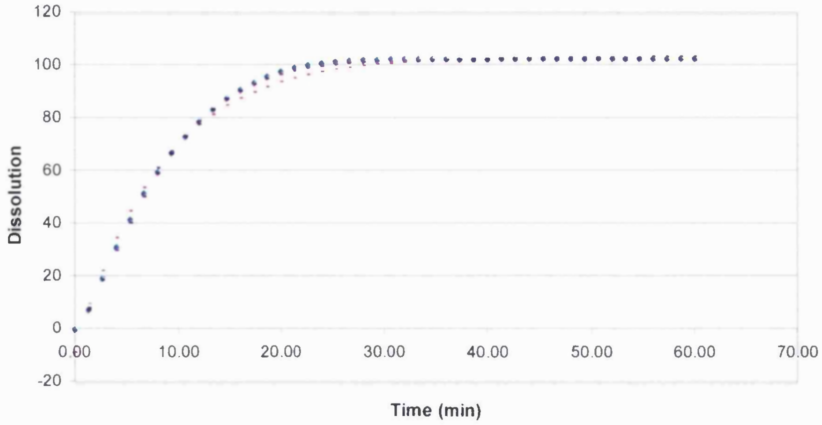

Figure 6-20: Overlay of actual dissolution profile and model values for three component study with sucrose with 7 minutes blending (◆) actual dissolution profile, (–) exponential, (–) Weibull and (–) Korsmeyer-Peppas model values.

Actual Dissolution Study

Transmission NIRS

The results from the transmission and reflectance NIRS for the three component study blends were comparable, therefore transmission NIRS was the only NIRS method applied to the actual dissolution study samples to avoid repetition of results.

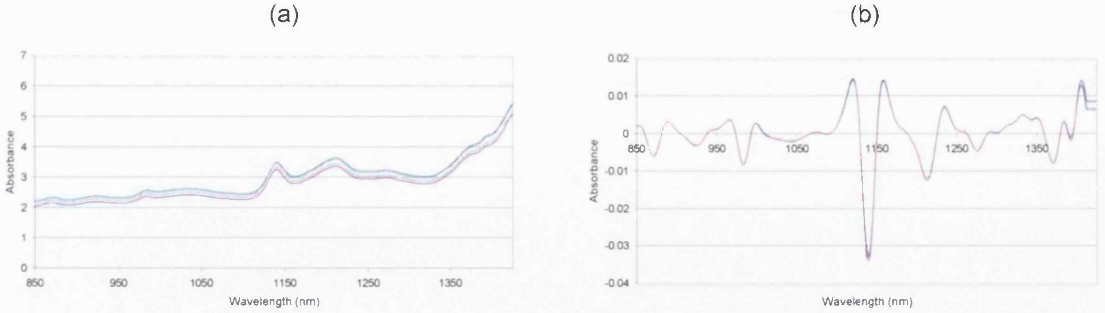

Figure 6-21: (a) Average raw and (b) second derivative transmission spectra for the actual dissolution study blends with pass (—), re-work (—) and OOS (—).

The raw spectra showed the sample wafers of the pass blend could have had a slightly different particle size than the re-work and OOS as the average spectrum was positioned above the other two with higher absorbance values, i.e. the light was reaching the detector quicker therefore the pathlength through the sample must have been shorter, Figure

6-21(a). The second derivative spectra were well grouped and practically overlaid. There was a slight variation at the API wavelength of 1140 nm where the pass blend had less of the response than the re-work and OOS, but otherwise they were very similar, Figure 6-21(b).

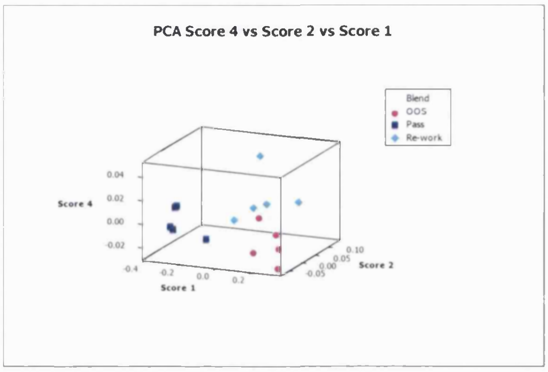

Figure 6-22: Comparison of PCA results of derivitised transmission data for the actual dissolution study blends with pass (■), re-work (◆) and OOS (●).

The results of PCA on the derivatised data illustrated a separation of the pass data points from the other blends along the score one values, as was observed in the raw spectra. The re-work and OOS results were discretely grouped to some extent by score one, but there was still a visible degree of overlap in the values. The other score values did not serve to separate the groupings further, but did illustrate that the re-work score values were the most variable of all the blends analysed.

Spectrum Spotlight 350-Line Mapping

Wafers were made from the three blends available and were scanned on the Spotlight. The processing used was the same as for the aging study images, whereby a second derivative was required due to the samples consisting of all five blend components, some of which had similar spectra.

RGB images were constructed after PLS was performed on the data. A visual comparison of the images did not highlight any obvious differences in the major components: API, lactose or sucrose. However, when the magnesium stearate was viewed as single channel images there appeared to be a difference between the blends that passed and the one which was OOS. Figure 6-23 shows examples of these single channel magnesium stearate images where there were apparently a greater number of domains in the OOS image compared to those seen in the pass and re-work images.

The sample and domain statistics were calculated, which would allow further investigation of the magnesium stearate observation as well as any other variations that may not have been obvious from the RGB images. The average values are given in Table 6-27.

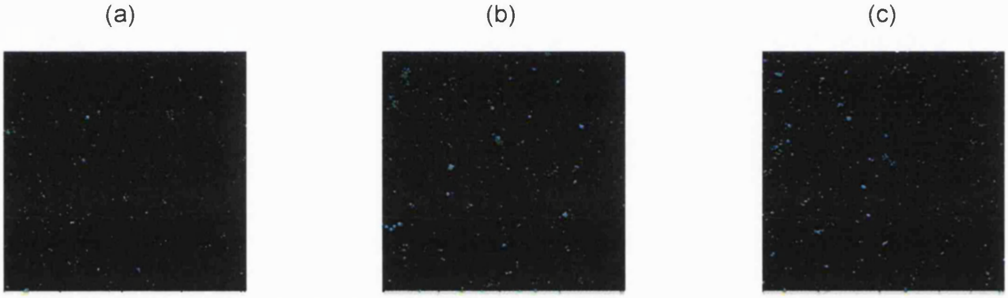

Figure 6-23: Single channel images of magnesium stearate (—) for (a) pass, (b) OOS and (c) pass after re-work blend wafers from the actual dissolution study.

Only two of the components displayed differences between the passing and OOS imaging. The values for API showed an increase in the number of domains going from pass to re-work to OOS accompanied by a decrease in the size of the domains, which wasn't evident from the RGB images alone. The other component that varied was the magnesium stearate, which was anticipated from the RGBs. Similarly to the API it showed an increase in the number of domains from the pass to OOS blends, but in this case the MED remained the same. The kurtosis values for lactose and sucrose actually decrease slightly moving from pass to the OOS blend, which would relate to the reduction of tailing in the pixel distributions from an increase in blending and mixing within the blend. Wafers of these blends were then dissolved in order to see if the profiles showed the same pattern as the site findings.

	MSV	% STD	Skew	Kurtosis	Number of Domains	MED (μm)	NN (μm)
Pass API	0.331	26.068	0.437	0.300	268.4	146.0	9.8
Re-work API	0.335	25.304	0.365	0.318	311.2	135.0	9.0
OOS API	0.342	26.827	0.441	0.153	328.6	131.0	8.7
Pass lactose	0.307	31.785	0.624	0.328	242.8	117.5	9.8
Re-work lactose	0.297	32.932	0.598	0.158	259.0	113.0	9.5
OOS lactose	0.297	32.510	0.631	0.143	235.6	119.5	9.9
Pass sucrose	0.346	24.001	0.829	1.540	318.2	98.5	8.9
Re-work sucrose	0.343	24.325	0.826	1.326	342.2	94.0	8.5
OOS sucrose	0.342	24.255	0.793	1.160	328.0	96.5	8.5
Pass magst	0.031	28.688	-0.056	0.392	423.8	40.5	7.0
Re-work magst	0.031	28.490	-0.051	0.356	540.2	40.5	6.2
OOS magst	0.031	29.244	-0.024	0.478	630.2	40.5	5.8
Pass talc	0.056	45.331	0.359	1.252	221.8	37.5	10.0
Re-work talc	0.063	41.252	0.231	0.580	183.4	39.5	10.9
OOS talc	0.061	43.409	0.224	0.599	223.2	37.0	9.8

Table 6-27: Sample and domain statistics for the actual dissolution study blends.

Dissolution Profiles

The wafers were dissolved using USP apparatus 2 and the conditions stated in section 6.2.4 then the profiles were converted into % dissolved vs. time, Figure 6-24. The average dissolution profiles obtained were consistent with the assignment of the blends with the OSS samples dissolving with increased rate compared to the other passing blends. The re-work sample dissolved slightly faster than the pass samples, but overall these two were very similar in performance.

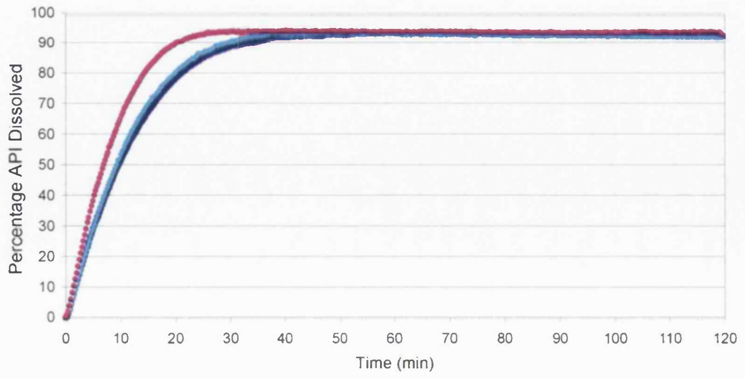

Figure 6-24: Average dissolution profiles for the actual dissolution study blends pass (■), re-work (◆) and OOS (●).

The actual profiles acquired however would not be the same as those from the site as the dissolution would have been performed on capsules not "tablets", which would have resulted in a lag time before the onset of dissolution while the capsule dissolved as well as a possible slowing of the profile as there would be less surface area exposed.

The dissolution parameters were calculated for the average profiles as previously mentioned in section 2.2.2 and are shown in Table 6-28.

Actual Dissolution Study	**t_{80} (min)**	**P_{10} (%)**	**k_0 (%/min)**	**k_e (min^{-1})**	**β**	**T_d (min)**	**t_L (min)**	**n**
Pass	20.81	51.77	4.990	0.087	1.168	11.962	-6.841E-06	0.867
Re-work	19.63	53.86	5.627	0.093	1.229	11.611	-0.175	0.902
OOS	14.22	65.90	6.240	0.128	1.315	8.981	-0.360	0.911

Table 6-28: Dissolution parameters for actual dissolution study profiles.

Many of the dissolution parameters in this case provided trends related to the dissolution order, as would be expected such as the t_{80} and P_{10} values which showed a decrease and an increase from pass to OOS, respectively. The initial rate, the exponential rate constant, the Weibull shape parameter and the power value for the Korsmeyer-Peppas model all increased from the pass to OOS dissolution. The Weibull rate parameter decreased from pass to OOS which made sense as it related to a percentage of API dissolved so the OOS as the fastest would reach that point before the others.

The fit of the models applied to the data was tested by calculation of the RSS for the predicted values compared to the actual dissolution values used, see Table 6-29 and Figure 6-25.

All the RSS values were around 1.5 and below for the models applied and out of those, the Weibull model results gave the lowest. These Weibull values were selected for the correlation to the imaging parameters along with the initial rate and single point values.

RSS-	Exponential	Weibull	Korsmeyer-Peppas
Pass	1.15	0.37	1.05
Re-work	1.38	0.97	1.45
OOS	1.68	0.50	1.21

Table 6-29: RSS values for actual dissolution study dissolution profiles.

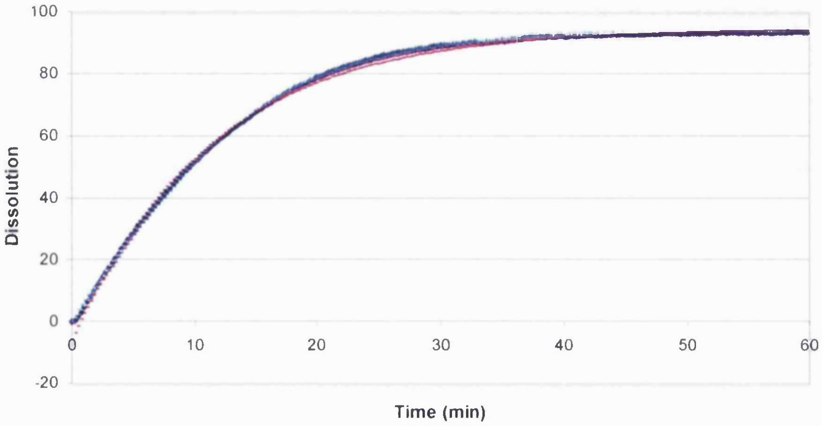

Figure 6-25: Overlay of actual dissolution profile and model values for actual dissolution component study pass data with (◆) actual dissolution profile, (–) exponential, (–) Weibull and (–) Korsmeyer-Peppas model values.

6.4 Conclusion

Pfizer product W has a history of variable dissolution which has subsequently lead to many internal and collaborative investigations in an attempt to identify the critical to quality attributes related to this physical process. One of these evaluations involved the assessment of the relative ages of the ingredients used for the capsule blends as it was thought that this caused differences in the API and lactose. The results from "traditional" dissolution had grouped the blends as passing or OOS dissolution. Capsule samples from six of these blends were available for imaging and dissolution. The sucrose was found to form large clusters in the blends that experienced very rapid, OOS dissolution, which weren't present in the two blends with acceptable performance. The sucrose used was consistent through all the blends produced. Therefore there must have been a difference in the interactions with the other four components to cause the clumps. These large domains may have resulted in a reduction on the ability of the matrix to bond together and reduce its stability, which resulted in a faster dissolution. In addition, the type of sucrose utilised was confectioner's sugar, known to be a cohesive solid, which may have aided the formation of the large domains.

Another hypothesis for the variable dissolution was concentrated on the degree of mixing of API and the magnesium stearate in the blends. The theory suggested that the longer the blending time, the more distributed the magnesium stearate became within the blend and coated the API particles, slowing any subsequent dissolution performed. Binary mixture filled capsule samples were produced using these two components as a small feasibility study where the blending time was varied as well as the compression used when manually filling the capsules. The extra blending was performed in a Turbula blender and was done to introduce more shear in the blend which was thought to encourage the coating of the API particles. The imaging results showed both the blending and compression to cause variations in the blend matrix for the magnesium stearate, but the dissolution profiles only showed variations when grouped by the compression used to show the effect of the blending time. The samples which were subjected to ten hours extra blending, run three, six and nine took longer to start dissolving compared to the others.

Following the outcomes from the aging and two component studies, the decision was made to manufacture a three component blend to evaluate the effect of the sucrose with the other two components, API and magnesium stearate, as it had been identified as a possible connection to the different dissolution results observed. Blends were made containing API, magnesium stearate then either sucrose or lactose and were exposed to five different blending times. The RGB images from the NIRM imaging highlighted the tendency for the sucrose to form very large domains as the blending time was extended. It was also noted that the API was behaving as filler around the discrete areas of sucrose formed, which may have left it more available for dissolving than in the case for the lactose blends, where the situation was reversed. The average dissolution profiles for both blend types were very similar in shape, but the individual profiles for the sucrose were more variable than those for the lactose blend samples. The variation was mainly seen in the % dissolved when the dissolution went to completion i.e. the plateau value. This was attributed to differences in the homogeneity in the sucrose blend caused by the formation of the large domains. There were general increases with blending seen within the sucrose dissolution parameters e.g. the initial rate showed a general increase, so the sucrose lumps seemed to allow the dissolution to progress slightly quicker, but in general there was a lack of trends with blending time.

The studies performed up to this point had been based on the product W, but no actual production lots of the product that had experienced variable dissolution had been analysed. In order to evaluate whether any of the findings from aging, two component and/or three component studies were relevant in the "real" product, samples were analysed from a site where they had found one particular lot produced had shown very rapid, OOS dissolution. Investigation at the site had also demonstrated that subsequent re-working of the OOS lot resulted in the dissolution falling within specification. NIRM image analysis of the OOS and re-work blends as well as a blend that had no dissolution issues highlighted an increase in the number of domains for the magnesium stearate and API upon comparison of the pass to OOS images. The sucrose also showed a change in the skew and kurtosis parameters, but this did not follow through into any domain variation related to the dissolution. The dissolution profiles obtained echoed the results of the dissolution performed at the site and showed the pass and re-work blend gave results that practically overlaid, although the re-work was slightly faster.

Overall, the combined findings from all four studies related to product W indicate that any variations observed in the dissolution performance would be related to the magnesium stearate and API with respect to the degree of mixing and presence in the matrix i.e. increased blending or increased number of domains gave a delay in the dissolution and/or changes of the sucrose in the matrix i.e. increase domain size lead to an increase in the dissolution rate. These component features in the NIRM images appear to be related to the dissolution and it could be these factors used for this product with respect to the controlling the process, for example if the blend was shown to have large domains of sucrose after blending, the dissolution would be likely to proceed at a faster rate than if the domains were found to be small.

7 Correlation of Imaging and Dissolution Parameters

This chapter will attempt to theorise the possible changes in the images, related to the matrices of solid dosage forms that may result in differences in the dissolution performance. The data acquired from the previous chapters will be utilised to test these hypotheses and identify any correlations between the two types of parameters.

7.1 Introduction

Within NIRM images, any differences observed related to differences in the blend matrix e.g. the presence of larger domains of one excipient or API in one image compared to that of another. In turn, this could be related to a physical change in the production of the samples such as blending time or input particle size. These variations in the sample matrix may lead to further differences in performance such as poor processability e.g. sticking of the blend in tablet press or poor flowability and on occasions have been attributed to causing poor or enhanced dissolution performance.

When blends have been compared for the same type of problem in a trouble-shooting capacity for different products, or even within samples of the same product, any variations found to correlate with the issue would not necessarily be related to the same component. This could have been due to different production methods for the same product from different manufacturing locations, or variations in the source of the excipients used. However, the main variation encountered between different product types was that pharmaceutical formulations varied widely and may not have shared any of the same components. This resulted in an inability to produce any general rules that could have been applied to any product system related to changes in the images and a particular property.

The possible changes in the samples and hence the NIRM images that may have effected the dissolution performance will be evaluated and discussed in the following section to allow a starting point for any attempted correlations.

7.2 Possible Factors Affecting Dissolution Behaviour

As the dissolution process occurs at the surface exposed to the dissolution medium, theoretically the larger the surface area available, the faster something will dissolve. This could translate as the smaller the domain size of the API, the faster it will dissolve, therefore domain size would be expected to have an effect on the dissolution. The number of domains might also give an indication of the domain size as the two values tend to be inversely related, so this could also have an effect on the dissolution rate of the API. In the case where there may be very large domains of API present, there would be differences observed between the abundance distribution over the NIRM image compared to one from a sample with no large lumps. This might show in the skew or the kurtosis value, so these may also show patterns with the dissolution behaviour. The % STD might also change if the abundance distribution of the API varies due the presence of large domains and would be another factor to consider.

Unlike traditional dissolution testing that is solely focussed on the API, the NIRM can provide information about the other components present in the tablet matrix and, although they are not present in a pharmacological capacity, they should provide a platform to enable the API to be administered as designed. Therefore, variations in these components could also give rise to differences in the dissolution performance even though there may not be any changes seen for the API.

The magnesium stearate in a product serves the purpose of a lubricant to aid the processing of the blend. It serves this purpose well as it has very small particle size and tends to "coat" other components within the blend allowing them to move freely. However this "coating" can be undesirable in certain situations such as dissolution due to the insoluble nature of magnesium stearate. If it preferentially coats the API, it may retard the dissolution and affect the performance. However that may be the aim of the magnesium stearate inclusion so the formation of magnesium stearate lumps in the tablets may result in the dissolution occurring too rapidly as it is not evenly distributed. Therefore number of domains, MED, skew and kurtosis values may be indicative of possible dissolution variation.

Changes in the other blend components that perform the functions of fillers and diluents, such as MCC in product V and sucrose in product W, have been shown in this work to be related to subsequent dissolution variations. The formation of large lumps of MCC when using a large input particle size of that excipient showed the dissolution rate to increase compared to that for samples with smaller domains of MCC. In the same study, changing the particle size of the API had not yielded any dissolution variation. MCC would not usually be associated with dissolution as it is not used as a disintegrant, but was thought that the larger lumps did not facilitate the MCC to mould around the API as well hence allowing the API to dissolve quicker into the dissolution medium. As for the API and magnesium stearate, this would continue the main argument that it would be related in some way to the surface area and hence the parameters that describe the number, size and distribution of these components in the NIRM images may be expected to show some correlation with the dissolution parameters.

In an attempt to try and identify any correlations between the NIRM imaging parameters and the dissolution parameters, the data were initially taken as a whole over all the products examined. This maximised the number of data points available for correlation as some of the individual studies contained only three data points.

All of the samples used contained an API and these were the first comparisons to be made. Each subsequent comparison was made for the other excipients that included all the data relevant to the products that contained them. Finally the individual projects were examined for any correlations missed in the general comparisons. This final step was to include the comparisons to the dissolution values obtained for the time to a particular % and the % at a specific time as these parameters were product specific due to the nature of their determination, see section 2.2.2.

7.2.1 General Comparisons of Imaging and Dissolution Parameters

API

In dissolution terms, the API is generally seen as the most important component in a product. Therefore changes with the API would be expected to have some kind of effect on the dissolution behaviour.

All of the different studies had the dissolution parameters from the initial dissolution rate and the Weibull model in common, so these were initially compared to all seven of the NIRM imaging parameters for the APIs present.

Figure 7-1 shows an example of the comparison of the API MSV against the initial dissolution rate. The data generally formed groups for the individual studies carried out. This was the case for all seven of the imaging parameters when compared to the initial dissolution rate. Isolation of the data for the product V API (D) and the product W API did not produce any overall patterns with the initial dissolution rate, but emphasised the groupings for each study.

The results of the three component study gave the most variable results.

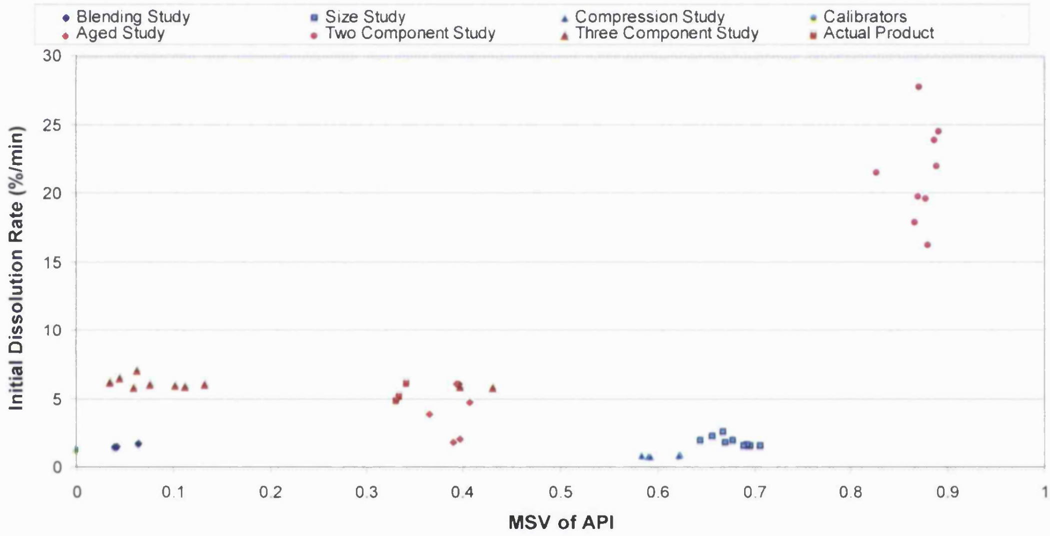

Figure 7-1: Comparison of MSV of the APIs with the initial dissolution rates for all products.

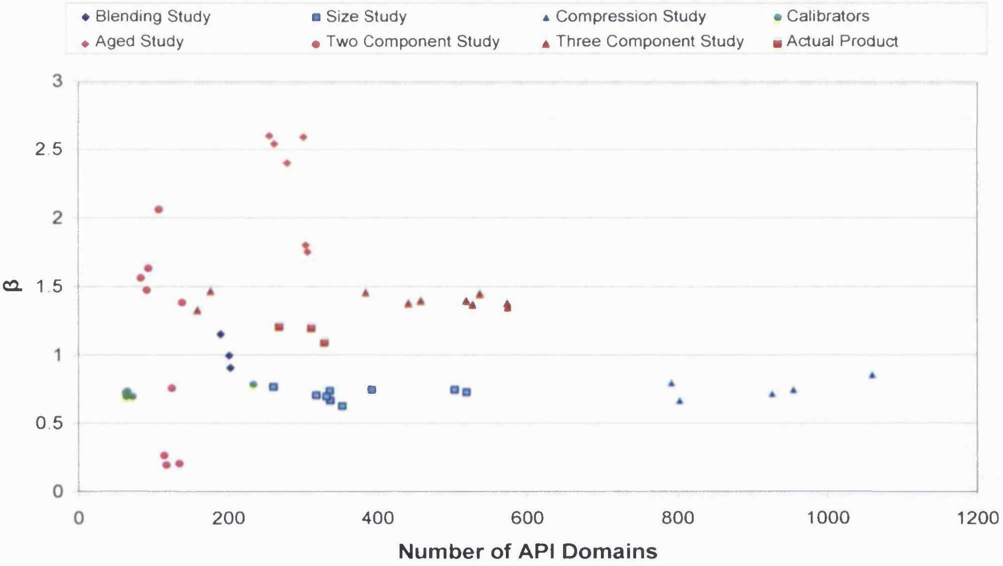

Figure 7-2: Comparison of the number of domains of the APIs with the β values for all products.

When the Weibull parameters of β, T_d and t_L were compared to the API imaging parameters, a similar situation occurred as for the initial dissolution rate. There were no general trends with the API NIRM parameters to the dissolution parameters and the data appeared to group for the individual studies, see Figure 7-2.

Magnesium stearate

All the data for the samples containing magnesium stearate[1] were compared for the initial dissolution rate and Weibull parameters to the imaging values to look for any general patterns. As Figure 7-3 and Figure 7-4 show, the data again grouped into the different studies and gave no general trends, even when separated into the different product types.

---

[1] The product V studies were included as the lubricant blend was 90% magnesium stearate and it performed the same lubricant function.

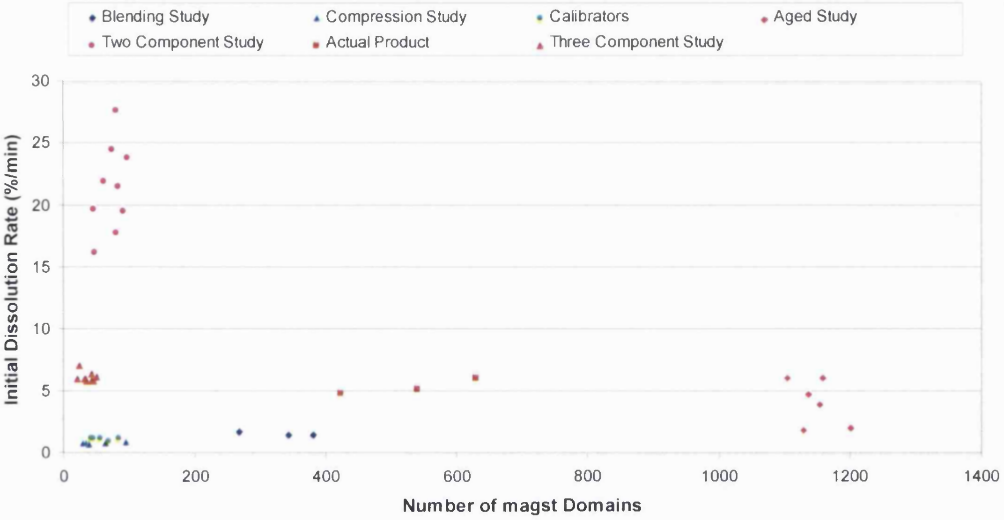

Figure 7-3: Comparison of the number of domains of the magnesium stearate with the initial dissolution rate.

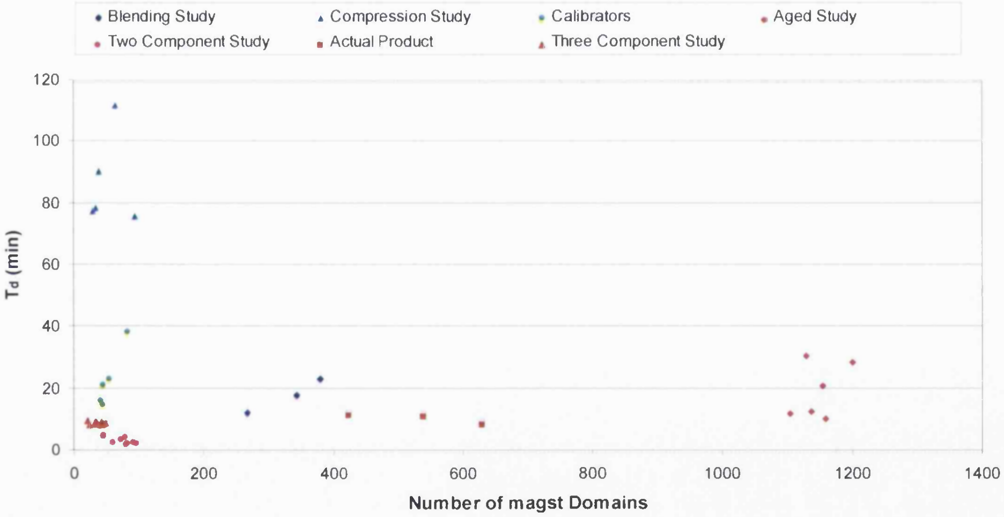

Figure 7-4: Comparison of the number of domains of the magnesium stearate with the T_d dissolution values.

MCC

The only relevant values for the MCC came from the V studies and the calibrators. These showed grouping within the separate studies when compared to the Weibull and initial dissolution rates, Figure 7-5.

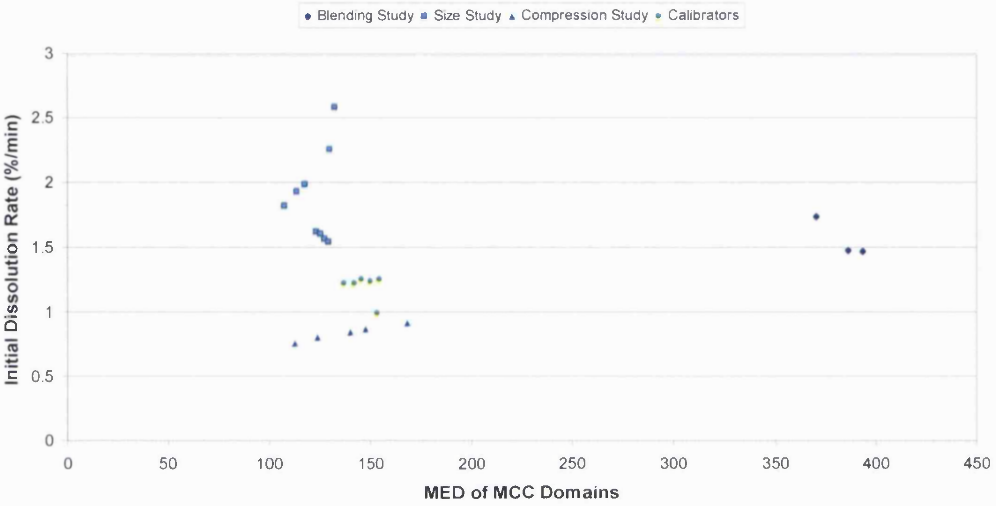

Figure 7-5: Comparison of the MED of the MCC domains with the initial dissolution rate.

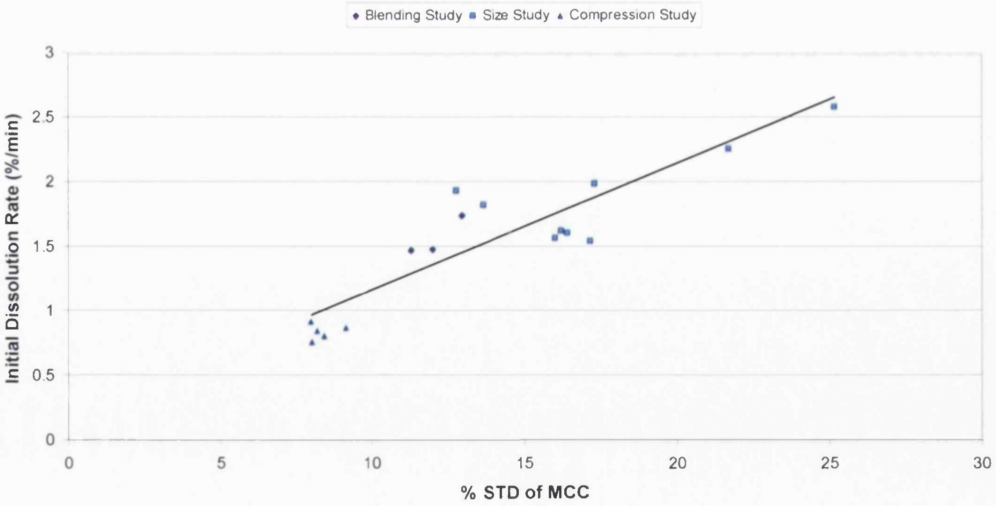

Figure 7-6: Comparison of the % STD of the MCC with the initial dissolution rate.

When the calibrator values were removed, the values for the % STD versus the initial rate appeared to show some linearity, see Figure 7-6. The best-fit linear trend line through the data points gave an r^2 value of 0.817. This was the only pattern observed at this point.

k_0 = 0.1799 + 0.0974*(% STD MCC)

This followed on from the results for the product V studies where the MCC distribution was found to be one of main features of the NIRM images that related to the variations observed in the dissolution rates.

Lactose

The values for the lactose component came from studies involving product W. As for the other components, the data grouped for the individual studies when the initial dissolution rate and the Weibull parameters were compared to the seven imaging parameters, Figure 7-7 and Figure 7-8.

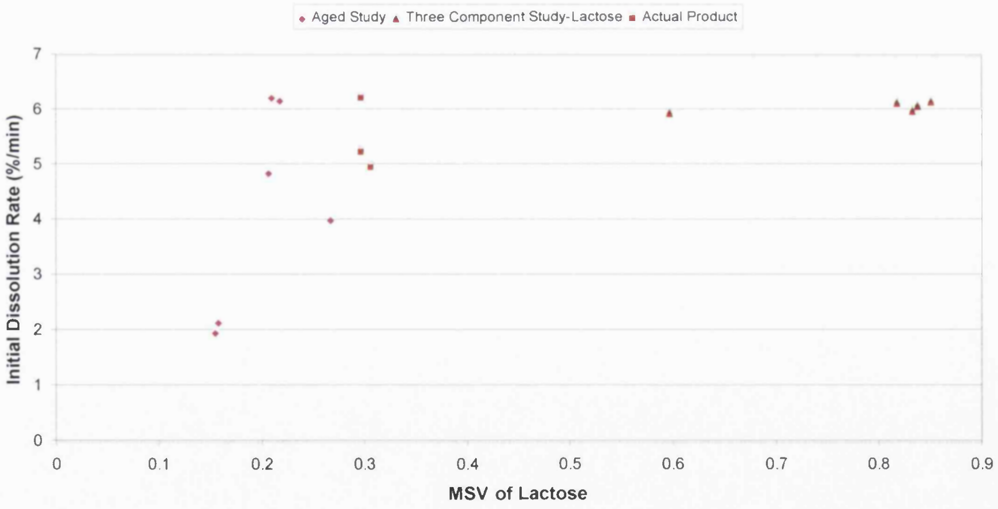

Figure 7-7: Comparison of the MSV of the lactose with the initial dissolution rate.

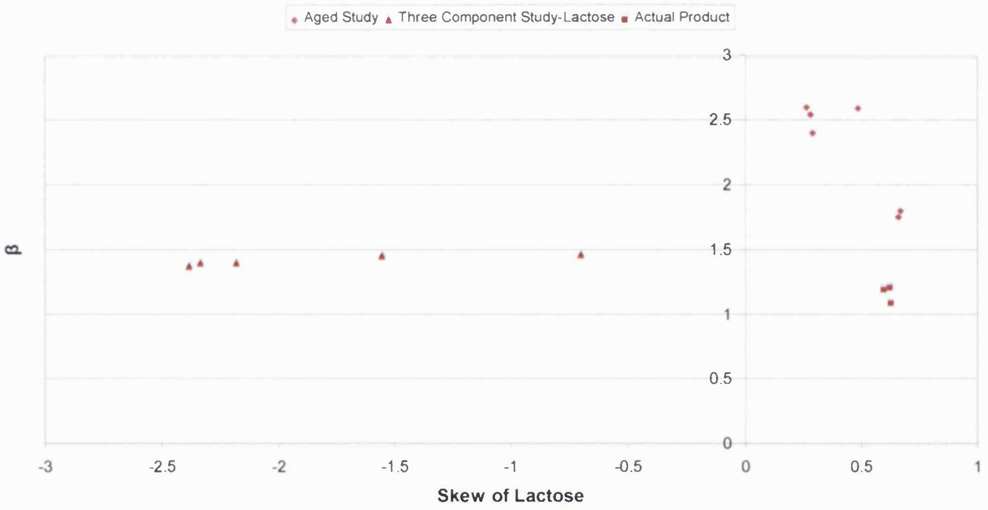

Figure 7-8: Comparison of the skew of the lactose with the β values.

Sucrose

The sucrose values came from the same studies as the lactose values. As for the all the previous components, the points grouped by individual study, see Figure 7-9 and Figure 7-10 (a). However, there were a couple of instances where it looked as though there may be a trend.

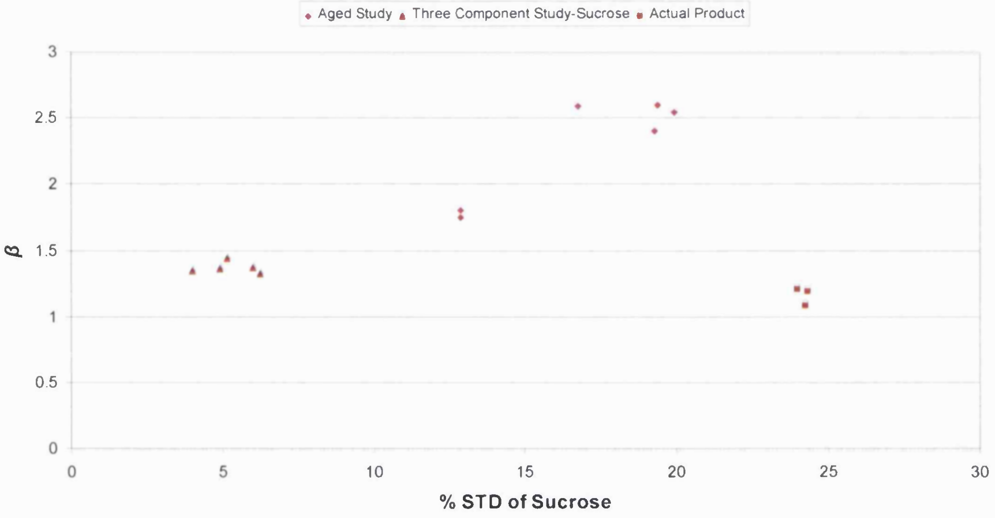

Figure 7-9: Comparison of the % STD of the sucrose with the β value from the dissolution parameters.

A quadratic polynomial trend line fits the data in Figure 7-10 with an r^2 of 0.82.

T_d = 0.0002*(number of domains sucrose)^2 – 0.1408*(number of domains sucrose) + 35.144

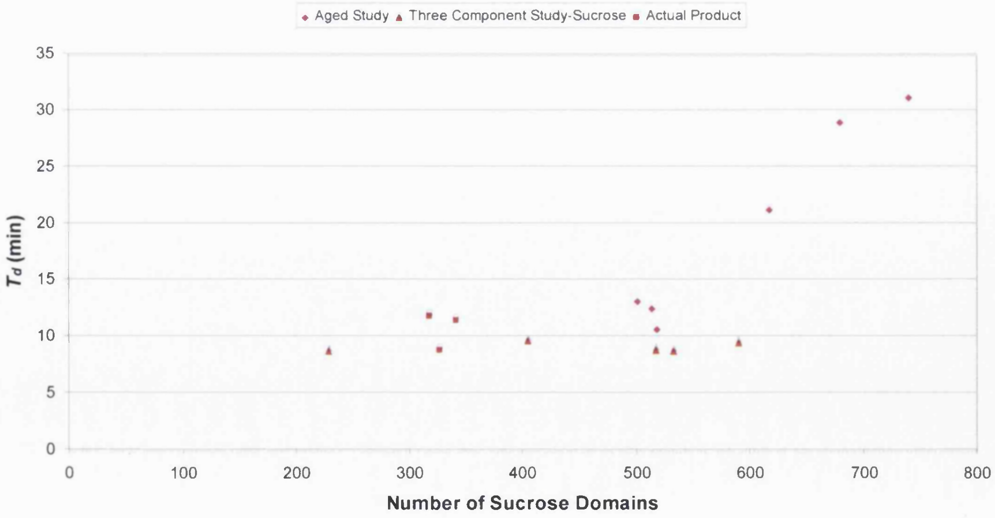

Figure 7-10: Comparison of the number of sucrose domains with T_d dissolution values.

It could be seen from the comparisons made for the components over all of the products that generally the data fell into groups related to the separate studies and did not necessarily group due to the API type. In this work it was difficult to compare the different studies on the same product types as each study did not necessarily include the same components as the full product blend and hence certain interactions may have been missing that could have affected the dissolution and/or images. However, it showed that the dissolution will be very specific to each individual set of samples, which may relate to the exact same product that has been manufactured at two different sites that do not use the same production process or equipment. As had been expected from previous personal experience in the pharmaceutical industry, it would not be possible to form any general statements regarding the NIRM imaging parameters and the dissolution data that would be applicable to any given product or even for the same type of product. There were three possible correlations observed from the data for the MCC (product V) and sucrose (product W), but these again were only related to the specific product data. However, they did follow the observations made from the individual studies of those products where MCC was important for product V and sucrose for product W. Any transferable correlations may have to be for samples of a specific pharmaceutical system known to contain the same components and that has been manufactured by the same method as the original samples the correlation was based on.

7.2.2 Comparisons of the Imaging and Dissolution Parameters within the Individual Product Studies

Blending Study for Product V

The results from this section in chapter four would lead to the expectation for some correlation with the values from the magnesium stearate component as the number of domains was found to increase with blending time, which in turn appeared to fit with the changes observed in the dissolution profiles. The other two components, MCC and D also showed some changes in the imaging parameters with the increased blending time, but some of the values were very similar for the ten and 15 minutes blends.

All of the relevant dissolution parameters were correlated in Excel to the seven image parameters for every component at each blend time from the Spotlight data. The correlations with a value of $r^2 = 0.994$ or above were focused on as this was the critical statistical value for three data points at the 5% significance level. Linear regression was performed on the data and the linearity of the relationship assessed.

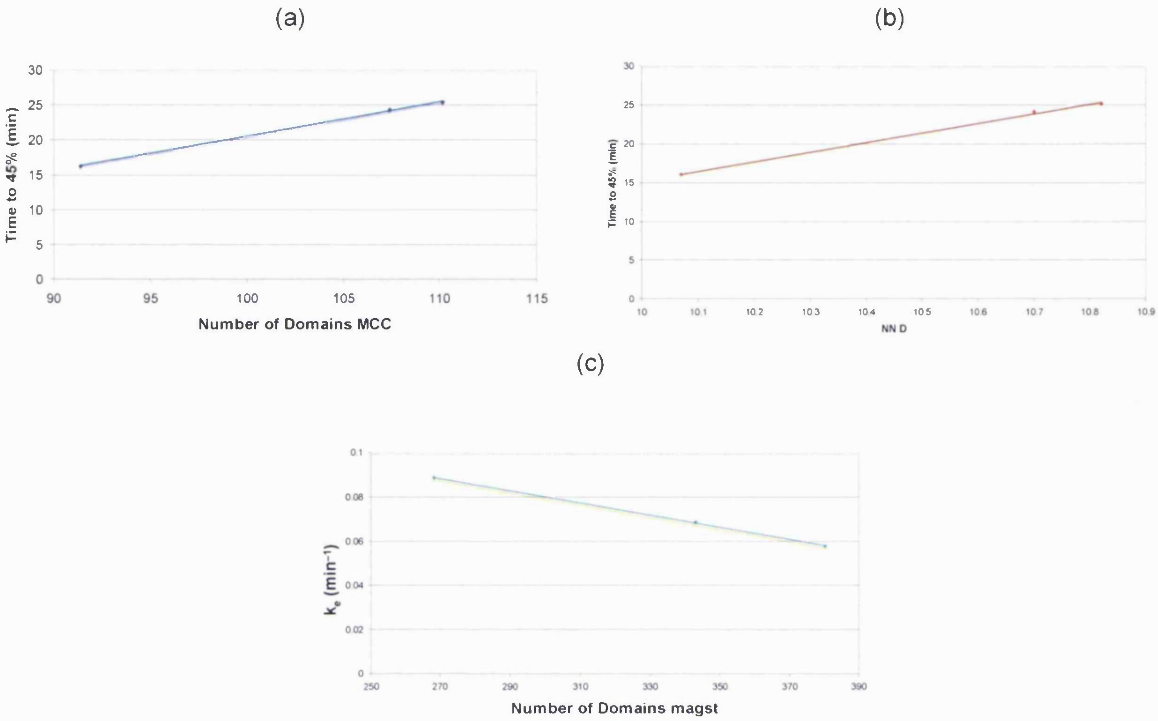

Figure 7-11: Examples of image parameters versus dissolution parameters for (a) MCC (—), (b) D (—) and (c) magnesium stearate (—) from the changing blending study.

Figure 7-11 shows an example for one of the regression trend lines for each component and Table 7-1 shows all the linear trends identified.

Regression Equations: Blending Study	r^2
k_e = 0.5824 – 0.0013*(MED MCC)	0.9969
k_0 = -2.3298 + 9.4598*(MSV MCC)	0.9974
t_{45} = –28.45 + 0.491*(number of domains MCC)	0.9988
t_{45} = –63.357 + 0.3278*(MED D)	0.9950
t_{45} = –107.99 + 12.357*(NN D)	0.9979
k_0 = 0.633 + 3.2457*(skew D)	0.9978
P_{20} = 120.65 – 0.2737*(MED D)	0.9998
k_e = 0.1631 – 0.0003*(number of domains magnesium stearate)	0.9994

Table 7-1: Regression equations for the blending study.

As was expected, the linear relationship for the magnesium stearate related to the number of domains present in the images. The regressions observed for the MCC followed the trend identified in the imaging parameter MED from chapter four, but there were a couple found that were not so obvious on first inspection. The results for D gave a similar outcome as MCC with regards to what was expected as well a few results that were not.

The dissolution of V in this case appeared to have a possible influence from all of the components present in the blend. The parameters related to the dissolution rate seemed to be related to the number of magnesium stearate domains as well as the size of the MCC domains. The "fixed point" values such as t_{45} had more of an affinity to the D results, which would follow the standard type of dissolution testing currently performed.

Changing Input Particle Size for Product V

The results from this section of chapter four showed that variations in the size fraction of the MCC used in a two components blend had a larger effect on the dissolution behaviour of the wafers than changes in the size fraction of the API, D used. An increase in the MCC size fraction showed the dissolution to initially progress faster, but if the size of the API was increased there was no apparent change in the dissolution observed. The imaging results had echoed these findings with a general increase in the size of the domains for the MCC and the D in the matrix when the size of the MCC was increased whereas the values stayed relatively similar for both components when the size of the D was varied. From these results it would be expected that there may be some relationships found between the imaging and dissolution data for the sieved MCC samples for both or either of the components with few or none found for the sieved D data.

The critical r^2 value used for the sieved MCC data was 0.771 and for the sieved D data it was 0.903.

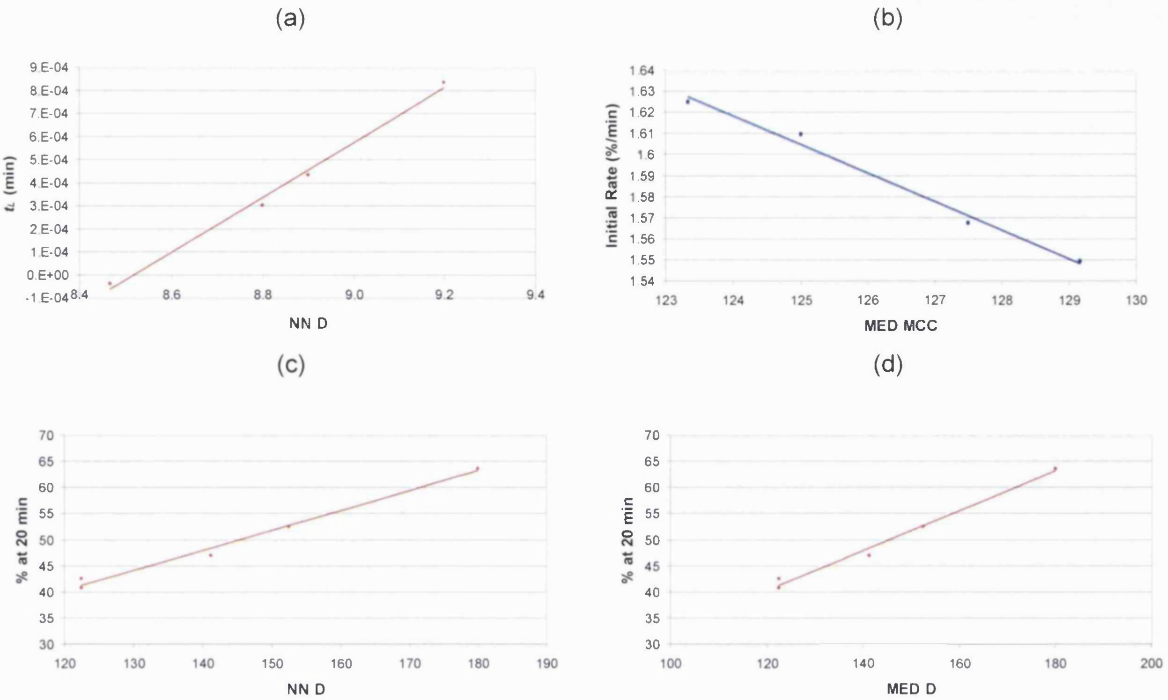
(a)
(b)
(c)
(d)

Figure 7-12: Examples of image parameters versus dissolution parameters for (a) D (—) and (b) MCC (—) in the sieved D blends and (c) and (d) D (—) in the sieved MCC blends from the changing input size study.

Figure 7-12 shows the best linear regressions. All the regression equations are shown in Table 7-2 and Table 7-3.

There were many more statistically significant correlations found for the sieved MCC blends than the sieved D blends. This was anticipated from the study results. These were split evenly between the two components as the change in the MCC size fraction caused differences in both the MCC and the D. There was also a fairly even split between the dissolution parameters related to the rate and those which were more of a fixed point value. However looking at the best of the correlations, the D seems to be associated more with the P_{20} and t_{60} values and the MCC had an affinity with the k_0 value. The sieved D blends only had five correlations and the majority were related to the D and the t_L. The only MCC correlation was with the k_0 value.

Regression Equations: Particle Size Study: Sieved MCC Blends	r^2
t_{60} = 39.315 – 1.4291*(% STD D)	0.822
P_{20} = 21.717 + 2.9512*(% STD D)	0.854
k_0 = 1.2099 + 0.0956*(% STD D)	0.811
t_{60} = 9.8176 + 0.0395*(number of domains D)	0.915
P_{20} = 82.195 – 0.0805 (number of domains D)	0.925
k_0 = 3.1759 – 0.0026*(number of domains D)	0.889
t_{60} = 52.338 – 0.1853*(MED D)	0.953
P_{20} = –8.3548 + 7.046*(MED D)	0.982
k_0 = 0.3283 + 0.0125*(MED D)	0.951
t_{60} = 53.79 – 3.4014*(NN D)	0.940
P_{20} = –5.1123 + 0.3821*(NN D)	0.988
k_0 = 0.2201 + 0.2302*(NN D)	0.948
t_{60} = 40.583 – 0.8214*(% STD MCC)	0.909
P_{20} = 19.163 + 1.6929*(% STD MCC)	0.940
k_0 = 1.1136 + 0.0556*(% STD MCC)	0.917
t_{60} = 0.0369 + 0.0575*(number of domains MCC)	0.849
k_0 = 3.8057 – 0.0038*(number of domains MCC)	0.802
t_{60} = 74.109 – 0.4028*(MED MCC)	0.907
P_{20} = –45.975 + 0.7972*(MED MCC)	0.865
k_0 = –1.1144 + 0.0269*(MED MCC)	0.893
t_{60} = 77.246 – 6.6617*(NN MCC)	0.892
P_{20} = –54.287 + 13.456*(NN MCC)	0.886
k_0 = –1.4193 + 0.4575*(NN MCC)	0.927

Table 7-2: Regression equations for the sieved MCC blends in the particle size study.

Regression Equations: Particle Size Study: Sieved D Blends	r^2
β = 1.6633 – 0.003*(number of domains D)	0.907
t_L = 0.0087 – 2E–5*(number of domains D)	0.990
t_L = –0.0122 + 8E–5*(MED D)	0.903
t_L = –0.0102 + 0.0012*(NN D)	0.993
k_0 = 3.3033 – 0.0136*(MED MCC)	0.989

Table 7-3: Regression equations for the sieved D blends in the particle size study.

Compression Force Study for Product V

The NIRM imaging results from chapter four showed that only the MCC had any specific trends with the increase in the compression force used to make the sample wafers. The number of domains increased, accompanied by a decrease in the mean size of the domains, which may have been the MCC becoming more spread out within the matrix. MCC acts as the glue or cement holding the rest of the blend together in a solid dosage form. If a force is applied to glue between two surfaces, it spreads out and becomes thinner, which was what appeared to be happening with the V blend upon increased compression force. In the region of steady state dissolution of the wafers produced, the profiles followed the order of compression force applied, with four tons as the fastest and 12 tons as the slowest. From these results, correlations would be anticipated between the MCC imaging parameters and the dissolution results.

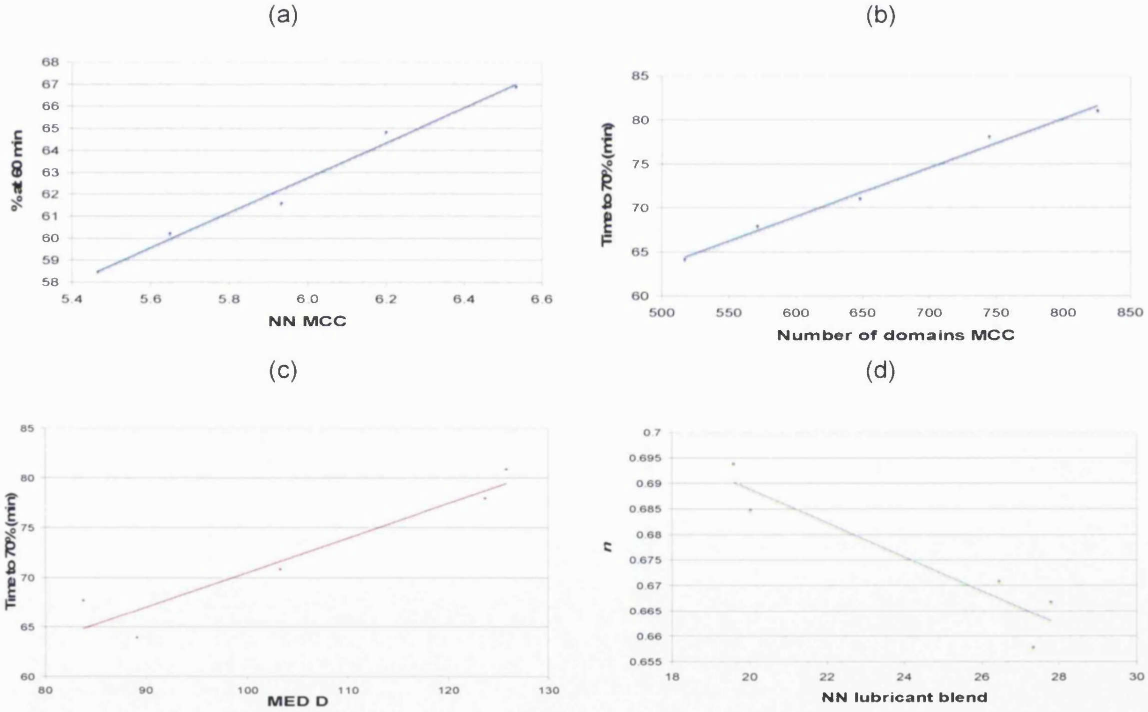
(a) (b) (c) (d)

Figure 7-13: Examples of image parameters versus dissolution parameters for MCC (—), D (—) and lubricant blend (—) from the changing compression force study.

Figure 7-13 shows the plots for the best linear correlations observed for each component. All of the regression equations for the relationships are given in Table 7-4.

Regression Equations: Compression Force Study	r^2
$n = 0.6501 + 0.0005*(\text{number of domains lubricant blend})$	0.787
$n = 0.7554 - 0.0033*(\text{NN lubricant blend})$	0.880
$t_{70} = 116.84 - 0.3202*(\text{MED MCC})$	0.969
$P_{60} = 80.046 - 0.0266*(\text{MED MCC})$	0.959
$k_0 = 0.4682 + 0.0027*(\text{MED MCC})$	0.994
$t_{70} = 169.36 - 16.258*(\text{NN MCC})$	0.972
$P_{60} = 15.085 + 7.9476*(\text{NN MCC})$	0.985
$k_0 = 0.0353 + 0.1351*(\text{NN MCC})$	0.977
$t_{70} = 35.66 + 0.0557*(\text{number of domains MCC})$	0.989
$P_{60} = 80.046 - 0.0266*(\text{number of domains MCC})$	0.959
$k_0 = 1.1432 + 0.0005*(\text{number of domains MCC})$	0.973
$\beta = 1.3791 + 0.8908*(\text{kurtosis MCC})$	0.921
$T_d = 66.033 + 29.941*(\text{kurtosis MCC})$	0.792
$t_L = -10.563 - 27.809*(\text{kurtosis MCC})$	0.913
$T_d = -376.68 + 1263*(\text{MSV MCC})$	0.785
$\beta = 1.3476 + 0.8528*(\text{kurtosis D})$	0.798
$T_d = 61.971 + 32.59*(\text{kurtosis D})$	0.886
$t_L = -8.4069 - 28.157*(\text{kurtosis D})$	0.884
$t_{70} = 126.33 - 0.0593*(\text{number of domains D})$	0.892
$P_{60} = 38.001 + 0.0269*(\text{number of domains D})$	0.780
$k_0 = 0.3972 + 0.0005*(\text{number of domains D})$	0.880
$t_{70} = 36.095 + 0.3463*(\text{MED D})$	0.903
$P_{60} = 79.623 - 0.1635*(\text{MED D})$	0.854
$k_0 = 1.1231 - 0.0027*(\text{MED D})$	0.793

Table 7-4: Regression equations for the compression force study.

The largest number of correlations were observed for the MCC and these gave the highest correlation coefficients compared the those from the D and lubricant blend. As for the previous two studies on this product, changes in the MCC appeared to have a major influence on the dissolution which could be related to variation in the NIRM images.

USP Prednisone Dissolution Calibrators

It was known that the USP dissolution calibrators could give variable dissolution dependant on their age. Several different lots of these tablets were sourced, one current and two expired, older lots. The initial NIRM imaging results for the tablets showed that the DCP appeared to change with the age of the tablet lot. Moving from the current lot at the time of the work, Lot O, to the oldest tablets, lot M there was an increase in the number of domains of DCP which decreased in size. However, the dissolution results did not show any trend with the age of the tablets. Lot M dissolved the slowest followed by lot O, leaving lot N with the fastest dissolution. Re-evaluation of the imaging results showed that generally, the greater the number of domains of stearic acid present in the tablets, the slower the dissolution would be. From these results, correlations would be expected for the stearic acid component for the NIRM imaging and dissolution parameters.

Upon correlating the NIRM imaging and dissolution parameters, using the critical r^2 value of 0.771, there were relationships observed for the stearic acid, API and DCP components, Figure 7-14.

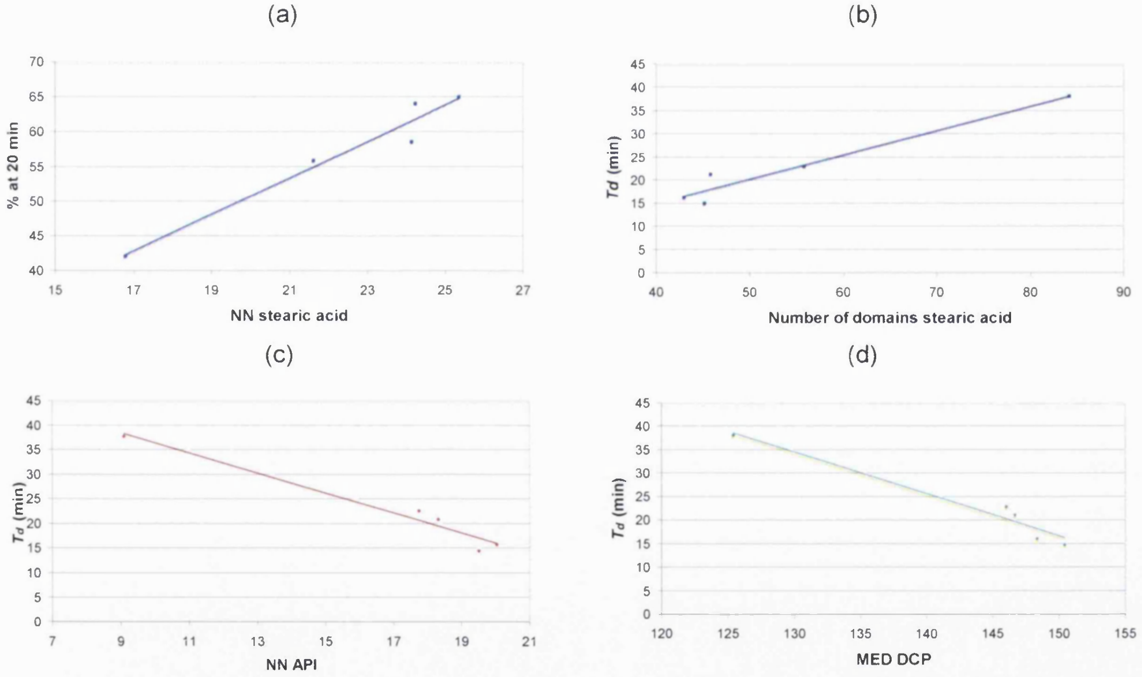
(a)
(b)
(c)
(d)

Figure 7-14: Examples of image parameters versus dissolution parameters for (a) and (b) stearic acid (—), (c) API (—) and (d) DCP (—) from the calibrator study.

All of the equations for the correlations are given in Table 7-5. As was anticipated from the trends observed in the study, the majority of the equations were related to the stearic acid component.

Regression Equations: Compression Force Study	r^2
T_d = 47.445 – 789336*(MSV stearic acid)	0.829
P_{20} = 64.127 – 2E–5*(% STD stearic acid)	0.850
P_{30} = 73.286 – 2E–5*(% STD stearic acid)	0.845
P_{20} = 85.902 – 0.5237*(number of domains stearic acid)	0.948
P_{30} = 94.02 – 0.4984*(number of domains stearic acid)	0.946
T_d = –5.9648 + 0.562*(number of domains stearic acid)	0.948
P_{20} = –1.7176 + 2.627*(NN stearic acid)	0.956
P_{30} = 10.599 + 2.5017*(NN stearic acid)	0.955
T_d = 81.325 – 2.6061*(NN stearic acid)	0.932
P_{20} = –67.212 + 0.8678*(MED DCP	0.917
P_{30} = –51.592 + 0.8252*(MED DCP)	0.914
T_d = 150.32 – 0.889*(MED DCP)	0.954
β = 0.874 – 433.05*(MSV API)	0.808
β = 0.9821 – 0.2524*(skew API)	0.849
P_{20} = 23.189 + 2.0063*(NN API)	0.952
P_{30} = 34.359 + 1.9082*(NN API)	0.949
T_d = 57.262 – 2.0284*(NN API)	0.964

Table 7-5: Regression equations for the calibrator study

There were also some correlations with the DCP component, which had shown some patterns with the age of the calibrators with respect to the number of domains and the amount of smaller domains present. The MED appeared to be related to the dissolution. The API also showed some correlations. Those with the highest correlation coefficients were related to the NN parameter, so on average, as the domain became more separated from each other, the dissolution would progress faster.

Aging Study for Product W

It was clear from the images in this study that the sucrose component dramatically changed in the lots that had OOS dissolution compared to those that had acceptable dissolution results. The images of the OOS samples contained very large domains of sucrose whereas the acceptable samples did not. The majority of the imaging parameters for the sucrose component showed a trend with the pattern observed in the dissolution profiles whereby the values for run three, four and five were similar to each other but different from the others. Run two and seven were also similar in value to one another and run one sat somewhere between the two groupings, but had a bias towards the group with the rapid dissolution rate in some cases. There was also an increase in the size of the API domains in the OOS samples, but this was to a much lesser extent than for the sucrose. Finally the skew for the lactose appeared to follow the dissolution trend; therefore relationships would be expected for these three components between the imaging and dissolution parameters. The critical value of the correlation coefficient was r^2 of 0.658 at the 5% significance level.

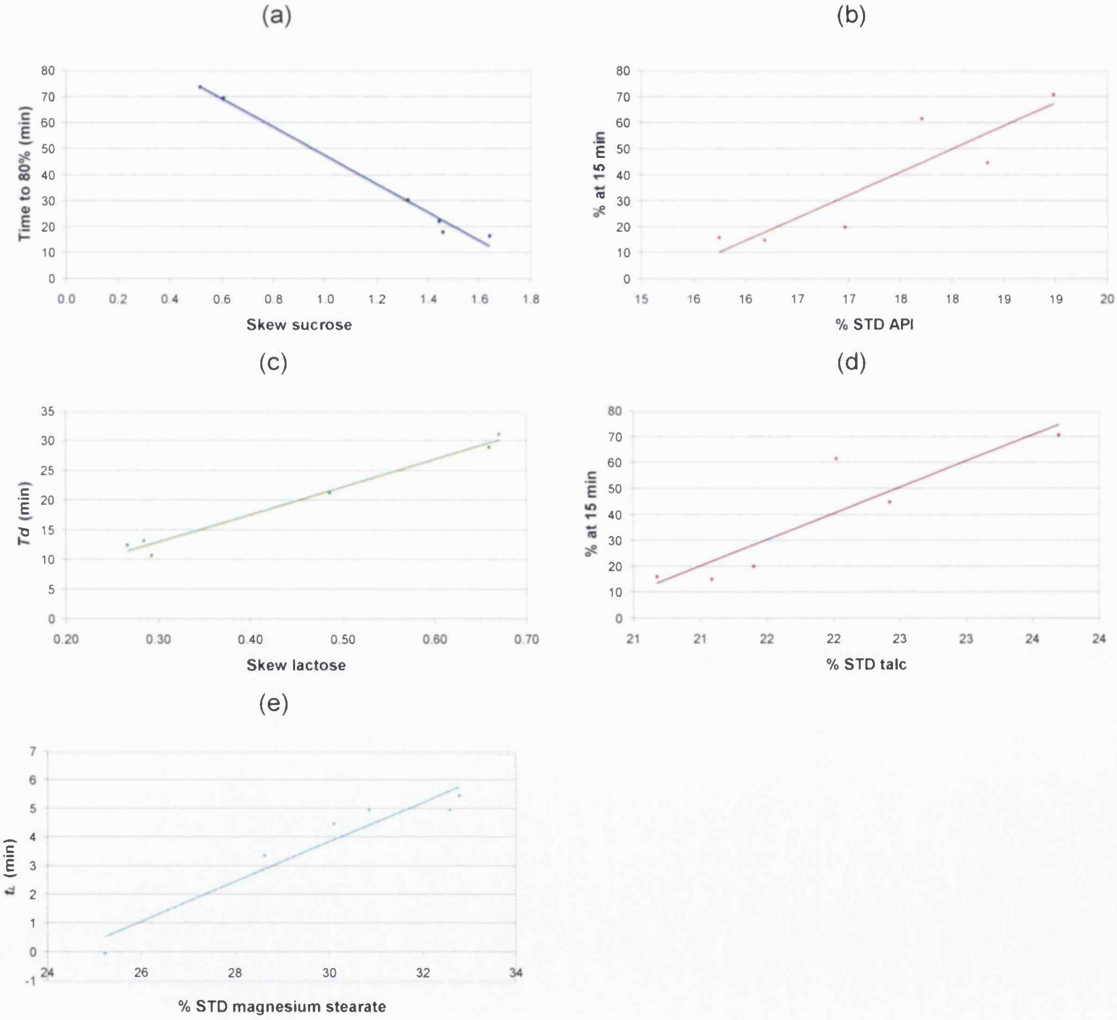
(a)

(b)

(c)

(d)

(e)

Figure 7-15: Examples of image parameters versus dissolution parameters for (a) sucrose (—), (b) API (—),(c) lactose (—), (d) talc (—) and (e) magnesium stearate (—) from the aged study.

Figure 7-15 shows examples of the relationships observed between the imaging and dissolution parameters with the highest correlation coefficients for each of the components. All the regression equations for all the relationships are shown in Table 7-6 and

Regression Equations: Aging Study Sucrose	r^2
t_{80} = 172.03 – 7.9187*(% STD sucrose)	0.967
P_{15} = –74.099 + 6.7017*(% STD sucrose)	0.787
k_0 = – 4.9429 + 0.5454*(% STD sucrose)	0.893
T_d = 65.072 – 2.6894*(% STD sucrose)	0.966
t_{80} = 102.09 – 54.44*(skew sucrose)	0.989
P_{15} = – 10.867 + 42.61*(skew sucrose)	0.689
k_0 = 0.1557 + 3.5083*(skew sucrose)	0.800
β = 0.9356 + 0.7399*(skew sucrose)	0.713
T_d = 40.257 – 17.58*(skew sucrose)	0.894
t_{80} = 100.37 – 17.768*(kurtosis sucrose)	0.948
k_0 = 0.4885 + 1.0811*(kurtosis sucrose)	0.683
β = 0.889 + 0.2616*(kurtosis sucrose)	0.802
T_d = 39.011 – 5.5384*(kurtosis sucrose)	0.798
t_{80} = –110.53 + 0.2506*(number of domains sucrose)	0.912
P_{15} = 170.39 – 0.2211*(number of domains sucrose)	0.807
k_0 = 14.717 – 0.0176*(number of domains sucrose)	0.875
T_d = –32.393 + 0.0876*(number of domains sucrose)	0.966
t_{80} = 363.57 – 2.727*(MED sucrose)	0.834
P_{15} = –278.25 + 2.6607*(MED sucrose)	0.903
k_0 = –19.592 + 0.2*(MED sucrose)	0.874
T_d = 137.71 – 0.9898*(MED sucrose)	0.953
t_{80} = 480.54 – 68.981*(NN sucrose)	0.892
P_{15} = –361.97 + 62.558*(NN sucrose)	0.834
k_0 = –28.176 + 5.0607*(NN sucrose)	0.935
T_d = 177.78 – 24.666*(NN sucrose)	0.988

Table 7-6: Regression equations for sucrose from the aging study.

Regression Equations: Aging Study	r^2
t_{80} = 363.3 – 18.746*(% STD API)	0.800
P_{15} = –266.21 + 17.611*(% STD API)	0.802
k_0 = – 17.251 + 1.2412*(% STD API)	0.683
T_d = 130.18 – 6.3755*(% STD API)	0.802
P_{15} = 300.82 – 0.9204*(number of domains API)	0.694
k_0 = 24.127 – 0.0698*(number of domains API)	0.685
T_d = –78.174+ 0.344*(number of domains API)	0.740
P_{15} = –510.42 + 2.4401*(MED API)	0.679
k_0 = –38.221 + 0.1887*(MED API)	0.696
T_d = 226.39 – 0.918*(MED API)	0.733
β = –0.1199 + 9.472*(MSV lactose)	0.883
β = 3.8152 – 0.062*(% STD lactose)	0.756
t_{80} = –20.458 + 132.78*(skew lactose)	0.921
P_{15} = 90.058 – 115.58*(skew lactose)	0.793
k_0 = 8.4886 – 9.5688*(skew lactose)	0.931
T_d = –0.8856 + 46.567*(skew lactose)	0.9816
t_L = 45.126 – 0.2873*(MED lactose)	0.811
β = 16.828 – 405.96*(MSV talc)	0.774
P_{15} = –405.44 + 20.3*(% STD talc)	0.807
β = –4.5177 + 112.41*(MSV magnesium stearate)	0.815
t_L = –16.852 + 0.6906*(% STD magnesium stearate)	0.919

Table 7-7: Regression equations for the API, lactose, talc and magnesium stearate from the aging study.

In this case for product W, the sucrose appeared to be a major influence on the dissolution as it produced the most correlations with the highest r^2 values. The correlations show that as the domains of sucrose increased in size with the component distribution widening, the dissolution rate increases. This was unexpected within the constraints of the study, as this was the only component to be kept consistent with respect to age throughout the blends. However, it was expected from the NIRM imaging and dissolution results.

The API and the lactose also gave correlations with r^2 above the critical value. They showed that, in a similar way to the sucrose, as the size of the API increased, the dissolution proceeded faster. However, the correlation with the skew of the lactose meant that as this value decreased the dissolution rate increase. A decrease in this value would point towards an increase in the homogeneity of the lactose as it means there was a decrease in the tailing on the right hand side, which relate to the presence of larger lumps.

The talc and the magnesium stearate also gave a few correlations, which showed that if the abundance present increased and decreased, respectively that the dissolution would proceed quicker. However, these relationships were not as strong as those for the sucrose.

Two Component Study for Product W

This particular study was split into two parts as the samples were from a design of experiment where the blending and compression applied to the blend was varied.

Initially the results were grouped according to the blending time in a Turbula, which would show if the variation in compression gave any effects. The dissolution of the capsule samples was very rapid; they all reached a plateau value by approximately ten minutes into the dissolution. Therefore, visually, it was difficult to distinguish if there were any differences between the profiles. There was a decrease in the number of magnesium stearate domains in the samples with no extra Turbula blending and there appeared to be the formation of smaller domains of both components for the one hour blending time samples. The ten hour blending consequently caused the opposite effect to the one hour, as there was an increase in the mean size for the domains of both components.

The relationships with a correlation coefficient value greater than or equal to the critical value of 0.994 at the 5% significance level were accepted. Evaluation of the data for relationships between the imaging and dissolution parameters showed that there were none found for either component for the one hour samples. The magnesium stearate showed correlations for the data from samples with none and ten hours Turbula blending Figure 7-16. The API produced correlations for only the ten hour sample data, Figure 7-17. The resulting equations are given in Table 7-8.

Regression Equations: Two Component Study			
API (S) Ten Hours Turbula	**r^2**	**Magnesium stearate No Turbula**	**r^2**
β = 34.985 –36.274*(MSV API)	0.999	P_5 = 151.04 – 8.3462*(% STD magst)	0.999
T_d = 14.019 – 0.0912*(number of domains API)	0.994	t_{45} = 3.1057 – 3.4047*(skew magst)	0.995
T_d = –12.931+ 0.0992*(MED API)	0.998	k_0 = 29.539 + 32.382*(skew magst)	0.997
Magnesium stearate Ten Hours Turbula	**r^2**		
β = –1.847 +38.99*(MSV magst)	0.997		
T_d = 4.0744 + 10.034*(skew magst)	0.995		
T_d = – 0.6438 + 0.1206*(MED magst)	1		

Table 7-8: Regression equations for the two component study in blending time order.

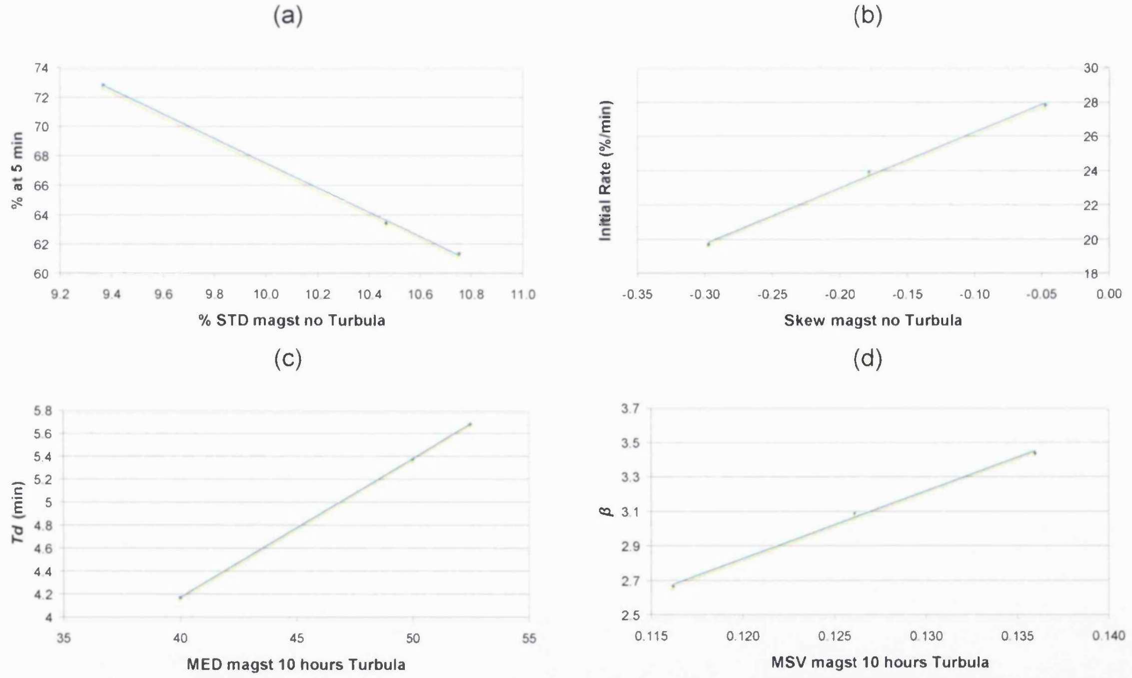
(a)

(b)

(c)

(d)

Figure 7-16: Examples of image parameters versus dissolution parameters for magnesium stearate (—) with no Turbula blending (a) and (b) and ten hours Turbula blending (c) and (d) from the two component study, blending order.

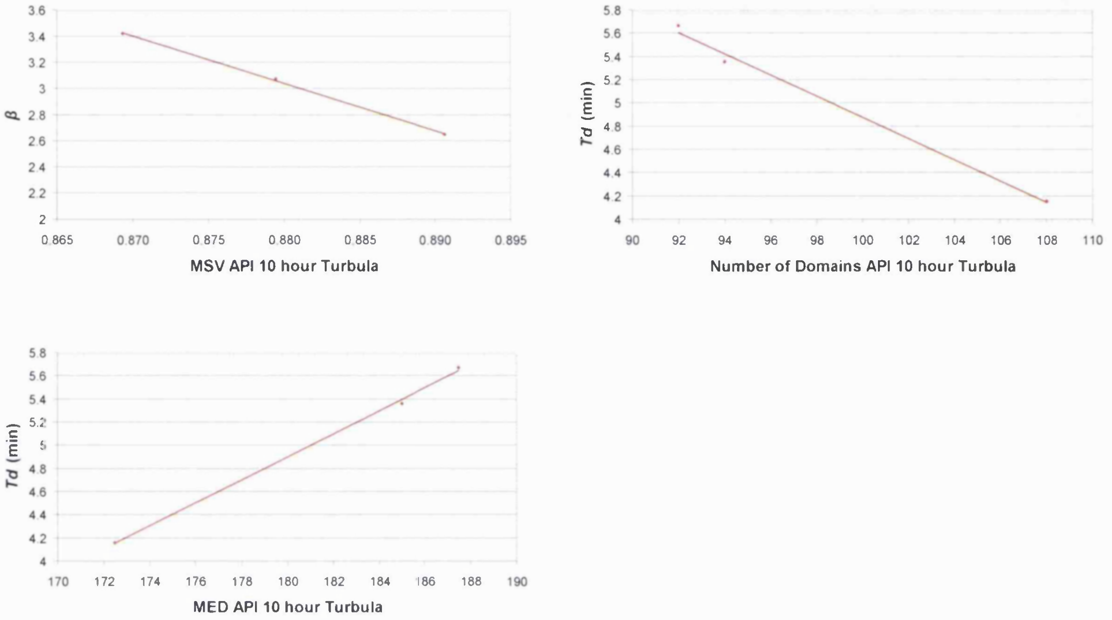

Figure 7-17: Examples of image parameters versus dissolution parameters for API (—) from the two component study, blending order.

The equations for the API showed that if the MED or MSV increased it would slow the dissolution, but if the number of domains increased then it would enhance the dissolution for the ten hour blend. Here the increase compression caused a decrease in the number and an increase in the size of the API domains which caused an increase in the T_d value which relates to the time to 63.2% dissolution.

The magnesium stearate in the samples with no Turbula blending showed, as the compression increased, the % STD of the distribution and the number of domains decreased i.e. the magnesium stearate became more integrated into the matrix. This caused the percentage dissolved at five minutes to increase, hence the dissolution was faster. For the ten hour blend, as the compression increased, the MED increased along with the skew of the distribution. This led to a decrease in the initial rate and consequently the T_d value increased as it was taking longer to dissolve. It can be concluded that the magnesium stearate had more correlation between the changes seen in the images and the dissolution caused by the variation of the compression applied. Also it appeared that an increase in the Turbula blending combined with an increase in the compression used to make the capsule samples would result in slower dissolution.

The data were then rearranged into compression order to evaluate any changes due to the extra blending time in the Turbula blender. The NIRM image parameters showed that the increase in blending from none to ten hours caused an increase in size of the magnesium stearate with a decrease in the number of domains present in the samples with mild and hard compression. The samples with no compression however had the largest domains in the one hour Turbula blend for both the magnesium stearate and API and the opposite effect was seen for the API in the hard compression samples. The mild compression sample showed an increase in the size accompanied with a decrease in the number for the API with the increased blending. The same dissolution profiles as in the previous section of the two component study were also rearranged and showed slightly more variation than before. Some of the dissolution parameters showed trends with the increase in blending applied, while others had two similar values and the third was either higher or lower.

Evaluation of the data for relationships between the imaging and dissolution parameters showed results for both components at all compression forces, see Figure 7-18 and Figure 7-19 for examples.

The equations related to the correlations are given in Table 7-9.

Regression Equations: Two Component Study

API Mild Compression	r^2	**Magnesium stearate Mild Compression**	r^2
k_0 = 54.529 – 39.727*(MSV API)	0.994	P_5 = 465.21 – 57.218*(NN magst)	0.998
P_5 = 357.82 – 1.8941*(MED API)	0.999		
API Hard Compression	r^2	**Magnesium stearate Hard Compression**	r^2
β = –2.3978 +3.0832*(% STD API)	0.994	P_5 = 26.6 + 283.89*(kurtosis magst)	0.999
P_5 = 55.74 + 217.22*(kurtosis API)	0.999	T_d =5.8788 – 19.716*(kurtosis magst)	0.998
k_0 = 22.988 + 60.811*(kurtosis API)	0.999		

Table 7-9: Regression equations for the two component study in compression order.

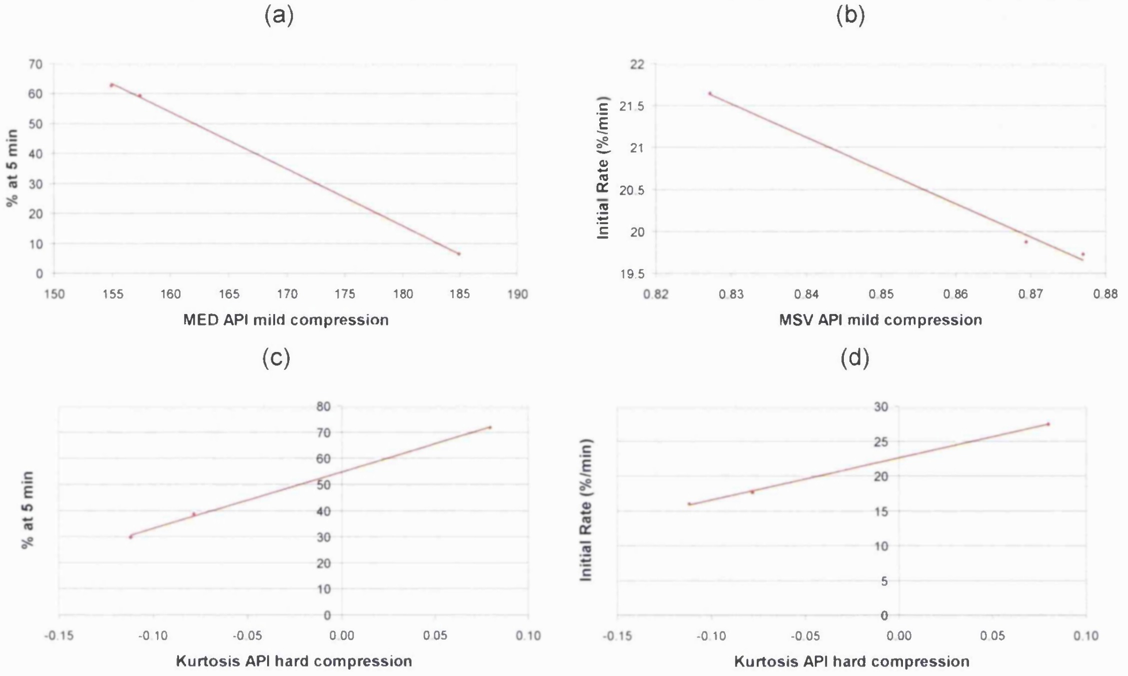
(a)

(b)

(c)

(d)

Figure 7-18: Examples of image parameters versus dissolution parameters for API (—) from the two component study, compression order with (a) and (b) mild and (c) and (d) hard compression.

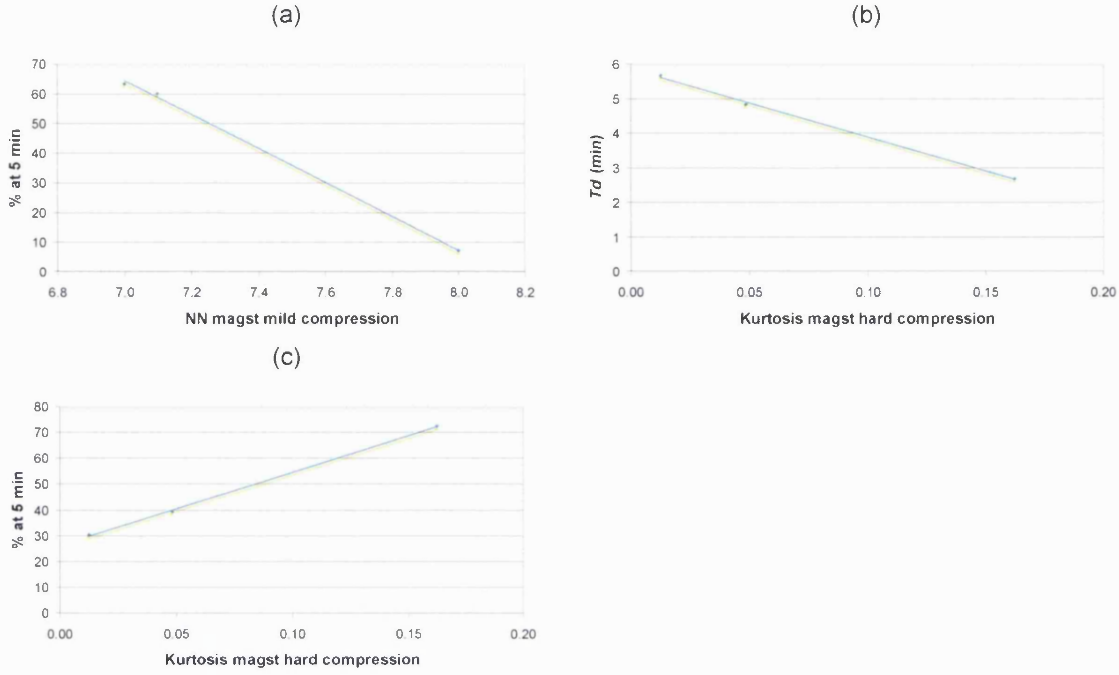

Figure 7-19: Examples of image parameters versus dissolution parameters for magnesium stearate (—) from the two component study, compression order with (a) mild and (b) and (c).hard compression.

For the blends mild compression, an increase in the abundance (MSV) or in the size of the domains for both API and magnesium stearate caused by the change in blending appeared to slow the dissolution rate. For the magnesium stearate an increase in the NN value would relate to the domains becoming further away from one another, which usually relates to an increase in the size. For the hard compression samples, the relationships found were related to the % STD and kurtosis value for the API and magnesium stearate. The increased blending combined with the hard compression resulted in the distributions of the components to change i.e. any tailing was reduced. This would usually be associated with the blend becoming more homogeneous, but combined with an increase in the % STD would point towards the decrease of long, thin tails to form more substantial, thicker ends to the distribution as more of the domains increase in size.

Generally, from the overall two components study, the larger the domains and the higher the abundance, the slower the dissolution will proceed. The magnesium stearate showed more correlations for changes due to the compression compared to the API. The correlations were fairly evenly distributed between the two components for the blending comparison, which introduced more variations in the images that could be related to the dissolution parameters than the changes in compression.

Three Component Study for Product W

Following on from the aging and two component studies, two types of three component blends were produced using varying blending times. The blends were API, magnesium stearate and either sucrose or lactose.

The NIRM images highlighted the tendency for the sucrose to form very large domains as the blending time was extended. It was also noted that the API was behaving as filler around the discrete areas of sucrose formed, which may have left it more available for dissolution. The opposite situation was observed for the lactose blends, with the lactose around the API. The average dissolution profiles for both blend types were very similar in shape, but the individual profiles for the sucrose were more variable than those for the lactose blend samples. There were general increases with blending seen within the sucrose dissolution parameters, e.g. the initial rate showed a general increase, so the sucrose lumps seemed to allow the dissolution to progress slightly quicker. In general there was a lack of trends with blending time for the imaging and dissolution parameters for both blend types therefore good correlations were not anticipated.

The correlations with a value of r^2 = 0.771 or above were focused on as this was the critical statistical value for three data points at the 5% significance level. There was only one correlation found for the sucrose blends and four for the lactose blends.

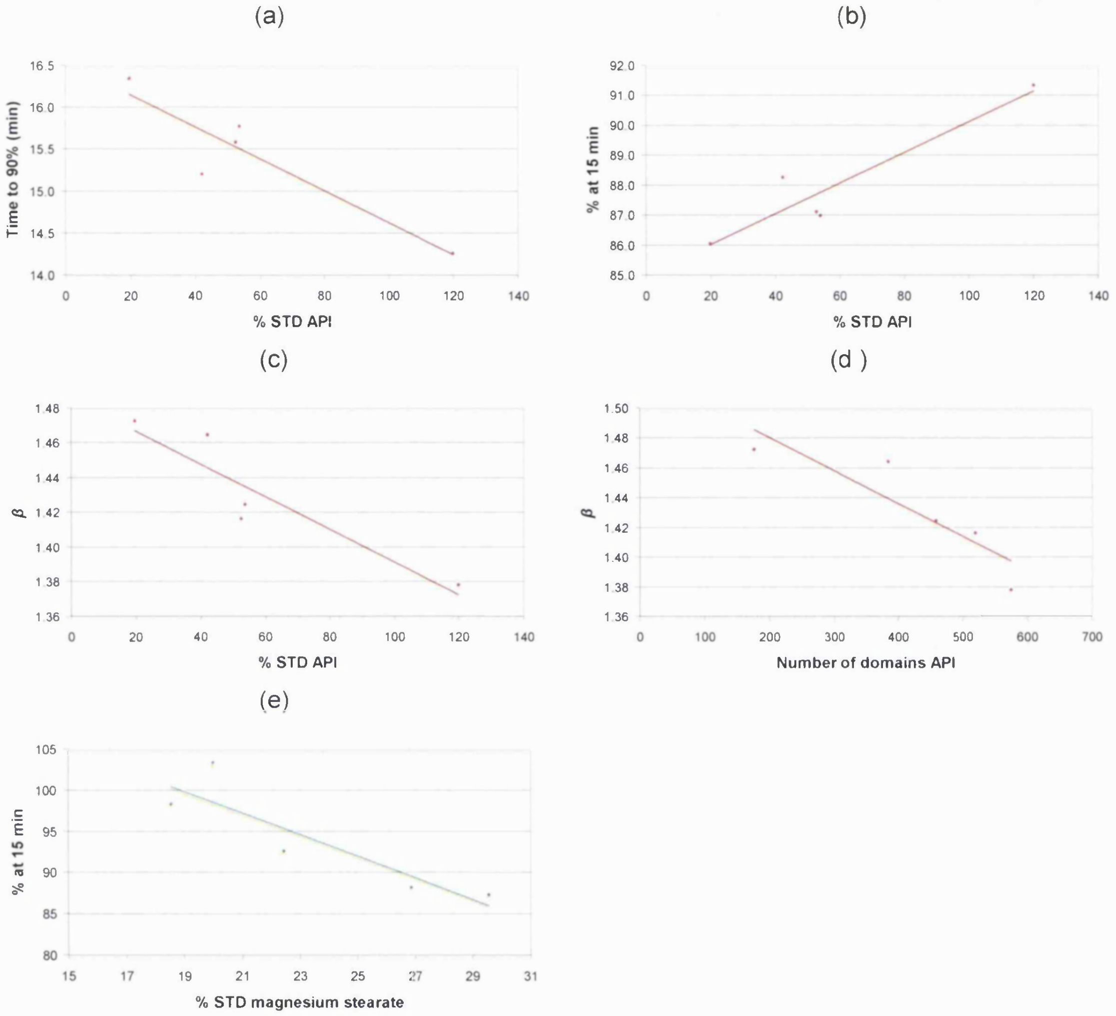

Figure 7-20: Examples of image parameters versus dissolution parameters for (a) - (d) API (—) from the lactose blends and (e) magnesium stearate (—) from the sucrose blends in the three component study.

Regression Equations: Three Component Study	r^2
P_{15} = 124.92 – 1.31.27*(% STD magnesium stearate)	0.793
t_{90} = 16.569 – 0.0191*(% STD API)	0.841
P_{15} = 85.087 + 0.0513*(% STD API)	0.872
β = 1.4871 – 0.0009*(% STD API)	0.845
β = 1.5261 – 0.0002*(number of domains API)	0.795

Table 7-10: Regression equations for the three component study.

In the lactose blends, it appeared that as the % STD and the number of domains of the API increased, the dissolution rate increased. This can be seen from the RGB images and the dissolution profiles. In the RGB of the 15 minute blend there are very large lumps combined with an increase in very small domains of API compared to the other blending times and it was this blend that gave dissolution profiles with a slightly faster dissolution than the others.

The correlation for the magnesium stearate from the sucrose blends showed that as the % STD decreased, the dissolution rate increased. Evaluating the other imaging parameters for the magnesium stearate in the sucrose blends it would appear that in this case the % STD did not relate to the homogeneity. For example, the distribution of magnesium stearate for the 7 minute blend did not have large tails as the domains were fairly well separated (high NN value) therefore the remainder of the distribution would have been spread wider than the others and hence it had a higher % STD, but it was not less homogeneous. In this case, the reverse could be seen to be true e.g. the 60 minute blend dissolved the fastest and it was the most heterogeneous with respect to the magnesium stearate.

The lack of correlation with the sucrose could have been due in part to the domain statistics. The increased blending caused the formation of a few very large clumps of sucrose. However, there were also smaller domains formed in a much larger proportion which appeared to skew the MED statistic as it is an average value. However, it was possible to see from the RGB images and the dissolution profiles that the sucrose was more variable with blending than the lactose, which caused changes in the dissolution.

Actual Dissolution Study

These were samples of product W that were from a manufacturing site that had experienced a dissolution problem. The OOS blend was dissolving too fast. It was found that re-working the OOS blend would subsequently cause it to pass the specification. The images of the three blends moving from the pass to re-worked then OOS samples showed that the number of API and magnesium stearate domains increased. The skew and kurtosis value for the sucrose and the kurtosis value of the lactose also showed a decrease moving in the same order. The dissolution profiles showed the OOS as the fastest followed by the re-work then the passing blends. Therefore some correlations would be anticipated between the imaging and dissolution parameters for the API, magnesium stearate and possibly the other two major components.

The critical value for the correlation coefficient was 0.994 for a 5% significance level. The comparison of the parameters showed relationships for the magnesium stearate and sucrose, Figure 7-21.

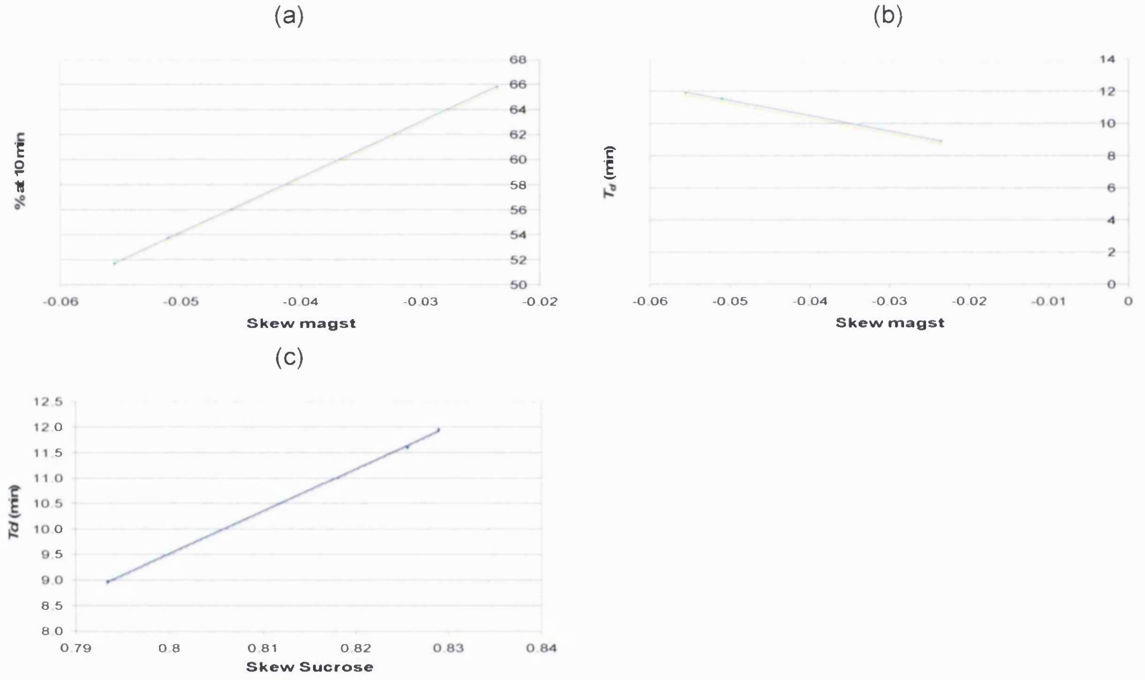

Figure 7-21: Examples of image parameters versus dissolution parameters for (a) and (b) magnesium stearate (—) and (c) sucrose (—) from the actual dissolution study.

The equations are given for all the correlations found in Table 7-11. The slight decrease in the skew of the sucrose from pass to re-work to OOS would have related to a small decrease in the tailing to the right hand side of the pixel distribution, usually associated with the presence of larger domains. In this case there was a decrease in the skew due to a general increase in domains that were larger e.g. longer, thinner tails caused by a few pixels of high abundance for the component became more integrated into the main body of the distribution, accompanied with an increase in the left hand tail due to the subsequent pixels that had an even lower abundance for the sucrose. This may have been the contributing factor towards the faster dissolution of the OOS blend. The skew for the magnesium stearate became less negative for the same sample order due to the presence of an increased number of domains in the OOS. Some were forming relatively distinct domains that were larger than the others, which would create pixels of a higher abundance of the magnesium stearate hence moving the skew towards the positive end.

Regression Equations: Actual Dissolution Study	r^2
P_{10} = 373.85 – 388.1*(skew sucrose)	0.997
T_d = –56.886 + 83.014*(skew sucrose)	0.999
t_{80} = 9.414 – 203.15*(skew magst)	0.999
P_{10} -=76.293 + 441.02*(skew magst)	1.000
T_d = 6.7672 – 94.208*(skew magst)	0.999

Table 7-11: Regression equations for the actual dissolution study.

7.3 Conclusions

The comparisons for all of the components over all of the products did not show any correlations between the imaging and dissolution parameters that could apply to any given pharmaceutical product. Therefore any general statements made related to a relationship between NIRM imaging and dissolution would be more product specific. This was seen for the MCC in the product V studies. If there was an increase in the % STD for the MCC, i.e. a spreading of the distribution caused by the formation of larger domains, then the dissolution rate would be predicted to increase. For product W, it would be predicted from the general comparison that an increase in the number of domains of sucrose (usually accompanied by an increase in their size) would lead to a decrease in the dissolution rate as the time to 63.2 % would increase.

The individual comparisons made for the product V studies showed that the changes in blending, size and compression force all caused variations in the MCC component, which could be correlated to dissolution rate. The API, D showed differences for the blending and size studies with correlation seen with the "fixed point" dissolution parameters. Changes in the magnesium stearate for the blending study were also correlated to the dissolution rate. For product V, the majority of the correlations were related to the MCC with some contribution from the remainder of the blend.

The USP dissolution calibrators showed the majority of correlations for the stearic acid component, which was anticipated from the NIRM imaging and dissolution results in chapter five. There were also some correlations with the DCP component, where the MED appeared to be related to the dissolution. There were also correlations with the API that showed as the domains became more separated from each other, the dissolution would progress faster.

The four studies for product W highlighted that the sucrose distribution and the magnesium stearate appeared to have a major influence on the dissolution behaviour as these provided nearly all of the correlations seen for the samples containing the full blend. The two component study showed that changing the compression used to produce the capsule samples had an effect on the magnesium stearate more than the API. When the amount of blending applied was increase, it affected both components whereby generally if there was a higher abundance or large domains then the dissolution rate would decrease. Blending time therefore had a large influence on the images and dissolution for product W. The three component study was an extension to the initial two studies, but as predicted from the results, there were not many statistically significant correlations found. The relationships that did exist were related to the API in the lactose blends and the magnesium stearate in the sucrose blends, not the sucrose itself as expected. The correlations showed that as there were large lumps of API formed, the dissolution would proceed faster. However it could also be seen from the NIRM images in a more qualitative way that the increase in blending caused the sucrose to form very large lumps, which subsequently caused the dissolution to occur faster. This emphasised the finding from the aging study where this was also seen. The final study on some real samples of product W produced more correlations for sucrose and magnesium stearate in relation to the distribution of the component in the images related to the overall size of the domains. It pointed towards the sucrose having slightly larger domains in the OSS, fast dissolution samples combined with slightly larger magnesium stearate domains, which could be observed from the RGB images.

It was concluded from all of the studies that in general any changes seen in the dissolution behaviour could be related to more than one component in the sample. These changes may also be observed in the NIRM images and in some cases correlation can be made between the two on a system by system basis.

8 Overall Conclusions

The dissolution test remains a vitally important, well established, standardised method that is a regulatory requirement for the approval of all new drugs by all regulatory authorities. It has acquired this status as it is the major test that provides information on the *in vitro* availability of a drug substance/API under simulated *in vivo* conditions i.e. the *in vitro* results might be applicable to the prediction of the *in vivo* behaviour of the drug. Traditionally the test monitors the duration of the API release using specific time point sampling and assaying the sample using HPLC or UV, which allows the user to determine if the product is within the QC specification. When the situation arises where the sample is not within the specification, no insight into what may have caused the failing result can be gained from the dissolution results and as with the majority of end-product testing, the sample is no longer available for further analysis. The actual process of dissolution can be subject to variability from a wide range of sources including tablet positioning, hydrodynamics, insufficient medium degassing and various changes in the mechanical aspect of the apparatus. It would be advantageous to be able to predict the dissolution performance of a sample via a non-destructive method that was less susceptible to variation out with that found in the sample. The aim of this work was to evaluate NIRM imaging as a means to predict dissolution performance by correlating the data from the imaging to data from dissolution with fibre-optic monitoring.

Individual projects were constructed to gain a wider understanding of factors that could influence the results from the imaging data and the dissolution profiles, which included variation of certain physical parameters e.g. blending time, particle size, compression and age of samples for blends produced based on Pfizer products as well as the evaluation of actual sample of products that had experienced variable dissolution.

Numerical parameters were a pre-requisite for the correlation between the imaging and dissolution data. The imaging parameters utilised described the distribution of the component within the image and also the average number and size of the areas. The parameters for the dissolution profiles were determined using various methods including measuring the % dissolved at a set time, as a reference to the standard measurements carried out as well as calculation of the initial rate of the steady state portion of the profile and the application of certain models to the profiles. There were many different modelling methods available and the ones selected were those found in the literature that had previously been used for dissolution profiles and were preferably not over complex.

The initial focus of the work fell on the imaging results to assess the feasibility of producing blends in the laboratory for the further studies to be conducted. Comparison of a blend manufactured based on a three component Pfizer product to samples of the commercial blend of that product highlighted some differences, but none of which could not be explained through differences introduced via the scaled down production method. The laboratory blend was found to be more consistent to a certain extent than the commercial blend from the NIRS results.

The MSV of the images was evaluated. The MSV was a measure of the average contribution for that component over all the pixels in the particular image. It had previously been stated that this value was related to the % m/m present in the formulation of the sample. It was apparent, however, that this was not a direct relationship in this case and the use of a calibration set of blends with various combinations of % m/m allowed a quadratic polynomial to be established. It was possible to accurately predict the % m/m of a validation set using the relationship created.

Having determined that blends could be produced in the laboratory, the next study was carried out to evaluate how changes in certain physical parameters of blends based on an actual product would affect the images and/or dissolution profiles. Sample blends were produced with differing blending time, input particle size and compression force applied to produce the wafer dosage forms modelled on a three component Pfizer product. All three blend variations produced changes in both the imaging and dissolution parameters measured. Increasing the blending time appeared to cause an increased integration of the lubricant blend into the matrix along with an increase in the size of the MCC domains. This was complemented by a slowing in the dissolution profile upon the first increasing blending time. The correlations found between the imaging and dissolution parameters were related to all the components in the blend. The MCC and lubricant blend appeared to be more correlated with the parameters associated with the dissolution rate and the API seemed to be related more to the parameters that were taken at a fixed point such as the % dissolved at 20 minutes. This showed that blending time can produce changes that will affect the entire blend with respect to NIRM imaging and dissolution.

The next results were acquired from blends where the API and the MCC were sieved and combined with unsieved fractions to investigate which component would exert the largest effect on the matrix. The results clearly showed the sieved MCC caused the formation of generally much larger domains of both components in the NIRM images with increasing size fraction used, which in turn caused an increase in the dissolution observed. The increase in the rate of dissolution was attributed to the inability of the larger particle sizes of MCC to mould around the API in the blend wafers upon compression, therefore leaving it more open and exposed to the medium during the dissolution process. Both sets of results for the sieved API, however, remained relatively consistent regardless of the size fraction present in the blend.

The dissolution progressed in two stages, possibly related to the wafer swelling then a burst effect and consequently all of the modelling was applied to the initial dissolution stage. The correlations observed for the NIRM imaging and dissolution parameters showed a similar theme as for the blending study. The only relationship related to the rate was with the MCC and the others were associated with the fixed point values and the API.

The final part of this physical study gave dissolution results that were expected due to knowledge that an increase in compression would be accompanied by an increase in the sample hardness and compaction, therefore it would take the dissolution medium longer to break the sample up to dissolve. The imaging results provided a definite trend with compression force applied for the MCC. As the force increased the number of the MCC domains increased in association with a decrease in their mean size. So it was as if it was being forced to spread out within the matrix, breaking up larger areas into smaller ones as it moulded around the other components. The API domains showed a general decrease with force used, but upon the correlation of the NIRM and dissolution parameters, all the subsequent regression equation were related to the MCC. The three sections of this study emphasised that differences observed in the MCC for this product seemed to be critical to the results of certain dissolution parameters, which could possibly be predicted from using imaging data combined with the regression equations.

Moving on from the laboratory manufactured samples, the successive project conducted involved a product which historically had a reputation for variable dissolution, the USP 10 mg prednisone, disintegrating, dissolution calibrator tablets. The FDA were aware that the calibrator dissolution could alter with time, but it was not stated or known what caused the change. These calibrators were supposed to function as a reference standard and a means for chemical calibration of dissolution apparatus. Therefore, the possibility for variable dissolution results would be far from an ideal situation with respect to this. Analysis of the NIRM imaging and dissolution results for the current calibrator lot compared to those from two expired lots obtained highlighted two main trends. The first was in the imaging data, which showed the number if domains of the DCP component generally increased with the age of the tablets. The dissolution profiles however did not mimic this trend and showed no relation to the age of the tablets. The pattern taken by the three lots of calibrators for the dissolution profiles was also observed in the imaging parameters for the stearic acid. Within this calibrator work, a number of tablets were exposed to a high temperature for a short period of time to attempt to force a change in the samples. The outcome was observed as a change in the stearic acid, although it was postulated that this was due to the component melting at the temperature used, however this was the only change observed. It appeared that the stearic acid had become more associated with the API domains. The resultant average dissolution profile was found to be slower than that of the same lot prior to the heating, highlighting the stearic acid to be critical to the dissolution performance for this product. The majority of the correlations found were related to the stearic acid as was anticipated, but there were some for the MED of the DCP and the NN of the API. This showed the DCP to have trends with the age of the calibrator (number of domains) and the dissolution (MED).

The final project carried out was again based on an actual Pfizer product, named W due to confidentiality. Since this product was acquired by Pfizer it had experienced continuing issues related to variable dissolution, resulting in many investigations to aid the identification of the probable cause or causes. The work for this project was performed on a number of samples supplied from a selection of these studies, including those from design of experiment studies and selected production blends in addition to a set of laboratory produced samples based on extending the initial findings. Variations in component age, blending and compaction applied to the blends were encompassed in the samples examined as well as evaluating the interaction of different components with each other. The first section of the work involved the samples with components with differing ages which had been pre-grouped into rapid, acceptable and steady dissolution performance. Imaging showed changes in the API and the sucrose components that followed the pre-grouping, whereas the size of the domains, especially for the sucrose which formed discrete clumps, increased the dissolution rate. The age of the components did not seem to cause differences in the images. The fibre-optic dissolution profiles produced results that fell within the pre-groupings and again were not related to age. The majority of the correlations observed were related to the sucrose with an additional one related to lactose.

The next study followed another theory that the dissolution would be variable due to interactions between the magnesium stearate and API upon increased blending i.e. the former was coating the latter to a greater extent, which caused a reduction in the ability of the API to solvate. Samples consisting of these two components were manufactured using three different blending times combined with three compression forces applied when preparing the filled capsules. Variations were observed in the images when grouped in blending or compression order, but the dissolution profiles only showed obvious changes when the blending order was examined. The main outcome was that the blending time caused more variations in both blend components that showed correlations between the NIRM images and the dissolution profiles. The variation in the compression did not provide as many correlations and of those, the majority were related to the magnesium stearate rather than the API.

Having identified the API, sucrose and magnesium stearate as significant with respect to imaging and dissolution, blends containing these three components were manufactured with several blending times accompanied with blends containing lactose for comparison. Similar to the previous results, the sucrose formed clumps and as a result the dissolution appeared to proceed slightly faster. The lactose blends produced profiles that were more consistent than those containing sucrose although the shape of the profiles remained very similar for all the blends dissolved. This may have contributed to the fact that there were no good correlations observed between the imaging and dissolution data for this study, but it could be seen qualitatively that the size of the sucrose was affecting the dissolution performance.

The concluding part of the project was carried out using blends from an actual production sample that had encountered variable dissolution to evaluate the relevance of the findings from the preceding work in the "real" product. The issue was related to rapid dissolution from one lot produced which gave results that were OOS, but performing certain re-working on the blend allowed the specification to be met. NIRM imaging results of this lot, before and after re-work and another passing lot showed the OOS samples showed an increase in the number of domains present for the magnesium stearate and the API accompanied by some variations in the sucrose sample statistics. The dissolution profiles followed the results from the site. More correlations were observed for sucrose and magnesium stearate in relation to the distribution of the components in the images, related to the overall size of the domains. It pointed towards the sucrose having slightly larger domains in the OSS dissolution samples combined with slightly larger magnesium stearate domains. These results showed that the dissolution for W was related to a combination of all the conclusions from the related studies, rather than one specific source or component. Changes observed in the sucrose, magnesium stearate and API all appeared to contribute in combination or, on occasion, individually to the dissolution behaviour for Product W.

This work has shown that NIRM imaging can be utilised as a means to investigate the dissolution behaviour of pharmaceutical products. It has first been used in a retrospective manner to gain a better understanding of the factors that influence both the images and dissolution. This was then applied to some real examples where the same differences were observed. It was found that any correlations observed were very product or system specific and that no general statements could be made about NIRM images and dissolution that would applicable to any given pharmaceutical product. For the examples looked at in this work, it was found that the most useful imaging parameters with respect to correlation with the dissolution were those associated with the size of the MCC and number of lubricant blend domains for product V. The descriptors for the distributions of the sucrose, API and magnesium stearate, as well as number of the magnesium stearate and API domains as well as the size of the sucrose domains were found to be most beneficial for product W. For the dissolution calibrators, the number of domains or the nearest neighbour of the stearic acid component appeared to give the best correlation to the dissolution.

The comparison of the various models applied to the dissolution profile data showed the Weibull model to be the most useful for all the products analysed. It provided the best fit to the data in every case and for product W it was the only model that was applicable. The correlations included a mix of the rate and fixed point dissolution parameters providing information similar to the conventional testing as well as some extra performance information.

The results of this work show that it should be possible to use NIRM imaging as a method to control a process at an intermediate stage in the manufacturing process. For example if Product W was imaged at the end of blending and the skew of the sucrose distribution monitored, the time to 63.2% (T_d) could be predicted and the blend would pass if this value fell within the critical levels set by the specification. This was also shown to be possible for a standard time-to-a-given-percentage value, as is the method used conventionally, that varies from product to product.

A process implementation of NIRM imaging to monitor blending is currently at the development stage. It involves an imaging system fibre-optically connected to a blender to measure the blend homogeneity as a function of time. It is still in the early stages, but there is a lot of interest within the industry for this facility to be available. It would enable an increase their product understanding within the manufacturing process and eventually may be used as a control mechanism, as has been concluded from this research.

According to the literature, this work performed combining these two techniques has not been previously attempted therefore it has provided another step forward for the use of NIRM imaging technology within the pharmaceutical industry as an alternative, non-destructive method for prediction of physical properties and enable the possibility of its use for process control.

References

A

J. Aaltonen, J. Rantanen, S. Siiriä, M. Karjalainen, A. Jørgensen, N. Laitinen, M. Savolainen, P. Seitavuopio, M. Louhi-Kultanen, and J. Yliruusi,.*Anal. Chem.,* 2003, **75**, 5267-5273.

J. Aaltonen, P. Heinänen, L. Peltonen, H. Kortejärvi, V. Pekka Tanninen, L. Christiansen, J. Hirvonen, J. Yliruusi, and J. Rantanen, *J.Pharm.Sci.*, 2006, **95 (12)**, 2730-2737.

O. Abbas, N. Dupuy, C. Rebufa, L. Vrielynck, J. Kister, and A. Permanyer,.*Appl. Spectrosc.,* 2006, **60 (3)**, 304-314.

C. Abrahamsson, J. Johansson, S. Andersson-Engels, S. Svanberg, and S. Folestad,.*Anal. Chem.,* 2005, **77**, 1055-1059.

A.S. Achanta, V.A. Gray, T.L. Cecil, and L.T. Grady,.*Drug Dev. Ind. Pharm.,* 1995, **21 (10)**, 1171-1182.

E. Adams, R. De Maesschalck, B. De Spiegeleer, Y.V. Heyden, J. Smeyers-Verbeke, and D.L. Massart,.*Int. J. Pharm.,* 2001, **212**, 41-53.

E. Adams, B. Walczak, C. Veraet, P.G. Risha, and D.L. Massart,.*Int. J. Pharm.,* 2002, **234**, 169-178.

P.K. Aldridge, S.S. Sekulic, H.W. Ward II, D.R. Brannegan, E.D. Stanley, C.L. Evans, S.T. Sciavolino, and P.A. Hailey,.*Anal. Chem.,* 1996, **68**, 509-513.

G.L. Amidon, H. Lennernäs, V.P. Shah, and J.R. Crison,. *Pharm. Res.,* 1995, **12 (3)**, 413-420.

N.H. Anderson, M. Bauer, N. Boussac, R. Khan-Malck, P. Munden, and M. Sardaro,.*J. Pharm. Biomed. Anal.,* 1998, **17**, 811-822.

J.J. Andrew and T.M. Hancewicz,.*Appl. Spectrosc.,* 1998, **52 (6)**, 797-807.

M.S. Arayne and N. Sultana,.*J. P. M. A.,* 1979, **(September)**, 193-200.

D.P. Ariana, R. Lu, and D.R. Guyer,.*Comput. Electron. Agric.,* 2006, **53**, 60-70.

K. Artyushkova and J.E. Fulghum,.*Surf. Interface Anal.,* 2002, **33**, 185-195.

E.M. Attas, M.G. Sowa, T.B. Posthumus, B.J. Schattka, H.H. Mantsch, and S.L. Zhang,.*Biopolymers,* 2002, **67**, 96-106.

B

I.C. Baianu, D. Costescu, T. You, P.R. Lozano, N.E. Hofmann, and S.S. Korban,.*94th AOCS Symposium Proceedings,* 2004, **12**.

V.J. Barclay, R.F. Bonner, and I.P. Hamilton,.*Anal. Chem.,* 1997, **69**, 78-90.

R. Barer, A.R.H. Cole, and H.W. Thompson,.*Nature,* 1949, **163**, 198-201.

R.J. Barnes, M.S. Dhanoa, and S.J. Lister,.*Appl. Spectrosc.,* 1989, **43 (5)**, 772-777.

S. Baronti, A. Casini, F. Lotti, and S. Porcinai,.*Chemometr. Intell. Lab. Syst.,* 1997, **39**, 103-114.

F.E. Barton II,.*Spectrosc. Eur.,* 2002, **14 (1)**, 12-18.

K.R. Beebe and B.R. Kowalski,.*Anal. Chem.,* 1987, **59 (17),** 1007A-1017A.

M. Blanco, J. Coello, H. Iturriaga, S. Maspoch, and C. de la Pezuela,.*Analyst,* 1998, **123**, 135R-150R.

M. Blanco, J. Coello, A. Eustaquio, H. Iturriaga, and S. Maspoch,.*Anal. Chim. Acta.,* 1999, **392**, 237-246.

M. Blanco and A. Villar,.*Analyst,* 2000, **125 (12)**, 2311-2314.

M. Blanco, A. Eustaquio, J.M. González, and D. Serrano,.*J. Pharm. Biomed. Anal.,* 2000, **22**, 139-148.

M. Blanco, R. Gozález Bañó, and E. Bertran,.*Talanta,* 2002, **56**, 203-212.

C. Bonifazzi, P. Carcagni, A.D. Patria, S. Ferriani, R. Fontana, M. Greco, M. Mastroianni, M. Materazzi, E. Pampaloni, and A. Romano,.*Proc. SPIE,* 2006, **6062**.

N.W. Broad, R.D. Jee, A.C. Moffat, and M.R. Smith,.*Analyst,* 2001, **126 (12)**, 2207-2211.

R. Brody and D.A. Clark,.*Eur. Pharma. Rev.,* 2003, **(2)**, 31-38.

C.K. Brown, H.P. Chokski, B. Nickerson, R.A. Reed, B.R. Rohrs, and P.A. Shah,.*Dissolution Technologies,* 2005, **12 (4)**, 6-12.

W. Brown,.*Dissolution Technologies,* 2002, **9 (2)**.

R.G. Buice, L.A. Cassis, and R.A. Lodder,.*Cell. Mol. Biol.,* 1998, **44 (1)**, 53-64.

J. Burmicz,.*Dissolution Technologies,* 2005, **12 (1)**, 33-34.

L. Buydens, W.H.A.M. van der Broek, D. Wienke, W.J. Melssen, and C.W.A. de Crom,.*Anal. Chem.,* 1995, **67**, 3753-3759.

K. Bynum, K. Roinestad, A. Kassis, J. Pocreva, L. Gehrlein, F. Cheung, and P. Palmermo,.*Dissolution Technologies,* 2001, **8 (4)**, 1-8.

C

L.A. Cassis, U. Shenoy, R.G. Buice, M. Fettinger, D. Joyce, and R.A. Lodder, 1997, http://kerouac.pharm.uky.edu/ASRG/Wave/Lipo/lipo.htm, accessed November 2004.

CDER,.FDA, 1997,_*Guidance for Industry: Dissolution Testing of Immediate Release Solid Dosage Forms*, http://www.fda.gov/cder/guidance/1713bp1.pdf, accessed September 2006.

CDER,.FDA, 2000,_*Guidance for Industry: Waiver of in vivo Bioavailability and Bioequivalence Studies for Immediate-Release Solid Oral Dosage Forms based on a Biopharmaceutics Classification System*, http://www.fda.gov/cder/guidance/3618fnl.pdf, accessed September 2006.

CDER,.FDA, 2004, *Guidance for Industry: PAT-A Framework for Innovative Pharmaceutical Development, Manufacturing, and Quality Assurance*, http://www.fda.gov/cder/guidance/6419fnl.pdf, accessed September 2006.

J.A. Centeno and F.B. Johnson,.*Appl. Spectrosc.,* 1993, **47 (3)**, 341-345.

K.L.A. Chan, S.V. Hammond, and S.G. Kazarian,.*Anal. Chem.,* 2003, **75 (9)**, 2140-2146.

K.L.A. Chan and S.G. Kazarian,.*Mol. Pharm.,* 2004, **1 (4)**, 331-335.

K.L.A. Chan, S.G. Kazarian, A. Mavraki, and D.R. Williams,.*Appl. Spectrosc.,* 2005, **59 (2)**, 149-155.

K.L.A. Chan and S.G. Kazarian,.*J. Comb. Chem.,* 2005, **7 (2)**, 185-189.

K.L.A. Chan and S.G. Kazarian,.*Analyst,* 2006a, **131**, 126-131.

K.L.A. Chan and S.G. Kazarian,.*J. Comb. Chem.,* 2006b, **8 (1)**, 26-31.

K.L.A. Chan and S.G. Kazarian,.*Lab Chip,* 2006c, **6**, 864-870.

J. Chen and X.Z. Wang,.*J. Chem. Inf. Comput. Sci.,* 2001, **41**, 992-1001.

D. Chenery and H. Bowring,.*Spectrosc. Eur.,* 2003, **15 (4)**, 8-14.

J.H. Cho, P.J. Gemperline, A. Salt, and D.S. Walker,.*Anal. Chem.,* 1995, **67**, 2858-2863.

S.S. Chrai and M. Burd,.*Pharm. Technol.,* 2004, **28 (3)**, 168-182.

E.W. Ciurczak, in *NIR Analysis of Pharmaceuticals*, *Handbook of Near-Infrared Analysis*, ed. D.A. Burns and E.W. Ciurczak, Marcel Dekker, New York, 1992, pp. 549-563.

F.C. Clarke, M.J. Jamieson, D.A. Clark, S.V. Hammond, R.D. Jee, and A.C. Moffat,.*Anal. Chem.,* 2001, **73 (10)**, 2213-2220.

F.C. Clarke, S.V. Hammond, R.D. Jee, and A.C. Moffat,.*Appl. Spectrosc.,* 2002, **56 (11)**, 1475-1483.

F.C. Clarke and S.V. Hammond,.*Eur. Pharma. Rev.,* 2003, **1**, 41-50.

F.C. Clarke,.*Vib. Spectrosc.,* 2004, **34 (1)**, 25-35.

F.C. Clarke, 2006, PhD Thesis.

I. Clegg and N. Everall,.*Eur. Pharma. Rev.,* 2003, **(3)**, 56-62.

P. Colarusso, L.H. Kidder, I.W. Levin, J.F. Fraser, J.F. Arens, and E.N. Lewis,.*Appl. Spectrosc.,* 1998, **52 (3)**, 106A-120A.

P. Corti, G. Ceramelli, E. Dreassi, and S. Mattii,.*Analyst,* 1999, **124 (5)**, 755-758.

P. Costa and J.M.S. Lobo,.*Eur. J. Pharm. Sci.,* 2001, **13**, 123-133.

C.A. Coutts-Lendon and J.L. Koenig,.*Appl. Spectrosc.,* 2005, **59 (8)**, 976-985.

D.C. Cox, C.C. Douglas, W.B. Furman, R.D. Kirchhoefer, J.W. Myrick, and C.E. Wells,.*Pharm. Technol.,* 1978, **2 (4)**, 41-53.

D.C. Cox and W.B. Furman,.*J. Pharm. Sci.,* 1984, **73 (5)**, 670-676.

D

A.M.C. Davies,.*Eur. Spectrosc. News,* 1987, **73**, 10-16.

A.M.C. Davies and T. Fearn,.*Spectrosc. Eur.,* 2004, **16 (6)**, 20-23.

T. Davies,.*Analusis,* 1998, **28 (4)**, M17-M19.

M. Day,.*Pharm. Technol. Eur.,* 2001, **(April)**, 22-27.

A. de Juan and R. Tauler,.*Anal. Chim. Acta.,* 2003, **500**, 195-210.

A. de Juan, R. Tauler, R. Dyson, C. Marcolli, M. Rault, and M. Maeder,.*Trends Anal. Chem.,* 2004, **23 (1),** 70-78.

O.S. Degenhardt, B. Waters, A. Rebelo-Cameirao, A. Meyer, H. Brunner, and N.P. Toltl,.*Dissolution Technologies,* 2004, **11 (1)**.

R.J. Dempsey, D.G. Davis, R.G. Buice Jr, and R.A. Lodder,. *Appl. Spectrosc.,* 1996, **50 (2)**, 18A-34A.

R.J. Dempsey, L.A. Cassis, and R.A. Lodder,.*New York Acad. Sci.,* 1997, **820**, 149-169.

M.W.J. Derkson, P.J.M. van de Oetelaar, and F.A. Maris,.*J. Pharm. Biomed. Anal.,* 1998, **17**, 473-480.

M. Donoso and E.S. Ghaly,.*Pharm. Dev. Tech.,* 2004, **9 (3),** 247-263.

M. Donoso and E.S. Ghaly,.*Pharm. Dev. Technol.,* 2005, **10,** 211-217.

G. Downey, J.D. Kelly, and C.P. Rodriguez,.*Spectrosc. Eur.,* 2006, **18 (3)**, 10-14.

J.K. Drennan III and R.A. Lodder,.*J. Pharm. Sci.,* 1990, **79 (7)**, 622-627.

J.K. Drennan III and R.A. Lodder,.*Spectrosc.,* 1991, **6 (8),** 34-39.

J.K. Drennen, E.G. Kraemer, and R.A. Lodder,.*Crit. Rev. Anal. Chem.,* 1991, **22 (6)**, 443-475.

J.K. Drennen and R.A. Lodder, in *Pharmaceutical Applications of Near-Infrared Spectrometry*, *Advances in Near-Infrared Measurements*, ed. JAI Press Inc, 1993, pp. 93-112.

J. Dubois, J.C. Wolff, J.K. Warrack, J. Schoppelrei, and E.N. Lewis, *Spectrosc.*, 2007, **(February)**.

E

A.S. El-Hagrasy, H. Morris, F. D'Amico, R.A. Lodder, and J.K. Drennen,.*J. Pharm. Sci.,* 2001, **90 (9)**, 1298-1307.

C. Elliasson, J. Engelbrektsson, A. Lorén, J. Abrahamsson, K. Abrahamsson, and M. Josefson,.*Chemometr. Intell. Lab. Syst.,* 2006, **81**, 13-20.

C.D. Ellison, R.C. Lyon, M.L. Harmad, E.H. Jefferson, and A.S. Hussain, *FDA Science Forum*, 2005,

G. ElMasry, N. Wang, A. ElSayed, and M. Ngadi, *J.Food Eng*, 2007, **81**, 98-107.

A.L. Enculescu and J.R. Steiginga,.*Am. Pharm. Rev.,* 2002, 81-88.

A. Eustaquio, P. Graham, R.D. Jee, A.C. Moffatt, and A.D. Trafford,.*Analyst,* 1998, **123 (11)**, 2303-2306.

D.L. Exline, R.L. Schuler, and P.J. Treado,.*Forensic Sci. Comm.,* 2003, **5 (3)**.

F

FDA, 2005, *Dissolution Apparatus- History and Sources of Variability*, www.fda.gov/ohrms/dockets/ac/05/briefing/2005_4137BI_05_Dissolution-summary.doc, accessed January 2006

M.C.F. Ferraro, P.M. Castellano, and T.S. Kaufman,.*J. Pharm. Biomed. Anal.,* 2001, **26**, 443-451.

M. Fischer and C.D. Tran,.*Anal. Chem.,* 1999, **71**, 953-959.

M. Fischer and C.D. Tran,.*Anal. Chem.,* 1999, **71**, 2255-2261.

K.A. Flisar, R.J. Forsyth, Z. Li, and J. Martin,.*Dissolution Technologies,* 2005, **12 (3)**, 6-10.

B. Foster,.*Am. Lab.,* 1997, **29 (4)**, 21-29.

T. Foster and W. Brown,.*Dissolution Technologies,* 2005, **12 (1),** 6-8.

M.P. Freitas, A. Sabadin, L.M. Silva, F.M. Giannotti, D.A. do Couto, E. Tonhi, R.S. Medeiros, G.L. Coco, V.F.T. Russo, and J.A. Martins,.*J. Pharm. Biomed. Anal.,* 2005, **39,** 17-21.

G

M.M. Galera, J.L.M. Vidal, A.G. Frenich, and M.D.G. García,.*J. Chromatogr. A,* 1997, **778,** 139-149.

J.M.L. Gallego and J.P. Arroyo,.*J. Pharm. Biomed. Anal.,* 2003, **31 (873),** 884-

P. Geladi and B.R. Kowalski, *Analytica Chimica Acta*, 1986, **185**, 1-17.

P.J. Gemperline, J.H. Cho, B. Baker, B. Batchelor, and D.S. Walker,.*Anal. Chim. Acta.,* 1997, **345**, 155-159.

A. Gerich, 2005, *Spectral Dimensions User Group Meeting*, Presentation.

R. Gimet and A.T. Luong,.*J. Pharm. Biomed. Anal.,* 1987, **5 (3)**, 205-211.

M.C. Gohel, M.K. Panchal, and V.V. Jogani,.*AAPS PharmSciTech,* 2000, **1 (4)**, 1-6.

M.C. Gohel and N.R. Mehta,.*Pharmainfo. net,* 2005.

H.C. Goicoechea and A.C. Olivieri,.*J. Pharm. Biomed. Anal.,* 1999, **20**, 681-686.

T. Golebiowski, A.S. Leong, and J.F. Panozzo,.*J. Near Infrared Spectrosc.,* 2005, **13**, 255-264.

J. González-Benito and J.L. Koenig,.*Macromolecules,* 2002, **35**, 7261-7367.

F. González and R. Pous,.*J. Pharm. Biomed. Anal.,* 1995, **13 (4/5)**, 419-423.

R.C. Gore,.*Science,* 1949, **110**, 710-711.

J. Gottfries, H. Depui, M. Fransson, M. Jongeneelen, M. Josefson, F.W. Langkilde, and D.T. Witte,.*J. Pharm. Biomed. Anal.,* 1996, **14 (11)**, 1495-1503.

V.A. Gray,.*Dissolution Technologies,* 2003, **10 (4)**, 33-36.

V.A. Gray,.*Dissolution Technologies,* 2004, **11 (3)**, 13-14.

V.A. Gray, M. Barot, P. Bhattacharyya, J. Burmicz, B. Crist, T. Foster, R. Hanson, H. Lam, L.J. Leeson, J. Mauger, T.W. Moore, W. Mueller, M. Oates, J.-L. Raton, and W. Brown,.*Dissolution Technologies,* 2005, **12 (1)**, 35-36.

V.A. Gray,.*Dissolution Technologies,* 2006, **13 (2)**, 6-9.

U. Grummisch,.*Pharm. Ind.,* 1998, **60 (11)**, 1002-1006.

N. Guilhaumou, P. Dumas, G.L. Carr, and G.P. Williams,.*Appl. Spectrosc.,* 1998, **52 (8)**, 1029-1034.

S. Gulian, T. Farrell, and R. Steffenino,.*AAPS Annual Meeting and Exposition,* 2005, Poster.

H

I.H.I. Habib and M.S. Kamel,.*Talanta,* 2003, **60 (1)**, 185-190.

P.A. Hailey, P. Doherty, P. Tapsell, T. Oliver, and P.K. Aldridge,.*J. Pharm. Biomed. Anal.,* 1996, **14 (5)**, 551-559.

A.S. Haka, L.H. Kidder, and E.N. Lewis,.*Proc. SPIE,* 2001, **4259**, 47-55.

S.J. Hamilton, A.E. Lowell, and R.A. Lodder,.*J. Biomed. Opt.,* 2002, **7 (4)**, 1-10.

S.J. Hamilton and R.A. Lodder,.*Proc SPIE,* 2002, **4626 (136)**.

S.V. Hammond and F.C. Clarke, in *Near-Infrared Microspectroscopy, Handbook of Vibrational Spectroscopy*, ed. J.M. Chalmers and P.R. Griffiths, John Wiley & Sons, Chichester, 2002, pp. 1405-1417.

S.H. Han and P.G. Faulkner,.*J. Pharm. Biomed. Anal.,* 1996, **14**, 1681-1689.

J. Haystead,.*Pharm. Technol.,* 2003, **(October)**, 18-19.

A.M. Healy, L.G. McCarthy, K.M. Gallagher, and O.I. Corrigan,.*J. Pharm. Pharmacol.,* 2001, **54**, 441-444.

W.I. Higuchi, S.J. Desai, P. Singh, and A.P. Simonelli,.*J. Pharm. Sci.,* 1966, **55 (11)**, 1230-1234.

W.I. Higuchi, J.B. Schwartz, and A.P. Simonelli,.*J. Pharm. Sci.,* 1968, **57 (2)**, 278-282.

A.W. Hixson and J.H. Crowell,.*Ind. Eng. Chem.,* 1931, **23 (8)**, 923-931.

A.W. Hixson and J.H. Crowell,.*Ind. Eng. Chem.,* 1931, **23 (9)**, 1002-1009.

J.H. Huang, H. Wium, K.B. Qvist, and K.H. Esbensen,.*Chemometr. Intell. Lab. Syst.,* 2003, **66 (141)**, 158.

C.W. Huck, R. Ohmacht, Z. Szabo, and G.K. Bonn,.*J. Near Infrared Spectrosc.,* 2006, **14 (1)**, 51-57.

A.S. Hussain, K.Y. Lo, L.J. Lesko, V.P. Shah, D. Volpe, and R.L. Williams,.*Dissolution Technologies,* 1999, **6 (2)**, 1-4.

I

ICH,.*ICH Guidelines,* 2005, Quality Topics (Q1(A) R2).

In-PharmaTechnologist.com, 2006, *Pharmaceutical Applications of Near Infrared Spectrometry.*

J

K. Jia and R.A. Williams,.*Dissolution Technologies,* 2006, **13 (2)**, 11-19.

J. Johansson, M. Cauchi, and M. Sundgren,.*J. Pharm. Biomed. Anal.,* 2002, **29**, 469-476.

M. Josefson, O. Svensson, K. Abrahamsson, J. Engelbrektsson, M. Nicholas, and H. Wikström,.*Chemometr. Intell. Lab. Syst.,* 2006, **In Press**.

H.L. Ju and S.J. Liaw,.*Drug Inf. J.,* 1997, **31**, 1273-1289.

K

P. Kabasakalian, E. Britt, and M.D. Yudis,.*J. Pharm. Sci.,* 1966, **55**, 642-642.

S.G. Kazarian and K.L.A. Chan,.*Macromolecules,* 2003, **36**, 9866-9872.

S.G. Kazarian and K.L.A. Chan, *Biochem.Biophys.Acta.*, 2006, **1758 (7)**, 858-867.

A. Kher, S. Stewart, and M. Mulholland,.*J. Near Infrared Spectrosc.,* 2005, **13**, 225-229.

L.H. Kidder, I.W. Levin, E.N. Lewis, V.D. Kleiman, and E.J. Heilwell,.*Opt. Lett.,* 1997, **22 (10)**, 742-744.

H. Kim and R. Fassihi,.*J. Pharm. Sci.,* 1997, **86 (3)**, 323-328.

J.D. Kirsch and J.K. Drennen,.*J. Pharm. Biomed. Anal.,* 1995, **13 (10)**, 1273-1281.

N.J. Kline and P.J. Treado,.*J. Raman Spectrosc.,* 1997, **28**, 119-124.

F.W. Koehler IV, E. Lee, L.H. Kidder, and E.N. Lewis,.*Spectrosc. Eur.,* 2002, **14 (3)**, 12-19.

J.L. Koenig, N.A. Wright, E.V. Mieso, and C.A. Coutts-Lendon,.*J. Control. Release,* 2003, **93**, 223-248.

H. Kornmann, M. Rhiel, C. Cannizzaro, and I. Marison,.*Biotechnol. Bioeng.,* 2003, **82 (6)**, 702-709.

R.W. Korsmeyer, R. Gurny, E. Doelker, P. Buri, and N.A. Peppas,.*Int. J. Pharm.,* 1983, **15**, 25-35.

K. Krämer and S. Ebel,.*Anal. Chim. Acta.,* 2000, **420 (2),** 155-161.

J. Kressler, R. Schäfer, and R. Thomann,.*Appl. Spectrosc.,* 1998, **52 (10)**, 1269-1273.

L

M. Laasonen, T. Harmia-Pulkkinen, C. Simard, M. Räsänen, and H. Vuorela,.*Anal. Chem.,* 2003, **75 (4),** 754-760.

F. Langenbucher,.*J. Pharmacol.,* 1972, **24**, 979-981.

F. Langenbucher,.*Pharm. Ind.,* 1976, **38 (5)**, 472-477.

M.S. Larrechi, M. Garrido, and F.X. Rius,.*Appl. Spectrosc.,* 2006, **60 (2)**, 174-181.

P. Lánský and W. Weiss,.*J. Pharm. Sci.,* 2003, **92 (8)**, 1632-1647.

E. Lee, W.X. Huang, P. Chen, E.N. Lewis, and R.V. Vivilecchia, *Spectrosc.*, 2006,

T.H. Lee and S.Y. Lin,.*Eur. J. Pharm. Sci.,* 2004, **23 (2)**, 117-122.

Y. Lee, S. Nah, H. Namkung, and H. Chung,.*Appl. Spectrosc.,* 2005, **59 (7),** 952-955.

L.J. Leeson,.*Dissolution Technologies,* 2000, **7 (2),** 16-17.

A.K. Leung, F.T. Chau, and J.B. Gao,.*Chemometr. Intell. Lab. Syst.,* 1998, **43,** 165-184.

E.N. Lewis, P.J. Treado, R.C. Reeder, G.M. Story, A.E. Dowrey, C. Marcott, and I.W. Levin,.*Anal. Chem.,* 1995, **67 (19),** 3377-3381.

E.N. Lewis, L.H. Kidder, J.F. Arens, M.C. Peck, and I.W. Levin,.*Appl. Spectrosc.,* 1997, **51 (4),** 563-567.

E.N. Lewis, J.E. Carroll, and F.C. Clarke,.*NIR News,* 2001, **12 (3),** 16-18.

E.N. Lewis, E. Lee, and L.H. Kidder, *Microsc.Today*, 2004, **(November).**

E.N. Lewis, J. Schoppelrei, and E. Lee,.*SpectroscopyOnline. com,* 2005, (**January**), 28-34.

E.N. Lewis, L.H. Kidder, and E. Lee, *NIR News*, 2005, **16 (5)**, 2-4.

G. Li, M. Thomson, E. Dicarlo, X. Yang, B. Nestor, M.P.G. Bostrom, and N.P. Camacho,.*Appl. Spectrosc.,* 2005, **59 (12)**, 1527-1533.

T.T. Lied, P. Geladi, and K.H. Esbensen,.*J. Chemom.,* 2000, **14**, 585-598.

T.T. Lied and K.H. Esbensen,.*Chemometr. Intell. Lab. Syst.,* 2001, **58**, 213-226.

F. Lindgren, P. Geladi, and S. Wold,.*J. Chemom.,* 1994, **8,** 377-389.

X. Liu, X. Chen, W. Wu, and Y. Zhang,.*Food Control,* 2006, **17,** 894-899.

Y. Liu, Y.R. Chen, M.S. Kim, D.E. Chan, and A.M. Lefcourt, *J.Food Eng*, 2007, **81**, 412-418.

R.A. Lodder, M. Selby, and G.M. Hieftje,.*Anal. Chem.,* 1987, **59**, 1921-1930.

X. Lu, R. Lozano, and P. Shah,.*Dissolution Technologies,* 2003, **10 (4)**, 6-15.

R.C. Lyon, D.S. Lester, E.N. Lewis, E. Lee, L.X. Yu, E.H. Jefferson, and A.S. Hussain,.*AAPS PharmSciTech,* 2002, **3 (3)**, 1-15.

R.C. Lyon, E.H. Jefferson, C.D. Ellison, L.F. Buhse, J.A. Spencer, M.M. Nasr, and A.S. Hussain,.*Am. Pharm. Rev.,* 2003, **6 (3)**.

R.C. Lyon, C.D. Ellison, E.H. Jefferson, E.N. Lewis, E. Lee, J.K. Drennan III, and A.S. Hussain, *FDA Science Forum*, 2005.

M

B.F. MacDonald and K.A. Prebble,.*J. Pharm. Biomed. Anal.,* 1993, **11 (11-12)**, 1077-1085.

I. Malik, M. Poonacha, J. Moses, and R.A. Lodder,.*AAPS PharmSciTech,* 2001, **2 (2)**.

J.R. Mansfield, M.G. Sowa, G.B. Scarth, R.L. Somorjai, and H.H. Mantsch,.*Anal. Chem.,* 1997, **69**, 3370-3374.

C.A. Martin,.*Dissolution Technologies,* 2003, **10 (4)**, 37-39.

P. Martinsen and P. Schaare,.*Postharvest Biol. Technol.,* 1998, **14**, 271-281.

N.R. Martos, A.M. Díaz, A. Navalón, I. De Orbe Payá, and L.F.C. Vallvey,.*J. Pharm. Biomed. Anal.,* 2000, **23**, 837-844.

C. Matthäus, S. Boydston-White, M. Miljkovic, M. Romeo, and M. Diem,.*Appl. Spectrosc.,* 2006, **60 (1)**, 1-8.

W.F. McClure and D.L. Stanfield, in *Near-Infrared Spectroscopy of Biomaterials, Handbook of Vibrational Spectroscopy*, ed. J.M. Chalmers and P.R. Griffiths, John Wiley & Sons, Chicester, 2002, pp. 212-226.

P. Merckle and K.-A. Kovar,.*J. Pharm. Biomed. Anal.,* 1998, **17 (3)**, 365-374.

B.A. Miller-Chou and J.L. Koenig,.*Macromolecules,* 2002, **35**, 440-444.

T.W. Moore, J.F. Hamilton, and C.M. Kerner,.*Pharm. Forum.,* 1995, **21 (5)**, 1387-1396.

T.W. Moore, R.F. Shangraw, and Y. Habib,.*Pharm. Forum.,* 1996, **22 (3)**, 2423-2424.

K.M. Morisseau and C.T. Rhodes,.*Pharm. Res.,* 1997, **14 (1)**, 108-111.

N

R. Nagarajan, P. Singh, and R. Mehrotra,.*J. Autom. Methods Manage. Chem.,* 2006, 1-4.

P. Nair and R.A. Lodder,.*Appl. Spectrosc.,* 1993, **47 (3)**, 287-291.

National Research Council Canada, *http://www.nrc-cnrc.gc.ca/highlights/2005/0506nir_spectroscopy-print_e.html*, 2005, accessed January 2007.

S.G. Nikolov, H. Hutter, and M. Grasserbauer,.*Chemometr. Intell. Lab. Syst.,* 1996, **34**, 263-273.

I. Nir, B.D. Johnson, J. Johansson, and C. Schatz,.*Dissolution Technologies,* 2001, **8 (2)**, 33-40.

C. Noory, N. Tran, L. Ouderkirk, S. Brown, J. Perry, J. Lopez, M. Colon, M. Faberlle, K. Henry, J. Rorberg, S.A. Ali, and V.P. Shah,.*Dissolution Technologies,* 1999, **6 (4)**, 1-2.

K.H. Norris and J.R. Hart,.*J. Near Infrared Spectrosc.,* 1996, **4**, 23-30.

A.A. Noyes and W.R. Whitney,.*J. Am. Chem. Soc.,* 1897, **(October)**, 930-934.

O

T.C. O'Haver and T. Begley,.*Anal. Chem.,* 1981, **53**, 1876-1878.

A.J. O'Neil, R.D. Jee, and A.C. Moffat,.*Analyst,* 1998, **123 (11)**, 2297-2302.

A.J. O'Neil, R.D. Jee, and A.C. Moffat,.*Analyst,* 1999, **124 (1)**, 33-36.

S.J. Oh and J.L. Koenig,.*Anal. Chem.,* 1998, **70 (9)**, 1768-1772.

P

J. Parnell and F.C. Clarke, 2005, Internal Pfizer Report, RCA_0083_00.

B.M. Patterson and G.J. Havrilla,.*Appl. Spectrosc.,* 2006, **60 (5)**, 471-478.

G. Payne, C. Wallace, B. Reedy, C. Lennard, R. Schuler, D.L. Exline, and C. Roux,.*Talanta,* 2005, **67**, 334-344.

Pharma Test, 2005, *USP Dissolution Instrument Calibration or PQ Standard Operating Procedure or SOP.*

W. Plugge and C. van der Vlies,.*J. Pharm. Biomed. Anal.,* 1996, **14**, 891-989.

J.E. Polli, G.S. Rekhi, L.L. Augsburger, and V.P. Shah,.*J. Pharm. Sci.,* 1997, **86 (6)**, 690-700.

N. Pomerleau-Dalcourt, R. Weersink, and L. Lilge,.*Appl. Spectrosc.,* 2005, **59 (11)**, 1406-1414.

J. Pontius, R. Hallett, and M. Martin,.*Appl. Spectrosc.,* 2005, **59 (6)**, 836-843.

Q

P.O. Quist and G. stling,.*J. Pharm. Biomed. Anal.,* 2002, **28**, 1081-1089.

P.O. Quist and M. Röst,.*J. Pharm. Biomed. Anal.,* 2003, **31**, 1129-1143.

S.A. Qureshi, H. Blume, S.L. Ali, and I.J. McGilveray,.*Drug Dev. Ind. Pharm.,* 1995, **21 (8)**, 925-942.

S.A. Qureshi and I.J. McGilveray,.*Eur. J. Pharm. Sci.,* 1999, **7**, 249-258.

S.A. Qureshi and J. Shabnam,.*Eur. J. Pharm. Sci.,* 2003, **19**, 291-297.

S.A. Qureshi,.*Eur. J. Pharm. Sci.,* 2004, **23**, 271-275.

S.A. Qureshi,.*Dissolution Technologies,* 2006, **13 (1)**, 25-30.

R

W.S. Rayens and A.H. Andersen,.*Chemometr. Intell. Lab. Syst.,* 2004, **71**, 121-127.

J.A. Reffner, J.P. Coates, and R.G. Messerschmidt,.*Am. Lab.,* 1987, **19 (4)**, 86-91.

Rendell, Hovelson, O'Connor, Cheung, Huard, Kong, Catania, and Rosenthal,.*Clin. Physiol.,* 1998, **18 (5)**, 426.

M.S. Reza, S.M.A. Islam, P. Akter, M. Khatun, and M.A. Quadir,.*Dhaka University Journal of Pharmaceutical Sciences,* 2004, **3 (1/2)**, 1-10.

T. Ribar, R. Bhargava, and J.L. Koenig,.*Macromolecules,* 2000, **33**, 8842-8849.

T. Ribar and J.L. Koenig,.*Macromolecules,* 2001, **34,** 8340-8346.

P. Robert, D. Bertrand, M.F. Devaux, and A. Sire,.*Anal. Chem.,* 1992, **64,** 664-667.

P. Rogers, P.A. Hailey, G.A. Johnson, V.A. Dight, G. Read, A. Shingler, P. Savage, T. Roche, and J. Mondry,.*Lab. Rob. Autom.,* 2000, **12**, 12-22.

Y. Roggo, N. Jent, A. Edmond, P. Chalus, and M. Ulmschneider,.*Eur. J. Pharm. Biopharm.,* 2005, **61**, 100-110.

R.J. Romañach, J.L. Ramirez, and M.K. Bellamy,.*AAPS PharmSciTech,* 2001, **2 (3)**, 1-10.

J.T. Rubino, L.M. Halterlein, and J. Blanchard,.*Int. J. Pharm.,* 1985, **26 (1-2)**, 165-174.

S.C. Rutan, O.E. de Noord, and R.R. Andréa,.*Anal. Chem.,* 1998, **70**, 3198-3201.

S

S.H.F. Scafi and C. Pasquini,.*Analyst,* 2001, **126 (12)**, 2218-2224.

M.D. Schaeberle, C.G. Karakatsanis, C.J. Lau, and P.J. Treado,.*Anal. Chem.,* 1995, **67 (4316),** 4321.

C. Schatz, M. Ulmschneider, R. Altermatt, S. Marrer, and H. Altorfer,.*Dissolution Technologies,* 2000, **7 (1)**.

C. Schatz, M. Ulmschneider, R. Altermatt, and S. Marrer,.*Dissolution Technologies,* 2000, **7 (1)**, 20-24.

C. Schatz, M. Ulmschneider, R. Altermatt, S. Marrer, and H. Altorfer,.*Dissolution Technologies,* 2001, **8 (2)**, 1-5.

C. Schatz, T. Kuny, M. Ulmschneider, S. Marrer, and H. Leuenberger,.*Dissolution Technologies,* 2003, **10 (1)**, 22-28.

K.T. Schatz, M. Ulmschneider, S. Marrer, and H. Leuenberger,.*Dissolution Technologies,* 2003, **10 (1)**, 22-28.

J.R. Schoonover, R. Marx, and S.L. Zhang,.*Appl. Spectrosc.,* 2003, **57 (5)**, 154A-170A.

P. Scott,.*Am. Pharm. Rev.,* 2002, **5 (1)**, 47-53.

P. Scott,.*Dissolution Technologies,* 2005, **12 (1)**, 18-21.

S.K. Setarehdan, J.J. Soraghan, D. Littlejohn, and D.A. Sadler,.*Anal. Chim. Acta.,* 2002, **452**, 35-45.

J.J. Seyer, P.E. Luner, and M.S. Kemper,.*J. Pharm. Sci.,* 2000, **89 (10)**, 1305-1316.

K.E. Shafer-Peltier, A.S. Haka, J.T. Motz, M. Fitzmaurice, R.R. Dasari, and M.S. Feld,.*J. Cell. Biochem. Supp.,* 2002, **39,** 125-137.

V.P. Shah, Y. Tsong, P. Sathe, and R.L. Williams,.*Dissolution Technologies,* 1999, **6 (3)**, 21-22.

V.P. Shah,.*Dissolution Technologies,* 2004, **11 (3)**, 11-11.

V.W. Smail, A.K. Fritz, and D.L. Wetzel, *Vib.Spectrosc.*, 2006, **42**, 215-221.

M.R. Smith, 2004, PhD Thesis.

M. Sohn, D.S. Himmelsbach, W.H. Morrison III, D.E. Akin, and F.E. Barton II,.*Appl. Spectrosc.*, 2006, **60 (4)**, 437-440.

Spectral Dimensions, *ISys User Manual*, 2005, Version 3.1.1.

L. Ståhle and S. Wold,.*J. Chemom.,* 1987, **1**, 185-196.

S. Šašic and D.A. Clark,.*Appl. Spectrosc.,* 2006, **60 (5)**, 494-502.

T

A.P. Tinke, K. Vanhoutte, R. De Maesschalck, S. Verheyen, and H. De Winter,.*J. Pharm. Biomed. Anal.,* 2005, **39 (5)**, 900-907.

C.J. Toher, P.E. Nielsen, A.S. Foreman, and A. Avdeef,.*Dissolution Technologies,* 2003, **10 (4)**, 20-25.

A.D. Trafford, R.D. Jee, A.C. Moffat, and P. Graham,.*Analyst,* 1999, **124 (2)**, 163-167.

C.D. Tran, Y. Cui, and S. Smirnov,.*Anal. Chem.,* 1998, **70 (4701)**, 4708.

C.D. Tran and M. Politi,.*Anal. Chem.,* 2002, **74**, 1604-1610.

E. Trenka and J. Oelichmann,.*Int. J. Vib. Specrosc.,* 2002, **6 (3)**, 2.

S. Tsuchikawa, K. Yamoto, and K. Inoue, *J.Wood Sci.*, 2003, **49**, 275-280.

M. Tsuta, J. Sugiyama, and Y. Sagara,.*J. Agr. Food Chem.,* 2002, **50**, 48-52.

U

USP, in *Near-Infrared Spectrometry*, *USP-NF*, ed. 2005, General chapter <1119>

USP, *Dissolution Technologies*, 2006, **13 (3)**, 25.

V

R.J. Voytilla and J.K. Drennan III,.*NIR News,* 2004, **15 (3)**, 8-9.

W

B. Walczak, B. van der Bogaert, and D.L. Massart,.*Anal. Chem.,* 1996, **68 (1742)**, 1747-

D.J. Wargo and J.K. Drennen,.*J. Pharm. Biomed. Anal.,* 1996, **14 (11)**, 1415-1423.

G.K. Webster, D.A. Farrand, E. Johnson, M.A. Litchman, N. Broad, and S. Maris,.*J. Pharm. Biomed. Anal.,* 2003, **33 (1)**, 21-32.

J. van der Weerd and S.G. Kazarian,.*Appl. Spectrosc.,* 2004a, **58 (12)**, 1413-1419.

J. van der Weerd, K.L.A. Chan, and S.G. Kazarian,.*Vib. Spectrosc.,* 2004, **35**, 9-13.

J. van der Weerd and S.G. Kazarian,.*J. Control. Release,* 2004b, **98**, 295-305.

J. van der Weerd and S.G. Kazarian,.*J. Pharm. Sci.,* 2005, **94 (9)**, 2096-2109.

W. Weibull,.*J. Appl. Mech.,* 1951, **(September)**, 293-297.

B.A. Weinstock, J. Janni, L. Hagen, and S. Wright,.*Appl. Spectrosc.,* 2006, **60 (1)**, 9-23.

I.J. Wesley, K. Ruggiero, B.G. Osbourne, and R.S. Anderssen,.*J. Near Infrared Spectrosc.,* 2005, **13**, 333-338.

D.L. Wetzel,.*Anal. Chem.,* 1983, **55 (12)**, 1185A-1176A.

O.H. Wheeler,.*Chem. Rev.,* 1929, 629-633.

S. Wold, M. Sjöström, and L. Eriksson,.*Chemometr. Intell. Lab. Syst.,* 2001, **58**, 109-130.

S. Wold, *GIT*, 2007, **11 (1-2)**, 22-25.

S.M. Wolfe, *Public Citizen's Health Research Group*, 1995.

J.C. Wolff, J.K. Warrack, and J. Schoppelrei,.*FACSS,* 2005, Poster.

M. Wolkenstein, H. Hutter, C. Mittermayr, W. Schiesser, and M. Grasserbauer,.*Anal. Chem.,* 1997, **69**, 777-782.

W. Wu, B. Walczak, D.L. Massart, K.A. Prebble, and I.R. Last,.*Anal. Chim. Acta.,* 1995, **315**, 243-255.

Y

H. Yu and J.F. MacGregor,.*Chemometr. Intell. Lab. Syst.,* 2003, **67**, 125-144.

N. Yuksel, A.E. Kanik, and T. Baykara,.*Int. J. Pharm.,* 2000, **209**, 57-67.

Z

P.N. Zannikos, W.I. Li, J.K. Drennan III, and R.A. Lodder,.*Pharm. Res.,* 1991, **8 (8)**, 974-978.

A. Zhang, W. Zeng, T.M. Niemczyk, M.R. Keenan, and D.M. Haaland,.*Appl. Spectrosc.,* 2005, **59 (1)**, 47-68.